UNIVERSITÀ DEGLI STUDI DI PALERMO

Corso di Dottorato di Ricerca in
“Energia e Tecnologie dell’Informazione - curriculum Fisica Tecnica e Ingegneria Nucleare”
Dipartimento di Ingegneria
Settore Scientifico Disciplinare ING-IND/19

THERMAL-HYDRAULIC STUDY IN SUPPORT OF THE DESIGN OF THE DEMO BALANCE OF PLANT

IL DOTTORE
IVO MOSCATO

Ivo Moscato

IL COORDINATORE
CH.MO PROF. MAURIZIO CELLURA

IL TUTOR
CH.MO PROF. PIETRO ALESSANDRO DI MAIO

IL CO-TUTOR
PH.D. PIERLUIGI CHIOVARO

Pierluigi Chiovaro

CICLO XXXII
ANNO CONSEGUIMENTO TITOLO 2020

To Melania, Francesco and Mara

Table of Contents

List of Figures

List of Tables

Abbreviations

Abbreviation	Definition
AGR	Advanced Gas Reactor
ASME	American Society of Mechanical Engineers
BC	Boundary Condition
BB	Breeding Blanket
BM	Blanket Module
BOL	Beginning of Life
BoP	Balance of Plant
BP	Back Plate
BPVC	Boiler and Pressure Vessel Code
BSS	Back Supporting Structure
CB	Cassette Body
CEA	Commissariat à l’Energie Atomique
CFD	Computational Fluid-Dynamic
CHF	Critical Heat Flux
DCLL	Dual-Coolant Lithium Led
DEMO	DEMOnstration Fusion Power Reactor
DI	Department of Engineering
DIV	Divertor

DN	Double Null
ELM	Edge Localized Mode
EOL	End of Life
EOS	Equation-of-State
ESS	Energy Storage System
EU	European Union
FW	First Wall
H&CD	Heating and Current Drive
HCLL	Helium-Cooled Lithium Led
HCPB	Helium-Cooled Pebble Bed
HEM	Homogeneous Equilibrium Model
HP	High Pressure
HPC	High Performance Computing
HTC	Heat Transfer Coefficient
HTR	High Temperature Reactor
IAPWS	International Association for the Properties of Water and Steam
IB	Inboard Blanket
IBL	Inboard Blanket Left (segment)
IBR	Inboard Blanket Right (segment)
IHTS	Intermediate Heat Transfer System
IHX	Intermediate Heat eXchanger
IVT	Inner Vertical Target
KAERI	Korean Atomic Energy Research Institute
KDII	Key Design Integration Issue

LMFBR	Liquid Metal Fast Breeder Reactor
LP	Low Pressure
NBI	Neutral Beam Injector
NMM	Neutron Multiplier Material
NPP	Nuclear Power Plant
NRC	Nuclear Regulatory Commission
NVG	Net Vapour Generation
OB	Outboard Blanket
OBC	Outboard Blanket Central (segment)
OBL	Outboard Blanket Left (segment)
OBR	Outboard Blanket Right (segment)
ONB	Onset Nucleate Boiling
OVT	Outer Vertical Target
PCS	Power Conversion System
PCD	Pre-Conceptual Design
PCRV	Pre-stressed Concrete Reactor Vessel
PES	Plant Electrical System
PFU	Plasma-Facing Unit
PHTS	Primary Heat Transfer System
PMU	Programme Management Unit
PWR	Pressurized Water Reactor
R&D	Research and Development
RAFM	Reduced Activation Ferritic/Martensitic
RANS	Reynolds Averaged Navier-Stokes

RCS	Reactor Coolant System
S&T	Shell and Tube
SG	Steam Generator
SMS	Single Module Segment
SN	Single Null
SS	Stainless Steel
SX	Super-X
TBR	Tritium Breeding Ratio
TFC	Toroidal Field Coil
TH	Thermal-Hydraulic
UPC	Upper Pipe Chase
US	United States
VV	Vacuum Vessel
WCLL	Water-Cooled Lithium Led

Disclaimer

Abstract

The European Research Roadmap to the Realisation of Fusion Energy, foresees that the Demonstration Fusion Power Reactor (DEMO) is going to be the successor of ITER reactor in the pathway towards the exploitation of nuclear fusion to produce electric energy on an industrial scale. It will, hence, have to deliver hundreds MW of electric power ensuring an adequate availability and reliability of operation over a reasonable time span.

EU-DEMO pre-conceptual design is being conducted by research institutions and universities from 26 countries of European Union, Switzerland and Ukraine, with the main aim to provide electric energy to the grid from nuclear fusion reactions by 2050.

However, where exactly DEMO should be located in between ITER and a commercial fusion power plant depends on the resources, the gaps towards a commercial plant as well as the development risks that can be accepted and the time scale to fusion deployment. It is worth to say that, due to the inherent different mission between the two machines, some of the technical solutions adopted for ITER are not DEMO relevant and a return of design and operational experiences cannot be expected from ITER in certain fields.

For instance, as DEMO has been conceived to deliver net electric power to the grid, the reactor design must be more oriented toward the Balance of Plant (BoP) issues than it is in ITER, where the heat power, available at a rather low temperature level, will be wasted to the environment heat sink without any energy conversion intended to civil applications and/or exploitation.

Therefore, since the early phase of the DEMO project, emphasis has been given to those engineering aspects and design integration issues that actually affect the architecture of a nuclear power plant, e.g. technology readiness, power conversion features, safety and related licensing aspects etc.

Within the framework of the R&D activities DEMO-oriented, promoted and supported by the EUROfusion Consortium, it has been carried out the research activity relevant to the XXXII cycle of the Ph.D. course in Energy and Information Technologies. In particular, the main objective of the theoretical research campaign has been to outline a pre-conceptual design of the Primary Heat Transfer System for the helium-cooled Breeding Blanket concept. The choice of the Breeding Blanket option, thus of the primary coolant, plays a pivotal role in the whole reactor Balance of plant architecture having a strong influence on plant operation, safety and maintenance.

The studies have been articulated in two main phases: in the first part of the work it has

been carried out a thermal-hydraulic and mechanical design of the main system components following and developing analytical/semi-analytical procedures by the adoption of the methodologies commonly used for this purpose; the second half of the activities has intended to verify the effectiveness of these procedures as well as the robustness of the design, therefore an assessment of the thermal-hydraulic behaviour of the primary heat transfer system has been made by means of a theoretical-computational approach based on the Finite Volume Method and adopting suitable releases of both 1-D and 3-D codes.

The Ph.D. activities, which were led from the end of 2016 to the second half of 2019, are going to be extensively described in this thesis.

Executive Summary

The present Ph.D thesis has been developed within the framework of the R&D activities DEMO-oriented, promoted and supported by the EUROfusion Consortium.

The first chapter provides a brief introduction on the DEMOnstration Nuclear Fusion Power Reactor, highlighting the main missions that the plant shall accomplish as well as the challenges that the reactor must face in order to provide electrical power by the ‘50s. Among the eight “Key Design Integration Issues” identified by the EUROfusion Consortium, the thesis focuses the attention on the fifth, which deals with the design and integration of the whole Balance of Plant system. In particular, the work concentrates the efforts on the thermal-hydraulic design of the Primary Heat Transfer System of the Helium-Cooled Pebble Bed Breeding Blanket concept.

The second chapter is devoted to a detailed description of the different DEMO Balance of Plant options currently under investigation. To cope with the pulsed operation of the Tokamak, several strategies are being studied: one conceiving an “indirect coupling” of the Breeding Blanket Primary Heat Transfer System to the Power Conversion System by means of the adoption of an Intermediate Heat Transfer System placed in between them; other three alternative design options feature a more “direct-coupling” of the primary systems to the Power conversion System. An overview of the main systems that compose the “heat transfer chains” aimed at transporting and converting the heat produced by fusion power into electrical power is also provided.

The third chapter provides an insight on the criteria that have been adopted in the design of the main equipment of the Primary Transfer System of the Helium-Cooled Pebble Bed Breeding Blanket. Attention has been given to the selection of a proper cooling loops segmentation and arrangement. Specifically, a final configuration that conceives 8 independent loops has been chosen as it has been judged the most promising between two possible alternatives. According to the selected segmentation, each cooling circuit feeds the BB segments related to 2 Tokamak sectors, therefore it delivers helium to 4 IB segments and 6 OB segments.

The fourth chapter describes the design of the different types of heat exchangers and steam

generators the primary system will be equipped with, depending on the specific BoP option under consideration. A careful literature review on the exchanger configuration usually adopted in nuclear industry is provided before going into the details of the design methodology and the thermal-hydraulic assessments followed to size the components.

Two possible options of Intermediate Heat Exchanger have been identified as suitable solutions to be employed in the “indirect-coupling” Balance of Plant options. They are both based on the shell and tube exchanger technology but one relies on the use of straight tube bundle while the second, oriented to be a modular component, encloses several bundles of helical tubes within its envelope. For the “direct-coupling” BoP options, a unique typology of Steam Generator has been selected. It shows geometrical features very similar to the second solution of intermediate heat exchanger described above.

To check the design methodology and the level of confidence of the results a preliminary evaluation of the uncertainty on the main thermal-hydraulic quantities has been made. Then a benchmark against numerical and experimental data has been also carried out to further validate the methodology adopted.

The fifth chapter deals with the design of the pipework connecting the In-Vessel circuits to the exchangers and the assessment of the overall pressure drops within the main segments of the entire primary system. The evaluations have been made for all the exchanger options previously investigated but no remarkable differences have been noticed.

The sixth chapter focuses on the sizing of the main circulators to be adopted in the primary system. After a literature review, a preliminary analysis addressed to select the most suitable circulator type has been performed.

A brief summary of the main achievements obtained from chapter 3 to chapter 6 is reported in the seventh chapter in order to provide, at a glance, an overview on the actual status of the Primary Heat Transfer System design and integration within the Tokamak Building.

The eighth chapter includes all the numerical simulations performed to verify the effectiveness of the procedures followed in the previous chapters as well as the robustness of the design achieved. To this purpose, an assessment of the thermal-hydraulic behaviour of the Primary Heat Transfer System has been made by means of a theoretical-computational approach based on the Finite Volume Method and exploiting the features of well-established and robust computer programmes such as Ansys CFX, a fully 3-D CFD tool, and the RELAP5-3D system code, a truly state-of-the-art program for the nuclear thermal-hydraulics.

Conclusions are given in the last chapter.

1 The DEMOnstration Fusion Reactor

1.1 Introduction

The realization, by 2050, of a DEMOnstration Nuclear Fusion Power Reactor (DEMO) as a ITER next step, with the capability of generating several hundreds of MW of net electric power, is viewed by European Union (EU) as the remaining crucial step towards the grand-scale exploitation of nuclear fusion power [1].

The recently updated EU fusion roadmap, developed within the framework of Horizon 2020 research programme, advocates for a pragmatic approach, based on the system engineering, and considers a pulsed "low extrapolation" DEMO. This should be based on mature technologies and reliable regimes of operation, as much as possible extrapolated from the ITER experience and on the use of materials and technologies adequate for the expected level of neutron irradiation and damage [1].

In order to promote and coordinate Research and Development (R&D) activities relevant to the DEMO pre-conceptual design, the EUROfusion Consortium has been created in 2014 thanks to the joint effort of European universities, associations, research centres and industries, with the main goal to achieve the milestones selected within the above mentioned European fusion roadmap.

DEMO in Europe is considered to be the last step before the first of a kind commercial fusion power plant being capable of:

1. resolving all remaining physics and technical issues foreseen in the plant and demonstrating the necessary reactor relevant technologies;
2. demonstrating production of several hundreds of MW of electric power;
3. achieving tritium self-sufficiency (DEMO must breed its own fuel);
4. operating with adequate availability/reliability over a reasonable time span [2].

Taking into account the many uncertainties that are still pending at this stage of development, a definitive choice of the main DEMO parameters seems premature, therefore more than one options are being investigated for the DEMO reactor design. In particular, in order to keep low the extrapolation from ITER physics and technology, the first studies are mainly focused on a pulsed tokamak concept, the so-called DEMO1, whereas the possibility to have a steady-state machine, namely the DEMO2 concept, is under active consideration [3] for the next future.

Nevertheless, due to the major challenges that must be faced for the latter options, in particular with regards to the Heating and Current Drive (H&CD) performances and reliability, the main DEMO systems are currently designed for a pulsed operative scenario [4].

The latest tokamak baseline for the DEMO1, released in June 2017, is depicted in Figure 1.1.

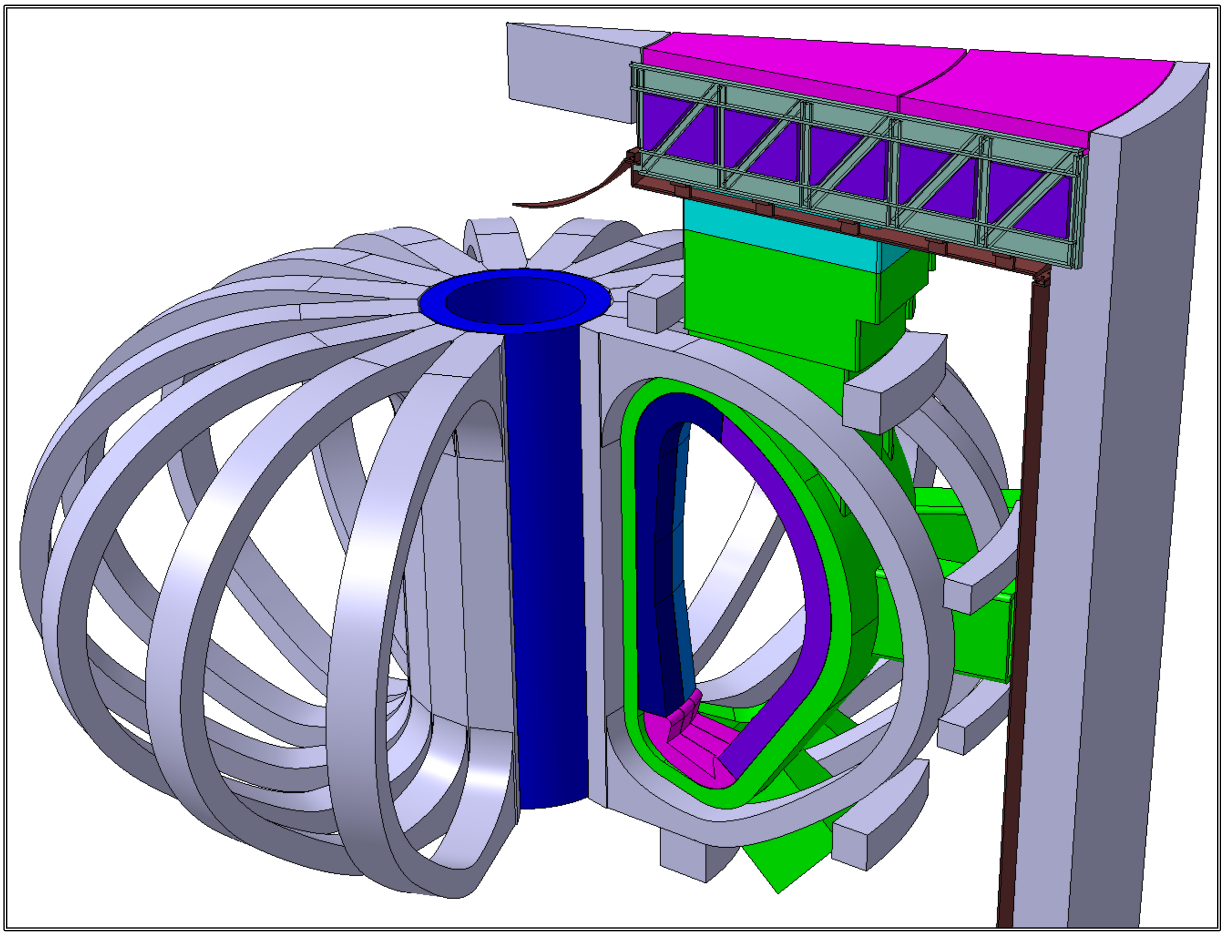

Figure 1.1. DEMO1 baseline tokamak 2017: CAD model [5]

The basic tokamak reactor parameters, relevant to the DEMO1 concept and used as starting point for the design and analyses of the main EUROfusion tasks, can be found in [6].

1.2 The DEMO Key Design Integration Issues

As the DEMO project is still in the Pre-Conceptual Design Phase (PCD), the first of the three main technical phases that are foreseen before its construction will start, different DEMO design options are being explored. This phase is focused on a design integration approach, relied on systems engineering, which is necessary from an early stage to identify and address the engineering and operational challenges, and prioritise the required technology and physics R&D [4]. In fact, the selection of suitable plant design parameters and technical characteristics of the systems to be integrated begins with the definition of the plant requirements and always involves trade-offs between the attractiveness and technical risk associated with the various design options considered. Certain design, physics or technology choices are so integral to the plant architecture, that they have significant implications on a large number of systems that must be integrated into the plant. If such choices are made in isolation, they could have adverse effects on the design of the plant as a whole, adding risks and complexity to the design and increasing the difficulties for the integration of one or more systems and, ultimately, the relevant costs. The risk of postponing integration, assuming that it restricts innovation and inhibits an attractive DEMO plant, is that designers remain oblivious to integration issues and develop design solutions that cannot be integrated in practice. Therefore eight design issues, the so-called “Key Design Integration Issues” (KDIIs), have been identified for being analysed during the PCD phase, as their impact on whole plant design architecture, safety, maintainability and licensing might be crucial [7].

The KDIIs are briefly described in the following.

1.2.1 KDII-1 - Wall protection to withstand plasma transients

Owing to the tritium self-sufficiency requirements, the First-Wall (FW) of DEMO must be relatively thin in order to minimize as much as possible the detrimental effect that it has on the neutrons flux entering into the breeding zone. This, together with the requirement of using Reduced Activation Ferritic/Martensitic (RAFM) steel like EUROFER for structures and cooling pipes of the BB, limits the FW power handling capability to ~1.5 MW/m^2 or ~1 MW/m^2 for water and helium cooled BB options, respectively. Although the heat fluxes should not exceed these limits under nominal conditions for the present DEMO blanket designs, concerns have arisen with regard to plasma transients, when surface heat loads dramatically increase for a limited time span. Therefore, if adequate provisions are not taken into account, a few occurrences of plasma transient events may severely jeopardize the first-wall or even lead to a break of its cooling channels and to the consequent loss of coolant into the vacuum chamber. To face this issue, several options are under assessment. They include the possibility to adopt a: 1) plasma conforming wall w/o limiters; 2) guard limiters; 3) double-null Divertor (DIV).

Additional information on this topic can be found in [8].

1.2.2 KDII-2 - Breeding Blanket design and ancillary systems: helium or water as a coolants

Due to the high number of ancillary systems that are linked to the Breeding Blanket, it plays a key role in the integration aspects for DEMO, hence the choice of the coolant affects the overall design layout of the plant, and bears a strong impact on design integration, maintenance and safety.

It is generally agreed that water should be considered as the coolant for the DEMO Divertor because it seems the only candidate that can manage the very high heat flux experienced by this components [9]. Otherwise, the choice of the coolant for the Breeding Blanket is still under discussion and two options are presently considered: water and helium. Technical issues influencing the choice encompass: (a) thermal power conversion efficiency; (b) pumping power requirements; (c) required power handling capabilities of the blanket first-wall; (d) mechanical properties of the structural material under n-irradiation; (e) n-shielding requirements (e.g. reduce the blanket thickness that is critical at the inboard side); (f) achievable tritium breeding ratio; (g) tritium extraction from the breeder; (h) tritium permeation, inventory and control; (i) chemical reactivity, coolant leakages and chronic release; (j) design integration and feasibility of BoP; (k) design of safety system.

Studies are progressing to investigate all the aspects related to the selection of the coolant for the blanket and, consequently, the BoP. Preliminary results are reported in [10].

1.2.3 KDII-3 - Advanced magnetic Divertor configurations

The selection of the Divertor configuration is another pivotal aspect to pursue a proper design integration. It is still unclear whether the design option adopted in ITER is also suitable for DEMO or whether an alternative solution is needed.

Lots of uncertainties are present regarding the prediction capabilities of the concepts developed for the energy confinement of highly-radiating plasmas, such that of ITER, and an adequate amount of experimental data will be available owing to ITER operation.

Attractive alternative Divertor configurations [11] including Double Null (DN), Snowflake (SF) and Super-X (SX), might offer the possibility of distributing the Divertor heat loads on larger “wetted” surfaces which result in either increasing the number of strike points accounting for flux expansion, or enhancing the level of SoL/divertor radiation to decrease the power density on the targets. The physics performances of these advanced Divertor configurations are being investigated, but there are serious concerns on the implications arising from their engineering requirements such as, for example, integrating additional coils which provide additional neutron-shielding and more complex remote maintenance provisions [13].

Specific work is underway to assess the impact of incorporating these alternative configurations into DEMO whilst respecting requirements on remote handling access, forces on coils, as well as plasma control and performance.

For further details it is recommended the reading of [13]

1.2.4 KDII-4 - Tokamak architecture based on vertical blanket segments

All the DEMO In-Vessel Components (IVCs) will be activated due to the high neutron flux coming from the plasma. Remote Handling (RH) of these components will be necessary to replace them after being damaged by particles irradiation as well as to prevent workers and operators from the radiation exposure.

Currently the BB segmentation relies on the adoption of large vertical segments [14]. However the handling of full blankets segments would be a very critical operation due to the limited space in the port, the control issues associated with the stiffness of the transporter and the payload, the seismic constraints and the potential consequences of dropped loads. For these reasons, alternative blanket segmentation concepts have been considered, becoming the topic of the fourth KDII to be solved in the concept design phase. So combining such a challenge with the opportunities coming from the KDII-1 and 3, alternative architectures that can meet the DEMO plant requirements are being considered [15].

1.2.5 KDII-5 - Indirect or Direct power conversion system option

Since DEMO must provide electric power to the grid, proper critical evaluations on the features of the Balance of Plant (BoP) are needed as it plays a pivotal role in the design and licencing of the overall plant. In the PCD phase, some activities have begun focusing on few important aspects of BoP [16], particularly the BB Primary Heat Transfer System (PHTS) [17] and the relevant Power Conversion System (PCS) because of their technical complexity and strong impact on design integration [18], maintenance and safety. Differently from a fission Nuclear Power Plant (NPP) where the BoP main components are basically designed to operate under steady state conditions and not to undergo very frequent/sudden transients, in DEMO the pulsed operation will be particularly demanding for all the BoP and Plant Electrical System (PES) components. Therefore, a BoP option contemplating an Intermediate Heat Transfer System (IHTS) equipped with an Energy Storage System (ESS) is currently being considered, which adds complexity and costs to the plant, affecting its reliability and availability. Alternative design options, featuring a more direct coupling of PHTSs to PCS and requiring, for instance, a very low steam flow for operating the turbine and, thus, much smaller storage of molten salt, are being studied [16].

1.2.6 KDII-6 - Integrated design of tokamak building concepts

Another major challenge to be faced in DEMO is the early identification of the main building and structures needed in order to properly place the equipment of different systems. Owing to the distinct requirements characterising the two BB cooling options (water and helium), likewise two plant layouts have been preliminary developed with the support of leading industries (ANSALDO, FRAMATOME, etc.) [19], taking advantage from their experience gained over tens of years in building nuclear facilities and power plants. In fact, the building design criteria must meet the strict safety and licensing requirements imposed by the National Nuclear Safety Regulator [20].

Further details on the on-going activities can be found in [21].

1.2.7 KDII-7 - Pumping concepts based on tritium direct recirculation

The management of both fuel and fusion exhaust gas products is an essential issue for the industrial exploitation of fusion energy. The challenges for a safe and efficient control of the fuel cycle are given by the need to handle significant tritium mass flow rates resulting in strong requirements on its containment and accountancy. The extrapolation of the fuel cycle concept adopted by ITER will not be feasible for DEMO because of the much larger throughput. Therefore a novel fuel cycle architecture, based on the concept of Direct Internal Recycling (DIR) [22] is being investigated to minimise the tritium inventory. Clearly, proofing the feasibility of this concept is a high priority. In order to replace the discontinuous pumping used in past fuel cycle architectures with continuous pumps operation, the so-called KALPUREX process is being developed [23]. It is based on mercury to be fully tritium-compatible and a large scale demonstration unit for this technology is under preparation [24]. This promising process conceives the separation of pure unburnt fuel from the exhaust gas close to the torus by means of a metal foil pump. Although superpermeation, the basic physics principle behind the behaviour of a metal foil pump, is well known, it has never been implemented in an engineering design of a technical component such a pump. A first proof-of-principle has been recently achieved [25], but a much more robust R&D programme is under implementation to check the performance and feasibility of this concept. Nevertheless, should the KALPUREX facing a show-stopper in the future, a backup solution that consists of a three-stage cryopump with distributed pumping is also being investigated.

1.2.8 KDII-8 - Development of a reliable plasma-operating scenario including supporting systems

The design of any fusion device is strongly affected by the assumed plasma operating scenario. The definition of the plasma scenario for DEMO is based on two high level criteria, ensuring a sufficiently high fusion power outcome to maintain a satisfactorily high net electrical output and saving the integrity of the PFCs for a sufficient operation time. Such requirements have to be met in an integrated approach to the reactor design. This means that a suitable plasma scenario for DEMO and, in general, for every next fusion device, has to be developed by taking into account all the constraints originating from the engineering and technological aspects of the design from the very beginning. In particular, the role of diagnostics, H&CD, and fuelling and pumping have been identified as crucial. Thus, the activities carried out in the PCD phase are being focussed not only towards a deeper understanding of the physics governing the DEMO plasmas, but also on a stricter interaction with the design and technological development process, in order to rely, from the earliest phases, on solutions which are compatible with an integrated and consistent approach to the reactor design [26]. This effort has led to the identification of large risks related to the problems of divertor detachment control and the effective reliability of ELMs mitigation schemes (to be demonstrated in ITER), as a small number of such events could cause serious damage to the divertor targets (see also section 2.3.2). In DEMO-1, a single Type-1 ELM event will be sufficient to melt the divertor target tungsten surface, and 50–100 unmitigated ELMs would result in the erosion of the entire target thickness [27]. As natural ELMs are foreseen with a frequency of ~1 Hz, ELM mitigation measures do not provide a credible solution for DEMO, and thus, it is very likely that an ELMy H-mode cannot be used as a plasma operating regime in DEMO. This is perhaps also true for ITER. Therefore ELM-free regimes, even at somewhat reduced H-factor and pedestal density, might need to be considered for DEMO. R&D in present devices must be focussed towards building knowledge on such regimes (e.g. I-Mode or QH-Mode), namely to find operating boundaries, confinement, L-H transition scalings, avoidance of transition to ELMy H-mode.

1.2.9 Final summary

As already mentioned, the KDIIs are somehow connected to one another, therefore it is worth to underline that the consequences of some decisions made in specific KDIIs would inevitably affect many of the other design options. As a matter of fact, it is clear how a hypothetically choice of the blanket coolant immediately implies the discharge of the BOP options based on the unselected BB concept as well as the adoption of a given building layout among the two possible options.

For such a reason, since this thesis takes place among the research activities carried out in the framework of the KDII-5, in particular it is mainly focused on the design of the BB PHTS for the helium cooled option, it is unavoidable to go into the details of the work without describing some general aspect related to the KDII-2 and its interconnection to the KDII-5.

A detailed description of the DEMO BoP options and the studies being done on this topic during this work will be provided in the next chapters while in the following a brief description of the BB of DEMO will be given, emphasizing those aspects proper of the helium-cooled BB option.

1.3 The Breeding Blanket concepts

Several breeding blanket concepts have been investigated by the scientific international community in the past. Within the framework of European blanket programmes, in particular major design studies were carried-out during the NET Program from 1990 to 1999 and under the Power Plant Conceptual Study (1999–2004) [28], being supported by EFDA. Since 2014 the EUROfusion Consortium has continued investigating the four BB concepts, namely the Helium Cooled Pebble Bed (HCPB), the Helium Cooled Lithium Lead (HCLL), the Water Cooled Lithium Lead (WCLL) and the Dual Cooled Lithium Lead (DCLL). In particular, as a consequence of the first years of studies carried out within the Work Package Breeding

Blanket (WPBB) of the EUROfusion action, in 2017 a revision of the WPBB program has suggested to focus the efforts on the 2 most promising concepts for the so-called DEMO “driver” BB, namely the HCPB and the WCLL BB. Conversely, the HCLL and DCLL BB options have been considered forecoming concepts, allowing limited R&D activities [10] [29]. According to this strategy, it has been also decided to make a re-alignment of the Test Blanket Module (TBM) Program of ITER in order to include a WCLL module in place of the envisaged HCLL one.

This downselection process is fully in agreement with the design and integration work conducted to date, aimed at bridging as soon as possible all the technology gaps that are still present in some areas.

With regards to the HCPB and the WCLL BBs, the former adopts helium as coolant and make use of a solid ceramic lithium with beryllium/beryllides material as breeder and neutron multiplier, whereas the latter is cooled by pressurized water under Pressurized Water Reactor (PWR) conditions and foresees the eutectic lithium-lead liquid mixture as breeder and neutron multiplier. On the other hand, in spite of their intrinsically differences, it can be recognized that their overall architectures have several points of contact, which is basically imposed by the adoption of a common DEMO baseline. They are both toroidally distributed in16 sectors, each including two inboard and three outboard BB segments, whose design commonly rely on the adoption of the Single Module Segment (SMS) concepts. Furthermore, both the concepts foresee the EUROFER97 RAFM steel as structural material. In particular, each segment is made up of a poloidally continuous EUROFER97 external box, composed of the first wall, the side walls, the bottom and top caps and the Back Plate (BP) and housing the Breeding Zone (BZ). Each segment is connected to the VV via the Back Supporting Structure (BSS), which acts as a backbone supporting the entire segment.

For the sake of completeness, additional details about the HCPB concept are reported below, while further info on the latest WCLL design may be found in [30].

1.3.1 HCPB BB concept

The current HCPB blanket design is based on the use of Li_4SiO_4+35mol%Li_2TiO_3 pebble beds as tritium breeder and on hexagonal prismatic blocks of $Be_{12}Ti$ as neutron multiplier. This reference design is developed with reference to the so-called DEMO1 tokamak Baseline 2017 [14, 4]. The coolant and purge gas pipework serving the BB is routed through the upper port to connect the fluids to their respective system, namely the PHTS and the Tritium Extraction System (TER). The pipes are connected to the segments by the so-called segment chimneys. The chimneys are basically large volumes which act as buffer tanks for the coolant in order to obtain the required flow distribution inside the segments. The maximum and minimum pipe dimensions are restricted by remote maintenance system requirements. In particular, the maximum size is limited by the maximum pipe thickness allowable by the in-bore cut-and-reweld tool, while the minimum size is driven by allowable miniaturization of that tool. Due to high neutron irradiation, the structural material of all BB pipes inside the VV will be the EUROFER97 as for the BB. These volumes may require in the future to be partially filled by a neutron shielding material in order to reduce the streaming to the Toroidal Field Coils (TFC), which come close to the chimneys and where the VV thickness reaches its minimum. The wall thickness of the chimneys to withstand the internal coolant pressure should amount to ≈80 mm.

The BB internals are shown in the cross sections A-A and B-B of Figure 1.2 a) and b). The BZ volume is delimited by the SW-FW-SW inner walls and the BP inner surface and it houses a number of hexagonal pressure tubes radially arranged to connect the FW with the BP, so to result the main structural support to prevent a failure against an in-box LOCA. The so-called fuel-breeder pins are housed into the pressure tubes and connected to the BZ backplate [31].

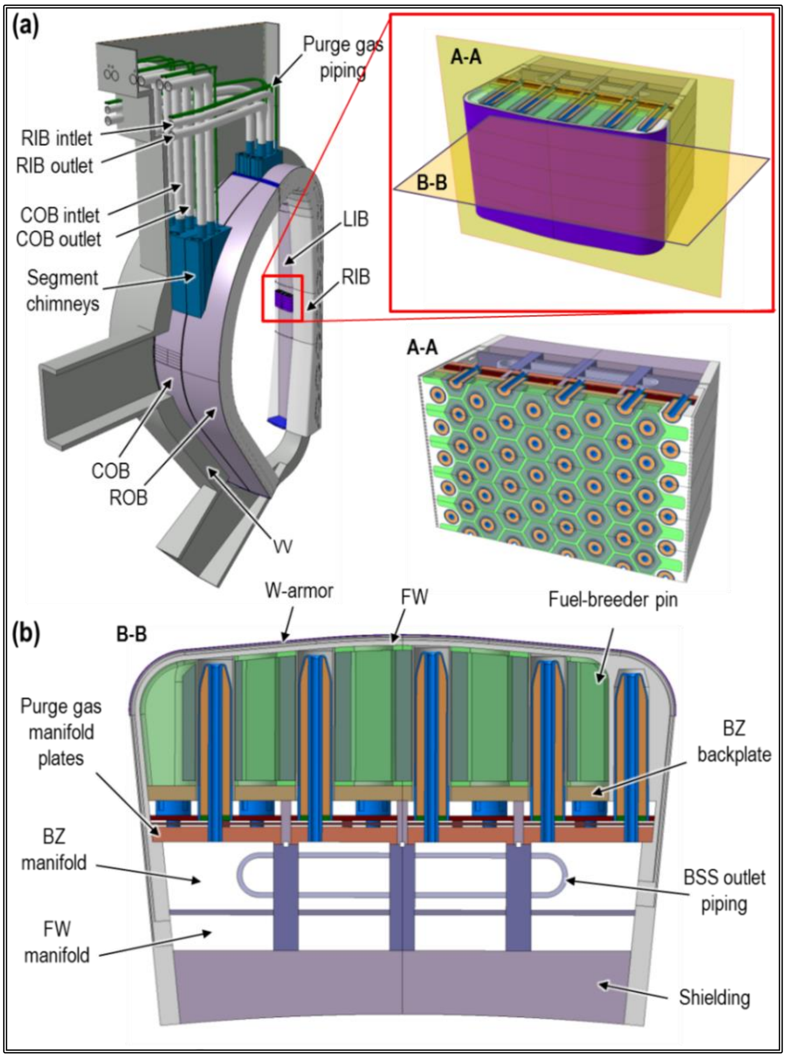

Figure 1.2. HCPB design with fuel-breeder pin hexagonal assembly [31]

A fuel-breeder pin, see Figure 1.3, is a system of 2 concentric cylinders, namely the outer and inner cladding, delimiting an annular region filled with a tritium Ceramic Breeder (CB) material, the so-called KALOS CB, which is in form of a pebble bed (pebble size 250 µm to 1250 µm). It contains Lithium enriched in ^{6}Li at 60% to ensure enough tritium breeding performances. An advantage of the fuel pin configuration is that the enrichment in a pin can be easily tailored along the radial direction of the pin, e.g. increasing the ^{6}Li content at the back of the pin to effectively tune and further enhance the radial distribution of tritium breeding, nuclear heating and temperature distribution. The $Be_{12}Ti$ has been selected as Neutron Multiplier Material (NMM) to ensure a proper tritium breeding due to its positive neutronic characteristics and enhanced safety features [32]. For the reasons discussed in [32], the $Be_{12}Ti$ is in form of a (hexagonal) prismatic block with a central bore, where the corresponding pressure tube finds its place, leaving a gas gap of 2 mm between both at the assembly [33].

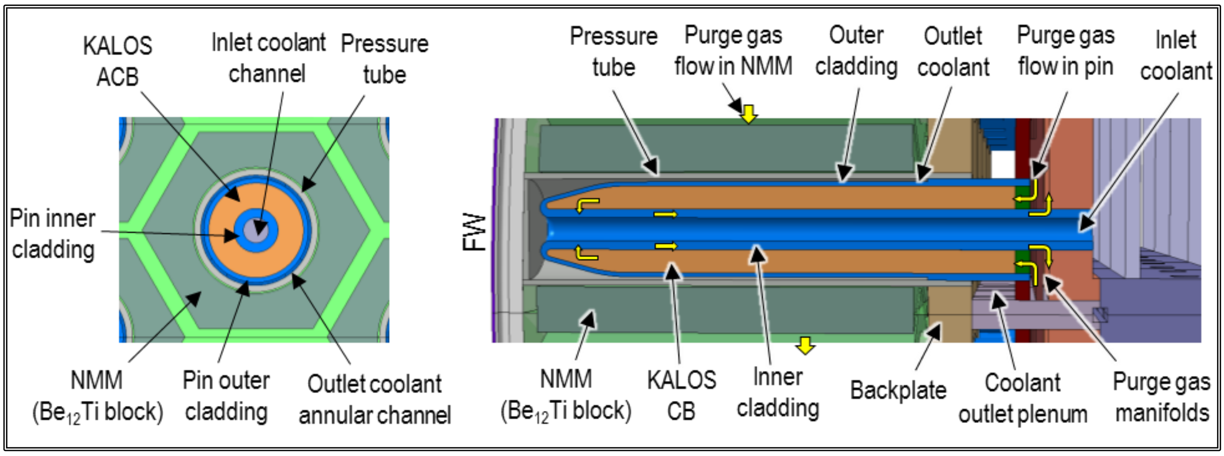

Figure 1.3. Fuel-breeder pin: a) poloidal-toroidal section, b) radial-toroidal section [33].

Between the blocks there is a gas gap of 10 mm. This large gap reduces the amount of NMM material, but it can be adjusted in the future to minimize the neutron streaming, if needed. Tritium is produced in both CB and NMM and it is extracted and transported out of the segments by means of a purge gas, which is He + 0.1% vol. H_2 [33]. The purge gas enters the NMM prismatic blocks first and sweeps them from top to bottom. In a second step, the purge gas enters the pins (all connected in parallel), flushing the CB beds from the BZ backplate to the front of the pins. The purge gas is collected into ducts machined in the 6 mm thick inner cladding and it is directed to the purge gas outlet manifold, on its way out of the segment (Figure 1.3).

Helium is used as the coolant of the blanket structures. The main drawback of gas cooling is its compressibility and low density, which can result in large parasitic plant power recirculation if attention is not given to reduce the pressure drop in the PHTS and limit its heat transfer capability. In order to enhance the heat transfer with a limited penalty on pressure losses, the adoption of turbulence promoters (i.e. augmented heat transfer structures), like V-ribs and increased surface roughness is essential. Therefore, the plasma side of the FW channels are equipped with V-ribs or at least with a surface roughness of R_a = 40-50 μm. The inner side of the pressure tube and the outer surface of the pin cladding are also foreseen with a $R_a \approx 40$ μm.

The segments are closed on top and bottom with the so-called caps (Figure 1.4). These components are formed by a thick plate (tentatively t ≈ 100 mm) in which deep holes of $Ø_{int}$ = 70 mm are drilled radially in order to house fuel-breeder pins. The cap makes thus the function of a row of (connected) pressure tubes, it is directly cooled by the same coolant as the pins and serves as structural element against in-box LOCA. The lateral pins at the side walls, as well as the FW cooling channels, are varied in their orientation in order to have a moderate transition from the segment to the cap region, thus avoiding large uncooled regions at the side walls.

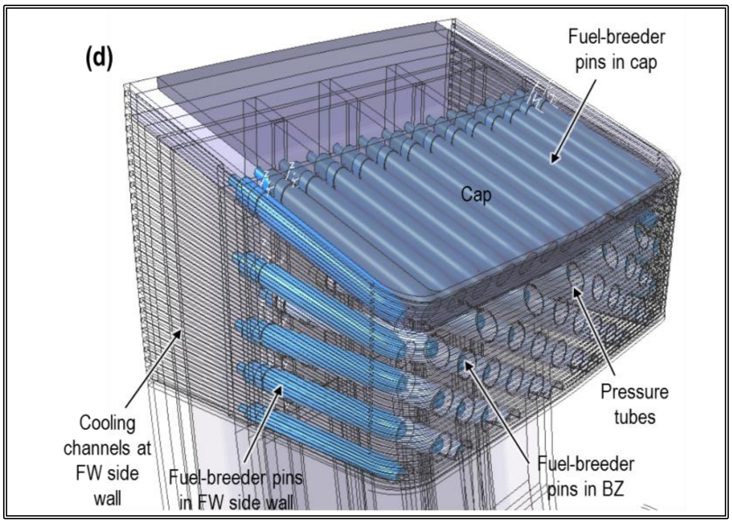

Figure 1.4. Detailed view of the segment top cap [33].

2 The DEMO HCPB Balance of Plant

2.1 Introduction

DEMO is going to be the first fusion device that will produce electricity and, hence, it shall be provided with a proper BoP system. Furthermore, being a nuclear facility, the DEMO BoP must meet many of those design criteria and safety requirements charactering the most common nuclear power station.

In particular, a parallelism between the NPPs and the DEMO reactor is not so trivial. For instance, in fission NPPs, there is a single primary system, namely the Reactor Coolant System (RCS), that is in charge of extracting the thermal power from the core and deliver it to the PCS through the Steam Generators (SGs) in order to be converted in mechanical and then into electrical power via the turbo-generator set. In DEMO, conversely, the first feature that makes the design unique and more complex compared to fission NPPs is the presence of separated PHTSs that remove power from the TOKAMAK. Such choice is needed because the three main components that extract the thermal power from the machine - BB, Div and VV - have different functions and requirements to be fulfilled making almost impossible and quite risky the use of a single coolant operating at the same thermal-hydraulic (T/H) conditions [34].

Furthermore, in fission NPPs the RCS works mainly under steady-state conditions transferring, a slightly varying or constant power output to the PCS, which is traditionally the main system of the BoP. In DEMO, instead, the pulsed nature of the plasma operating modes adds a further degree of complexity enhancing the dependence of PCS operation on the BB, DIV and VV PHTSs performances. In fact, the duty cycle of DEMO foresees a continuous sequence of 2 main phases connected by 2 transitional phases: 1) the plasma ramps-up within about 100 seconds bringing its power from zero to the maximum value, 2) when the full power level is reached this condition is kept alive for 2 hours, then 3) a ramp-down of around 100 seconds begins leading the system into 4) the dwell phase which lasts 10 minutes and where almost no power is generated (the decay heat 1 s after shut-down is around 2% of the nominal power).

The DEMO power duty cycle is depicted in Figure 2.1.

This scenario enables the DEMO PHTSs to become central actors of the BoP because their inherent un-steady operation must be carefully handled in order to soften the propagation of the fluctuating power through the mutually interacting circuits.

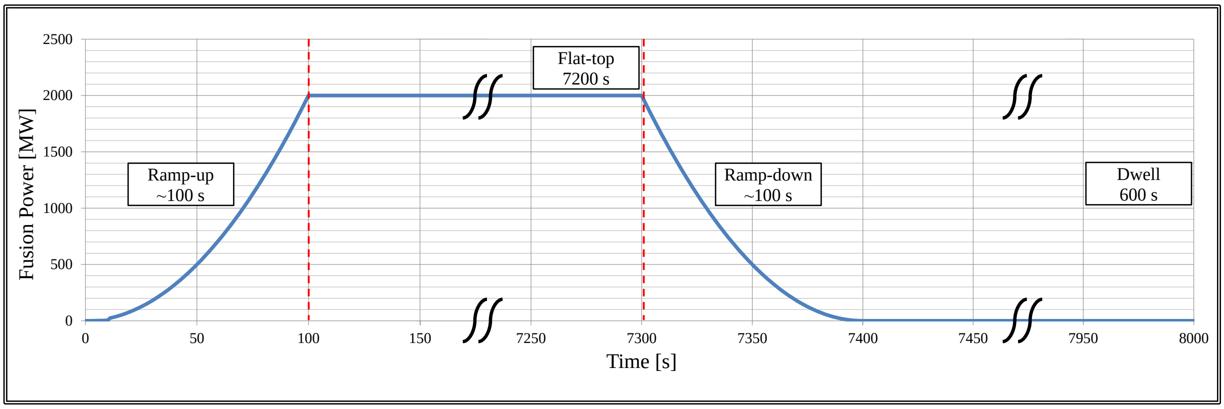

Figure 2.1. DEMO duty cycle.

It is obvious, indeed, that oscillating loads might challenge the qualified lifetime of the main BoP equipment inducing undue thermal and mechanical cycling. Although it is rather impossible to prevent the occurrence of such cycling in PHTs components, several strategies are being considered to eliminate or, at least, mitigate the potential negative effects of the pulsed operations on PCS main components, such as turbine and steam generators. The study and the development of multiple configurations is being pursued in order to achieve an effective identification of the best solution and minimize technological risks.

In this direction the leading approach followed is similar to that used in the solar energy industry, attempting to thermally decouple the PCS from the PHTSs interposing among them an Intermediate Heat Transfer System (IHTS) equipped with an Energy Storage System (ESS). The aim of this intermediate system would be to act as a bridge between the PHTSs and the PCS, allowing to collect a portion of the thermal power transferred by the PHTSs during the Pulse period in order to save thermal energy to deliver to the PCS during the Dwell time. In this way the turbine would ideally work under steady-state conditions during both Pulse and Dwell time of the reactor duty cycle. This option could take credit from the adoption of consolidated components already proven in both fission NPPs and Concentrated Solar Power (CSP) plants so reducing specific R&D needs for the DEMO project.

On the other hand, it would imply the introduction of additional systems that might increase the complexity of the whole BoP design. Therefore, alternative solutions envisaging a more direct coupling of the PHTSs to the PCS are also being investigated. In this case, also the PCS would experience load changes with their detrimental effects on the main components.

A careful identification of proper PCS architecture, suitable operating procedures and design provisions capable to soften the transients on the turbine and on other PCS components would have to be addressed in order reach safe and reliable operations despite the reactor pulsating modes. So, as the steam turbine has been considered as the most sensitive PCS component, three modes of possible operation have been investigated for the PCS starting from it:

1) the steam turbine starts and stops with the same periodicity of DEMO plasma power profile;

2) the steam turbine is un-loaded during the dwell time while the electrical generator is actively motorized in order to keep the turbo-generator set synchronous to the grid;

3) the steam turbine is operated at a minimum steam load, about 10%, during the dwell using steam generated with a small auxiliary boiler or provided by a small Energy Storage System (ESS) (decoupled from the PHTSs) [16].

Such “direct-coupling” options represent a tentative of simplification of the BoP, to avoid the impact of a huge ESS, at least as far as design integration implications and costs are concerned. Clearly, they are more demanding in terms of engineering challenges and R&D programmes, nevertheless any effort to reduce the complexity of the DEMO BoP, through simplification and a rationalisation of its main systems design is expected to have some beneficial returns on the overall DEMO design and systems integration [4].

Finally, it can be reasonably stated that in DEMO the BoP acquires, in a more general sense, the meaning of “a complex chain of systems devoted to the extraction of the thermal power directly or indirectly generated by the plasma in a pulsed mode and to its conversion into electricity”.

The two above described BoP design approaches are presently under investigation for both WCLL BB and HCPB BB BoPs but, in agreement with the objective of this thesis, the next paragraphs are intended to provide information about HCPB BoP system architecture only. The interested reader can obtain further details on the water cooled BoP option elsewhere in [18].

2.2 Overview of HCPB BoP system architecture

The BoP architecture that is currently considered the most promising for the DEMO based on the helium-cooled blanket technology foresees the implementation of an intermediate system with its related energy storage system [16]. As already said, this “indirect-coupling” solution can be developed relying on better established technologies, whose technology readiness level seems to be above the laboratory test, at least for the majority of its equipment.

A conceptual scheme of the proposed indirect-coupled BoP for the HCPB DEMO is depicted in Figure 2.2.

Strictly speaking, in spite of its definition, a thorough examination of the concept puts in evidence the hybrid nature of the chosen architecture, which connects only one of its PHTSs to IHTS, namely the BB, leaving the DIV and VV directly connected with the PCS.

The main rationale behind this approach dates back to the initial studies on the BoP configuration [35] when, as a result of preliminary thermodynamic considerations, it was decided to link the IHTS, thus the ESS, only with the blanket heat removal system.

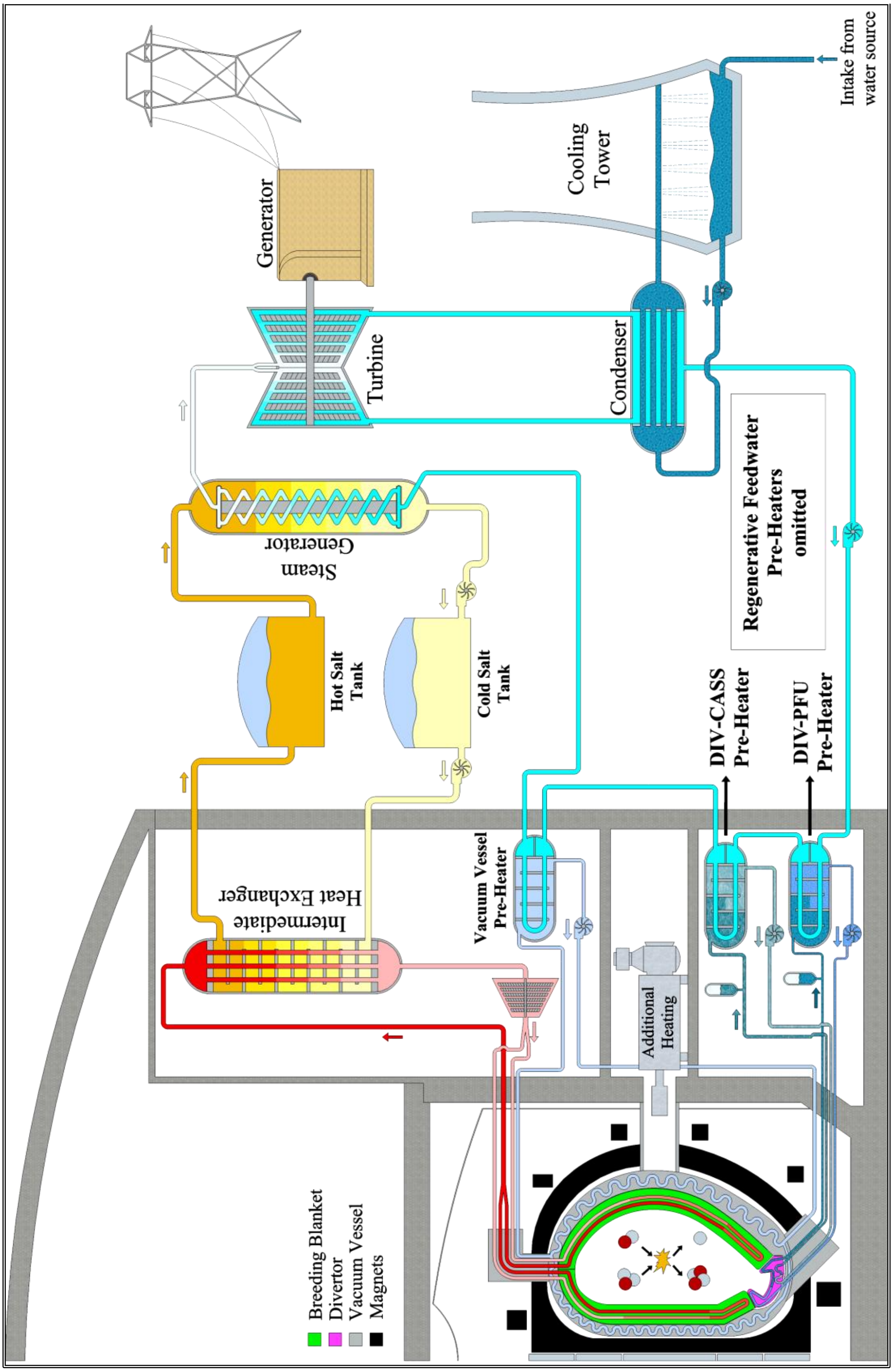

Figure 2.2. Simplified conceptual scheme of BoP - Indirect-coupling option

Indeed, since the BB has to extract about 85% of the whole DEMO thermal power, the energy delivered to the intermediate system during the 2 hours of Pulse is, in principle, enough to design a storage system that manages to satisfy the PCS power demand during the dwell time.

In addition, Divertor and Vacuum Vessel have coolant temperature windows that are rather lower than those considered in the blanket system therefore, after a first survey on the storage technology, some concerns have arisen about the compatibility of these temperature levels with the freezing point of the most suitable storage media (see sections 2.4 and 3.2.1.1.3).

This has definitely formalized the role of the BB as the main hub of the DEMO heat transfer chain also for the "indirect-coupled" BoP configuration and, hence, the development of a feasible design for its PHTS has been seen from the EUROfusion Programme Management Unit (PMU) as the first priority of the BoP actions [34].

Nevertheless, the primary cooling circuits of Divertor and Vacuum Vessel are totally integrated in the BoP scheme and the thermal power removed from these in-vessel components shall be used to pre-heat the PCS feed-water, together with the most common regenerative heaters fed by the steam extraction lines (see section 2.5).

With regard to the "direct-coupling" options, Figure 2.3 illustrates a simplified conceptual scheme for the option 1) and 2) briefly presented in the previous section.

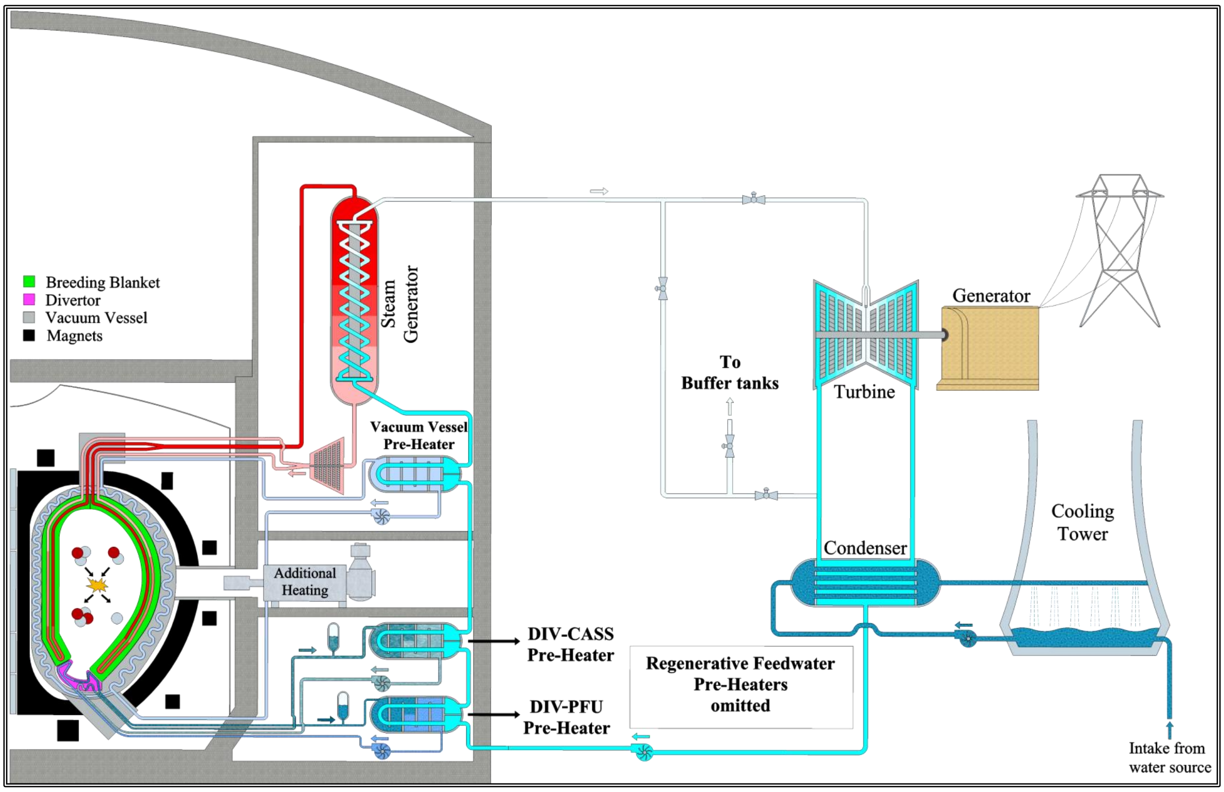

Figure 2.3. Simplified conceptual scheme of BoP - Direct-coupling options 1&2.

In both cases all the PHTSs are directly coupled to the PCS and there is not any system foreseen to provide the turbine with additional steam during the Dwell. Actually, a turbine by-pass, dumping the steam in excess toward either the condenser or some buffer tanks, has to be implemented in order to prevent the turbine from the failure due to its impossibility to follow the sudden plasma shut-down/ramp-up. In fact, even "fast" unloading and uploading operations of the steam turbine would usually require more than the typical 100 s transition time between Pulse and Dwell phases.

Therefore, for the case 1), the continuous sequence of starts and stops during the day (about 11 cycles/day) would cause those cyclic mechanical loads that may determine a untimely turbine wear and its consequent structural failure in few years of operation. Furthermore, similar issues can occur in other PCS components such as boiler feed pumps and feed-water preheaters where transient flow conditions might cause too high stresses and unacceptable thermal cycling reducing the lifetime of the whole system which would need, in any case, much more maintenance with the consequence of increasing the cost of operations. In addition, the electric generator could be also damaged during one of the several sudden turbine disconnections or during its continuous attempts to be re-connected to the grid after having lost the synchronism.

In the case 2) no significant drawbacks are instead expected for the electric generator because, being theoretically a "reversible" machine, its motorization should not bring about too high stresses, neither electromechanical nor electro-dynamic. Moreover, in this scenario the turbine would be driven at nominal speed by the alternator during the Dwell therefore it would be possible to keep the synchronism to the grid.

However, the dragging effect can adversely impact the turbine leading to high frequency vibrations of the blades, ventilation effects and blade erosion especially in the last stages due to water droplet. In view of these preliminary considerations, the development of these options is currently in stand-by [16].

For what concern the option 3), simplified schemes depicting the two variants for the "direct-coupling" option 3) are reported in Figure 2.4 and Figure 2.5. Although in this configuration the PHTSs are directly coupled to the PCS too, it envisages the employment of an auxiliary system that can aid the turbine in doing ramp-down, ramp-up and any supposed operation at low load. Such additional system would be attached to the PCS in parallel to the PHTSs and it would become the main source of steam supplied to the turbine when the Dwell approaches and the main PHTS steam generator would be able to provide only a little quantity of steam due to the TOKAMAK decay heat. The goal is to lighten the turbine operation, making the unloading/uploading processes more similar to the procedure applied in other industrial applications. Thus a supporting system equipped with either a conventional auxiliary boiler or a small energy storage system (based on an external electrical heating source) can be used in order to keep temperature and pressure at the turbine inlet during Dwell as close as possible to those under Pulse conditions.

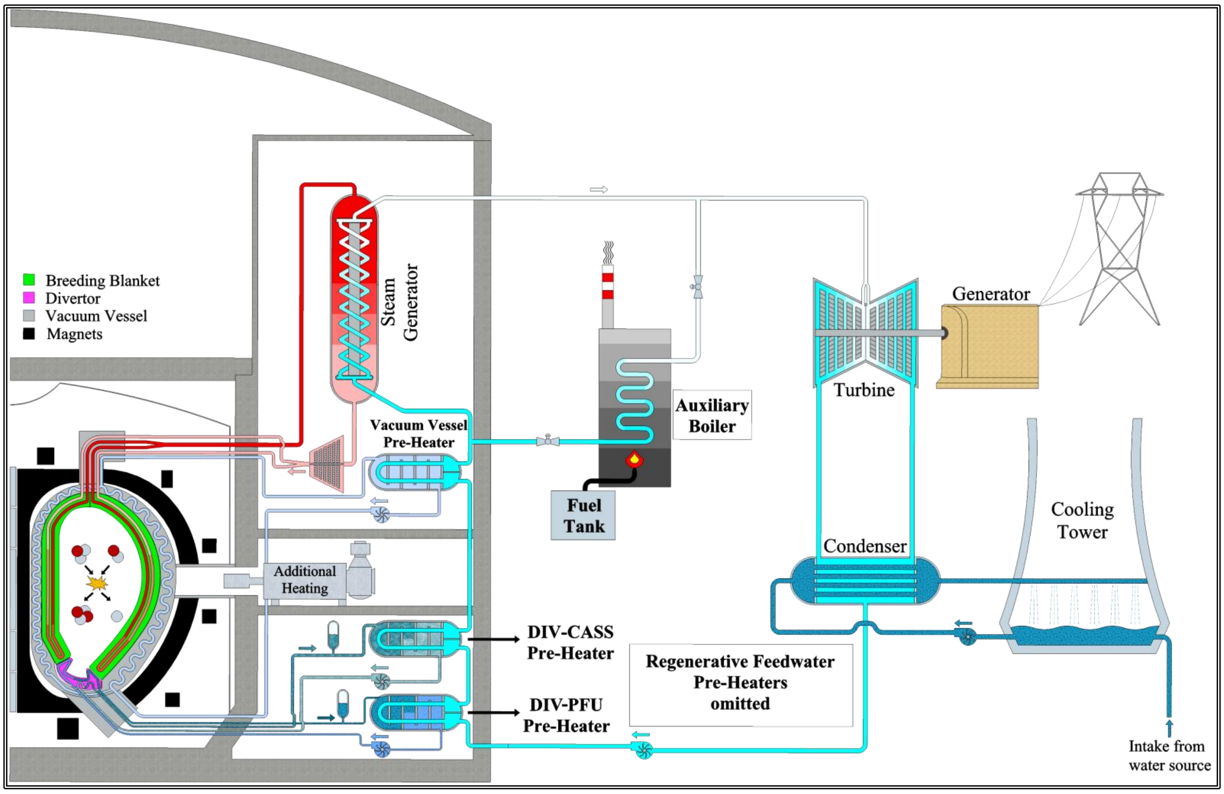

Figure 2.4. Simplified conceptual scheme of BoP - Direct-coupling options 3 with aux. boiler.

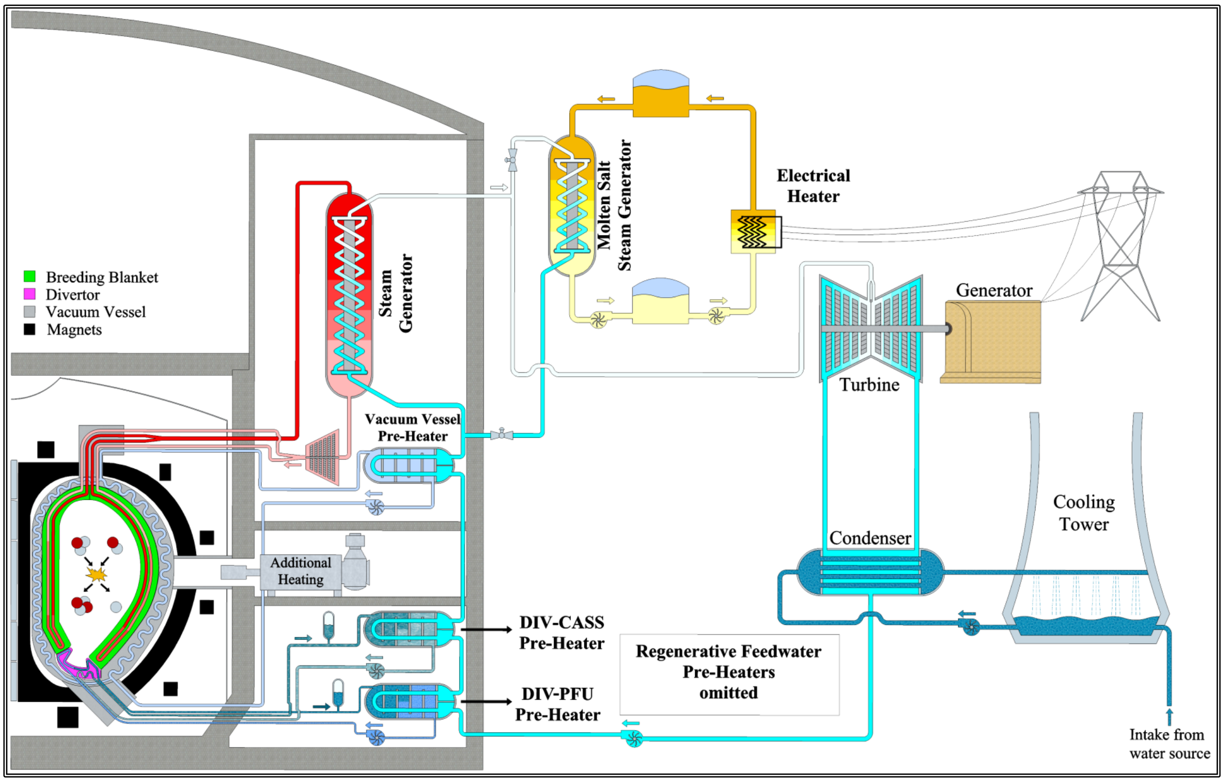

Figure 2.5. Simplified conceptual scheme of BoP - Direct-coupling options 3 with small ESS.

A preliminary evaluation suggests that the ancillary system should be sized to obtain about 10% of nominal steam flow. Nevertheless, it is worth to underline that this operation mode would be usually classified as “OFF-design”, therefore a verification of the behaviour of the turbine is required to assess if the occurrence of unwanted effects (thermal cycling, vibrations etc.) might occur. Moreover, the impacts of such operation mode on turbine control, plant reliability and on the remaining Balance of Plant components have to be carefully addressed too [16].

Regardless of the BoP architecture pursued, the PHTSs will undergo plasma power transients, efforts must hence be mainly focused onto their design which has to cope with this unconventional heat source. In order to better understand the requirements to be fulfilled by the primary circuits, a brief description of the structure of the cooling schemes being under development for the BB, DIV and VV will be given in the following. Then, the overall characteristics of the PHTSs interfaces, namely the IHTS and/or the PCS, will be discussed too.

2.3 The Primary Heat Transfer Systems

DEMO presents four independent PHTSs. The largest PHTS is devoted to remove the thermal power from the BB, two PHTSs are necessary to extract heat from the DIV while the last one is intended to cool the VV.

Although each primary circuit is, of course, made up of one or more closed loops, historically it is customary to divide each PHTS in two main functional regions, namely the In-Vessel and the Ex-Vessel cooling circuits. The latter is roughly referred to, for simplicity, as the PHTS of the component under consideration. This distinction might appear somehow fanciful and it could bring to misleading interpretations, however the reason why the two portions of the primary circuit are kept formally (not physically!) separated, is grounded on the fact that everything belonging to any given In-Vessel component is considered as integral part of the component itself. It is hence developed within the framework of the activity focussed on the design of the component. Moreover, even if the In-Vessel cooling circuits of BB, DIV and VV circuits are designed by three different teams, the respective three Ex-Vessel parts are jointly developed by the BoP team , being this the common interface. Nonetheless, it is not trivial to remark that since the two functional regions of the PHTS are inextricably bonded, any assessment made on one part must be compliant with the requirements of its counterpart.

2.3.1 Breeding Blanket Primary Heat Transfer system

The current HCPB BB PHTS is designed to fulfil requirements and constrains dictated by its so-called “fuel-pin” concept (already described in section 1.3.1), and developed for the EU

DEMO 2017 TOKAMAK baseline [14], where the blanket is subdivided in 16 sectors, each one of 22.5°. Each one of the 16 houses two Inboard Blanket (IB) segments and three Outboard Blanket (OB) segments, that are, in turn, subdivided in FW and BZ where cooling channels are housed. The coolant flow scheme of the In-Vessel cooling circuits is shown in Figure 2.6 while the integral flow scheme in the segment is shown in Figure 2.7.

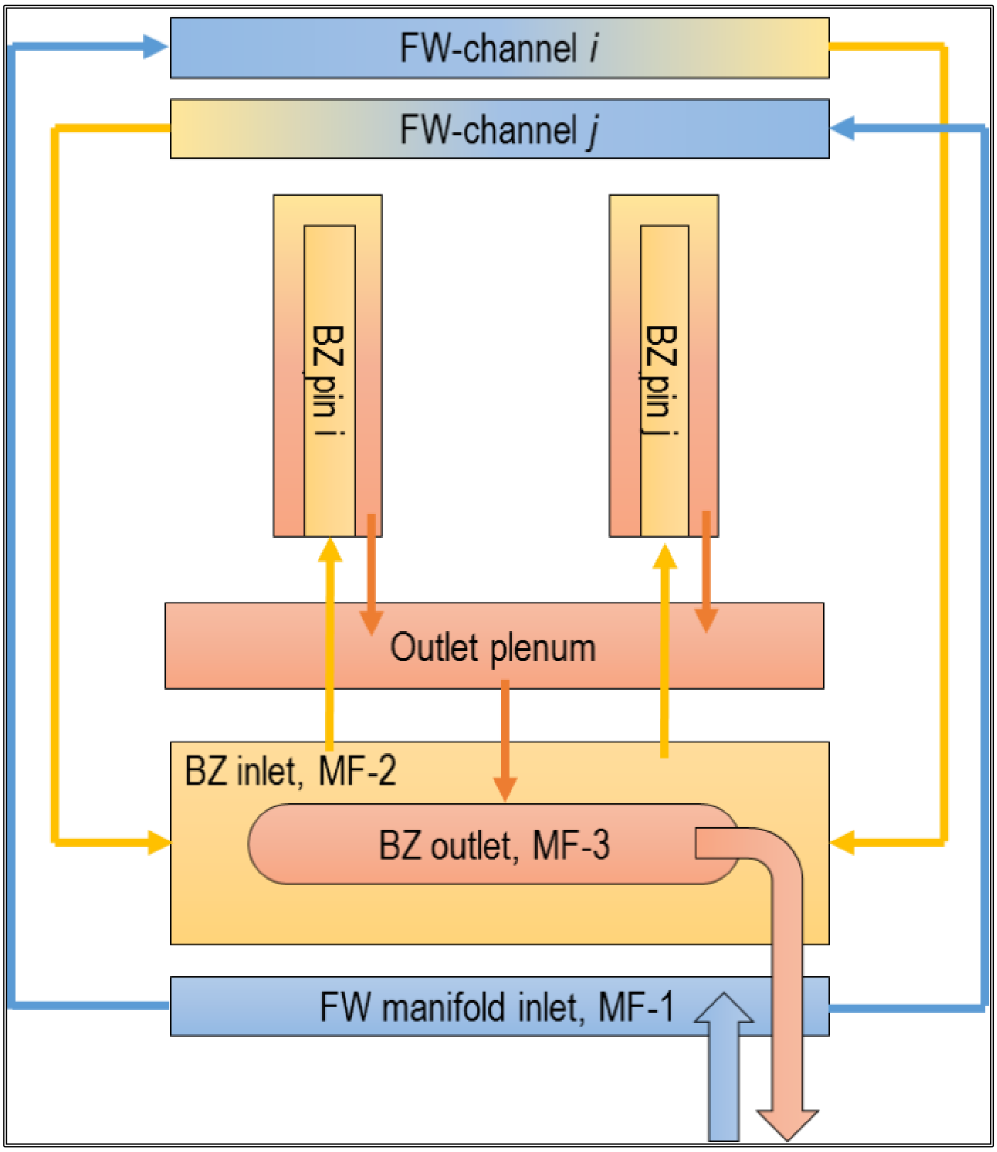

Figure 2.6. Schematic flow scheme of the In-Vessel cooling circuits [33].

Helium coolant enters the segment at a temperature of 300 °C with an operating static pressure of 8 MPa. It first flows from the FW manifold inlet (MF-1) to the FW cooling channels, which are cooled in a counter-current flow mode to flatten the structure temperature distribution. The coolant flows are routed to the BZ inlet manifold (MF-2),where they are collected and mixed to cope with the different temperatures due to the poloidal distribution of the heat loads coming from plasma [36]. In fact the FW cooling requirements are different at various poloidal positions, therefore the local FW outlet temperature varies poloidally. However, the FW outlet coolant from different poloidal positions is mixed in the MF-2, reaching an average temperature of about 350 °C.

From the MF-2, helium is then distributed among the fuel pins in the BZ. The coolant is then collected from the pins in the outlet plenum and redirected to the BZ outlet (MF-3), at an expected bulk temperature of 520 °C [33]. The outlet temperature is higher than the formerly achievable in the previous HCPB design [37], namely 500 °C, due to the improved heat transfer performances of the BZ.

A “1-side bottom-top” arrangement [33] is currently selected to connect the Ex-Vessel cooling pipes with the In-Vessel components: inlet and outlet pipes are all routed through the upper port reducing the integration problems identified for the BoP with the former “2-side bottom-top” arrangement [17] as well as decreasing the complexity of RM operations [38].

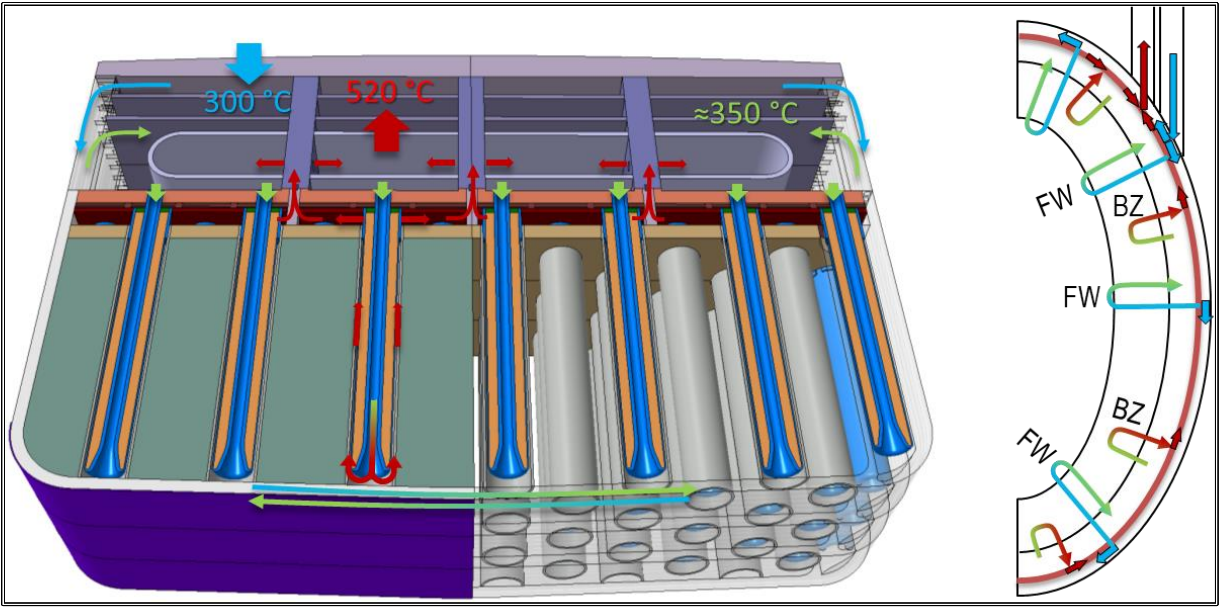

Figure 2.7. Integral flow scheme in the HCPB segment [33]

Once the helium leaves the different blanket segments it is conveniently collected into bigger hot legs located into the Upper Pipe Chase (UPC) region, then it reaches the heat exchanger, which can be either a helium/molten salt heat exchanger or a helium steam generator depending on the BoP option adopted. After having exchanged its thermal power to the secondary coolant, close to the heat exchanger exit, the coolant enters the pumping group that let it circulate through the cold leg, towards the distributors from which it is routed to the BB segments to start again its thermal cycle.

Table 2.1 summarises the main Thermal-Hydraulic (T/H) design parameters of the BB PHTS [39].

Table 2.1. DEMO BB main T/H design parameters.

Coolant [-]	Helium
Thermal power [MW]	2029.1
Coolant inlet pressure [MPa]	8.0
Coolant inlet temperature [°C]	300.0
Coolant outlet temperature [°C]	520.0
Coolant mass flow rate [kg/s]	1777.9

2.3.2 Divertor Primary Heat Transfer System

The Divertor is primarily a high heat flux component whose main function is to extract the alpha particle power, helium and impurities, It has, hence, to sustain the heat load coming from the plasma Scrape-Off Layer (SOL) under the normal and off-normal events.

According to DEMO Baseline 2017, the DEMO Divertor is articulated in 48 toroidal cassettes, three for each toroidal sector of the reactor, to ease their remote handling procedure.

Each cassette is composed of a Cassette Body (CB), equipped with a Shielding Liner and two Reflector Plates (RPs), and two Plasma Facing Components (PFCs), namely an Inner Vertical Target (IVT) and an Outer Vertical Target (OVT). Figure 2.8 shows the CAD model of the Divertor cassette.

Due to the different heat loads they have to withstand and to the requirements agreed to guarantee the structural material integrity, the CB (with its Liner) and the PFCs must be cooled by two separate circuits, fed by water coolant at different T/H conditions. As a matter of fact, the two PFCs have to sustain the nuclear power deposited by neutrons and gammas, as well as the high heat fluxes due to irradiation and particles arising from plasma (up to 20 MW/m^2). On the other hands, the heat flux impacting the CB Liner (mainly due to radiation) is around 1 order of magnitude weaker than that experienced by VTs. Therefore, the main source of power deposited within the CB comes from nuclear heating.

In order to withstand these huge heat fluxes and achieve a safe margin against the occurrence of the Critical Heat Flux (CHF), the PFCs need to be cooled at higher pressure and lower temperature compared to the operating conditions adopted for the CB which, in turn, cannot be cooled at too low temperatures to prevent the approaching of the MDTT temperature raised by the excessive degradation of the material properties due to neutron irradiation [40].

The In-Vessel cooling circuits of CB and PFCs are shown in Figure 2.9 and Figure 2.10.

The CB presents a box-shaped structure that allows the water coming from inlet manifold, routed through the lower port, to enter from the outboard side and flow in the CB top part up to the Liner and the Reflector Plates inlets that are fed in parallel. Once the coolant has been routed through these sub-circuits, removing the deposited power, they are mixed, continuing jointly their path toward the inboard side of the Cassette. From this region, the water goes downward and, after flowing through the bottom part of the CB, it reaches the outlet manifold that routes the coolant outside the VV through the lower port.

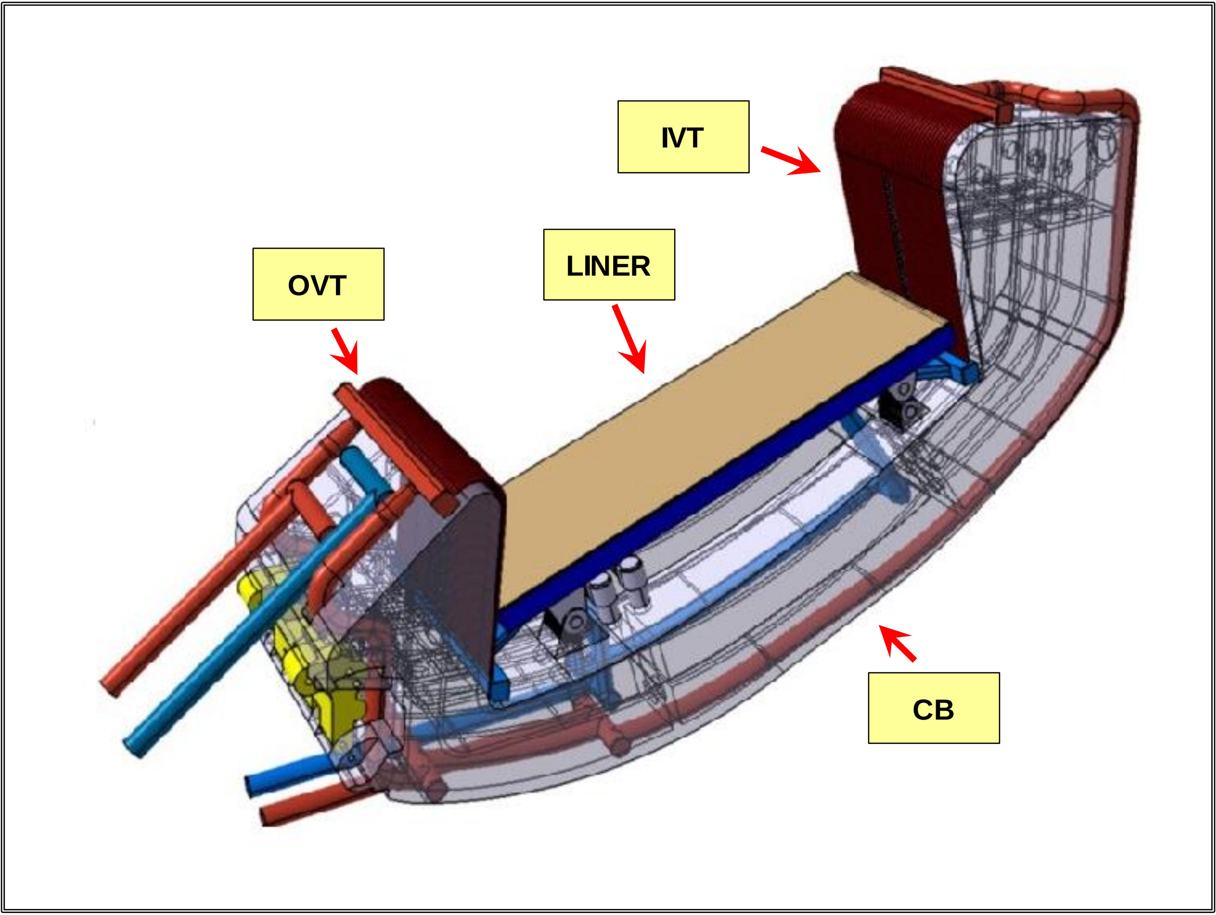

Figure 2.8. Model of the DEMO divertor assembly [40].

As to the PFCs cooling circuits, also in this case its inlet and outlet manifolds are routed from the bioshield through the lower port. Water coolant at 130°C and 50 bar is distributed in parallel from a manifold to the IVT and OVT inlet diffusers. Coolant is then routed to the PFU channels, equipped with a Swirl Tape (ST) turbulence promoter to enhance the coolant heat transfer capabilities, enhancing its CHF value. It flows upward, across the channels until it reaches the outlet collectors, from which is routed to a common outlet manifold that redirect the high energy coolant to the Ex-Vessel PHTS.

The Ex-Vessel portions of the two DIV PHTS are conceptually identical, the only remarkable difference between the CB and PFC PHTSs is related to the pipework size that depends upon the mass flow rates, for a given design velocity.

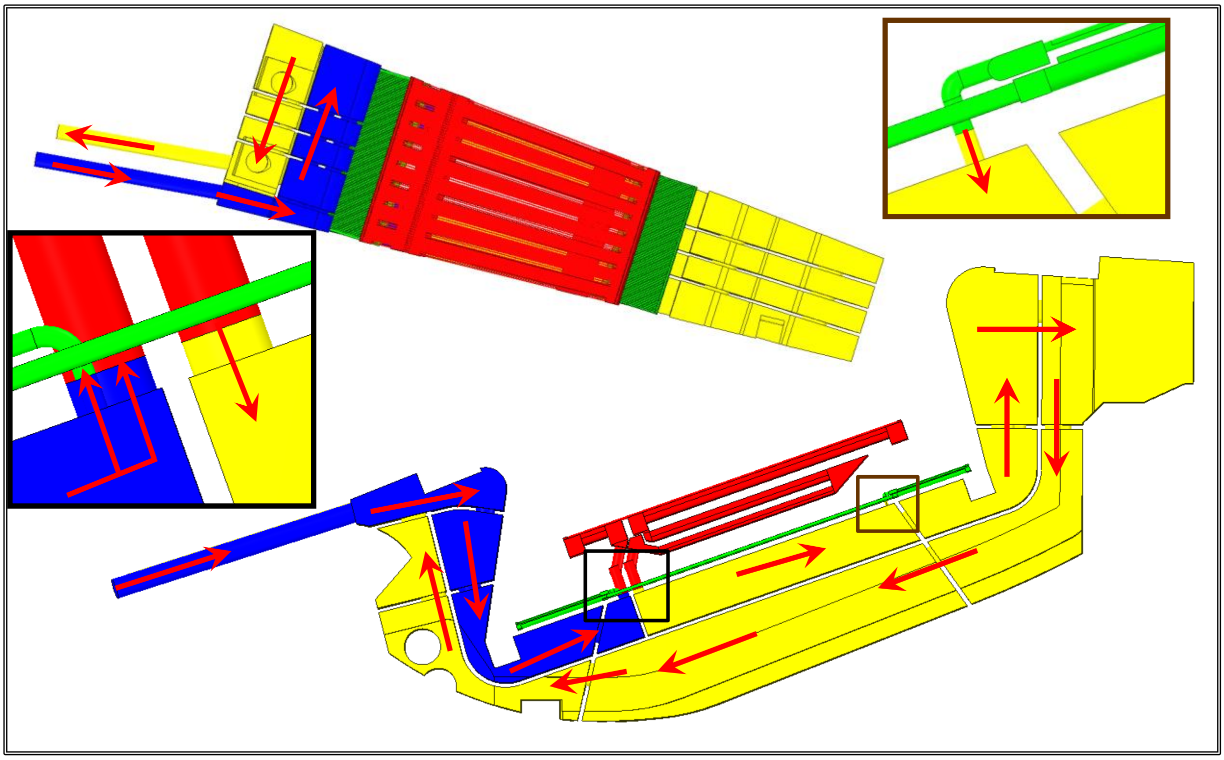

Figure 2.9. DEMO Cassette Body cooling circuits [40].

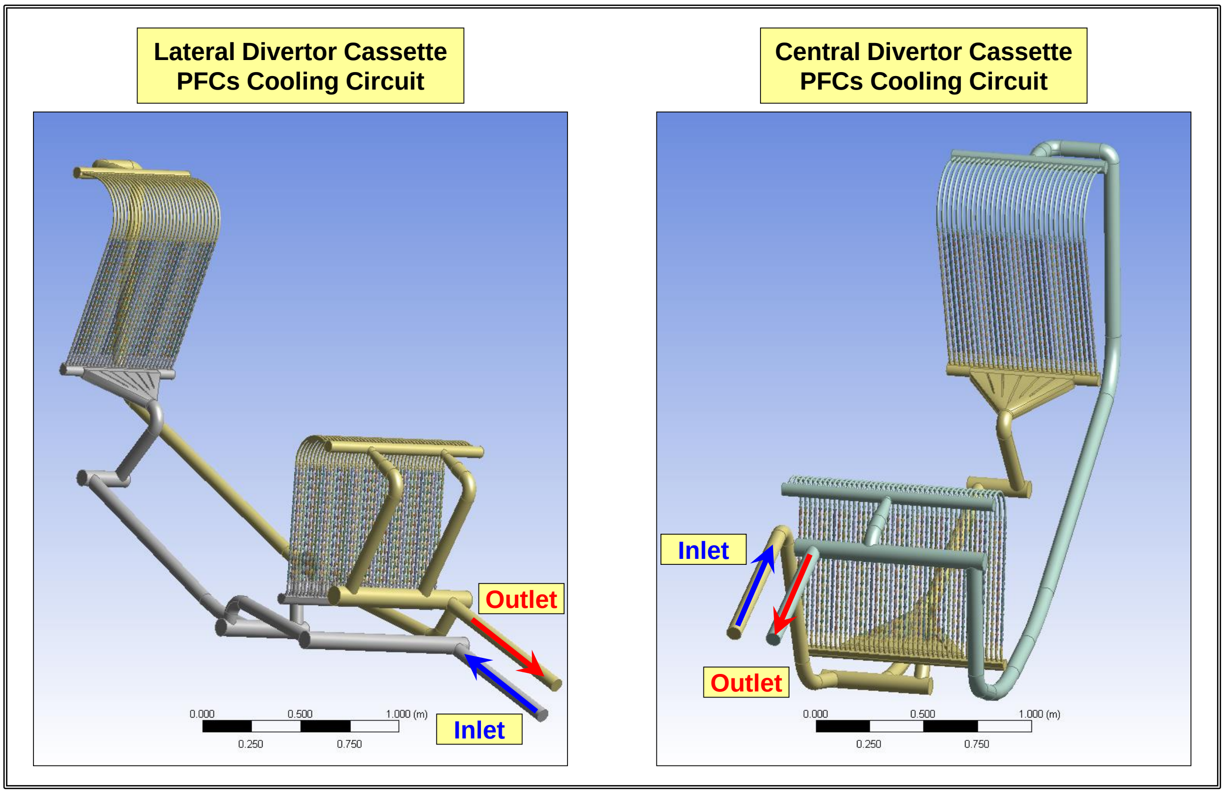

Figure 2.10. DEMO PFCs cooling circuits [40].

Hence, in both cases the Ex-Vessel cooling scheme is the same. The hot rings running into the Lower Pipe Chase (LPC) collect water coming from the cassettes; hot water reaches the heat exchangers via the hot legs and its thermal power is used to heat-up the PCS feed-water. At the heat exchanger exit, the cold water is routed toward the pumps that send it to the cold rings via the cold legs. Finally, the coolant is distributed into the cold feeding pipes that let the water go to the In-Vessel cooling circuits [34].

Table 2.2 summarises the main Thermal-Hydraulic (T/H) design parameters of the DIV PHTSs.

Table 2.2. DEMO DIV main T/H design parameters.

	CB	***PFCs***
Coolant [-]	Water	Water
Thermal power [MW]	115.2	136.0
Coolant inlet pressure [MPa]	3.5	5.0
Coolant inlet temperature [°C]	180.0	130.0
Coolant outlet temperature [°C]	210.0	136.0
Coolant mass flow rate [kg/s]	861.8	5321.3

2.3.3 Vacuum Vessel Primary Heat Transfer system

The Vacuum Vessel is a torus-shaped pressure vessel that provides the primary vacuum (at very low pressure, ~$5\cdot10^{-8}$ mbar, and at very high purity in order to optimize the D-T fusion reaction) and contributes to shielding the magnet system from neutrons, contributing to support all internal components and accommodating their differential displacements. Although this components has not been developed in detail yet, its design should be reasonably based on the same concept chosen for the ITER VV, i.e. a double shell steel structure with a sufficient quantity of ribs for structural reinforcement in between inner and outer shells. Water has been selected as the coolant of the component and, despite a clear In-Vessel cooling scheme has not been defined, the coolant should enter from the lower port into the VV, flow through the stiffening steel plate and exit to hot feeding pipes routing it to the upper port. The water inlet/outlet temperatures have been preliminary set to 190/200 °C, even if they are still under discussion [41].

Even though the In-Vessel cooling circuit is not mature, an Ex-Vessel PHTS has been preliminary outlined taking into account the T/H data foreseen for this component. Until the coolant temperatures will be kept at relatively high values, the VV PHTS is suitable to be integrated into the BoP, using its thermal power to directly pre-heat the feed-water. As for the

DIV PHTSs, the main components of this system will be the hot/cold rings, hot/cold legs, primary heat exchangers and pumps [34]. However, as the VV will be the system devoted to extract the decay heat from tokamak in case of an accident, the PHTS will be equipped also with a fully redundant active system consisting of an emergency heat exchanger and an emergency pump. These additional equipment will be installed in all the VV PHTS loop in parallel with the main VV heat exchanger [42]. Table 2.3 summarises the main Thermal-Hydraulic (T/H) design parameters of the VV PHTS.

Table 2.3. DEMO VV PHTS main T/H design parameters.

Coolant [-]	Water
Thermal power [MW]	86.0
Coolant inlet pressure [MPa]	3.2
Coolant inlet temperature [°C]	190.0
Coolant outlet temperature [°C]	200.0
Coolant mass flow rate [kg/s]	1928.0

2.4 Intermediate Heat Transfer System

The Intermediate Heat Transfer System is foreseen for the indirect-coupling DEMO BoP option. The introduction of an intermediate circuit in between the primary and the secondary loops has been already adopted in several fission NPPs. In particular it is commonly adopted in fast sodium reactors [43] and its installation is planned in many Gen IV reactor concepts as well [44]. Whilst in fission reactors the intermediate loop is mainly employed to fulfil safety requirements (prevent the direct interaction of reacting coolants), its first objective in DEMO is to mitigate the imbalance between steam generators/turbine power demand and the TOKAMAK generated power. Nevertheless, the NPPs experience can give useful information for the design of the main equipment of this circuits. For instance, a survey of the technical solution conceived to deal with potentially corrosive materials at rather high temperatures and in a harsh nuclear environment can be a good starting point to address the preliminary assessments for the DEMO IHTS design.

However, as already mentioned, the main scope of the DEMO IHTS is not to physically decouple PHTS from the PCS, but to obtain a thermal decoupling of these two system, an Energy Storage System must be hence added to the IHTS to totally accomplish its original purpose.

This practice is very common in the solar energy field. In particular the CSP plants rely on a thermal energy storage to compensate for the lack of the energy source during the night hours or under cloudy weather conditions. Studies on the possibility to accumulate thermal energy by means of several methods and storage media have proliferated in the last decades [45]. However looking at the state-of-art of the CSP solutions developed on large industrial scale, it can be observed that the two-tanks molten salt storage system is the most widely used [46], therefore it has been chosen as first reference for the indirect-coupling DEMO BoP option.

The intermediate circuit layout conceptually consists of two tanks, which are focal point of the system, the Intermediate Heat eXchangers (IHXs) on the primary side, the SGs on the secondary side and the connecting pipes with the coolant pumps to let molten salt circulate through the components.

The working principle of the ESS method relies the foundation on the accumulation of sensible heat during the Pulse period with its consequent release when the power source is unavailable under the Dwell phase. In particular, in the simplest hypothesis of neglecting the power transitional phases so that a square wave profile can be assumed for the evolution in time of the DEMO generated power, during the Pulse period the molten salt is pumped from a cold receiver, namely the cold tank, to the Intermediate Heat eXchanger (IHX), where the BB thermal power is removed increasing the salt enthalpy. The hot molten salt is then delivered to a hot receiver, the hot tank, where a certain amount of the coolant mass is collected and kept hot while the remaining part continues to be directed toward the PCS steam generator in order to produce the proper amount of steam feeding the turbine. At the steam generator exit, the cold salt is sent by a second train of pumps toward the cold tank. As it can be noted, during the Pulse, also called charge time, the mismatch between inlet and outlet mass flow rates causes a net increase of molten salt mass in the hot receiver, as well as a decrease in the cold receiver, so that, at the end of this period, the hot tank will be filled up of hot coolant going to the detriment of the cold tank which will get empty. In its turn, however, when the Dwell period starts, an inversion of the mass trend takes place. In fact, the power of the BB drops to very low values and the IHX needs, hence, to be fed with a small mass flow rate of cold molten salt while the rate of mass extraction from the hot tank is kept almost constant with the aim of allowing a continuous turbine operation under steady (or quasi steady) state conditions. Therefore, during this period, namely the discharge time, a reduction of the molten salt mass stored into the hot tank in favour of the cold tank whose inventory increases. In conclusion, during the Pulse the hot tank is charged of molten salt and the cold tank is emptied while during the Dwell period this latter tank is charged with molten salt and the former is emptied instead.

Of course, charging and discharging speeds of the two tanks are inversely proportional to the duration of Pulse and Dwell times and to how they are distributed over the whole TOKAMAK period. The longer is the Pulse period (compared to the Dwell), the slower is the hot tank charging rate. Vice-versa, the shorter is the Dwell, the faster is salt discharge from the hot tank to the cold one.

A proper balance of the masses among the two tanks must be ensured to guarantee a stable operation of the whole PCS and provide sufficient cooling of the BB PHTS during the entire DEMO duty cycle. Moreover, as the IHTS is linked with the blanket primary circuit only, the energy stored during the Pulse exploiting just the BB thermal power must have an adequate provision in order to compensate the heat of DIV and VV which is also lost during the Dwell.

Details of the global heat balances for the whole BoP are given in [47], while Table 2.4 reports the molten salt operating conditions.

Table 2.4. DEMO IHTS coolant operating conditions.

Coolant [-]	Molten Salt
Thermal power (PHTS side) [MW]	2029.1
Tanks pressure [MPa]	~1
Coolant cold temperature [°C]	270.0
Coolant outlet temperature [°C]	465.0
Coolant mass flow rate (PHTS side) [kg/s]	6945.8

2.5 The Power Conversion System

Two preliminary conceptual designs of PCS have been proposed for DEMO, one for the BoP option envisaging the indirect-coupling, a second for the case in which the PHTSs are directly coupled to the turbine circuit. Both solutions, studied with the support of Siemens [47], are based on variants of the classical Rankine cycle with superheated steam.

Hence the PCS schemes foresee all the equipment that are usually present in a commercial power plant, in particular: steam generators, reheaters – in between high and low pressure turbine stages - feedwater pre-heaters, deaerator and condenser.

The low pressure steam reheaters are operated with the high pressure steam coming directly from the steam generators; this technical solution has been judge more feasible and simpler than those exploiting molten salt or helium as heat sources, respectively for the option with/without ESS, although the latter would have potentially been thermodynamically more efficient.

Two main typologies of feedwater pre-heaters are adopted: the condensing type or single phase-to-single phase fluid type. The former are fed by the turbine bleeding line extracting steam from the different stages of the turbine, whereas the latter are represented by the heat exchangers of the DIV and VV PHTSs which are integrated in PCS as additional (low temperature) heat sources to improve the overall system efficiency.

A two-steam pressure stages molten salt steam generator is used to provide live steam to the turbine in case of indirect-coupling options. This configuration recalls the power cycles of the Magnox reactors that, being unable to reach high steam temperature due to limitation on their fuel element materials, chose to improve their efficiencies employing different steam pressures [48]. Regardless of its origin, even in DEMO exists a limitation on the maximum allowable temperature related to the In-Vessel structural material, therefore taking into account the additional temperature drop caused by the IHTS, the maximum achievable steam temperature results to be around 450 °C, which is definitely lower than the values reach in modern steam power station [48]. This has suggested to use the same approaches adopted in the past for the gas-cooled fission NPPs.

On the other hand, a single pressure cycle is foreseen for the PCS when it is directly coupled to all the PHTSs. Actually, the decision to design a steam generator as simple as possible has been made in order to avoid the introduction of an additional complication to the PCS, already challenged by the pulsed operations. Moreover, the lack of an intermediate loop allows to increase both maximum temperature and pressure achieving values of about 480°C and 140 bar, respectively.

Further information on the expected DEMO power cycles can be found in [49].

3 The design of the BB PHTS

3.1 Introduction

The HCPB BB PHTS is designed to remove about 2029 MW of thermal power using Helium at an inlet pressure of 8 MPa and working temperatures of 300-520 °C, see par. 2.3.1.

The selected pressure is in the range of values already considered in the past for a helium-cooled DEMO blanket [50]. It has been chosen as likely optimum value to achieve: a reduction of circulator power according to $1/p^2$ (at constant geometry) and a limitation of costs (which increase with p) for pressure vessels, pipes and related engineered safeguards as expansion volumes [51].

The temperature window exhibits a jump across the BB which is modest if compared to those usually employed in fission gas reactors, where the ΔT normally achieved is from 2 to 3 times higher [52]. In DEMO however these minimum and maximum temperatures are currently imposed by the lower and upper design limits of the low activation structural steel EUROFER97, so until advanced steels will not be technologically mature enough to replace the actual solution, it will be rather difficult to further stretch such a window [3].

Considering these two main thermal-hydraulic constrains, the study of the Ex-Vessel HCPB BB PHTS have been focused on the achievement of a conceptual design for the main components, assessing their sizes and the overall performances. The aim has been to identify technical feasibility issues, understand commercial availability and R&D needs, establish layout integration and safety requirements [19].

3.2 General design criteria

Taking into account design requirements and needs of the In-Vessel components, additional strategies and objectives have been pursued especially to implement general safety and integration requirements [42]:

- Segmentation and separation of the cooling loops to limit the potential consequences of Loss of Cooling Accident (LOCA) as well as the size of pipework, heat exchangers and steam generators.
- Introduction of redundancy on the circulators to mitigate the effects of a Loss of Flow Accident (LOFA) due to a single circulator failure and to keep dimensions and rating of these components within acceptable ranges.

- Integration of the PHTS outside of the tokamak bio-shield but as close as possible to be compliant with the high DEMO safety requirements limiting the helium coolant inventory and guaranteeing components and instrumentation qualified life.
- Trade-offs between high thermal plant efficiency, reasonable costs and favourable safety features such as minimization of coolant inventories and radioactive materials.

Moreover, as general recommendation and approach, the main equipment would be designed and selected with emphasis on technological limits of the components. Therefore, in order to be in line with the state-of-art technology as much as possible, design parameters has been often chosen considering the solutions adopted in Helium and CO_2 gas-cooled fission reactors and, to a certain extent, some considerations will involve also the developments achieved in liquid metal reactors and solar industry.

3.2.1 Input data and boundary conditions

The first function of the BB PHTS is to ensure the extraction of the thermal power from the In-Vessel components by means of the main heat exchangers, which can be either single-phase to single-phase IHX or steam generators depending on the BoP option. Thus the design shall respect the input data as well as the thermal-hydraulic conditions conceived for both the primary circuit and the interfacing secondary system. In particular, focusing on the In-Vessel cooling circuits architecture, the PHTS layout must allow to feed each single blanket segment and, in addition, the helium mass flow rates distribution shall be weighted on the different IB and OB thermal powers in order to be compliant with the cooling requirements.

However it is worth to remark that, stating the uncertainties that are still present in DEMO, some fundamental parameters have not been definitely fixed yet, rather it has been suggested a working range respect to average values. Probably the most emblematic case concerns the nominal thermal power of the BB that, due to the provisions taken on the achievable Tritium Breeding Ratio (TBR), can vary from a reference value to a maximum/minimum value, namely from 2029 MW to 2126 or 1971 MWs [39]. Being the thermal power of the circuit the starting point for all the possible assessments, the possibility of making a deep, parallel investigation of the three configurations has been discarded. In fact, with regard to the relative small power window to be studied (+5/-3 % respect to the reference value), it has been judged that outcomes obtained taking into account the reference power value only would have been sufficient to extrapolate indicative design values even in case of a slight changes in power since it would not have dramatically affected the results. Nevertheless, to preserve an inherent conservative tendency in the design of main components, sometimes further margins have been added to cover the likelihood of a little power increase.

Table 3.1 summarized the parameters used as inputs and boundary conditions to perform the detailed design of the main PHTS components [39]. They are a partial integration of the data given in the paragraphs 2.3.1, 2.4 [47] and 2.5 [49].

Table 3.1. Input data and boundary condition.

Primary side	
Coolant [-]	Helium
IB segments [-]	32
OB segments [-]	48
IB power [MW]	575.4 (28.4% of BB)
OB power [MW]	1453.7 (71.6% of BB)
IB/OB inlet pressure [MPa]	8.0
IB/OB inlet temperature [°C]	300.0
IB/OB outlet temperature [°C]	520.0
IB/OB pressure drop [kPa]	79.9
Secondary side – Indirect-coupling option	
Coolant	Molten salt
Tanks pressure [-]	Atmospheric (+ gravity head)
Cold tank temperature [°C]	270.0
Hot tank temperature [°C]	465.0
Secondary side – Direct-coupling option	
Coolant	Water
SG outlet pressure [MPa]	13.6
SG inlet temperature [°C]	235.4
SG outlet temperature [°C]	480.0

3.2.1.1 Thermo-physical properties of the coolants

A literature survey of the working fluids has been necessary before beginning any assessment. In particular, attention has been mainly put on the selection of the most suitable molten salt to be used as characteristics and behaviour of helium and water are absolutely well-know at the given operating conditions.

3.2.1.1.1 Helium

Since the beginning of the nuclear era, helium has been seen as a very promising candidate to be used as primary coolant in a reactor [53]. It has a thermal conductivity rather higher than the one of other gases such as CO_2, nitrogen and air, and many other nuclear and chemical advantages: it has no significant neutron interaction at practical pressures and it does not become activated; it is inert so no reactions with the neutron multiplier or the breeder material are foreseen and it cannot cause corrosion in structural material as well; its tritium content can be removed with relatively low effort. However it exhibits a very low density therefore it shows a rather low thermal capacity and marked tendency to leak from systems.

For a noble gas such as helium, an Equation-of-State (EOS) based on the ideal gas law deviates little from the real gas law at the pressure and the temperatures expected in the blanket. In fact, at 80 bar and 773.15 K, the discrepancies between the two laws are around 1.7 %. Similarly, thermal conductivity and viscosity might be deducted from general gas theories with modest errors, nonetheless it has been chosen to use properties derived from Petersen [54] and the NIST chemistry webBook [55] in order to minimize the propagation of errors that will be naturally introduced by many other assumptions or correlation formula.

The density ρ, in kg/m^3, has been calculated according to:

$$\rho = 48.14 \frac{p}{T}\left[1 + 0.4446 \frac{p}{T^{1.2}}\right]^{-1} \tag{1}$$

The thermal conductivity k, in $Wm^{-1}K^{-1}$, has been calculated according to:

$$k = 2.682 \cdot 10^{-3}\left(1 + 1.123 \cdot 10^{-3} p\right) T^{\left(0.71\left(1 - 2 \cdot 10^{-4} p\right)\right)} \tag{2}$$

The dynamic viscosity μ, in Pas, has been calculated according to:

$$\mu = 3.674 \cdot 10^{-7} T^{0.7} \tag{3}$$

The specific heat capacity C_p at constant pressure, in $Jkg^{-1}K^{-1}$, has been set to:

$$C_p = 5187.6 \tag{4}$$

where T and p are temperature and pressure expressed in Kelvin and bar, respectively.

3.2.1.1.2 Water

Water is the most common components on Earth and so it has been studied for a very long time, then any further information risk to be excessively long-winded. It has very good cooling capabilities and its exploitation is at the basis of the majority power conversion cycles. Currently, the set of equations collected in IAPWS-IF97 are the internationally agreed upon equations for industrial calculations of the most relevant thermos-physical properties of water and steam, therefore all the relevant properties of this fluid will be calculated according to this standard [56].

3.2.1.1.3 Molten salt - HITEC

As already mentioned, molten salt has been judged the optimal candidate for being the coolant/storage media employed in the IHTS. Some of the desirable features that such a fluid should include are:

- low freezing temperature;
- high maximum operational temperature
- high heat capacity, density and thermal conductivity;
- good thermal stability;
- low corrosion;
- low cost.

Several nitrate and nitrate/nitrite molten salt mixtures can be used as heat storage media and in the last years the studies on new, most performing mixtures have growth exponentially [57], however the most commonly adopted in large plants are the Solar Salt and HITEC salt [65].

Solar Salt is a nitrate mixture composed by 60 wt% $NaNO_3$+40 wt% KNO_3, with melting point of ~220 °C and thermally stable up to 600 °C, while HITEC is a ternary system, which contains 7 wt% $NaNO_3$+53 wt% KNO_3+40 wt% $NaNO_2$, with a melting point of 142 °C and with a good thermal stability up to 535°C [58] or even more if operated under an inert atmosphere [59]. This latter ternary mixture was the first molten salt employed as a storage fluid in the THERMIS experimental solar plant in France in the ‘80s, however owing to the need to use a cover gas to avoid its undue thermal decomposition at the solar plant relevant temperatures (max. about 565 °C) it has been gradually replaced over the time with the Solar Salt that can achieve higher temperature under air atmosphere [60]. Nevertheless, it remains a very promising fluid for these applications [61] and lots of recent studies are aimed at further improving the features of its base mixture by adding nanoparticles [63] or little changes in the compositions [62].

With regards to the cost and corrosiveness considerations, the nitrates and nitrites are the most suitable salts as heat transfer and thermal storage material in solar thermal power plants. In fact nitrate and nitrate molten salts are less corrosive than chlorides, carbonates, and fluorides and generally cheaper. The price of Solar and HITEC salts are 0.5 US $/kg and 0.93 US $/kg respectively [57], while other compounds, especially in presence of lithium, can cost more than 1 $/kg [62].

The corrosion of nitrate and nitrites salts have been deeply investigate during last decades so that a widespread literature is available [66] [67] to know the effects on several alloys such as stainless steels [71], carbon steels [69], low Cr or Cr-Mo alloy steels [70] and Ni based alloys [68]. As general trend, the results indicate that high Ni or Cr content results in better corrosion resistance to the nitrite and nitrate attack thanks to the formation of stable NiO or Cr_2O_3 protective oxide scale on the surface of the alloy during corrosion [72]. For instance, for temperatures up to 630 °C, the data of Bradshaw and Carling [73] suggest that many stainless steel and Nickel based alloys are adequate for handling nitrate salts, while low alloy steels show good resistance capabilities under 500 °C. According to the results of Coastal Chemical [74], one of the major HITEC developers, data from Slusser [75], and many other recent studies [76] [77] [78], nitrite salts behave very similar to nitrate salt.

Some results from [73] are reported in Table 3.2.

Table 3.2. Corrosion rates of selected metals and alloys in molten $NaNO_3$-KNO_3 [73].

Alloy	**Temperature [°C]**	**Corrosion rate [µm/yr]**
Carbon steel	**460**	**120**
2.25Cr-lMo	**460** **500**	**101** **26**
9Cr-lMo	**550** **600**	**6** **23**
Aluminized Cr-Mo steel	**600**	**<4**
12Cr steel	**600**	**22**
304SS	**600**	**12**
316SS	**600** **630**	**7-10** **106**
Alloy 800	**565** **600** **630**	**5** **6-10** **75**
Inconel 600	**600** **630**	**7-1** **106**
Nickel	**565**	**>500**
Aluminium	**565**	**<4**

The thermo-physical properties of both nitrate and nitrate/nitrite salts are comparable. In particular, with a density in a range of 1700-1800 kg/m^3, a thermal conductivity which generally varying from 0.3 to 0.6 W/mK, a specific heat capacity around 1.5/1.6 kJ/kgK and a viscosity of 0.1-0.6 Pa·s, at the high working temperatures their behaviour is not too different from the cold water one [79].

Furthermore, looking in the early studies on the Molten Salt Demonstration Reactor (MSDR) [80], it is possible to recognize that HITEC salt was already envisaged as intermediate heat transfer fluid in a nuclear system. At that time, the main purpose of interposing a HITEC loop in between the nuclear molten salt circuits and the turbine loop was to trap the tritium formed in the reactor during its diffusion paths through the exchangers in the direction of the steam system. Practically, the HITEC circuit would have been expected to oxidize the tritium to tritiated water, which would have been readily removed for safe disposal. In fact, at those temperatures and pressure, the water content in the system would be in the form of steam, therefore it would accumulate in the cover gas that might be easily stripped and sent to a purification system. In addition, the molten salt would enhance the formation on the heat exchangers alloys of a thin layer of protective oxides which would further inhibit tritium diffusion among the systems [81].

Despite the IHTS in DEMO is not supposed to act as additional tritium barrier since the first safety goal is to keep the tritium permeation from the PHTS to the secondary system below the environmental release limits [83], the selection of the HITEC salt might provide a further help to cope with the tritium issues [82].

Then, from thermodynamic and heat transfer considerations, the nitrate/nitrite mixture seems to better suit the working window foreseen in the IHTS and the temperature requirements coming from the PCS cycle. Indeed, being the maximum primary temperature 520°C, the molten salt loop will never reach higher temperatures during normal or up-set operations (accident and severe-accident conditions should be further assessed), hence the potential occurrence of thermal decomposition can be excluded if a proper control of the cover gas is ensured. On the other hand, the inlet feed-water temperature is currently set to around 230°C, which is already below the first crystallization temperature of the Solar Salt [84], namely 238 °C, and very close to its bulk solidification temperature, thus if such a salt was chosen the risk of a freezing occurrence would be high.

For these reasons, HITEC has been selected as the optimal solution for the DEMO needs.

The main salt properties has been calculated according to the data provided by Coastal Chemical in his report [74]. As the report gives the data in graphical form, they have been best fitted and converted in more practical functions [85].

The density ρ, in kg/m^3, has been calculated according to:

$$\rho = 2080 - 0.7324(T - 273.15) \tag{5}$$

The thermal conductivity k, in Wm^{-1}K^{-1}, has been calculated according to:

$$k = 0.4465 + 1.7888 \cdot 10^{-4}\left(T - 273.15\right) - 1.1486 \cdot 10^{-6}\left(T - 273.15\right)^2 \tag{6}$$

The dynamic viscosity μ, in Pas, has been calculated according to:

$$\mu = 2.1554 \cdot 10^{-4} e^{\left\{ 1006.4132 / \left[(T - 273.15) - 83.7755 \right] \right\}} \tag{7}$$

The specific heat capacity C_p at constant pressure, in Jkg^{-1}K^{-1}, has been set to:

$$C_p = 1560.0 \tag{8}$$

Where T is the temperature expressed in Kelvin.

3.3 Rationale behind the PHTS layout

The first step toward the assessment of the main equipment size has been the selection of the PHTS segmentation and of the overall circuits layout. Two preliminary attempts, as described in [17] and [38], have been previously made on the basis of the BB arranged with a 18 sector layout foreseen in the DEMO tokamak baseline 2015 [3]. However due to the new baseline [5], which adopts 16 VV sectors, a review of the loop arrangement has been needed.

In agreement with the general specifications, in order to fix the number of cooling circuits, additional criteria have been preliminary chosen:

- the maximum nominal pipe diameter must not exceed DN 1300 for reason of manufacturing [50];
- coolant speed in the main hot and cold legs should not exceed 50 m/s as in AGR and HTR [51];
- the maximum construction height tolerable for tube bundle of a once-through type heat exchanger/steam generator should be about 15 m for reason of manufacturing [50];
- the maximum circulator pressure ratio should not exceed 1.05 and, furthermore, the maximum circulator power should not overtake 6 MW for reason of transferability with other designs and projects [86].

These criteria will be further discussed and analysed in the next chapters, however they have been used as starting point to outline the PHTS layout.

A parametric analysis have been performed to select the number of loops, the most suitable circuits architecture and also to understand if it would have been worth to keep IB and OB cooling circuit separate or it would have been better that each loop would collect helium from both IB and OB segments.

In the hypothesis of steady-state operation, the total mass flow rate G required to extract the power from the blanket can be obtained from the following equation:

$$\dot{Q} = G\left(h_{out} - h_{in}\right) \tag{9}$$

where $\dot{Q}$ is the blanket thermal power, h_{out} and h_{in} are the fluid enthalpies at the blanket outlet and inlet, respectively.

As said, in the given working range, the helium behaviour can essentially be described by the ideal gas law so that the enthalpy of the helium is a function of the temperature only and hence, Equation (9) can be then rewritten as follow:

$$\dot{Q} = Gc_p\left(T_{out} - T_{in}\right) \tag{10}$$

where c_p is the specific heat capacity at constant pressure and T_{out} and T_{in} are the outlet and inlet temperatures of the BB.

Then, assuming that each loop will deliver helium to the main heat exchanger via a single hot leg, the internal diameter D_i of this pipe can be calculated through the following equation:

$$G = N\frac{\pi}{4}D_i^2\rho u \tag{11}$$

where N is the number of loops, while ρ and u are the coolant density and velocity, respectively.

As the aim of the analysis is to select the optimal number of PHTS cooling circuits, combining equations (10) and (11) is possible to get the pipe internal diameter as function of the number of loops and the coolant average speed:

$$D_i\left(N,u\right) = \left(\frac{4\dot{Q}}{\pi c_p \Delta T \rho}\right)^{0.5}\left(u\right)^{-0.5}\left(N\right)^{-0.5} \tag{12}$$

As expected, for given blanket power and coolant parameters, the higher is the velocity (number of loops) selected, the smaller is the pipe diameter. In particular, it can be noted that the pipe diameter is inversely proportional to the square root of both coolant velocity and loops number.

Now, using the number of loops as independent variable and varying the coolant velocity as free parameter, it is possible to plot on a 2-D graph a sufficient amount of configurations to be analysed. Therefore, two main layout philosophies have been considered:

- Case I, IB cooling loops are kept separate from OB ones;
- Case II, each loop feeds both IB and OB segments within its area of competence;

Then the required hot leg diameter has been drawn from equation (12) for both cases. It is worth to underline that it has been assumed an uniform toroidal distribution of the blanket power in both cases. Moreover, in Case I the thermal power used in (12) has been selected according to the blanket power distribution described in Table 3.1, while in the Case II the value given corresponds to the total BB power.

The hot leg diameters, which will be the largest pipes in each loop due the lower helium density (for a given design velocity), are depicted from Figure 3.1 to Figure 3.3. The design constrains are also highlighted in the graphs.

Considering the tokamak sectors, the number of loops shall be selected within the submultiple of 16 if an equal power distribution must be pursued among the loop of the same typology, therefore the suitable solutions can be restricted a-priori to 1, 2, 4, 8 and 16 loops (in Case I, IB and OB PHTSs are two separate entities so each one can be separated up to 16 sectors).

So, taking into account the constrains on coolant speed and pipework manufacturing, it can be seen from Figure 3.1 and Figure 3.2 that in Case I the IB PHTS only the 1 loop option cannot be selected, whereas the OB PHTS can be segmented into 8 or 16 loops. Also for Case II the allowable options are 8 and 16 loop arrangements, see Figure 3.3.

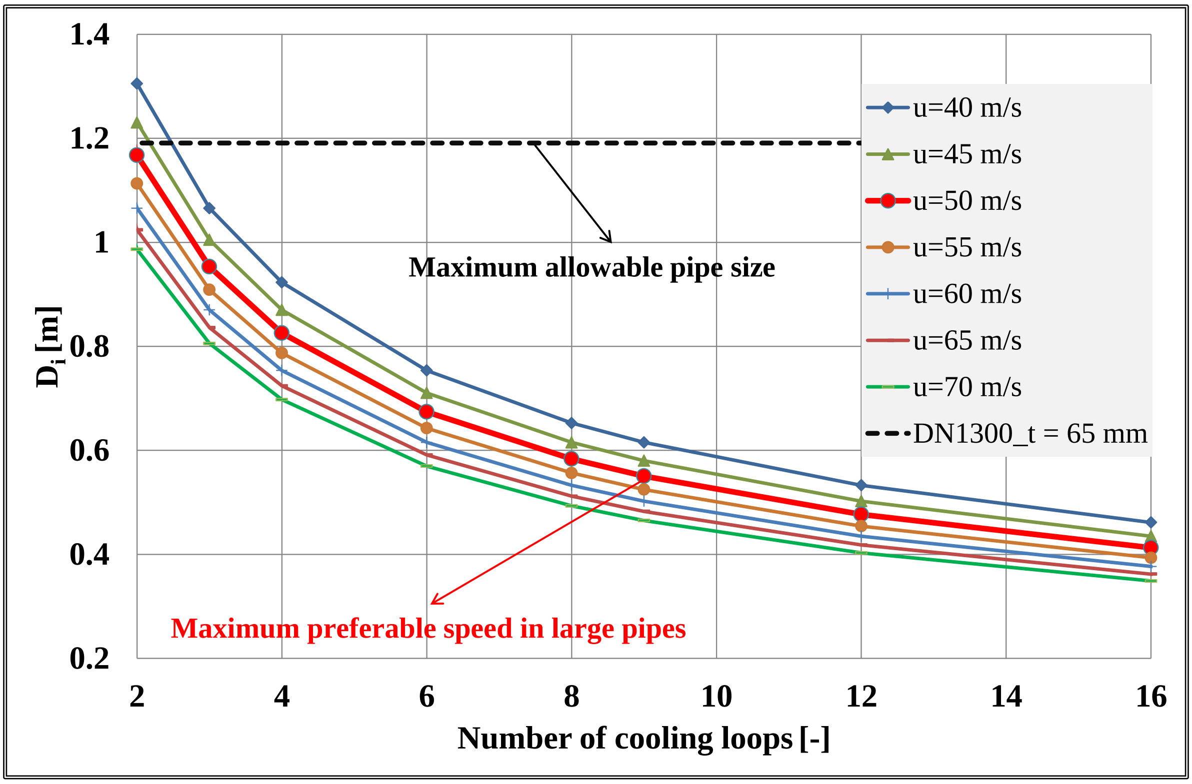

Figure 3.1. Case I- IB loops hot leg diameter. IB and OB loops kept separate.

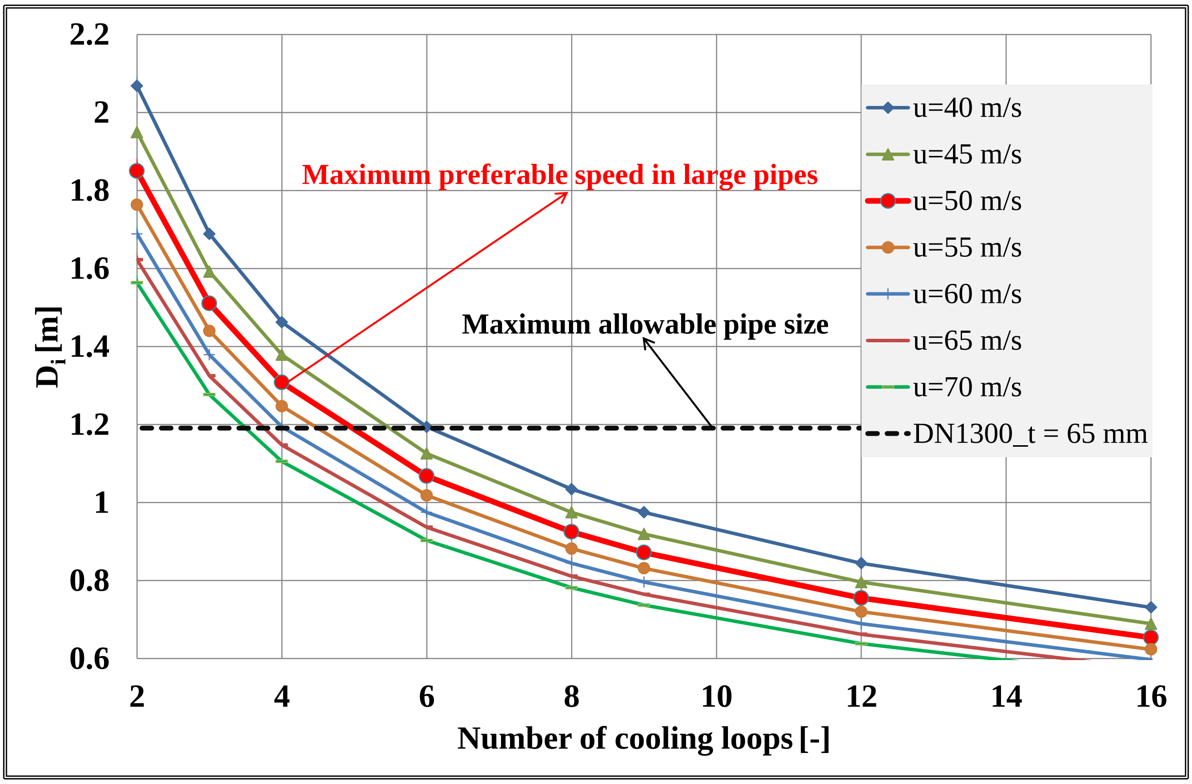

Figure 3.2. Case I – OB loops hot leg diameter. IB and OB loops kept separate.

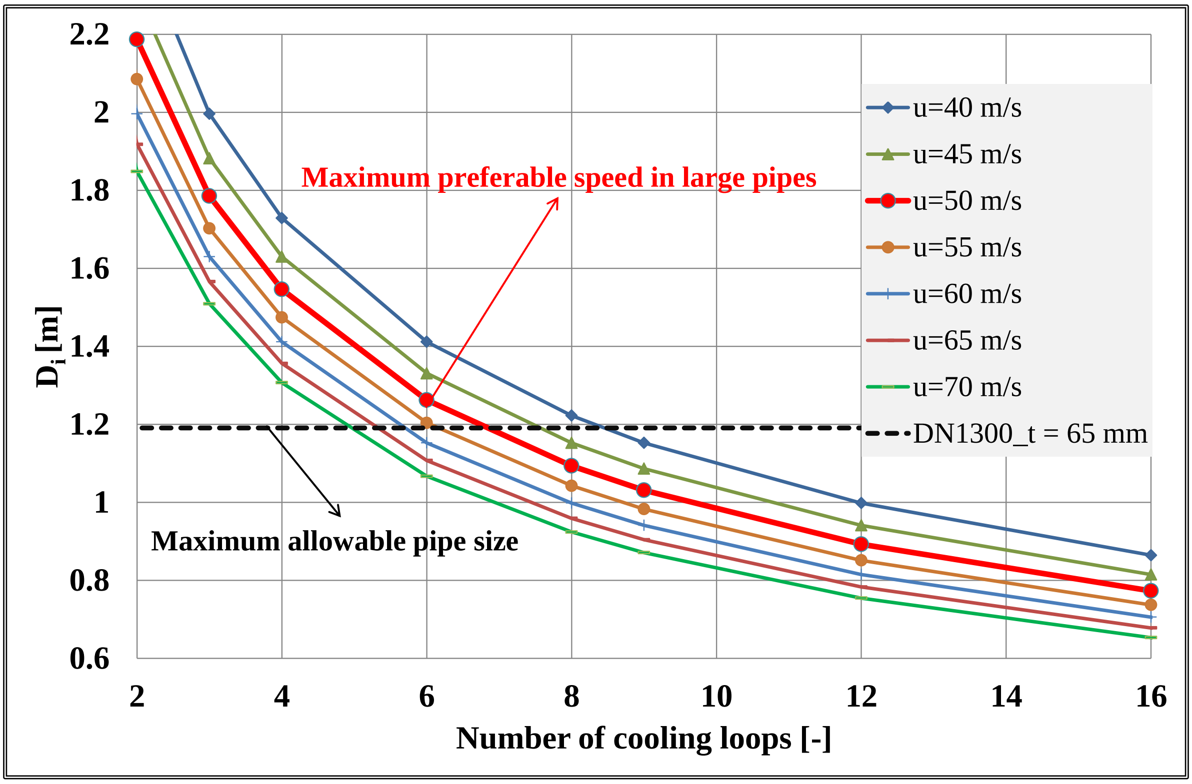

Figure 3.3. Case II – IB+OB loops hot leg diameter. IB+OB collected in each loop.

It should be remarked that for the Case I, IB and OB PHTSs would be separate, thus this configuration can be identified with a minimum number of 10 circuits, 2 for the IB and 8 for the OB.

Considering the need of integrating all the BB PHTS components inside the tokamak building and even in view of the physiological increment of costs with the growing of the number of units, it has been decided that loops should not be more than 12, which implies a single chance only for the Case 2, and leaves open the opportunity to have 2 or 4 IB loops for the Case 1.

On the other hand, if we look at other nuclear power stations, it is very unusual to have such a number of loops in combination with heat exchangers and circulators. As a matter of fact (excluding the contrast with the PWR where the loops are in a range of 2 to 4) in comparison with the solutions adopted in liquid metal or gas-cooled reactors, the choice of 12 loops seems already a borderline factor.

For instance, the Phénix and Superphénix NPPs had 6 and 8 IHXs respectively, while the Russian BN-600 and BN-800 reactors are both operated with 6 IHXs [87]; AGRs have usually been built with 4 steam generators (consisting of 2/3 parallel modules) [88]; THTR-300 [89] and Fort St. Vrain [90] helium-cooled reactors were operated with 6 and 2 loops respectively, however the former had one steam generator per loop while in the latter each loop share the helium mass flow among 6 small steam generator modules. Furthermore, to fulfil the safety requirements on circulators redundancy, which catches also the need to contain the power consumption per turbomachinery, the adoption of 12 loops would imply the presence of 24 blowers which is too high and definitely unusual for a nuclear power plant.

As consequence of these observations, the following PHTS layouts have appeared the most suitable trade-off choice:

- Case I, shown in Figure 3.4, comprehends 2 IB loops (blue) and 8 OB loops (green);
- Case II, depicted in Figure 3.5, is made up of 8 IB+OB loops.

Stating that both layouts might meet the prescribed requirements, it has been finally decided to address the efforts toward the configuration representative of the Case 2. Such a choice lays its basis on following observations.

According to the Table 3.1 and the segmentation, in Case 1 each IB loop would be designed to remove about 288 MW, whereas the OB circuits would transfer to the secondary system about 182 MW each. This large discrepancy would makes really remote the perspective of using the same components (i.e. heat exchangers and circulators) for the two portions of the BB PHTS.

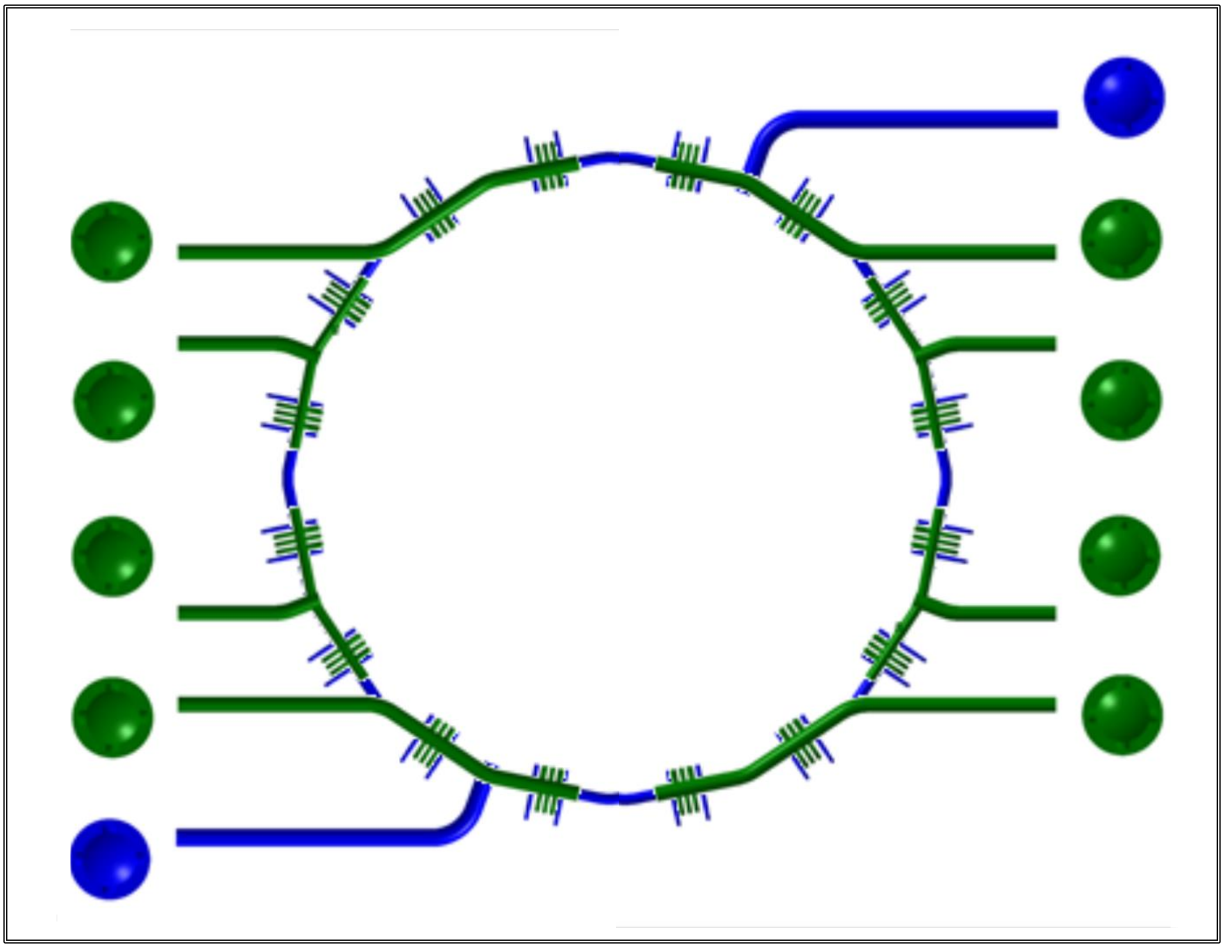

Figure 3.4. Simplified top view sketch for Case 1 selected layout (IB in blue, OB in green).

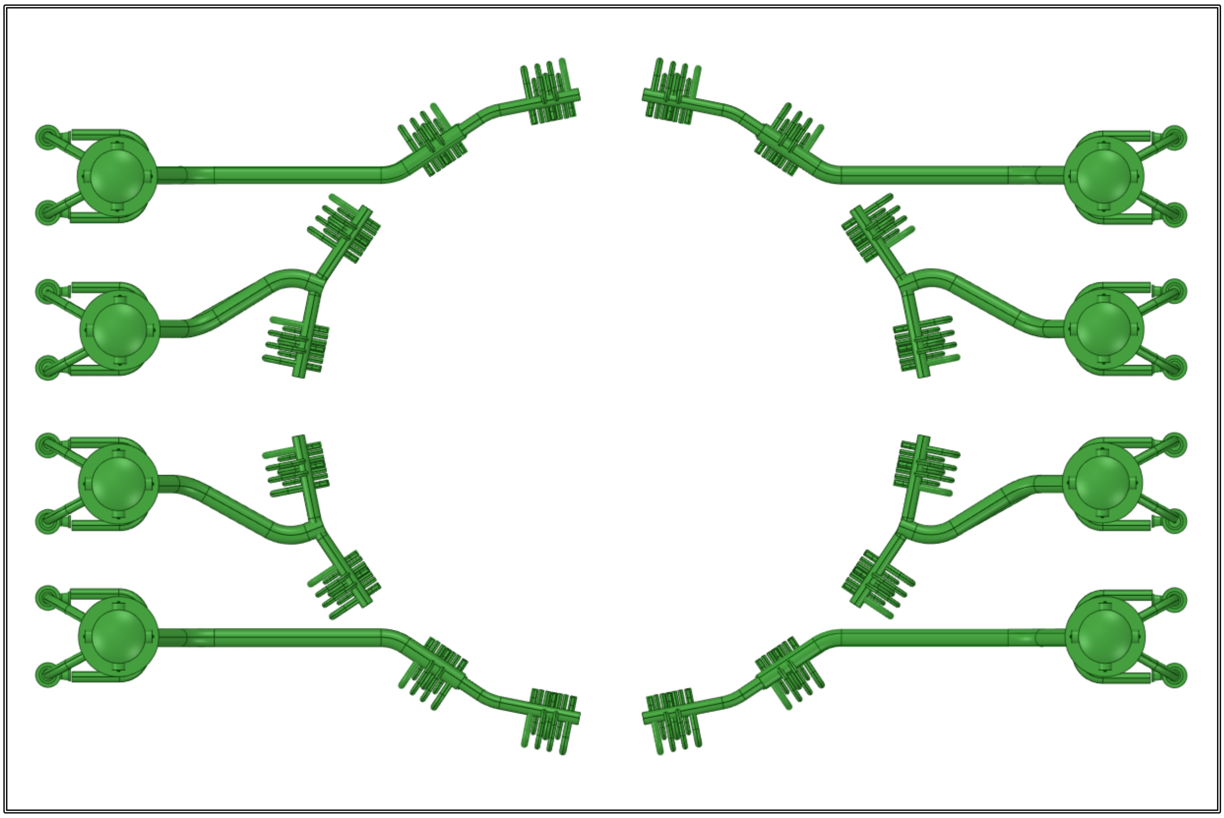

Figure 3.5. Simplified top view sketch for the Case 2 selected layout.

In addition, the thermal power duty of the single IB loop would be about 13% higher than the one of a single loop of the Case 2: every loop of the Case 2 would exchange the same power, namely 254 MW, while the power foreseen for the IB loop of the Case 1 would be 288 MW. This would mean that the Case 1 would imply the maximum possible efforts in the design and manufacturing of pipework, heat exchangers and circulators: their cross-sectional area is proportional to the mass flow rate, thus for eq. (10) to the thermal power.

Moreover, Case 1 would imply a lay out in which, due to the higher distance between the last sector grabbed by the IB loop and the heat exchanger, a relatively higher pressure drops would be expected for a fixed design velocity. Thus the design condition of the circulator would further worsen because its power is proportional to the loop pressure head. On the other hand, although this effect might be reduced decreasing the coolant speed, the immediate drawback would be the increase of the overall PHTS volume, which conflicts with the purpose of limiting the helium inventory, thus the energy stored into the system.

These reasons have finally led to crown the Case 2 as the most promising layout for the next BB PHTS assessments. According with the adopted segmentation, each cooling circuit feeds the BB segments related to 2 tokamak sectors, therefore it delivers helium to 4 IB segments and 6 OB segments.

4 Intermediate Heat Exchanger and Steam Generator design

4.1 Introduction

Being the larger components of the Ex-Vessel circuits, the heat exchangers have been investigated as first priority because they can play an important role in the final disposition of the PHTS circuitry. If on the BB side the pipes must be channelled into the upper port annexes to reach the segment chimneys, on the exchangers side the arrangement of both hot and cold legs is driven by the heat exchanger topology, thus its inlet and outlet position strongly influence the overall PHTS layout.

According to the definition of Shah and Sekulić [91], a heat exchanger is a device that transfers thermal energy between two or more fluids, at differing temperatures and in thermal contact, usually without external heat and work interactions. The fluids may be single compounds or mixtures. Typical applications involve heating or cooling of a fluid stream of concern, evaporation or condensation of a single or multicomponent fluid stream, and heat recovery or heat rejection from a system. In some heat exchangers, the fluids exchanging heat are in direct contact, while in others, the heat transfer between fluids takes place through a separating wall.

The design of a heat exchanger is multidisciplinary as it involves considerations that include: process/design specifications, thermal-hydraulic design, mechanical design, manufacturing and cost considerations, and trade-offs and system-based optimization, with possible strong interactions among these considerations.

Nevertheless, the exchanger design process foresees a sort of hierarchical definition of the precedence because, if on one hand thermal-hydraulics and thermo-mechanics have continuous points of contact and interaction during the design evolution, on the other hand the analysis of costs is carried out once a preliminary design has been already made. In addition, while the thermal, hydraulic and the structural designs analyse are mainly analytical or numerical most of the other major design considerations involve qualitative and experience-based judgments, trade-offs and compromises. Hence, it is worth to underline that it does not exist an unique solution to designing a heat exchanger for a set of specifications.

Since the PHTS design has started from scratch, the heat exchanger design activity has followed the same prioritizations described above, giving more emphasis on the thermal and mechanical design without, however, neglecting a survey of the technical solutions already exploited in other nuclear plants with the scope of steering the design toward options which manufacturability have been demonstrated, at least for those parts that can be equated.

As already mentioned, a proper heat exchanger design needs a combination of thermal-hydraulic and thermo-mechanical elements to meet all the prescribed requirements and, since that the ideal combination of these elements might not be possible or practical, a choice of compromise is usually necessary. In fact, a deep analysis aimed at selecting criteria and procedures to be followed in order to find the optimal solution, often shows conflicting needs of process conditions, operations and maintenance. It is, therefore, a duty of the designer to take into account one or several design solutions, depending upon the relative importance of these factors.

For instance, the selection of the fluid that will be on the tube side will affect the selection of the exchanger typology and require an evaluation of many factors to arrive at a satisfactory compromise. The most important factors are herewith reported, however it should be underlined that these general guidelines must be evaluated case-by-case, taking into account the specificity of the application in which the heat exchanger will be operated [92].

- The fluid at higher pressure should be placed in the tubes. Otherwise, due to the larger diameter, a thick-wall shell will be necessary causing an increase of the cost.
- The high-temperature fluid should be inside the tubes. High temperatures reduce the allowable stresses in materials, and the effect is similar to high pressure in determining shell thickness. Furthermore, safety of personnel may require the additional cost of insulation if the high-temperature fluid is in the shell.
- When the pressure drops can be critical the need of high accuracy in their prediction is a requirement, the placement of fluid inside the tubes is suggested. The tube side pressure drop can be calculated with less error, while in some exchanger the pressure drop in the shell can experience wider deviations from the theoretical estimation due to the shell leakage clearances.
- The more hazardous or expensive fluid should be put on the tighter side of the exchanger, which is usually the tube side of the exchangers.
- The use of corrosive fluids or processes requiring high cleanliness may dictate the use of special alloys which are expensive; therefore, the more corrosive fluids will be circulated inside the tubes in order to save the cost of an alloy shell.
- The shell is usually more difficult to clean hence fluids showing a marked tendency to foul should pass through the tubes.

As can be gathered from these not totally exhaustive points, for the DEMO relevant fluids and working conditions, the choice of the tube-side coolant is not so straightforward.

Helium is the hottest fluid in DEMO BoP and, flowing within a nuclear primary circuit, it is a carrier of radioactive particles (mainly tritium). Furthermore, a good prediction of its pressure losses may be helpful to assess the circulators size.

However helium is the high-pressure fluid only when the “indirect-coupling” solution is employed whereas if a steam generator is used, the secondary coolant will be operated at higher pressure. Moreover, deposits caused by water or molten salt are expected to be more frequent and more aggressive compared to helium which, in principle, is a clean, inert gas.

These conflicting features make hard an a-priori selection of a design solution that easily suits all the demands. Therefore, in order to provide a context which can support the final decision, a recognition of the nuclear heat exchangers/steam generators state-of-the-art has been carried out. A design descriptions of existing and proposed designs will be discussed.

4.2 Overview of the main solutions adopted in nuclear industry

The current NPPs fleet consists of 449 reactors in operation (including those in long-term shutdown), 52 reactors under construction and 178 permanently shut-down [93]. Among these almost 700 reactors, many configurations have been developed and fruitfully confirmed over the years while the fate has relegated some others to be the first as well as the last that kind. It is known that Light Water Reactors (LWR), in particular the PWR type, have always covered the majority of these power stations. However experiences that have involved gas-cooled reactors, with both helium and CO_2, and Liquid Metal Fast Breeder Reactors (LMFBRs) have not been lacking. This has allowed to test and check a huge number of different technical solutions. In particular, the first lesson that one can learn regards the exchanger architecture used: all the heat exchangers/steam generators constructed for the main NPPs are Shell and Tube type but, within this construction class, several different tube bundle configurations have been proposed.

Despite the clear differences between the helium-heated heat exchangers of the BB PHTS and a PWR steam generator (different coolants, temperatures and pressure), a quick overview of the main features for this latter component could be useful to further understand the manufacturing capabilities of the nuclear industry. To date, three major PWR steam generator designs have evolved:

- vertical "U-tube" units, Figure 4.1, where the primary fluid enters and leaves the tubes at the lower end of the shell while the feed-water is fed through a nozzle into the downcomer where it mixes with recirculating water draining from the moisture separators placed in the shell upper section, at the top of the U-tube bundle;
- vertical once-through units, in which the primary fluid flows downward within the tubes in counter-current flow to the secondary flow; also in this case the feed-water enters via a downcomer which brings it at the bottom of the heating section, then the secondary coolant flows upward among the bundle see Figure 4.2;
- horizontal once-through evaporators, where primary fluid flows in a horizontal U-tube bundle while the steam is separated on the shell side mainly by gravity, see Figure 4.3.

Steam generators of the vertical recirculating type are widely used in both PWR and

CANDU, some once-through steam generators are present in US-PWRs reactors while Russian plants adopts horizontal type steam generators. The U-tube steam generators are typically 20–23 m tall and with a bundle height of 9-11 m, while once-though vertical steam generators have a tube bundle in a range of 15-16 m. The diameter, due to the larger dome in their upper part, can exceed 6 m.

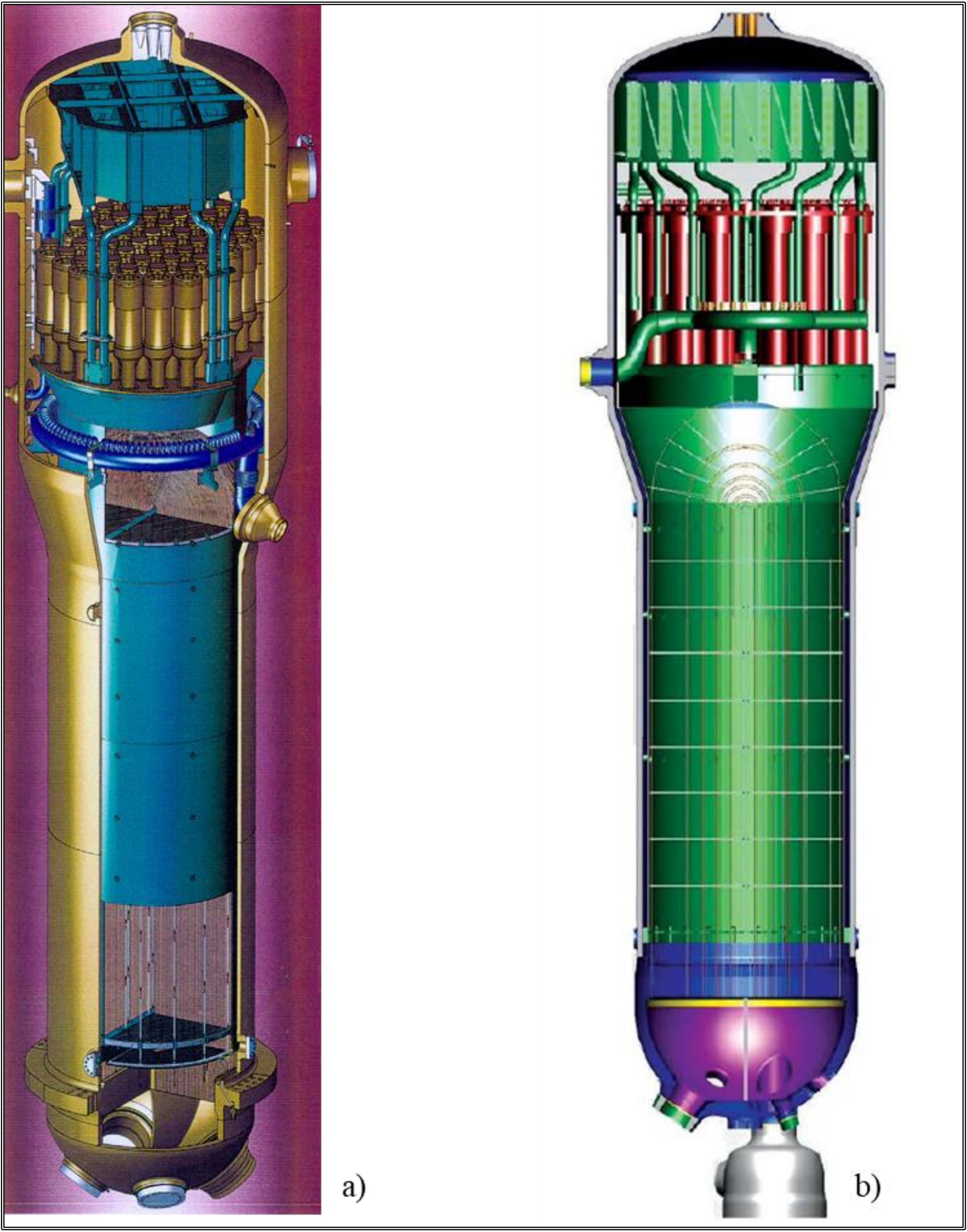

Figure 4.1: U-tube type steam generators: a) Siemens Konvoi, b) Cumming AP1000 [94].

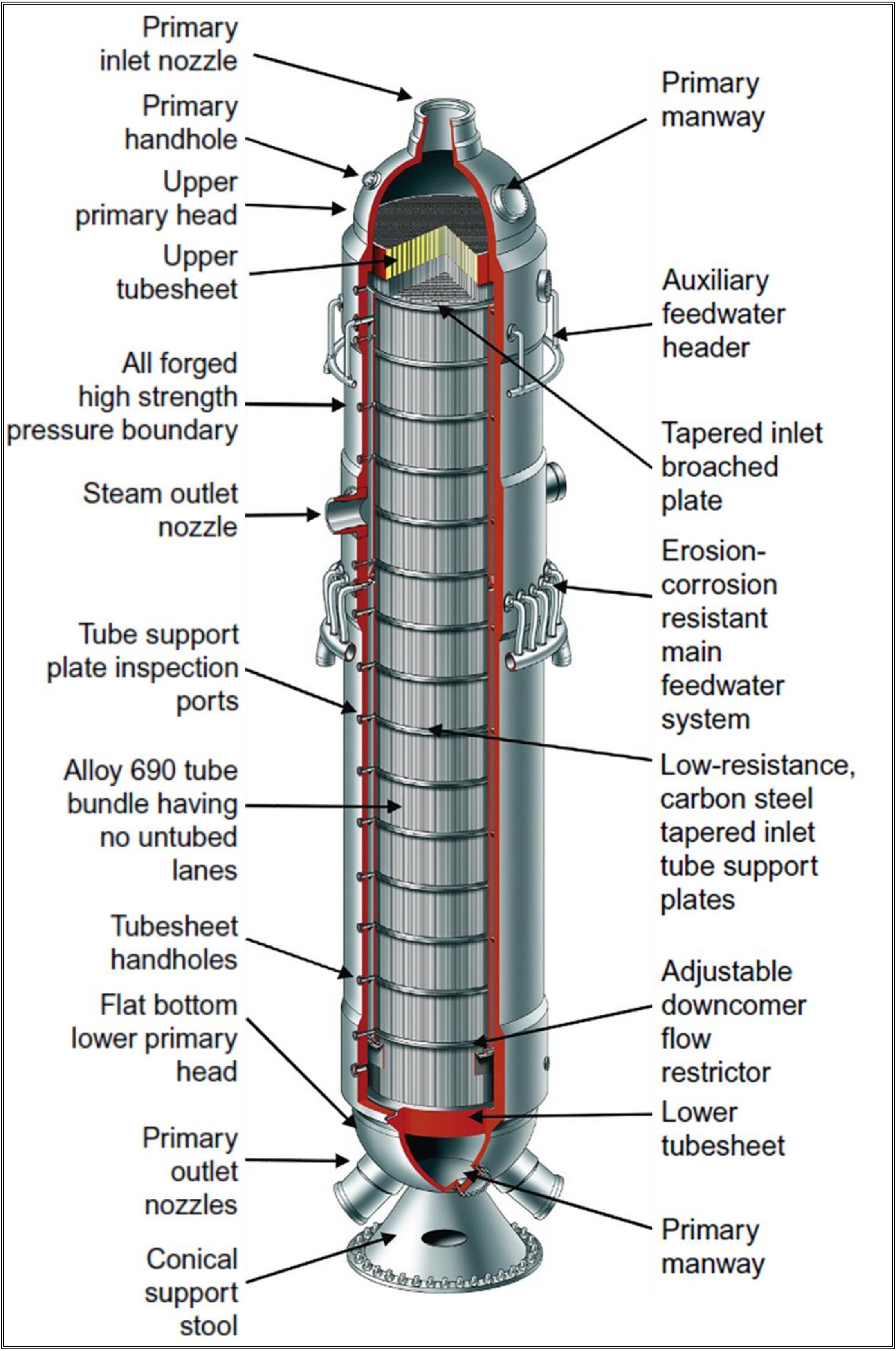

Figure 4.2: Once-through type steam generator: B&W 177 model [95]

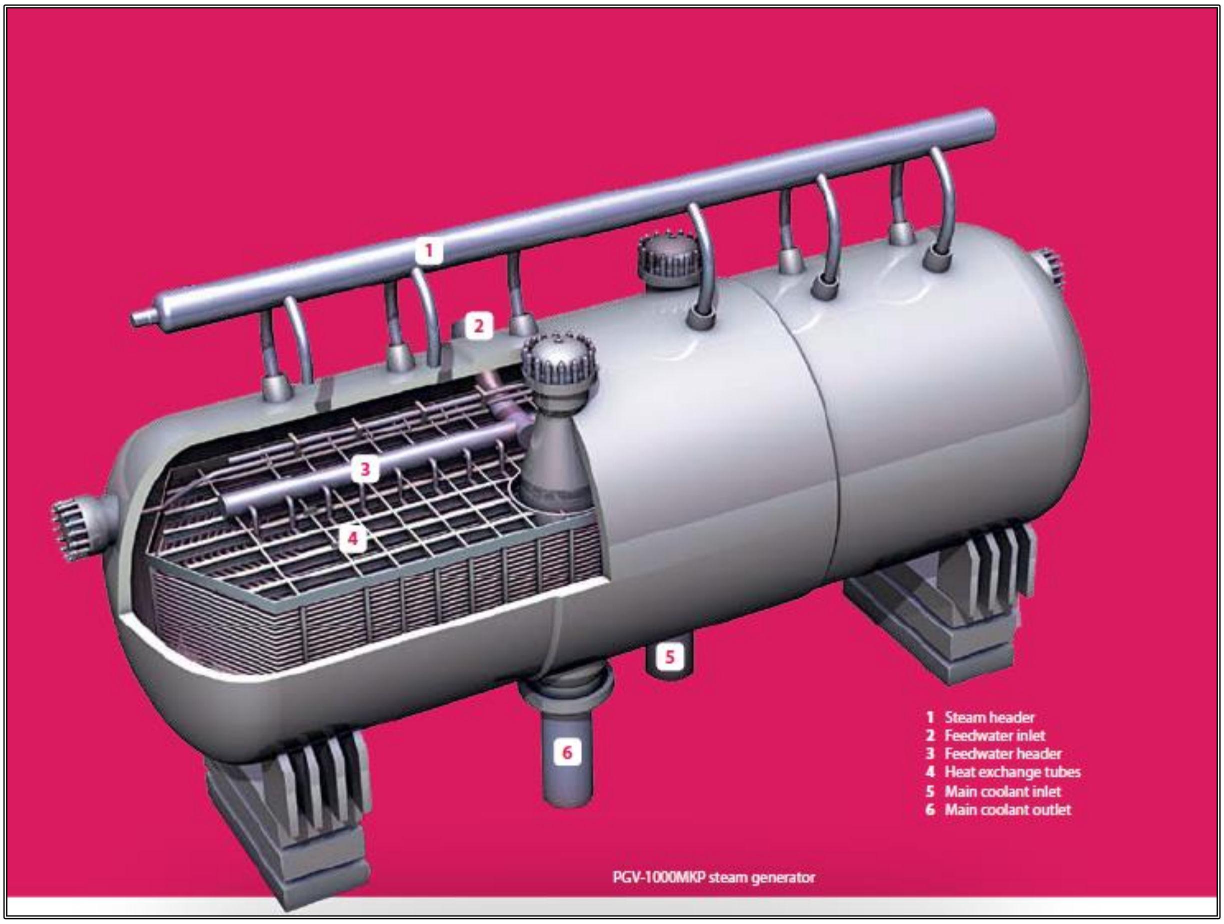

Figure 4.3: Horizontal once-through type steam generator: VVER-1200 model [96].

Usually a PWR steam generator is sized to exchange from 900 to 1500 MW and weighs in the range of 300–500 tons. However the newer steam generators for the AP1000 reactors weigh around 600 tons each and some designs of the Combustion Engineering weigh as much as 800 tons [95].

The steam generators can contain from 3000 to 16000 tubes, which diameters are usually in a range of 15-19 mm. The current trends are to use mainly Alloy 690 tubing (instead of the former Inconel 600) although Alloy 800 is also occasionally used [94]. The pressure retaining parts are essentially made from ASME 106, SA 533 (plates) and SA 508 (forged nozzles) and the thicknesses achieved can vary from 400 to 600 mm in the tubesheets and reach 250 mm in the shell parts.

As far as concern the LMFBRs, recalling what we said in section 2.4, these reactors transfer the heat from the primary radioactive sodium circuit, by means of an IHX, to the secondary non-radioactive sodium loop, and then via a steam generator to a water system to produce superheated steam which supplies a conventional turbine-generator. Since the first sodium cooled reactor EBR-I, which was commissioned in 1951 in the U.S.A., the general scheme with an intermediate loop has been retained for all LMFBRs, as well for the loop type as for the pool type, with minor modifications appearing only at the IHX level. In all countries it is recognized that the IHX and the SG are two major components that deserve most attention from the designer and from the manufacturer, because the economy of the plant depends strongly on their reliability. Beside its obvious heat exchange function, the IHX acts as a barrier between the primary radioactive core coolant and the non-radioactive section of the LMFBR plant and, as such, must retain its tightness even in case of a sodium-water reaction occurring in the steam generator.

The IHX is located either within the reactor tank (pool type reactor) or near this tank in a separate vault (loop type reactor) but in any case within the reactor building, acting as safety containment for the environment [97]. The presence of two type of exchangers, with different functions and operating at temperatures similar to those foreseen in the DEMO BoP, makes a comparison between the technologies and solution more engaging.

All IHXs proposed are of the shell and tube type, as well as in the PWR steam generators, several different tube configurations have been chosen [87]:

- U-shaped tube bundle installed in a parallelpipedic shell in the BN-350;
- helical tube bundle and no tube sheet for KNK reactor;
- straight tubes welded to tube sheets for EFFBR, EBR-II, FFTF (U.S.A.), Kalimer-600 (Korea), PFPR (India), Rapsodie, Phénix and SuperPhénix (France) and BN-600/800 (Russia) [98].

It seems that the straight tube in straight vertical shell configuration is now generally preferred because of its greater simplicity of design and construction.

Figure 4.4 shows a common IHX layout where the two coolant streams follow a counter-current flow arrangement with the primary coolant usually placed on the shell side.

In spite of its simplicity, thanks to the good heat transfer capabilities of sodium, this configuration has been considered already acceptable guaranteeing a relatively small heat transfer area respect to the rated thermal power, which is commonly in a range of 300-400 MW (higher values can be also achieved) [87]. In fact, even though the overall exchanger can reach about 19 m, see Figure 4.5 [99], the bundle height is in a range of 5-8 meters [87].

In this case the IHX has often a floating head at the lower end and/or some means to accommodate the differential thermal expansion between the tubes, for instance a sine wave bend has been adopted in Fermi, Rapsodie, PFR, FFTF, BN-600 and BN-800 reactors. However in some other cases this expansion bend has been found an unnecessary feature (EBR-II, Phénix, SuperPhénix, KALIMER, PFPR) [98].

As it is operated at temperatures commonly exceeding 500°C, the sodium-sodium intermediate heat exchanger is generally constructed of 304, 316, or 321 austenitic stainless steels, all materials being known to be resistant to corrosion by oxide-free sodium at this temperature [97]. More recently, high Cr ferritic alloys have received some attention (9Cr-1Mo) [98]. Nonetheless, although the high temperatures achieved, an extra tube wall thickness of 0.1 mm is only sometimes recommended because clean sodium shows non-corrosive attitudes hence provision for corrosion allowance is not mandatory.

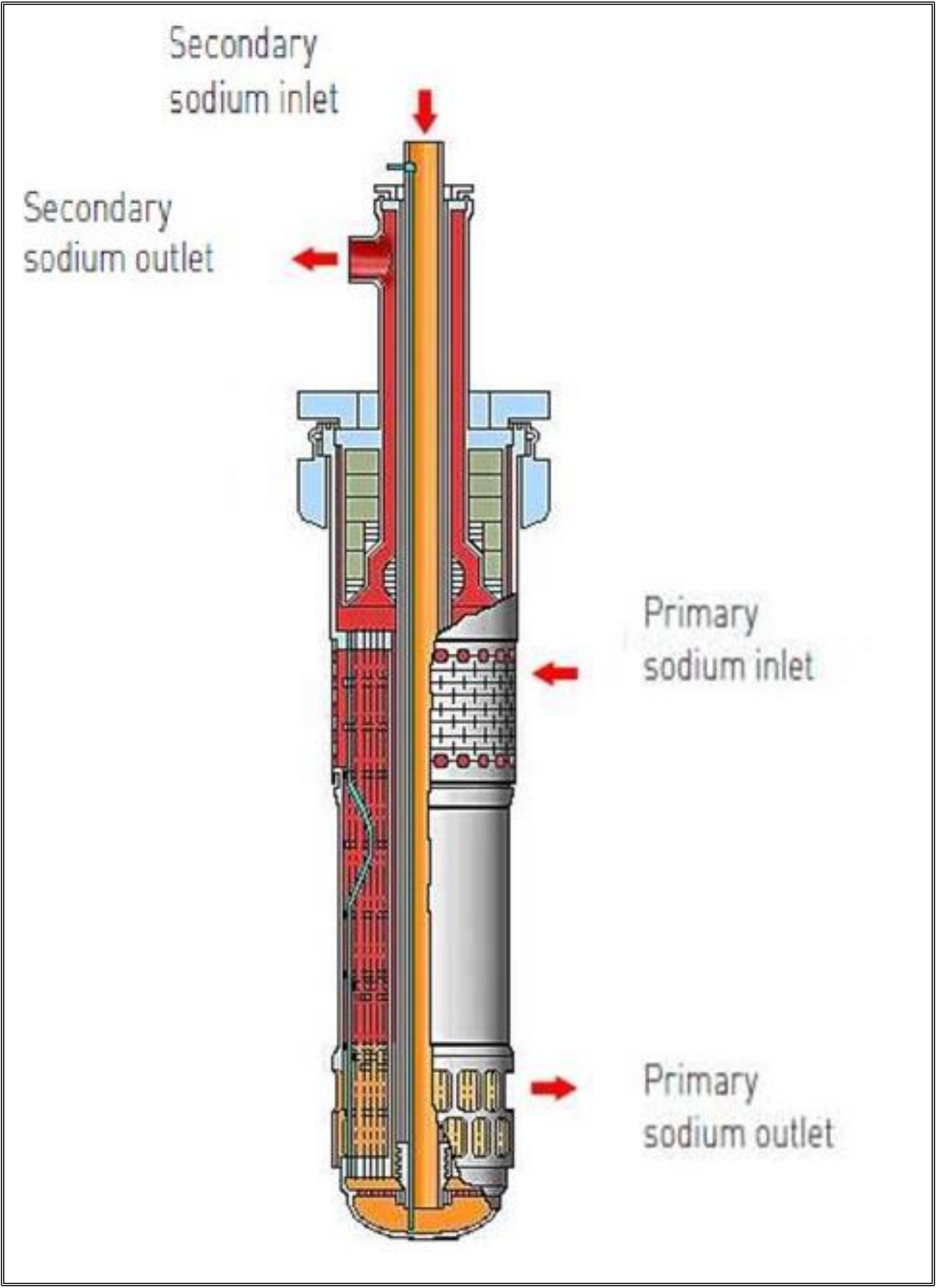

Figure 4.4: Typical sodium IHX with straight tube bundle: BN-600/800 reactor [98].

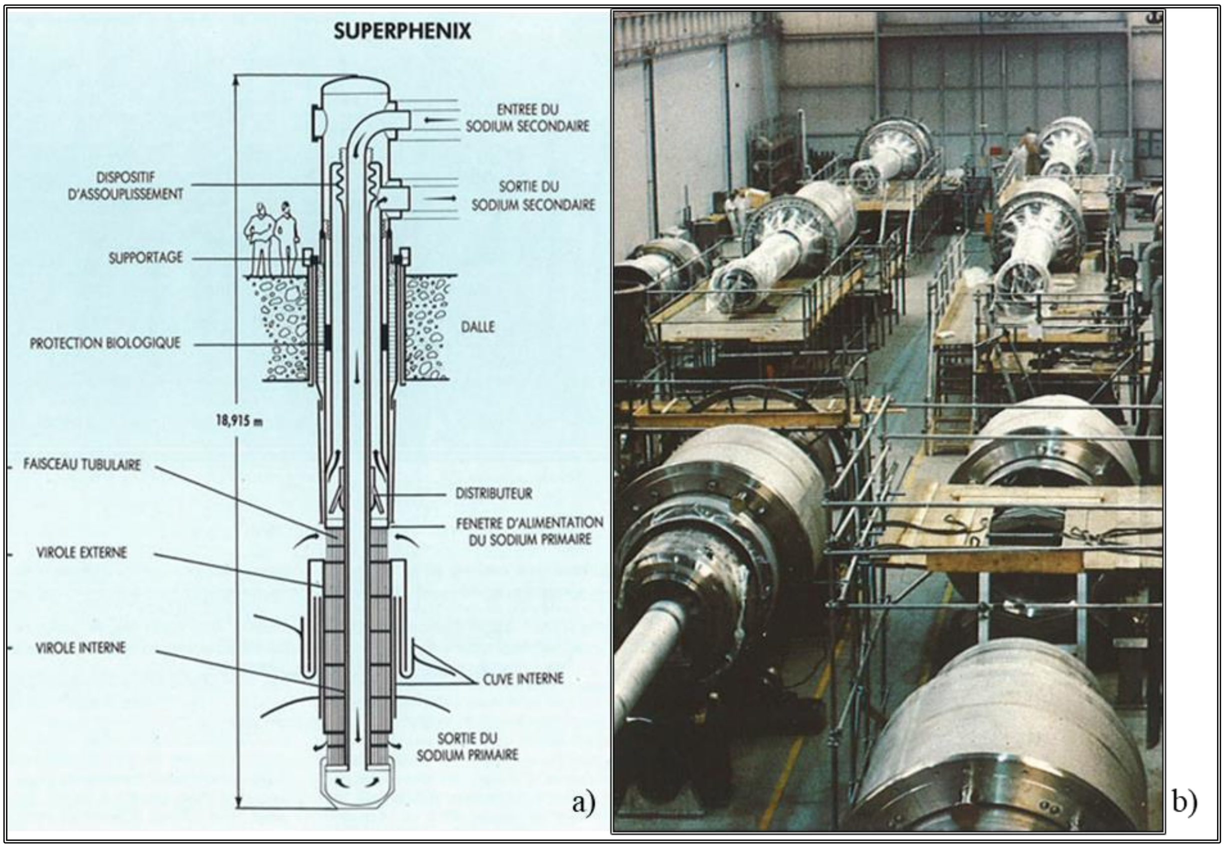

Figure 4.5: Superphénix IHX: a) Descriptive outline b) Manufacturing line [99].

With regard to the sodium steam generators, a number of configurations have been proposed, depending on the size and shape of the tubes. They are all shell and tube heat exchangers with the water/steam that flows inside the tubes, which are more adequate than the shell to sustain the high pressure involved.

The steam generator can be roughly classified in two categories [97]:

- straight and relatively short tubes of small diameter;
- coiled and long tubes of larger diameter.

An example of the first type can be found in the PFBR steam generator [100], which is a vertical, counter-current shell and tube type heat exchanger with sodium on shell side, flowing from top to bottom, and water/steam on tube side. Each of its 547 tubes is 17.2 OD, 2.3 mm thick and 23 m long; the steam generator is rated for 158 MW, its overall length and diameter are about 26 and 1.2 meters, respectively.

To deal with the axial temperature gradient, tubes are provided with expansion bends in sodium flow path. Its location is in lower portion of single water phase water zone for steady state operation of 20 to 100% power operation.

Modified 9Cr-1Mo ferritic steel has been selected as main structural component for both tubes and shell [101]. Figure 4.6 shows a conceptual scheme of the PFBR steam generator.

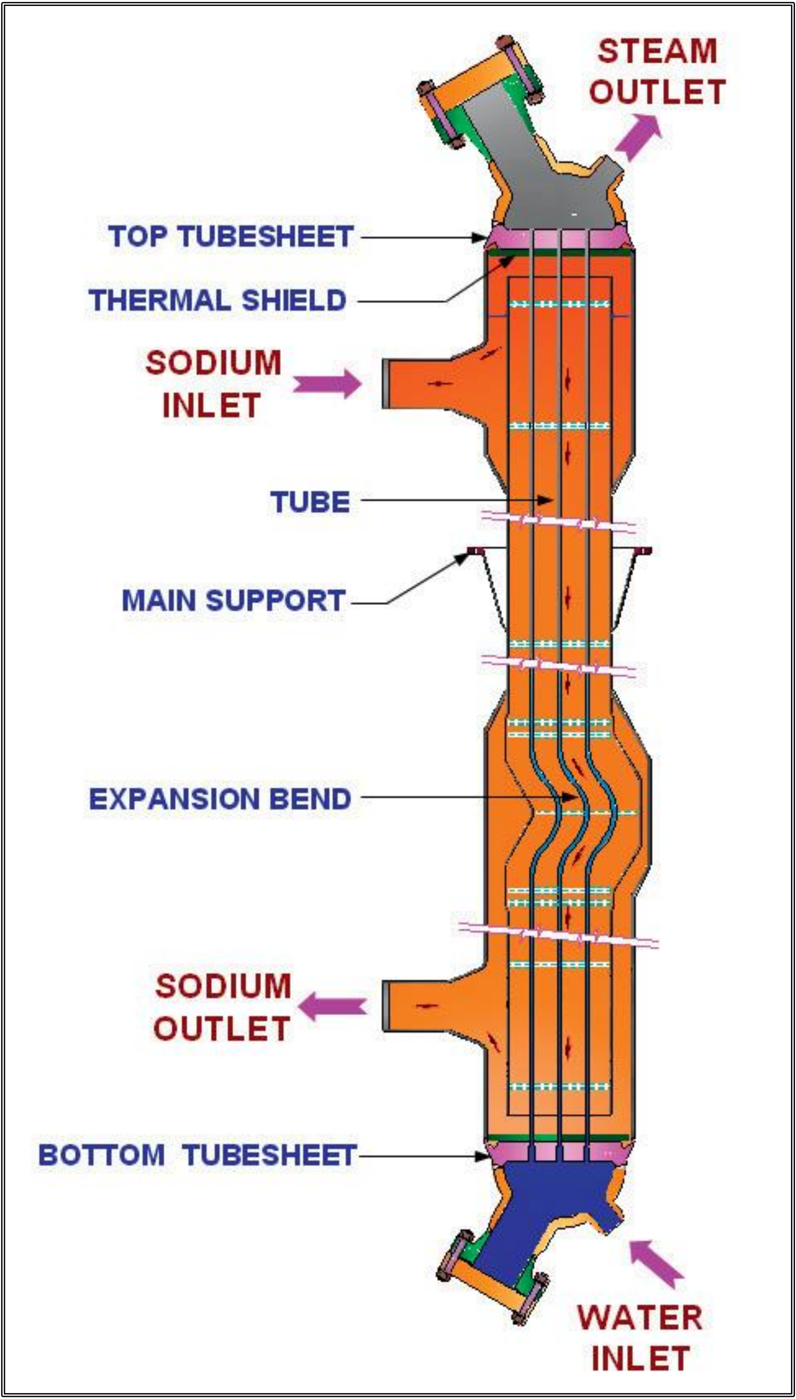

Figure 4.6: PFBR steam generator [98].

The second type, with longer helically wounded tubes (60 to 100 m) of larger outer diameter is best exemplified by the SuperPhénix steam generator [97]. In this configuration, (Figure 4.7) a typical heat transfer tube leaves a water box and penetrates the cylindrical shell through a thin and elastic thermal sleeve (a feature already tested in Phenix reactor). It is shaped successively in an expansion bend, a helical coil, and another expansion bend and penetrates again the shell wall through another thermal sleeve before joining a steam box tubesheet. A particular of the expansion bend ensuring the connection between the bundle tubes and the sleeves enabling to go through the external envelope is depicted in Figure 4.8. In order to exchange 750 MW of thermal power, the tube bundle consists of 357 tubes, helically wound around the central body, in 17 alternate concentric layers, with the same slope and the same effective length (91.5 m). To do so, each layer has one more tube than the previous layer.

The component weighs about 194 tons, is 22.5 m long and 2.9 m in diameter. Materials used are Alloy 800 for the tubes and several austenitic stainless steels to ensure the fulfilment of the requirements in the different zones of the shell [99].

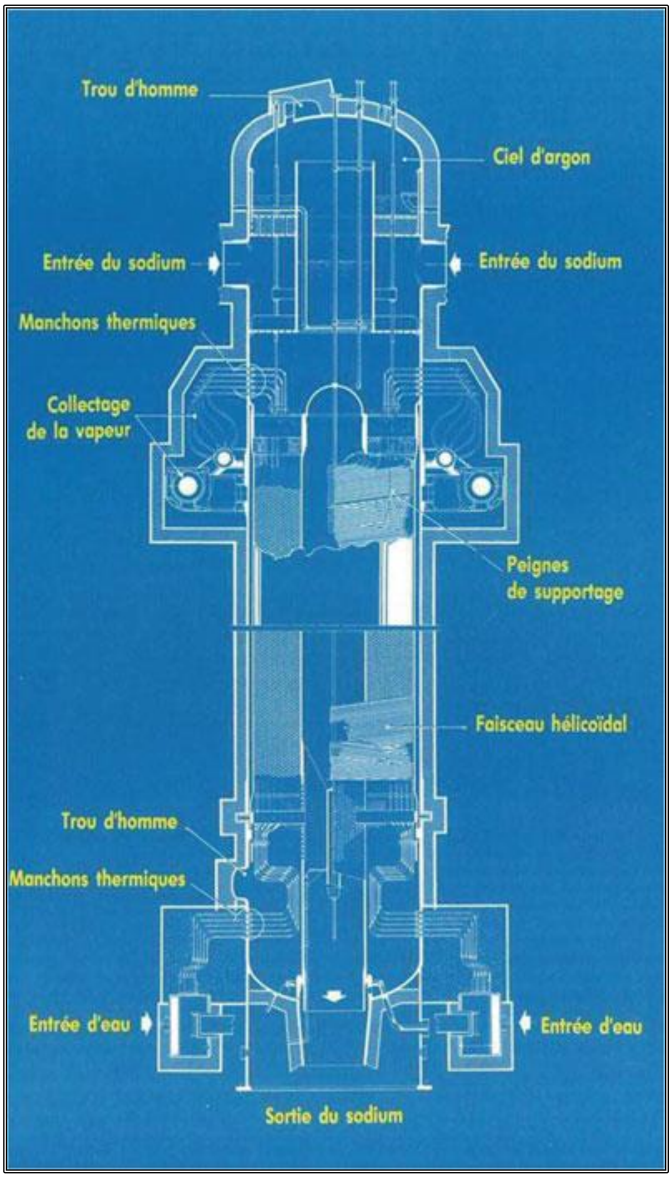

Figure 4.7: Overview of Superphénix steam generator [99].

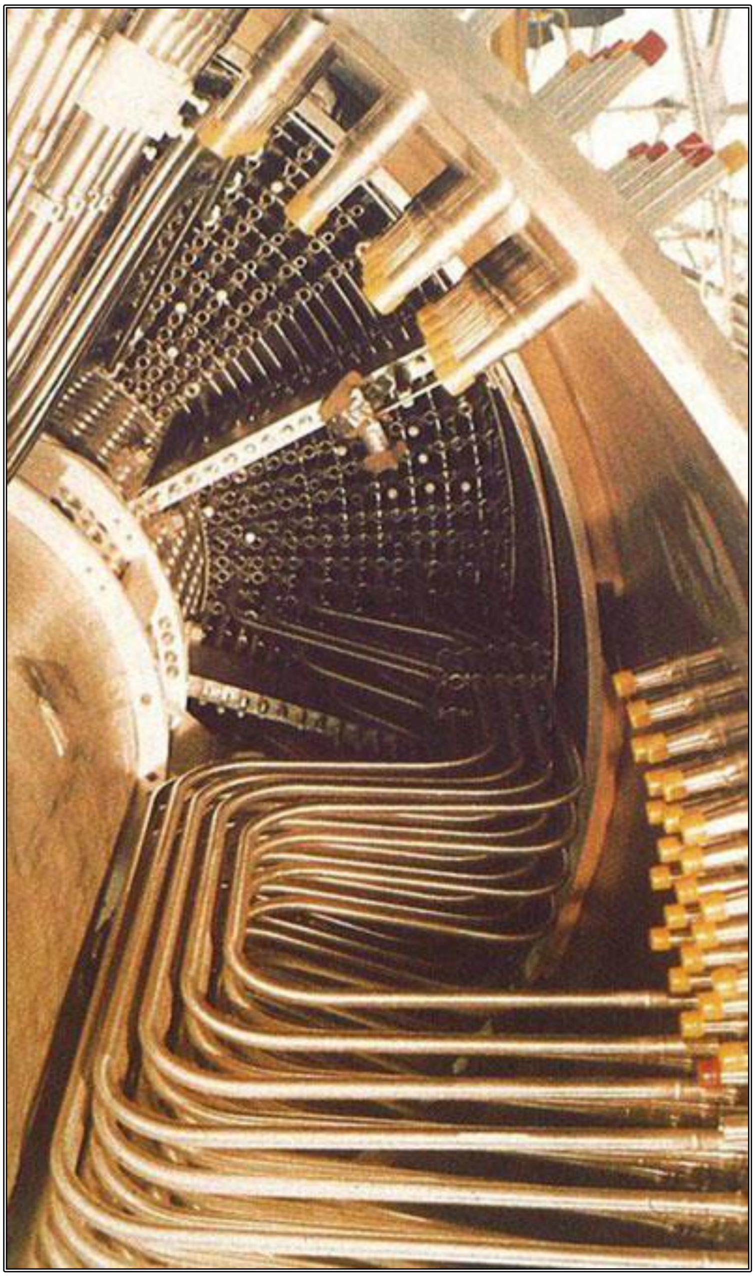

Figure 4.8: SuperPhénix steam generator: bundle internal expansion loops [99].

Some of the features proven in the Superphénix steam generator are present also in KALIMER-600 [102], a recent project developed by Korean Atomic Energy Research Institute (KAERI) in the framework of the research activities on the Generation IV [103]. Each of the two KALIMER steam generators is designed to transfer 765 MW via an helical bundle inserted in a shell of 4.1 m in diameter and about 18 m long. The heat exchange section is 8.5 m tall and contains 715 tubes of about 72 meters. The main material for tubing, internal structures and shell of steam generator is modified 9 Cr-1Mo steel, which characteristics have been judged acceptable against erosion and stress corrosion cracking [98].

Looking at the gas-heated exchangers, a good experience has been gained in U.K and France with the CO_2 reactors, both for the first generation of these NPPs, namely the Magnox reactors, and with the Advanced Gas Reactors (AGR). The Magnox reactors were relatively small in size and they commonly adopted boilers where the carbon dioxide flow over the meander type tubes (serpentine layout) were water got boiled. This configuration was progressively abandoned with the transition to the AGRs whose latest steam generators, still in operation, are of helical type, see Figure 4.9.

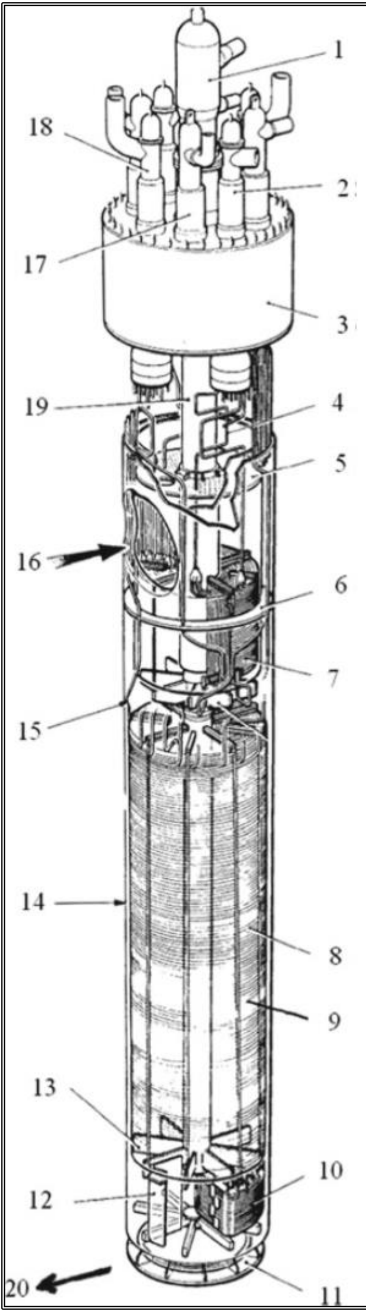

1: feed water inlet (200°C),
2: reheated outlet (530°C/4 MPa),
3: boiler closure,
4: compensation,
5: top gas baffle.
6: annulus gas baffle,
7: reheater,
8, 9: preheater and evaporator,
10: compensation for feed water inlet,
11: boiler/circulator gas seal,
12: noise baffle,
13: support,
14: boiler casing,
15: compensation for super heater,
16: CO_2 inlet (615℃),
17: central support,
18: live steam outlet (540℃/16.6 MPa),
19: reheated inlet (350℃),
20: CO_2 outlet (250℃)

Figure 4.9: Hartlepool AGR steam generator [104].

In a single AGR helical steam generator the CO_2 transfers about 200/250 MW of thermal power to 285 tubes being equal in length thanks to changes in helix pitch to compensate for changes in row diameters. There are 19 rows, six tubes in the inner row, increasing one tube per row to 24 tubes in the outer row. The heating surface consists, from the cold zone to the hot, of carbon steel, 9Cr-1Mn steel and austenitic type 316 stainless steel tubing welded into a composite length utilizing welded transition pieces. Superheated steam leaves the boiler through one of four superheater outlet headers. A helical steam reheater is also used, it is located above the superheater [105].

Although the examples of helium-heated steam generators are less than those found for Magnox reactors and AGRs, several countries, all over the World, have embarked the adventure of designing a helium High Temperature Gas-Cooled Reactor (HTGR), developing their own technologies. Noticeable experiences can be found in U.S.A, Europe (Germany in particular), and lastly China.

The design of steam generators/heat exchangers to equip this type of reactors have evolved over time from relatively simple pendant-U-tube, forced-recirculation units of Peach Bottom (U.S.A) [106] to the more compact helically coiled once-through units, as in the Fort St. Vrain HTGR station (U.S.A) [107], in the THTR-300 (Germany) [108] and the most recent HTR-PM Chinese reactor [109]. Thus, since the ‘70s the design of the large steam generating units in the HTGRs has been somehow frozen with the tube bundle which evolves following an helical path; however, the steam generators design evolution has, of course, been closely coordinated with other major design changes in helium cooled reactors: if the early designs made use of the Pre-stressed Concrete Reactor Vessel (PCRV), particularly of the multiple cavity variety, which provided separate cavities for the Reactor Core and Steam Generators, the subsequent steam generator designs have been patterned after the development of a reactor global envelope employing three interconnected pressure vessel, one for the core, the second for the steam generator/heat exchanger and the third acting as connecting concentric duct which let helium circulate among the system.

THTR-300 is a power plant representative of the first design philosophy, see Figure 4.10, while the HTM-PM reactor, which is going to begin the commercial operations in the late 2019, stands for the second typology, see Figure 4.11. At first glance, it immediately emerges that both reactor layouts are far apart from the DEMO BB PHTS. However, having helium at high pressure and temperature on the primary side of their exchangers, most of the HTGR equipment can be easily taken as reference for those technologies and nuclear applications which deal with such a coolant. Indeed, the bulk of the steam generator design is hardly dependent on the kind of heat source or the path followed by the coolant before reaching the component ingress. Obviously, in a nuclear system many decisions can be affected by safety reasons and it is not so unequivocal that a fusion power plant must satisfy the same safety requirements of a fission reactor. Nevertheless, at these early stages of the DEMO project, the differences are too subtle to deeply influence the choice of a component in place of another.

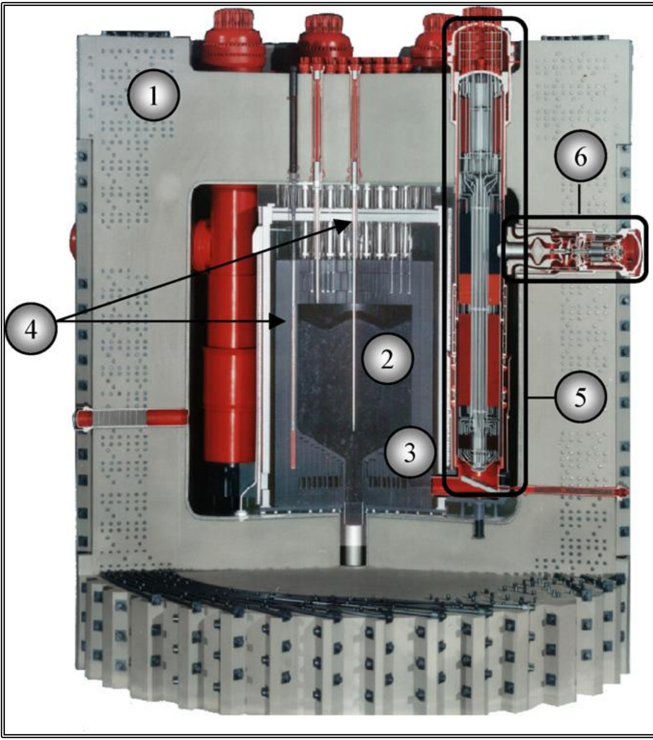

1 - Pre-stressed Concrete Reactor Vessel
2 - Reactor core
3 - Ceramic core structures
4 - Control rods
5 - Steam generators
6 - Helium circulators

Figure 4.10: THTR-300 reactor cutaway view [110].

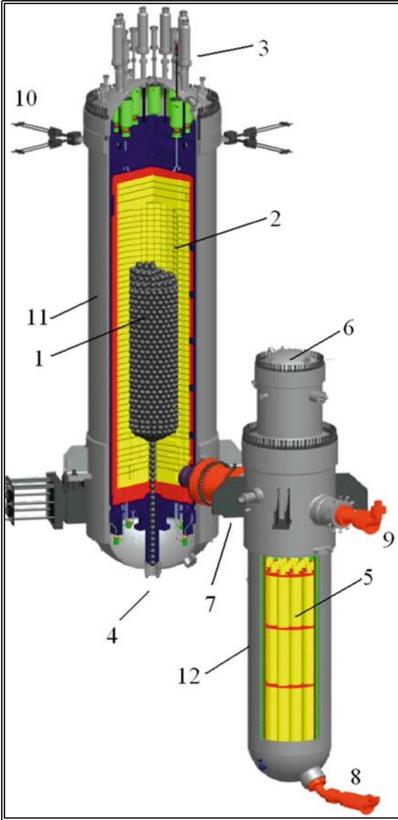

1 - Core
2 - Reflector
3 - Control Rods
4 - Discharge system
5 - Steam generator’s modules
6 - Helium circulator
7 - Connecting vessel with coaxial duct
8 - Feed-water supply
9 - Steam outlet
10 - Shock dampers
11 - Reactor pressure vessel
12 - Steam generator pressure vessel

Figure 4.11: HTR-PM reactor cutaway view [111].

Therefore, the concepts adopted in helium cooled NPPs have been deeply assessed and taken in great consideration for the design of the BB PHTS exchanging equipment.

For instance, great attention has been paid at the THTR-300 steam generator, Figure 4.12, operated for about 5 years with a helium inlet temperature of 750° without any relevant issues [112].

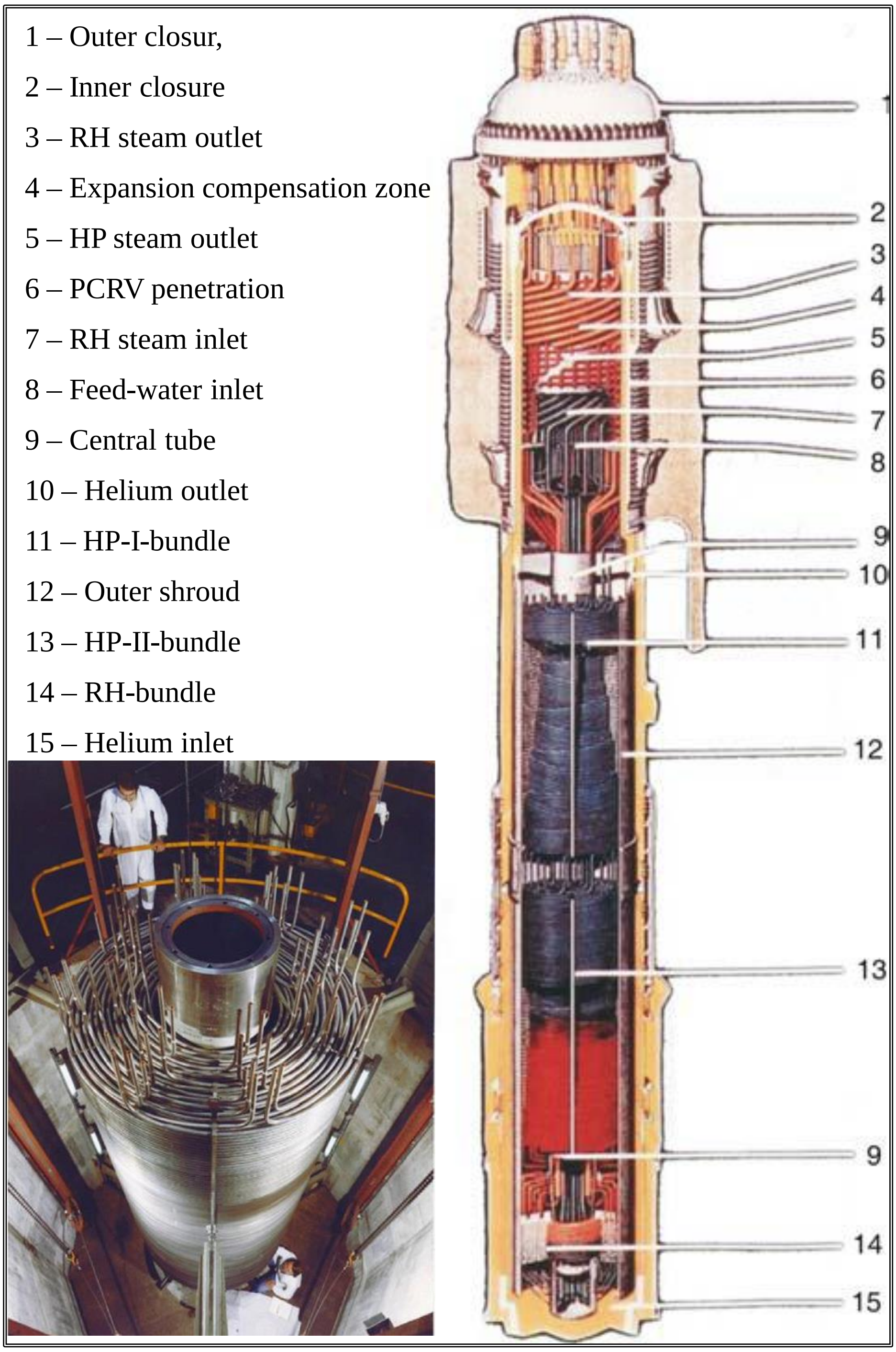

1 – Outer closur,
2 – Inner closure
3 – RH steam outlet
4 – Expansion compensation zone
5 – HP steam outlet
6 – PCRV penetration
7 – RH steam inlet
8 – Feed-water inlet
9 – Central tube
10 – Helium outlet
11 – HP-I-bundle
12 – Outer shroud
13 – HP-II-bundle
14 – RH-bundle
15 – Helium inlet

Figure 4.12: THTR-300 steam generator: bundle manufacturing and cutaway view [110].

The steam generator consists of 3 tube bundles, one is used as low pressure (LP) steam reheater (RH), while the other two form the main heating section with superheater, evaporator and economizer. The two High Pressure (HP) bundle are helicoidally wounded around a central tube, the smaller reheater consists of straight tubes. The helium flow direction within the steam generators is from the bottom to the top, in counter-current respect to the water. Thus, on its way the coolant passes along the tubes of the reheater and, then, flows across the HP helical bundles. The thermal power of one steam generator is 128 MW of which 111 MW are transferred to the two high pressure bundles and 17 MW are exchanged in the reheater.

Hence, regardless of the small reheating portion, the steam generator is basically a helical exchanger. The HP-bundles of the steam generator have a total height of 8.3 m and consist of 15 multi-start coils for a total amount of 80 tubes, which outer diameter is 25 mm. As often happened in the AGR steam generators, the tubes were made of more than one material, in particular two different low alloyed steels were used in the colder region of the bundles, while Alloy 800H was chosen as steel for the high temperature parts [113].

A further evolution in the design of a helium-heated helical steam generator can be noticed in Chinese HTM-PM reactor, where the exchanger is positioned in a pressure vessel side by side to the reactor vessel [114]. Thanks to the particular connection between the vessels, see Figure 4.11, the hot helium enters the component at the top of the steam generator where it is distributed among 19 modular steam generator bundles in order to cross them from top to bottom [115], see Figure 4.13. The steam generator modules are designed in form of helical wound tubes. Each module is almost 8 meters tall and contains 35 tubes which are about 60 meters long, with an external diameter of 19 mm and 3 mm thick. Both pressure vessels – about 25 m long and weighting up to 700 tons - are composed of SA533-B steel as the plate material and the SA 508-3 steel as the forging material [116].

Although the HTR-PM has been fully developed in China and its plenty of technological innovations, the idea behind this reactor grounded its roots on the conceptual designs of the German HTR-module [117] and the US MHTGR [118]. The former, in particular, deserves some last words before completing this brief, non-thorough, review on the exchangers and its related parts.

The concept of the HTR Module has been developed by Interatom/Siemens as a nuclear heat source to deliver not only electrical power but also process heat. The process-heat can be produced in form of process steam to be used, for instance, into a steam reforming or a coal gasification system. However the process steam might be also used to supply high temperature to other chemical or industrial processes that do not necessarily need water vapour.

In order to fulfil these requirements, the reactor should be equipped with an intermediate heat exchanger providing a clear separation between the nuclear plant and the heat application.

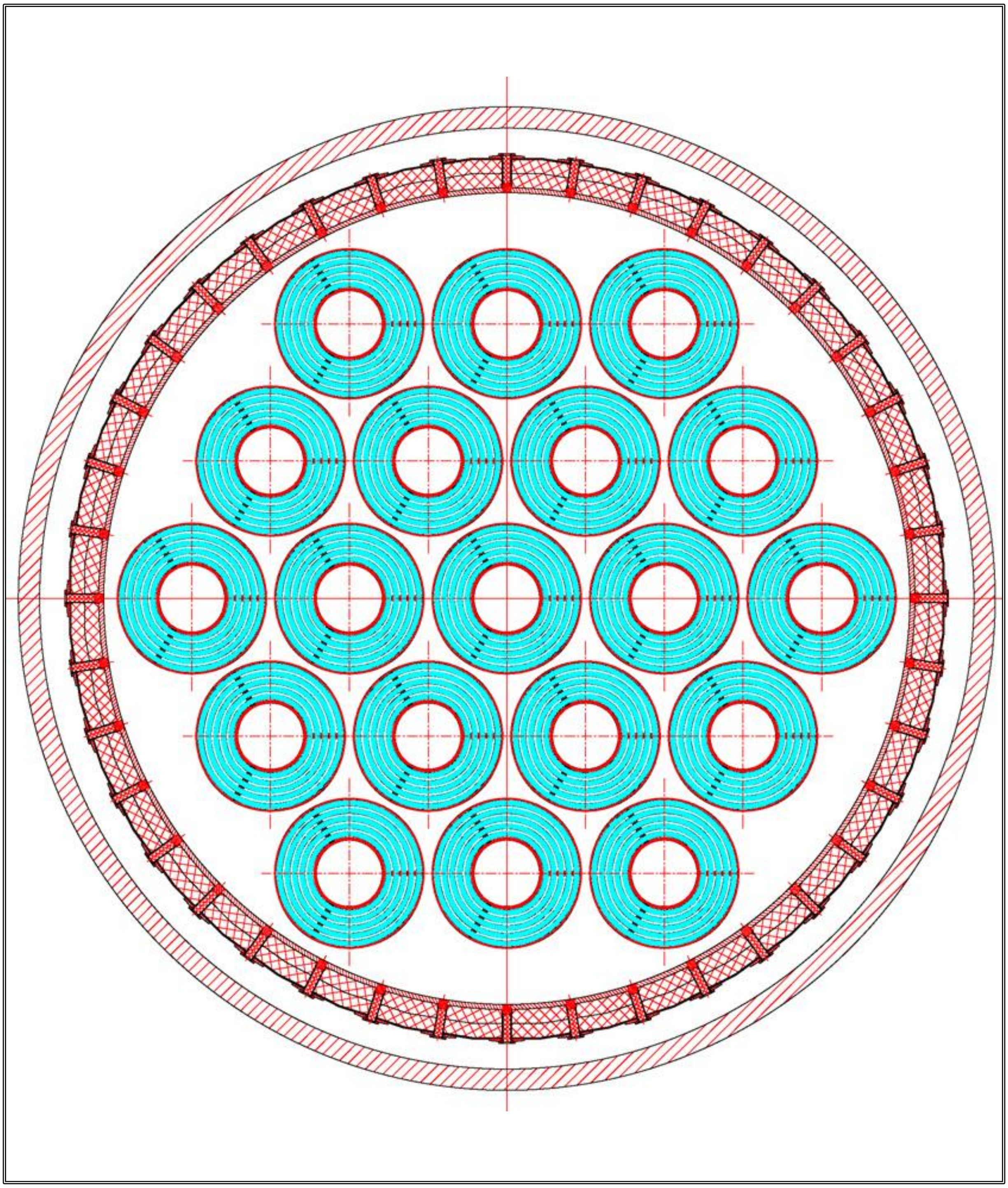

Figure 4.13: Cross section of the HTR-PM steam generator with 19 assemblies [115].

The concept of a combination of the HTR Module with an IHX is shown in Figure 4.14.

As can be seen, the German reference design of a process-heat HTR Module is very similar to the Chinese reactor, with the two pressure vessels in a side-by-side arrangement. The thermal power of the nuclear reactor is 170 MW.

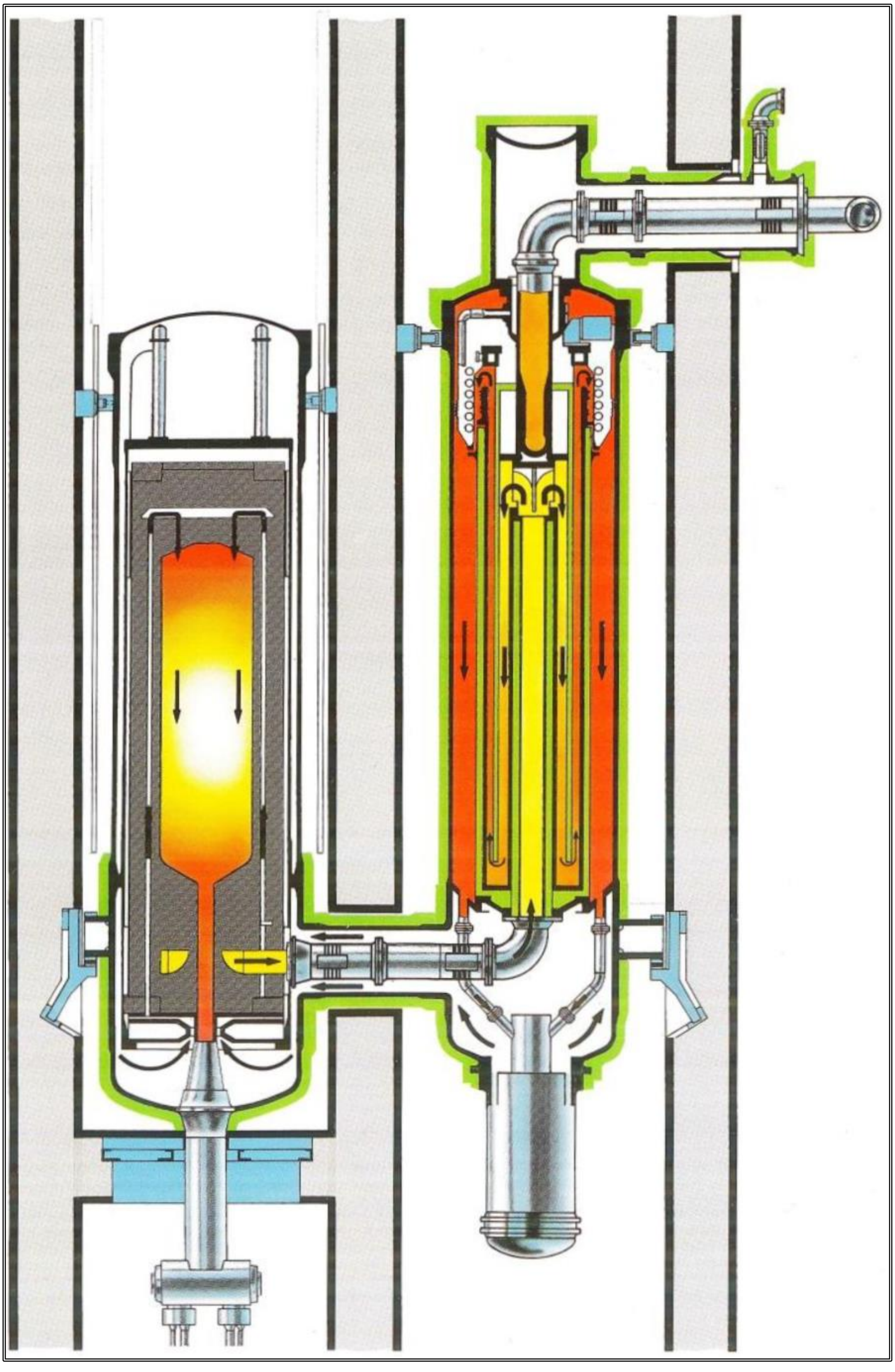

Figure 4.14: HTR module: reactor pressure vessel (left) and IHX vessel (right).

The IHX of the HTR-Module is an helium/helium exchanger that could be equipped either with an U-tube bundle or with helical tubes. The investigation of these two geometries and their relevant configurations has been also pursued achieving good results and showing the feasibility of both alternatives [119]. In particular, within framework of PNP project [120] the Interatom built in Germany the KVK component test facility, which was aimed at testing high temperature helium components. The two helium/helium IHX concepts foreseen for the HTR-Module were successfully constructed and tested. Although the thermal power of the test facility was 10 MW, the exchangers were designed to be able to allocate as much tubes as required to transfer 170 MW.

Of course, the real number of tubes used to perform the experiments was compliant to the actual thermal power of the facility but it was judged enough to conclude that the two heat exchanger variants could be used in a plant of 170 MW operating a 950 °C (helium max temperature) with a lifetime of 100000 hours [98].

The main characteristics of some IHXs and SGs investigated are summarized in Table 4.1 and in Table 4.2, respectively.

Table 4.1. Main features of intermediate heat exchangers for LMFBRs and HTGRs.

Reactor	SuperPhénix	BN-800	HTR-Module 1	HTR-Module 2
Primary coolant	Sodium	Sodium	Helium	Helium
Secondary coolant	Sodium	Sodium	Helium	Helium
Design status	Shutdown	Operation	Conceptual	Conceptual
Tube configuration	Straight	Straight	Helical	U-tube
Power [MW]	373	350	172	172
Primary temp. [°C]	542/392	547/354	950/292	950/292
Secondary temp. [°C]	345/525	309/505	200/900	200/900
Tube number	5380	4956	1612	2470
Tube diameter [mm]	14	16	22	22
Tube thickness [mm]	1	1.4	2	2
ΔT_{LOG} [°C]	29.5	43.5	69.0	69.0
U_{avg} [W/m^2°C]	8121	4856	585	530
S_{ext} [m^2]	1557	1657	4254	4700
L_{tubes} [m]	6.5	6.6	38.2	30.0

Table 4.2. Main features of steam generators for LMFBR and HTGRs.

Reactor	SuperPhénix	PFBR	HTR-PM	THTR-300
Primary coolant	Sodium	Sodium	Helium	Helium
Secondary coolant	Water	Water	Water	Water
Design status	Shutdown	Concept	Commissioning	Shutdown
Tube configuration	Helical	Straight	Helical	Helical
Power [MW]	750	158	250	128
Primary Press. [MPa]	<2	<2	7.0	4.0
Steam Press. [MPa]	18.4	~180	13.3	19.0
Primary temp. [°C]	525/345	525/355	750/250	750/250
Secondary temp. [°C]	237/490	235/493	205/566	180/545
Tube number	357	547	665	80
Tube diameter [mm]	25	17.2	19	25
Tube thickness [mm]	2.6	2.3	3	2.6
S_{ext} [m^2]	2565	667	2340	1191 (w/o RH)
L_{tubes} [m]	91.5	23	59.0	189.5 (avg)

4.2.1 Selection of the exchanger layouts for the different DEMO BoP options

According with the analyses of different IHXs and steam generator designs, both existing and being developed, the adoption of shell and tube exchangers appears the most logical choice if the application of proven manufacturing technologies wants to be pursued.

Among the Shell&Tube (S&T) families, the helical bundle seems the most suitable to be employed as reference for the steam generator design in case of “direct-coupling” DEMO BoP, (Figure 2.3 to Figure 2.5). The details on this exchanger configuration will be discussed in paragraph 4.5 and the final results concerning the steam generator calculations will be described in paragraph 4.5.3, in Table 4.18 and Table 4.19.

On the other hand, for the “indirect-coupling” DEMO option (Figure 2.2) it seems still premature to make a categorical decision on the bundle configuration. Indeed, stating that a helium/HITEC heat exchanger was never built, neither tested on significant scale, the first attempts of choosing the tube layouts should be made in the extent to which is possible to extrapolate the solutions adopted in other nuclear applications.

However, although qualitative assessments are useful in the early stages of a project to exclude a remarkable amount of alternatives, they must be supported by quantitative evaluations before arriving to a definitive choice. For example, in the liquid metal technology the range of temperatures of both the primary and secondary fluids is comparable with the DEMO one, therefore to take in consideration a simpler solution with straight tube bundle might be a possibility. The experience has demonstrated that there are several methods to deal with this temperature window avoiding the occurrence of unacceptable thermal stresses on the structures.

Moreover, due to the modest thermo-physical properties of the two media (at least in comparison with the sodium systems), in the DEMO IHX it can be expected to achieve heat transfer performances similar to those obtained in the helium/helium exchangers. Thus, with respect to a sodium/sodium IHX, the potential need of having longer tubes to exchange a given power might jeopardise the previous assumption.

For these reasons, as the manufacturability of both helical and straight heat exchangers have been tested, it has been decided to investigate both the solutions to get useful data and develop proper design strategies. Results are reported in paragraphs 4.4.3 and 4.5.3.

4.3 Thermal-hydraulic design methodology

The design of new heat exchanger means, in a broad sense, the determination of the exchanger construction type, flow arrangement, heat transfer surface geometries and materials, and the physical size of an exchanger to meet the specified heat transfer and pressure drops. The heat exchanger design problems are basically of two types: the rating and sizing problems. Determination of heat transfer and pressure drop performance of either an existing exchanger or an already sized exchanger is referred to as the rating problem. The rating problem is also sometimes referred to as the performance problem. On the other hand, the design of a new or existing-type heat exchanger is referred to as the sizing problem.

However, from the viewpoint of quantitative thermal-hydraulic analysis, the exchanger type, flow arrangement, and materials have already been selected thus, in the sizing problem, it has to be determined the physical size (length, width, height) and surface areas on each side of the exchanger. The sizing problem is sometimes referred to as the design problem [91].

Therefore the objective is to find the proper set of equations which can relate: the heat transfer rate exchanged between primary and secondary fluids, heat transfer surface area, the fluid terminal temperatures and flow rates in a heat exchanger. One of the most popular method which is widely used to approach such a heat exchanger design analysis is the so-called Logarithmic Mean Temperature Difference (LMTD). A deep discussion about the origin of this well-known method is beyond the scope of this thesis but the interested reader can find a detailed description of the basic principle behind this theory in [122].

However, in the following the most important quantities will be recalled in order simplify the discussion.

From the energy conservation principle, in the hypothesis of:

- adiabatic heat exchanger, meaning that heat transfer between the surrounding environment and the system taken into consideration are null or negligible;
- there are no energy or work sources (sinks) in the heat exchanger;
- the flow is steady-state.

in an exchanger having an arbitrary flow arrangement, the heat transfer from the hot fluid to the cold one must be equal thus, in formulas:

$$\dot{Q} = G_{Hot}\left(h_{out}^{Hot} - h_{in}^{Hot}\right) \tag{13}$$

$$\dot{Q} = G_{Cold}\left(h_{out}^{Cold} - h_{in}^{Cold}\right) \tag{14}$$

Where the equations (13) and (14) are of the same form of the (9), with unchanged meaning of the quantities but just referred to the hot and the cold streams.

Assuming, then, an isobaric heat transfer, the previous equations can be write as follow:

$$\dot{Q} = G_{Hot} c_p^{Hot}\left(T_{out}^{Hot} - T_{in}^{Hot}\right) \tag{15}$$

$$\dot{Q} = G_{Cold} c_p^{Cold}\left(T_{out}^{Cold} - T_{in}^{Cold}\right) \tag{16}$$

where the temperatures appearing in the expressions refer to the bulk fluid temperatures at the designated location.

Once that the energy conservation equations for the two fluids have been written, it is important to find an expression for the heat transfer rate that flows through the surface dividing the two fluids in thermal contact. Reminding that, from the second principle of thermodynamics, the heat goes from the hottest parts to the coldest parts, we can write a constitutive law which can be seen as an extension of the Newton’s law of cooling [121], thus proportional to the temperature difference of the two fluid, $\Delta T=(T^{Hot}-T^{Cold})$. In particular, focusing on an infinitesimal portion of the heating surface, we can write that the local heat transfer rate is related to the local temperature difference of the two fluid streams:

$$d\dot{Q} = U_{Local}\left(T^{Hot} - T^{Cold}\right)_{Local} dS \tag{17}$$

being U_{Local} the overall heat transfer coefficient, locally defined, and dS the infinitesimal heat transfer surface.

The U term is a quantity that indicates the global attitude of the system, consisting of the two fluids and the separating wall, to transfer the heat from the hot to cold fluid. Therefore it takes into account the two main mechanisms of heat transfer occurring into an heat exchanger, namely the conduction in the solid wall and the convection in the fluids (thermal radiation can be usually neglected for practical working conditions).

In an exchanger employing cylindrical tubes, the overall heat transfer coefficient can be defined on both the internal and external heat transfer surfaces. The convention, that will be adopted further on, is to refer this quantity to the external wall, which is the shell side in a Shell and Tube heat exchanger. Then U_{Local}, U_e from now on, can be defined as follow:

$$U_e = \left[\frac{1}{h_i} \frac{d_e}{d_i} + f_i \frac{d_e}{d_i} + \frac{d_e / 2 \ln\left(d_e / d_i\right)}{k_{tube}} + f_e + \frac{1}{h_e} \right]^{-1} \tag{18}$$

where *h* is the heat transfer coefficient of the fluids, d is the tube diameter, k is the wall thermal conductivity while f is the so-called fouling factor; with the subscripts “i” and “e” meaning internal and external sides of the tube, respectively. It is important to acknowledge that the fouling factors are an easy way to treat the skin thermal resistance localized on the tube walls due to deposits and rust, which is influenced by several causes such as working conditions, fluid typology and velocity and length of service of the exchanger.

Taking into account all these definitions, in the additional hypotheses of:

- negligible axial heat flow;
- every element of fluid that enters the heat exchanger in a given stream has an equal opportunity to encounter heat transfer surface.
- constant thermo-physical properties of the media;
- pure counter-current flow of the two stream.

It would be possible to demonstrate [121] that a concomitant integration of the equation (17) together with the differential forms of the equations (15) (16), would give the following total heat transfer rate:

$$\dot{Q} = U_e S_e \Delta T_{LM} \tag{19}$$

where

$$\Delta T_{LM} = \frac{\left(T_{in}^{Hot} - T_{out}^{Cold}\right) - \left(T_{out}^{Hot} - T_{in}^{Cold}\right)}{\ln\left[\frac{\left(T_{in}^{Hot} - T_{out}^{Cold}\right)}{\left(T_{out}^{Hot} - T_{in}^{Cold}\right)}\right]} \tag{20}$$

with ΔT_{LM} defined as the LMTD for a pure counter-current flow heat exchanger.

Therefore, by means of the equation (15) and (16) - or (13) and (14) – and the expression (19), the relationships we were looked for have been established.

However, to set up this model it has been necessary to start assuming several hypotheses and working conditions. Some of them are easily achievable and verifiable, such as negligible axial conduction, perfect thermal insulation of the heat exchanger, no heat sources and steady state conditions; on the opposite side, certain premises shall be further discussed before proceeding to the design of the exchanger in order to ensure that the predictability of the model lays its fundaments upon well-grounded assumptions and, when necessary, on reliable approximations. For instance, it should be noted that when the flow paths are not in pure counter-current, the equation (19) can be equally applied, but the ΔT_{LM} should be corrected with a proper factor “F” which results to be lower than the unity [92].

Nevertheless, in spite of some effects on a small scale, when the heat exchanger options on which the design activity is focused are characterized by a motion on a large scale whose dominant direction of the two streams are in counter-current [92], the correction factor is not required. In fact, also for a plate-baffled shell and tube exchanger, the temperature rise (or drop) per baffle pass is small compared to the overall temperature rise (or drop) of the shell fluid in the exchanger; so that the shell fluid can be treated as perfectly mixed (at uniform temperature) at every cross section (in a direction normal to the shell axis). This would imply that the number of plate should be high, ideally infinite, in order to considerer very small the temperature variations within the single baffle compartment. According to Shah and Pignotti [123], in case of “TEMA E” type counter-flow exchanger [124], the number of segmental baffles above which the flows can be assumed as pure counter-current is 10 (deviations < 2%). As it will be clear later, this assumption is widely confirmed for the selected geometries, hence, from now on, the expression (19) will be used without any corrective factor, unless explicitly stated or required.

With regard to the fluid bypasses, a further extension and slackening of the previous ideal hypotheses can be made. It is clear that some clearances are required for the construction of a plate-baffled exchangers, thus if this shell and tube layout is employed, the designer should take the risk of moving away from the ideal tube bundle configuration. In fact the fluid on the shell side can leak or bypasses through these clearances with or without flowing past the tubes. The clearances associated with a plate baffle are essentially three: tube-to-baffle hole clearance, bundle-to-shell clearance, and baffle-to-shell clearance. Several leakage streams associated with these clearances are identified elsewhere [125], see Figure 4.15.

As shown in the picture, the leakage stream A through the gap between the tubes and the tube holes in the baffle (tube-to-baffle-hole clearance) stems from the pressure difference on the two sides of the baffle. Since the annular spaces is very tiny the heat transfer coefficients is usually high hence this leakage is usually considered fully effective.

The baffle-to-shell leakage stream E experiences practically no heat transfer; the bundle-to-shell bypass stream C denotes some heat transfer; on the contrary, due to the low effective mass flow rate crossing the core of the bundle, the crossflow stream B shows larger temperature changes, threatening to pinch or go beyond the temperature profile of the fluid on the tube side. This would finally result in an actual bulk outlet temperature that can be much lower than the B stream outlet temperature, thus resulting in an indicated temperature difference larger than it is really. So, the overall exchanger performance will be lower than the design value. Since the bypass and leakage streams can exceed 30 percent of the total flow, the effect on the mean temperature difference can be very large, especially for close temperature approaches. However, following the Bell-Delaware design method, it is possible to take into consideration the detrimental effects caused by the clearances avoiding to miss the hypothesis of applicability of the LMTD method [126], see section 4.4.2.3.

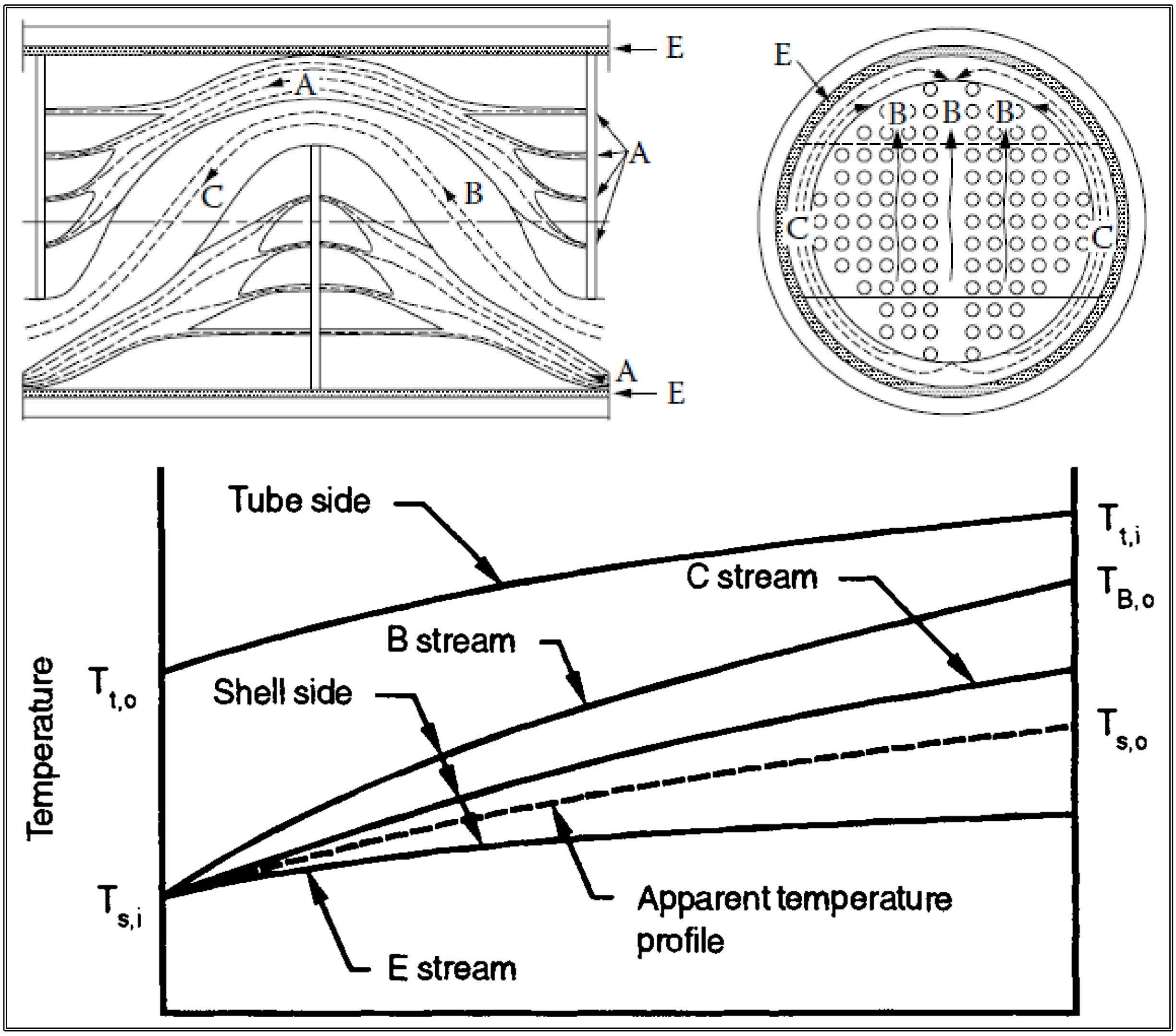

Figure 4.15: Effect of bypass and leakages on the temperature profile of a S&T exchanger.

Finally, it should be pointed out that, because of the integration, the overall heat transfer coefficient appearing in the equation (19) is no longer a local value, as it is in (17), but it represents a mean quantity which has been averaged over the entire heat transfer surface.

This is a direct consequence of the idealization involving constant thermo-physical properties. Thus, according to the assumption, the overall heat transfer coefficient between two fluids is uniform throughout the exchanger and invariant with time. However, as it can be imagined, the local heat transfer coefficients on each fluid side can vary. Whether its variations will be slight or significant will depend upon two main effects:

- changes in the fluid temperatures cause variations in its properties;
- developing of thermal and hydraulic boundary layers (entrance effects).

The latter effect is generally not significant in turbulent flow except for liquid metals (low Prandtl number fluids) therefore, it can be reasonably neglected for the nominal working conditions of the DEMO heat transfer equipment. However, the former effect can play a significant role if the fluid properties are strongly dependent on the temperature and the exchangers is designed to experience large temperature differences or, even more, phase changes. In addition, this effect consists, in turn, of two main components: (1) distortion of velocity and temperature profiles at a given flow cross section due to fluid property variations (it mainly acts in radial direction, from the wall to the bulk of the fluid and vice-versa); (2) variations in the fluid bulk temperature along the flow prevailing direction in the exchanger, this effect is often referred to as the “temperature effect” and the resultant axial changes in the overall mean heat transfer coefficient can be significant [91].

It should be mentioned that the heat transfer coefficient can also depends upon other variables such as flow maldistribution and manufacturing imperfections. However these last variables can be ideally eliminated, at least minimized, following a proper and accurate design of the exchanger geometries and arrangements, while the non-uniformities due to the thermal effects cannot be excluded, they will simply exist and the higher will be their dependency on the temperature, the higher will be the local distortions respect to the mean overall heat transfer coefficient. So, one might suppose that in some practical situations the assumption of uniform fluid properties becomes too binding to allow a widespread use of the LTMD method. However, it is worth to highlight that in deriving the relationships between the heat transfer rate though the heating surface and the energy balances of the fluids, no explicit statements have been made on the need to calculate the “inlet” and “outlet” fluid quantities at the actual entry and exit sections of the exchanger. Thus, the expressions (13), (14) and (19) could be applied only to a portion of the exchanger, in between two arbitrary flow cross-sections, keeping their general validity. The smaller will be the section taken into consideration, the smaller will be variations of the coolant properties.

In practice, this means that, when the fluid properties changes are judged too high, the calculation can be performed by dividing the exchanger total heat transfer load in an appropriate number of heat duty zones and subsequently writing auxiliary energy balances based on enthalpy differences for each zone. One shall simultaneously establish the corresponding temperature variation trends, corresponding zonal mean overall heat transfer coefficients, and mean temperature differences. As a result, one can calculate the heat transfer surface for each zone using an expression of the same form as (19).

In particular, it is set a total number Z of thermal sections in which the shell is subdivided. Then, starting from the hot fluid inlet, the calculation proceeds from each section “k” (k=1, 2,

…, Z) to the next, taking as thermal input parameters of a given section the results of the previous one so that:

$$\begin{cases} T^{k}_{Hot_{in}} = T^{k-1}_{Hot_{out}} \\ \Delta T^{k}_{Cold} = (T^{k}_{Cold_{out}} - T^{k}_{Cold_{in}}) \end{cases} \tag{21}$$

with $k = [1; Z], T^{0}_{Hot_{out}} = T_{Hot_{inlet\ of\ HX}}$ and $T^{1}_{Cold_{out}} = T_{Cold_{outlet\ of\ HX}}, T^{Z}_{Cold_{in}} = T_{Cold_{inlet\ of\ HX}}$

where, for the general section “k” the quantities will be calculated from (15), (16) and (19) as:

$$\begin{cases} T^{k}_{Hot_{out}}\left(\Delta T^{k}_{Cold}, T^{k}_{Hot_{in}}, G_{Cold}, G_{Cold}\right) = T^{k}_{Hot_{in}} - \dfrac{G_{Cold} c_{p_{Cold}} \Delta T^{k}_{Cold}}{c_{p_{Hot}} G_{PHTS}} \\ S^{k}_{e}\left(\Delta T^{k}_{Cold}, T^{k}_{Hot_{in}}, G_{Cold}, G_{Hot}\right) = \dfrac{G_{Cold} c_{p_{Cold}} \Delta T^{k}_{Cold}}{U^{k}_{e}\left(\Delta T^{k}_{Cold}, T^{k}_{Hot_{in}}, G_{Cold}, G_{Hot}\right) \Delta T^{k}_{LM}\left(\Delta T^{k}_{Cold}, T^{k}_{Hot_{in}}\right)} \end{cases} \tag{22}$$

Finally, the total external heat transfer area will be:

$$S_e = \sum_{k=1}^{Z} S^{k}_{e} \tag{23}$$

Of course, the overall temperature difference must be saved, therefore the following constrain shall be applied:

$$\Delta T_{Cold_{TOT}} = \sum_{1}^{Z} \Delta T^{k}_{Cold} \tag{24}$$

Finally, by means of this approach, also the last hypothesis on which the LMTD design method is based can be respected.

The procedure just described is strongly suggested when one or both fluids experience a condensation/evaporation because their properties during a phase change can be subjected to dramatic variations that cannot be neglected. So, it has been the basic approach for the thermal-hydraulic design of the BB PHTS Steam Generator.

Moreover, as it can also enhance the reliability of the calculations for a single-phase to single-phase heat exchangers, the abovementioned method has been adopted also for the IHX. Nevertheless, before beginning a detailed calculation for the helium/HITEC intermediate heat exchanger in case of straight bundle configuration, it has been decided to conduct a preliminary, simplified, parametric analysis in order to drive the decision toward the most suitable solutions, avoiding the risk to begin a deep investigation of options which are far away from the most promising ones.

4.4 Standard Shell and Tube configuration

It has been possible to noticed that in the nuclear industry all the solution adopt shell and tube heat exchanger. Among this family, the “standard” configurations with straight or U-tube bundles are undoubtedly the most popular. Moreover, it is worth to underline that this kind of shell and tube heat exchangers is widely used also outside the nuclear industry, indeed it is basically the “workhorse” of any heat transfer industrial process for several reasons [127]. It is custom designed for virtually any capacity and operating conditions, such as from high vacuums to ultra-high pressures (over 100 MPa), from cryogenics to high temperatures (up to 1100°C), and any temperature and pressure differences between the fluids (the limitations come from the materials of construction). These heat exchangers have been designed for lots of special operating conditions: vibration, heavy fouling, highly viscous fluids, erosion, corrosion, toxicity, radioactivity, multicomponent mixtures, and so on. They are the most versatile exchangers made from a variety of metal and non-metal materials and in sizes from small to super-giant (from 0.1 m^2 to over 100000 m^2). They are extensively used as process heat exchangers in the petroleum-refining and chemical industries; as steam generators, condensers, boiler feed water heaters, and oil coolers in power plants; as condensers and evaporators in some air-conditioning and refrigeration applications; in waste heat recovery applications with heat recovery from liquids and condensing fluids; and in environmental control [128].

They usually are the cheapest exchangers to manufacture, employing well-established manufacturing techniques. Furthermore this layout can have the following advantages helping their integration in the DEMO tokamak building:

- Drainable on both sides;
- Easiest to maintain, including tube inspection and replacement;
- Requires least floor space (low footprint).

Hence, for the “indirect-coupling” BoP, first priority has been given to such an option because a positive assessment could exclude, at least limit, the need of investigating heat exchangers more complicated to manufacture.

4.4.1 Preliminary assessments and selection flow arrangement

Assessments has been made on the two flow configurations of the shell fluid. In fact, keeping always an overall counter-current flow configuration between the primary and secondary coolants, the fluid which circulates on the shell side can ideally assume two main different flow patterns respect to the longitudinal axis of the bundle:

- Pure parallel flow;
- Pure cross-flow.

The pure parallel flow is the easiest to obtain because, in a standard E-shell type, the inlet and outlet nozzles are on the two opposite ends of the shell, see Figure 4.16, thus the coolant would naturally travel along the longitudinal axis of the exchanger, over the tube bundle.

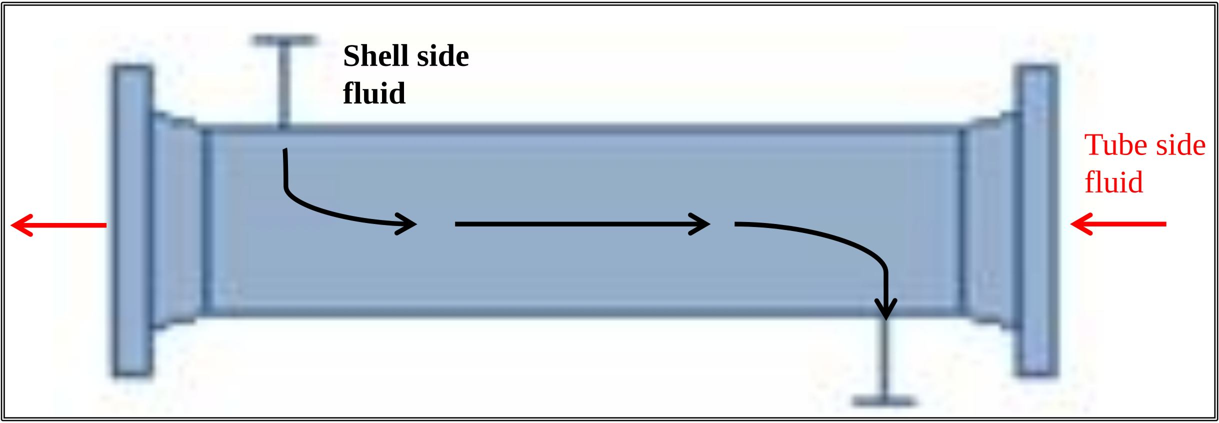

Figure 4.16: One pass, counter-current flow E-type Shell.

When, instead, a cross-flow pattern wants to be obtained, the shell shall be equipped with segmental baffle which enforces the shell fluid to radially flow across the whole bundle in each baffle compartment, see Figure 4.17. Of course, with this baffles arrangement, a longitudinal component of the velocity remains to let the coolant reach the exit and the departure from the pure cross-flow path will be as much lower as much higher will be the penetration of the baffle from one side to the other of the shell. The drawing on top, left of the Figure 4.15, provides a schematic view of how the streamlines of the fluid should look like in such an exchanger.

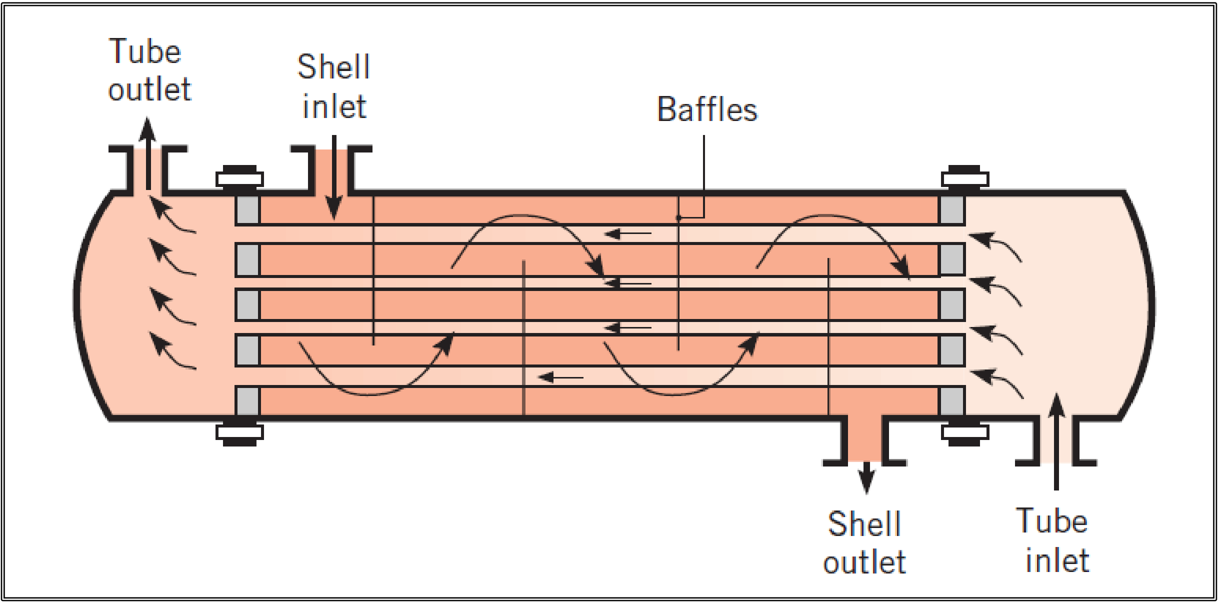

Figure 4.17: One pass, counter-current flow with segmental baffle E-type Shell [121].

The deviations from the ideal case have been only considered in the detailed design phase, while they have been neglected during the preliminary analyses because they have been aimed at achieving just an approximate sizing of the exchanger.

Before starting with the first assessments, additional considerations and assumptions have been needed to circumscribe the boundaries within which to move, they will be introduced in the following.

As we have seen, in the gas-cooled reactor the primary side coolant is often placed on the shell side of the heat exchanger/steam generator. This helps to promote the heat transfer as in cross-flow the turbulence is enhanced, but it is mainly suggested because the secondary fluid works at much higher pressure. In DEMO, the intermediate circuit is operated a very low pressure hence putting the HITEC salt on the secondary side could contribute to reduce the cost of manufacturing for this component. Furthermore, although this aspect should be studied case by case as general safety guideline it is suggested to let primary coolant circulate through the tube bundle. For these reasons it has been decided to put helium on tube side, placing the molten salt into the shell side. However, since the molten salt has a more pronounced tendency to create fouling, corrode and solidify, an option envisaging a HITEC flow within the tubes has been assessed too. It will be discussed later on.

In agreement with the outlined BB PHTS layout, the heat exchanger shall be sized to transfer the thermal power of two blanket sectors, so the majority of the input data and boundary condition can be gathered from the Table 3.1. However it is important to underline that the thermal power that will be transfer to the secondary side is the sum of the BB heat and the power that the compressors introduce into the fluid to let it circulate through the PHTS.

Moreover, being helium a gas, its compression causes a sensible increase of temperature, which must be taken into account in the exchanger design calculations. As a matter of fact, since at its entrance the BB requires helium at 300°C, the coolant must be delivered by the circulator at this temperature, which implies that the turbomachinery inlet temperature (equal to the heat exchanger outlet temperature) will be unavoidably lower. Such a situation can strongly affects the exchanger size due to a reduction of the LMTD between primary and secondary coolants. The outlet helium temperature is a fundamental boundary condition for the heat exchanger sizing, hence it shall be estimate before starting calculation. Assuming, then, a compressor outlet temperature of 300°C and an adiabatic (but non-isentropic) compression, from thermodynamic considerations the inlet circulator temperature will be:

$$T_{\mathrm{in}}^{\mathrm{Circulator}} = \frac{\eta_{\mathrm{Is}} T_{\mathrm{out}}^{\mathrm{Circulator}}}{\left(\beta^{\frac{\gamma-1}{\gamma}} - 1 + \eta_{\mathrm{is}} \right)} \tag{25}$$

where η_{is} is the turbomachinery isentropic efficiency, β is the circulator pressure ratio, and γ is the helium adiabatic exponent.

Unfortunately, on the right hand of this equation two terms, namely the isentropic efficiency and the pressure ratio, are unknowns and, although the efficiency can be opportunely chosen from several references, the real issue comes from the pressure ratio that depends upon the total pressure drop of the cooling circuit, which is missing.

This situation obviously calls for an iterative procedure because the total pressure drop influence the exchanger outlet temperature and the exchanger design affects the global head losses of the circuit. In particular, the heat exchanger design conditions the total pressure drops both directly and indirectly because:

- the component itself will offer a certain resistance to the fluid flow;
- a part of the PHTS pipework disposition depends on the exchanger layout, thus the exchanger influences the piping pressure losses too.

Therefore, in order to begin this iterative procedure, it is possible to recall the criterion aimed at containing the maximum power per circulator, see section 3.3, and use it in order to obtain an estimation of maximum pressure ratio that could be achieved without going beyond 6 MW per circulator.

In particular, combining the following definition of the circulator power:

$$W_{Circulator} = \frac{G_{He} c_{p_{He}} T_{in}^{Circulator}}{\eta_{is}} \left(\beta^{\frac{\gamma-1}{\gamma}} - 1 \right) \tag{26}$$

with equation (25) it can be obtained the pressure ratio as function of it power and efficiency as well as the gas parameter:

$$\beta = \left(\frac{W_{Circulator} (\eta_{is} - 1) + G_{He} c_{p_{He}} T_{out}^{Circulator}}{G_{He} c_{p_{He}} T_{out}^{Circulator} - W_{Circulator}} \right)^{\frac{\gamma}{\gamma-1}} \tag{27}$$

where $W_{Circulator}$ is the circulator power and the subscript “He” is referred to helium quantities.

Then, assuming as a goal for the circulator isentropic efficiency a value of 0.85 [129], with a circulator power of 6 MW, a compressor pressure ratio β=1.04 is obtained. This quantity is even lower than the value initially established to avoid too much extrapolation with other circulator designs. Moreover, in the neighbourhood of 8 MPa, a pressure ratio of 1.04 would allow to have a total PHTS pressure drop slightly above 300 kPa.

This means that the sum of exchanger and piping pressure drops should be kept within 220 kPa since the BB experiences about 80 kPa of pressure loss. From the calculated pressure ratio and the assumed isentropic efficiency, by means of equation (26), the inlet compressor temperature results about 289.6 °C.

Once the temperature at the outlet of the IHX has been calculated, it has been possible to set all the exchanger preliminary boundary conditions, see Table 4.3.

Table 4.3. IHX input data and boundary condition.

	Tube side	**Shell side**
Coolant [-]	**Helium**	**HITEC**
Thermal Power [MW]	**265.6 (BB + 2 circulators per loop)**	
Inlet temperature [°C]	**520.0**	**465.0**
Outlet temperature [°C]	**289.6**	**270.0**
Inlet pressure [MPa]	**7.8**	**1.0**
Mass flow rate [kg]	**222.2**	**873.2**

Keeping this values in mind, a preliminary assessment has been carried out in order to investigate the dependence of the IHX configuration parameters on the selected independent variables.

A total of 2100 configurations have been investigated for each flow configuration considered, each one identified by a specific triad of independent variables: the tube internal diameter “d_i”, the helium maximum velocity “u_{He} ” and the molten salt velocity “u_{HITEC}”. Their values ranging as follow:

- $0.010 \text{ m} \leq d_i \leq 0.020 \text{ m}$
- $10 \text{ m/s} \leq u_{He} \leq 50 \text{ m/s}$
- $0.5 \text{ m/s} \leq u_{HITEC} \leq 1.5 \text{ m/s}$

For a given triad of these values, one can calculate the total number of tubes in the exchanger “N”, the tube external diameter “d_e”, the shell side flow area “A_{cross}” (or ratio pitch over diameter “P/d_e”) and, finally, the length of the tubes “L”.

It is worth to highlight that in case of pure parallel flow the shell side flow area is closely connected to the number of tubes and the tube lattice. Therefore, for prescribed velocities of the coolants and tubes layout, the ratio pitch over diameter shall be univocally defined. On the contrary, when a pure cross-flow path is adopted, the shell flow area becomes a free parameter because it is possible to play on the interspace between the baffles to reach the wanted velocity.

As in the preliminary evaluations many of the parameters are the same, the equations used for both the options will be written in the following, then a unique description will be provided to avoid repetitions.

In order to make simpler the understanding of the results, the functional dependence of the calculated parameters on the independent variables has been explicitly written in the equations, gathering together the homogeneous quantities.

4.4.1.1 *Shell coolant in pure parallel flow*

For the configuration based on pure parallel flows, a square tube lattice has been considered and the quantities have been calculated as follow:

$$N\left(d_i, \Delta T_{He}, u_{He}\right) = \frac{4\dot{Q}}{\pi d_i^2 c_{p_{He}} \Delta T_{He} \rho_{He} u_{He}} \tag{28}$$

$$d_e\left(d_i\right) = d_i\left(1 + \frac{1.15 p_{He}}{\sigma_a}\right) \tag{29}$$

$$\frac{P}{d_e}\left(\Delta T_{MS}, \Delta T_{He}, u_{MS}, u_{He}\right) = \left\{\frac{\pi}{4}\left[\left(1 + \frac{1.15 p_{He}}{\sigma_a}\right)^{-2}\left(\frac{\rho_{He}}{\rho_{MS}}\right)\left(\frac{c_{p_{He}}}{c_{p_{MS}}}\right)\left(\frac{\Delta T_{He}}{\Delta T_{MS}}\right)\left(\frac{u_{He}}{u_{MS}}\right) + 1\right]\right\}^{\frac{1}{2}} \tag{30}$$

$$L\left(d_i, \Delta T_{MS}, \Delta T_{He}, u_{MS}, u_{He}\right) = \frac{\rho_{He} c_{p_{He}} d_i \Delta T_{He} u_{He}}{4\left(1 + \frac{1.15 p_{He}}{\sigma_a}\right) U\left(\Delta T_{MS}, \Delta T_{He}, u_{MS}, u_{He}\right) \Delta T_{LM}\left(\Delta T_{MS}, \Delta T_{He}\right)} \tag{31}$$

Where, in addition to the parameters already described in the previous sections, the subscript “MS” is referred to the molten salt quantities.

4.4.1.2 *Shell coolant in pure cross flow*

Likewise the pure parallel flow, a similar sets of equations have been used to calculate the main quantities in case of pure cross-flow on the shell side. In particular, no changes have been necessary to evaluate the number of tubes, the external diameter and the bundle length therefore equations (28), (29) and (31) have been used again. Whereas, for the reasons explained before, the eq. (30) has been replaced as follow:

$$A_{Crossflow}\left(\Delta T_{MS}, u_{MS}\right) = \frac{\dot{Q}}{c_{p_{MS}} \Delta T_{MS} \rho_{MS} u_{MS}} \tag{32}$$

with the cross flow area “$A_{Crossflow}$” that is supposed to be obtained by means of an unconstrained shrinkage/extension of the distance between two baffle plates. It should be clear that the proper allocation of the baffles must be compliant with some spacing criteria to avoid flow maldistribution or tubes vibration, however they have been neglected at this level of analysis. Also for the this case a square layout has been chosen as bundle lattice. In particular, since the tube distance is decoupled from the T/H conditions of the two coolants, a reference P/d_e of 1.4 has been selected because such a value is quite frequent in nuclear exchangers [130].

4.4.1.3 General description of the equations and their quantities

The number of tubes and the flow areas have been calculated assuming that the two given velocities are the maximum values achievable by the two coolants for that case under examination. A design pressure of 9.2 MPa have been chosen [131] (15% above the blanket inlet pressure) to calculate the tube external diameter in (29). For this reason the factor 1.15 appears in that equation. In particular the wall thickness has been estimated following the simple Mariotte's formula for thin shells [132].

To calculate the allowable stress, Alloy 800H has been considered as tube material in both options. Due to its good thermo-mechanical behaviour at high temperatures (e.g. resistance to creep fatigue from cyclical heating and cooling), it finds application in many typologies of nuclear steam generators and heat exchangers, from LWRs to LMFBRs and Gas-Cooled reactors, see paragraph 4.2. Furthermore, it shows an excellent resistance to corrosion attack also high corrosive environment, see Table 3.2. Apart from this, the added value that it might bring to the exchanger design, if compared to a cheaper austenitic stainless steel showing similar mechanical and corrosion resistance features [137], is its remarkable lower tritium permeability after a brief period of exposure in oxidizing environment [133]. Therefore, should tritium become an issue for the BB PHTS [138], a pre-oxidised Alloy 800H could be employed in order to put an "easy-to-built" barrier which prevents the migration of this radioactive product from the primary to the secondary side [136]. This may particularly help when water is the secondary fluid [134] (steam generator case) because it naturally behaves as oxidizing medium, hence a self-healing action on the tube can be actually expected [135].

The overall heat transfer coefficient and the LMTD have been calculated according to the eq. (18) and (20). In particular, to obtain the heat transfer coefficients, the thermo-physical properties of the coolants (thus their derived quantities) have been evaluated at the arithmetic mean temperature between inlet and outlet sections. The HITEC fouling factor has been set to 8.8E-5 m^2K/W according to [124] and [139], while no fouling factor has been used for the helium, being confident in its high cleanliness during operation. Wall conductivity has been calculated in agreement with the values provided in [140]. The heat transfer model used to calculate the heat transfer coefficient are herewith reported:

4.4.1.4 Tube-side heat transfer model

Among the broad number of correlations proposed for Newtonian, non-metallic fluids in turbulent flow within circular straight ducts, the *Gnielinski* correlation [141] is surely the most popular and widely accepted for its high accuracy in predicting heat transfer in tubes, therefore the choice has fallen on this. It is valid from 2300<Re<5E6 and 0.5<Pr<200.

$$\mathrm{Nu} = \frac{(\lambda/8)(\mathrm{Re}-1000)\mathrm{Pr}}{1+12.7(\lambda/8)^{1/2}\left(\mathrm{Pr}^{2/3}-1\right)} \tag{33}$$

where λ is the Darcy-Weisbach turbulent friction factor for smooth tubes defined as:

$$\lambda = \left[0.79 \ln(\mathrm{Re}) - 1.64\right]^{-2} \tag{34}$$

4.4.1.5 Shell-side heat transfer models – Pure parallel flow

To calculate the heat transfer of the molten salt when flowing parallel to the tube bundle, the correlation of *El-Genk et al.* [142] has been employed. The model was originally developed for cold water with a maximum Pr number of about 9. In cold conditions, the molten salt can achieve higher Pr numbers (max. ~14). However: 1) at temperature averaged conditions, the HITEC Prandtl assumes values that are within the range for which the correlation was tested; 2) taking into account the description given in the section 3.2.1.1.3 on the molten salt behaviour, the model is expected to predict the heat transfer coefficient within a reasonable range of uncertainties.

$$\begin{cases} \mathrm{Nu} = \left(2.97 - 1.76\, P/d_e\right) \mathrm{Re}^{\left(0.56\, P/d_e - 0.3\right)} \mathrm{Pr}^{0.33} \quad \text{if } \mathrm{Re} < \mathrm{Re}_{tr} \\ \mathrm{Nu} = \left(0.028\, P/d_e - 0.006\right) \mathrm{Re}^{0.8} \mathrm{Pr}^{0.33} \quad \text{if } \mathrm{Re} \geq \mathrm{Re}_{tr} \\ \text{where} \\ \mathrm{Re}_{tr} = 9.93 \times 10^{3} \left(P/d_e - 1\right) \end{cases} \tag{35}$$

4.4.1.6 Shell-side heat transfer models – Pure cross-flow

To calculate the HITEC heat transfer coefficient while it crosses the tube bundle, the correlation of Zukauskas, as reported in [121], has been proposed. It range of validity is 0.7<Pr<500 and Re up to 2E6, therefore it is suitable for almost all common heat transfer media.

$$\begin{cases} \mathrm{Nu} = C\, \mathrm{Re}^{n} \mathrm{Pr}^{0.36} \\ \text{where} \\ C \text{ and } n \text{ depending on } \mathrm{Re} \end{cases} \tag{36}$$

In this phase, corrective factors have not been used neither to consider the temperature differences from the bulk of the coolant to the wall nor to account for the axial temperature differences.

4.4.1.7 Shell diameter and pressure drops

Once the total amount of tubes has been fixed, an estimation of the shell internal diameter can be carried out according to:

$$D_i = 1.05 \cdot d_e \left(\frac{P}{d_e} \right) \sqrt{\frac{4N}{\pi}} \tag{37}$$

where the diameter is calculated from a circle with an area equivalent to total bundle cross-sectional area. As the method predicts the diameter within approximately 5% of accuracy if the tubes are relatively small compared to the shell [92], a factor of 1.05 has been added for conservativism.

Then, knowing the length of the bundle, the calculation of pressure drops can be done. In a heat exchanger the pressure losses are mainly due to the distributed resistances that both internal and external walls offer to the fluid; this is particularly true for the coolant flowing into the tube. Therefore, according to the scope of the preliminary analyses, local resistances such as the sudden contraction (expansion) that occurs at the tube bundle inlet (outlet) have been neglected. The models used for the pressure drop calculation are reported below.

On tube side, pressure drop have been calculated as follow:

$$\Delta p = \lambda \frac{L}{d_i} \rho_{He} \frac{(u_{He})^2}{2} \tag{38}$$

with λ calculated as for the *Gnielinski* model.

Instead, for the shell side, the Cheng and Todreas [143] model has been selected to calculate the Darcy coefficient in case of pure parallel flow.

$$\begin{cases} \lambda = \dfrac{a + b_1\left(P/d_e - 1 \right) + b_2\left(P/d_e - 1 \right)^2}{Re^n} \\ \text{where:} \\ a, b_1, b_2 \text{ depend on } P/d_e \\ n \text{ depends on flow regime} \end{cases} \tag{39}$$

and the pressure drop calculated as in equation (38).

For pure cross-flow pattern the *Jakob* formula has been adopted as discussed in [144]. To calculate pressure drops the equation needs a slight modification respect to the (38). In particular:

$$\Delta p = 2\lambda N_{rows} \frac{(\rho u_{MAX})_{MS}^2}{\rho_{MS}} \tag{40}$$

with

$$\lambda = \left\{ 0.044 + \frac{0.08\left(P_L / D_e\right)}{\left[\frac{\left(P_T - d_e\right)}{d_e}\right]^{\left(0.43+1.13\, d_e / P_L\right)}} \right\} \mathrm{Re}^{-0.15} \tag{41}$$

where P_L and P_T are the longitudinal and the transversal lattice pitches, respect to the main normal direction of the fluid. In the hypothesis of square layout, they are equal; N_{row} is the number of in-line tube rows crossed by the fluid; "u_{MAX}" is maximum velocity that occurs through the minimum frontal area presented to the incoming free stream velocity.

4.4.1.8 Preliminary results

The equations and models from (28) to (41) have been contextually used to perform a total of 4200 preliminary calculations in order to narrow the field of possible options among which detailed design should be done.

The selected cut-off points to consider feasible an option have been:

- Maximum tube length $L \leq 15$m;
- Maximum internal shell diameter $D_i \leq 5$m;
- Maximum tubes number $N \leq 15000$;
- $1.1 \leq P/d_e \leq 1.65$;
- Maximum helium pressure drop $\Delta p_{He} \leq 80$ kPa;
- Maximum molten salt pressure drop $\Delta p_{MS} \leq 600$ kPa.

The geometrical constraints have been mainly based on the data already discussed in the paragraph 3.3 in order to avoid too much extrapolation respect to the state-of-art technology limit. On the other hand, taking into account that the In-Vessel circuits experience a pressure drop of about 80 kPa, it has been decided that also the exchanger should not exceed this value; pressure drops of HITEC should not cause much concerns however, to keep the mean circuit pressure at reasonable low levels, they have been provisionally limited to 600 kPa.

Results have shown that in case of parallel flow none of the 2100 configurations have met all criteria at the same time.

This is mainly due to the particular combination of the thermal-hydraulic parameters of the coolants. As mentioned, in parallel flow the coolants flow areas are strictly related each other and, for the given range of fluid velocities, many configurations would require a P/d_e much smaller than 1.1; in some cases tubes intersection can also occurs. These latter configurations are obviously unphysical while the former are not feasible from a technological point of view. This could have been previously foreseen through an inspection of the equation (30) that shows the need to have very high ratio between the coolants speed to be able to compensate the huge differences in densities.

However, it must be underlined that the spectrum of velocities which have been investigated is already wide and touches those maximum and minimum values that can be considered acceptable. In fact, increasing the maximum velocities would cause not only too large pressure drops but also vibrations or erosion problems (in particular on the secondary side), while with a decrease of the minimum speeds the heat transfer would reach very low values, leading to extremely large heating surfaces.

On the contrary, if the IHX is equipped with baffle plates, many configurations are possible therefore it has been chosen to focus the attention on this option to be studied in detail.

Results concerning the exchanger configuration with the shell coolant in pure cross-flow are reported from Table 4.4 to Table 4.10.

Each table summarizes 300 results: for a given internal diameter, the feasibility of a configuration based on all possible coupling between the velocities of the coolants is highlighted using two different colours. The red marks means that at least 1 of the 6 abovementioned criteria has not been satisfied, while the green coloured boxes are used when the option has accomplished all the objectives.

In particular, the trends are exactly those that can be anticipated from the equation (31). As a matter of fact, looking at the numerator, the higher is the internal diameter the lower must be the helium velocity otherwise the tubes become too long. This is a direct consequence of the little amount of tubes that are available when both velocity and diameter are high: in this scenario the heat transfer area required to exchange the whole power must be found via an increase of tube bundle length. However, low velocities have a detrimental effect on the heat transfer coefficient and this is why the highest diameters the acceptable solutions are a few: although the product "$d_i \cdot u_{He}$" at the numerator of the (31) is kept as constant as possible, the overall heat transfer coefficient gets low, hence the tubes length increases. Moreover, the hydraulic constrains on both sides pressure drops have a global tendency to shrink the useful domain, not allowing helium velocities higher than 40 m/s and leaving accessible only molten salt speeds lower than 1.15 m/s.

Therefore, the configurations that provide more margins are those employing tubes with internal diameters between 12 mm and 15 mm. But, if a limitation of the heat transfer surface wants to be also pursued, for a given molten salt velocity, the helium speed should be maintain at high values.

Since the option with tubes of 15 mm seems the most penalizing among the three possibilities, it has been discarded.

The additional considerations made to select which of the two internal diameters should be adopted are described in the next section.

Table 4.4. Preliminary IHX results for shell coolant in cross-flow. Case with d_i=10mm.

		Helium velocity [m/s]														
		10.0	**12.5**	**15.0**	**17.5**	**20.0**	**22.5**	**25.0**	**27.5**	**30.0**	**32.5**	**35.0**	**37.5**	**40.0**	**45.0**	**50.0**
HITEC velocity [m/s]	**0.50**	🟥	🟥	🟥	🟥	🟥	🟥	🟥	🟥	🟥	🟥	🟥	🟥	🟥	🟥	🟥
	0.55	🟥	🟥	🟥	🟥	🟥	🟥	🟥	🟥	🟥	🟥	🟥	🟥	🟥	🟥	🟥
	0.60	🟥	🟥	🟥	🟥	🟥	🟥	🟥	🟥	🟥	🟥	🟥	🟥	🟥	🟥	🟥
	0.65	🟥	🟥	🟥	🟥	🟥	🟥	🟥	🟥	🟥	🟥	🟥	🟥	🟥	🟥	🟥
	0.70	🟥	🟥	🟥	🟥	🟥	🟥	🟥	🟥	🟥	🟥	🟥	🟥	🟥	🟥	🟥
	0.75	🟥	🟥	🟥	🟥	🟥	🟥	🟥	🟥	🟥	🟥	🟥	🟥	🟥	🟥	🟥
	0.80	🟥	🟥	🟥	🟥	🟥	🟥	🟥	🟥	🟥	🟥	🟥	🟥	🟥	🟥	🟥
	0.85	🟥	🟥	🟥	🟥	🟥	🟥	🟥	🟥	🟥	🟥	🟥	🟥	🟥	🟥	🟥
	0.90	🟥	🟥	🟥	🟥	🟥	🟥	🟥	🟥	🟥	🟥	🟥	🟥	🟥	🟥	🟥
	0.95	🟥	🟥	🟥	🟥	🟥	🟥	🟥	🟥	🟥	🟥	🟥	🟥	🟥	🟥	🟥
	1.00	🟥	🟥	🟥	🟥	🟥	🟥	🟥	🟥	🟥	🟥	🟥	🟥	🟥	🟥	🟥
	1.05	🟥	🟥	🟥	🟥	🟥	🟥	🟥	🟥	🟥	🟥	🟥	🟥	🟥	🟥	🟥
	1.10	🟥	🟥	🟥	🟥	🟥	🟥	🟥	🟥	🟥	🟥	🟥	🟥	🟥	🟥	🟥
	1.15	🟥	🟥	🟥	🟥	🟥	🟥	🟥	🟥	🟥	🟥	🟥	🟥	🟥	🟥	🟥
	1.20	🟥	🟥	🟥	🟥	🟥	🟥	🟥	🟥	🟥	🟥	🟥	🟥	🟥	🟥	🟥
	1.25	🟥	🟥	🟥	🟥	🟥	🟥	🟥	🟥	🟥	🟥	🟥	🟥	🟥	🟥	🟥
	1.30	🟥	🟥	🟥	🟥	🟥	🟥	🟥	🟥	🟥	🟥	🟥	🟥	🟥	🟥	🟥
	1.35	🟥	🟥	🟥	🟥	🟥	🟥	🟥	🟥	🟥	🟥	🟥	🟥	🟥	🟥	🟥
	1.40	🟥	🟥	🟥	🟥	🟥	🟥	🟥	🟥	🟥	🟥	🟥	🟥	🟥	🟥	🟥
	1.50	🟥	🟥	🟥	🟥	🟥	🟥	🟥	🟥	🟥	🟥	🟥	🟥	🟥	🟥	🟥

Table 4.5. Preliminary IHX results for shell coolant in cross-flow. Case with d_i=12mm.

		Helium velocity [m/s]														
		10.0	**12.5**	**15.0**	**17.5**	**20.0**	**22.5**	**25.0**	**27.5**	**30.0**	**32.5**	**35.0**	**37.5**	**40.0**	**45.0**	**50.0**
HITEC velocity [m/s]	**0.50**	🟥	🟥	🟥	🟥	🟥	🟥	🟥	🟥	🟩	🟩	🟩	🟩	🟩	🟥	🟥
	0.55	🟥	🟥	🟥	🟥	🟥	🟥	🟥	🟥	🟩	🟩	🟩	🟩	🟩	🟥	🟥
	0.60	🟥	🟥	🟥	🟥	🟥	🟥	🟥	🟥	🟩	🟩	🟩	🟩	🟩	🟥	🟥
	0.65	🟥	🟥	🟥	🟥	🟥	🟥	🟥	🟥	🟩	🟩	🟩	🟩	🟩	🟥	🟥
	0.70	🟥	🟥	🟥	🟥	🟥	🟥	🟥	🟥	🟩	🟩	🟩	🟩	🟩	🟥	🟥
	0.75	🟥	🟥	🟥	🟥	🟥	🟥	🟥	🟥	🟩	🟩	🟩	🟩	🟩	🟥	🟥
	0.80	🟥	🟥	🟥	🟥	🟥	🟥	🟥	🟥	🟩	🟩	🟩	🟩	🟩	🟥	🟥
	0.85	🟥	🟥	🟥	🟥	🟥	🟥	🟥	🟥	🟩	🟩	🟩	🟩	🟩	🟥	🟥
	0.90	🟥	🟥	🟥	🟥	🟥	🟥	🟥	🟥	🟩	🟩	🟩	🟩	🟩	🟥	🟥
	0.95	🟥	🟥	🟥	🟥	🟥	🟥	🟥	🟥	🟩	🟩	🟩	🟩	🟩	🟥	🟥
	1.00	🟥	🟥	🟥	🟥	🟥	🟥	🟥	🟥	🟩	🟩	🟩	🟩	🟩	🟥	🟥
	1.05	🟥	🟥	🟥	🟥	🟥	🟥	🟥	🟥	🟩	🟩	🟩	🟩	🟩	🟥	🟥
	1.10	🟥	🟥	🟥	🟥	🟥	🟥	🟥	🟥	🟥	🟥	🟥	🟥	🟩	🟥	🟥
	1.15	🟥	🟥	🟥	🟥	🟥	🟥	🟥	🟥	🟥	🟥	🟥	🟥	🟥	🟥	🟥
	1.20	🟥	🟥	🟥	🟥	🟥	🟥	🟥	🟥	🟥	🟥	🟥	🟥	🟥	🟥	🟥
	1.25	🟥	🟥	🟥	🟥	🟥	🟥	🟥	🟥	🟥	🟥	🟥	🟥	🟥	🟥	🟥
	1.30	🟥	🟥	🟥	🟥	🟥	🟥	🟥	🟥	🟥	🟥	🟥	🟥	🟥	🟥	🟥
	1.35	🟥	🟥	🟥	🟥	🟥	🟥	🟥	🟥	🟥	🟥	🟥	🟥	🟥	🟥	🟥
	1.40	🟥	🟥	🟥	🟥	🟥	🟥	🟥	🟥	🟥	🟥	🟥	🟥	🟥	🟥	🟥
	1.50	🟥	🟥	🟥	🟥	🟥	🟥	🟥	🟥	🟥	🟥	🟥	🟥	🟥	🟥	🟥

Table 4.6. Preliminary IHX results for shell coolant in cross-flow. Case with d_i=14mm.

		Helium velocity [m/s]														
		10.0	**12.5**	**15.0**	**17.5**	**20.0**	**22.5**	**25.0**	**27.5**	**30.0**	**32.5**	**35.0**	**37.5**	**40.0**	**45.0**	**50.0**
HITEC velocity [m/s]	**0.50**	🟥	🟥	🟥	🟥	🟥	🟩	🟩	🟩	🟩	🟩	🟥	🟥	🟥	🟥	🟥
	0.55	🟥	🟥	🟥	🟥	🟥	🟩	🟩	🟩	🟩	🟩	🟥	🟥	🟥	🟥	🟥
	0.60	🟥	🟥	🟥	🟥	🟥	🟩	🟩	🟩	🟩	🟩	🟥	🟥	🟥	🟥	🟥
	0.65	🟥	🟥	🟥	🟥	🟥	🟩	🟩	🟩	🟩	🟩	🟩	🟥	🟥	🟥	🟥
	0.70	🟥	🟥	🟥	🟥	🟥	🟩	🟩	🟩	🟩	🟩	🟩	🟥	🟥	🟥	🟥
	0.75	🟥	🟥	🟥	🟥	🟥	🟩	🟩	🟩	🟩	🟩	🟩	🟥	🟥	🟥	🟥
	0.80	🟥	🟥	🟥	🟥	🟥	🟩	🟩	🟩	🟩	🟩	🟩	🟩	🟥	🟥	🟥
	0.85	🟥	🟥	🟥	🟥	🟥	🟩	🟩	🟩	🟩	🟩	🟩	🟩	🟥	🟥	🟥
	0.90	🟥	🟥	🟥	🟥	🟥	🟩	🟩	🟩	🟩	🟩	🟩	🟩	🟥	🟥	🟥
	0.95	🟥	🟥	🟥	🟥	🟥	🟩	🟩	🟩	🟩	🟩	🟩	🟩	🟩	🟥	🟥
	1.00	🟥	🟥	🟥	🟥	🟥	🟥	🟩	🟩	🟩	🟩	🟩	🟩	🟩	🟥	🟥
	1.05	🟥	🟥	🟥	🟥	🟥	🟥	🟥	🟥	🟥	🟩	🟩	🟩	🟩	🟥	🟥
	1.10	🟥	🟥	🟥	🟥	🟥	🟥	🟥	🟥	🟥	🟥	🟥	🟥	🟥	🟥	🟥
	1.15	🟥	🟥	🟥	🟥	🟥	🟥	🟥	🟥	🟥	🟥	🟥	🟥	🟥	🟥	🟥
	1.20	🟥	🟥	🟥	🟥	🟥	🟥	🟥	🟥	🟥	🟥	🟥	🟥	🟥	🟥	🟥
	1.25	🟥	🟥	🟥	🟥	🟥	🟥	🟥	🟥	🟥	🟥	🟥	🟥	🟥	🟥	🟥
	1.30	🟥	🟥	🟥	🟥	🟥	🟥	🟥	🟥	🟥	🟥	🟥	🟥	🟥	🟥	🟥
	1.35	🟥	🟥	🟥	🟥	🟥	🟥	🟥	🟥	🟥	🟥	🟥	🟥	🟥	🟥	🟥
	1.40	🟥	🟥	🟥	🟥	🟥	🟥	🟥	🟥	🟥	🟥	🟥	🟥	🟥	🟥	🟥
	1.50	🟥	🟥	🟥	🟥	🟥	🟥	🟥	🟥	🟥	🟥	🟥	🟥	🟥	🟥	🟥

Table 4.7. Preliminary IHX results for shell coolant in cross-flow. Case with d_i=15mm.

		Helium velocity [m/s]														
		10.0	**12.5**	**15.0**	**17.5**	**20.0**	**22.5**	**25.0**	**27.5**	**30.0**	**32.5**	**35.0**	**37.5**	**40.0**	**45.0**	**50.0**
HITEC velocity [m/s]	**0.50**	🟥	🟥	🟥	🟥	🟩	🟩	🟩	🟩	🟥	🟥	🟥	🟥	🟥	🟥	🟥
	0.55	🟥	🟥	🟥	🟥	🟩	🟩	🟩	🟩	🟥	🟥	🟥	🟥	🟥	🟥	🟥
	0.60	🟥	🟥	🟥	🟥	🟩	🟩	🟩	🟩	🟥	🟥	🟥	🟥	🟥	🟥	🟥
	0.65	🟥	🟥	🟥	🟥	🟩	🟩	🟩	🟩	🟩	🟥	🟥	🟥	🟥	🟥	🟥
	0.70	🟥	🟥	🟥	🟥	🟩	🟩	🟩	🟩	🟩	🟥	🟥	🟥	🟥	🟥	🟥
	0.75	🟥	🟥	🟥	🟥	🟩	🟩	🟩	🟩	🟩	🟥	🟥	🟥	🟥	🟥	🟥
	0.80	🟥	🟥	🟥	🟥	🟩	🟩	🟩	🟩	🟩	🟩	🟥	🟥	🟥	🟥	🟥
	0.85	🟥	🟥	🟥	🟥	🟩	🟩	🟩	🟩	🟩	🟩	🟥	🟥	🟥	🟥	🟥
	0.90	🟥	🟥	🟥	🟥	🟩	🟩	🟩	🟩	🟩	🟩	🟥	🟥	🟥	🟥	🟥
	0.95	🟥	🟥	🟥	🟥	🟩	🟩	🟩	🟩	🟩	🟩	🟥	🟥	🟥	🟥	🟥
	1.00	🟥	🟥	🟥	🟥	🟥	🟥	🟩	🟩	🟩	🟩	🟥	🟥	🟥	🟥	🟥
	1.05	🟥	🟥	🟥	🟥	🟥	🟥	🟥	🟥	🟥	🟩	🟩	🟥	🟥	🟥	🟥
	1.10	🟥	🟥	🟥	🟥	🟥	🟥	🟥	🟥	🟥	🟥	🟥	🟥	🟥	🟥	🟥
	1.15	🟥	🟥	🟥	🟥	🟥	🟥	🟥	🟥	🟥	🟥	🟥	🟥	🟥	🟥	🟥
	1.20	🟥	🟥	🟥	🟥	🟥	🟥	🟥	🟥	🟥	🟥	🟥	🟥	🟥	🟥	🟥
	1.25	🟥	🟥	🟥	🟥	🟥	🟥	🟥	🟥	🟥	🟥	🟥	🟥	🟥	🟥	🟥
	1.30	🟥	🟥	🟥	🟥	🟥	🟥	🟥	🟥	🟥	🟥	🟥	🟥	🟥	🟥	🟥
	1.35	🟥	🟥	🟥	🟥	🟥	🟥	🟥	🟥	🟥	🟥	🟥	🟥	🟥	🟥	🟥
	1.40	🟥	🟥	🟥	🟥	🟥	🟥	🟥	🟥	🟥	🟥	🟥	🟥	🟥	🟥	🟥
	1.50	🟥	🟥	🟥	🟥	🟥	🟥	🟥	🟥	🟥	🟥	🟥	🟥	🟥	🟥	🟥

Table 4.8. Preliminary IHX results for shell coolant in cross-flow. Case with d_i=16mm.

		Helium velocity [m/s]														
		10.0	**12.5**	**15.0**	**17.5**	**20.0**	**22.5**	**25.0**	**27.5**	**30.0**	**32.5**	**35.0**	**37.5**	**40.0**	**45.0**	**50.0**
HITEC velocity [m/s]	**0.50**	🟥	🟥	🟥	🟩	🟩	🟩	🟥	🟥	🟥	🟥	🟥	🟥	🟥	🟥	🟥
	0.55	🟥	🟥	🟥	🟩	🟩	🟩	🟩	🟥	🟥	🟥	🟥	🟥	🟥	🟥	🟥
	0.60	🟥	🟥	🟥	🟩	🟩	🟩	🟩	🟥	🟥	🟥	🟥	🟥	🟥	🟥	🟥
	0.65	🟥	🟥	🟥	🟩	🟩	🟩	🟩	🟥	🟥	🟥	🟥	🟥	🟥	🟥	🟥
	0.70	🟥	🟥	🟥	🟩	🟩	🟩	🟩	🟥	🟥	🟥	🟥	🟥	🟥	🟥	🟥
	0.75	🟥	🟥	🟥	🟩	🟩	🟩	🟩	🟥	🟥	🟥	🟥	🟥	🟥	🟥	🟥
	0.80	🟥	🟥	🟥	🟩	🟩	🟩	🟩	🟩	🟥	🟥	🟥	🟥	🟥	🟥	🟥
	0.85	🟥	🟥	🟥	🟩	🟩	🟩	🟩	🟩	🟥	🟥	🟥	🟥	🟥	🟥	🟥
	0.90	🟥	🟥	🟥	🟩	🟩	🟩	🟩	🟩	🟥	🟥	🟥	🟥	🟥	🟥	🟥
	0.95	🟥	🟥	🟥	🟥	🟩	🟩	🟩	🟩	🟥	🟥	🟥	🟥	🟥	🟥	🟥
	1.00	🟥	🟥	🟥	🟥	🟥	🟥	🟩	🟩	🟥	🟥	🟥	🟥	🟥	🟥	🟥
	1.05	🟥	🟥	🟥	🟥	🟥	🟥	🟥	🟥	🟥	🟥	🟥	🟥	🟥	🟥	🟥
	1.10	🟥	🟥	🟥	🟥	🟥	🟥	🟥	🟥	🟥	🟥	🟥	🟥	🟥	🟥	🟥
	1.15	🟥	🟥	🟥	🟥	🟥	🟥	🟥	🟥	🟥	🟥	🟥	🟥	🟥	🟥	🟥
	1.20	🟥	🟥	🟥	🟥	🟥	🟥	🟥	🟥	🟥	🟥	🟥	🟥	🟥	🟥	🟥
	1.25	🟥	🟥	🟥	🟥	🟥	🟥	🟥	🟥	🟥	🟥	🟥	🟥	🟥	🟥	🟥
	1.30	🟥	🟥	🟥	🟥	🟥	🟥	🟥	🟥	🟥	🟥	🟥	🟥	🟥	🟥	🟥
	1.35	🟥	🟥	🟥	🟥	🟥	🟥	🟥	🟥	🟥	🟥	🟥	🟥	🟥	🟥	🟥
	1.40	🟥	🟥	🟥	🟥	🟥	🟥	🟥	🟥	🟥	🟥	🟥	🟥	🟥	🟥	🟥
	1.50	🟥	🟥	🟥	🟥	🟥	🟥	🟥	🟥	🟥	🟥	🟥	🟥	🟥	🟥	🟥

Table 4.9. Preliminary IHX results for shell coolant in cross-flow. Case with d_i=18mm.

		Helium velocity [m/s]														
		10.0	**12.5**	**15.0**	**17.5**	**20.0**	**22.5**	**25.0**	**27.5**	**30.0**	**32.5**	**35.0**	**37.5**	**40.0**	**45.0**	**50.0**
HITEC velocity [m/s]	**0.50**	🟥	🟥	🟩	🟩	🟥	🟥	🟥	🟥	🟥	🟥	🟥	🟥	🟥	🟥	🟥
	0.55	🟥	🟥	🟩	🟩	🟥	🟥	🟥	🟥	🟥	🟥	🟥	🟥	🟥	🟥	🟥
	0.60	🟥	🟥	🟩	🟩	🟥	🟥	🟥	🟥	🟥	🟥	🟥	🟥	🟥	🟥	🟥
	0.65	🟥	🟥	🟩	🟩	🟥	🟥	🟥	🟥	🟥	🟥	🟥	🟥	🟥	🟥	🟥
	0.70	🟥	🟥	🟩	🟩	🟩	🟥	🟥	🟥	🟥	🟥	🟥	🟥	🟥	🟥	🟥
	0.75	🟥	🟥	🟩	🟩	🟩	🟥	🟥	🟥	🟥	🟥	🟥	🟥	🟥	🟥	🟥
	0.80	🟥	🟥	🟩	🟩	🟩	🟥	🟥	🟥	🟥	🟥	🟥	🟥	🟥	🟥	🟥
	0.85	🟥	🟥	🟩	🟩	🟩	🟥	🟥	🟥	🟥	🟥	🟥	🟥	🟥	🟥	🟥
	0.90	🟥	🟥	🟩	🟩	🟩	🟥	🟥	🟥	🟥	🟥	🟥	🟥	🟥	🟥	🟥
	0.95	🟥	🟥	🟥	🟥	🟩	🟥	🟥	🟥	🟥	🟥	🟥	🟥	🟥	🟥	🟥
	1.00	🟥	🟥	🟥	🟥	🟥	🟥	🟥	🟥	🟥	🟥	🟥	🟥	🟥	🟥	🟥
	1.05	🟥	🟥	🟥	🟥	🟥	🟥	🟥	🟥	🟥	🟥	🟥	🟥	🟥	🟥	🟥
	1.10	🟥	🟥	🟥	🟥	🟥	🟥	🟥	🟥	🟥	🟥	🟥	🟥	🟥	🟥	🟥
	1.15	🟥	🟥	🟥	🟥	🟥	🟥	🟥	🟥	🟥	🟥	🟥	🟥	🟥	🟥	🟥
	1.20	🟥	🟥	🟥	🟥	🟥	🟥	🟥	🟥	🟥	🟥	🟥	🟥	🟥	🟥	🟥
	1.25	🟥	🟥	🟥	🟥	🟥	🟥	🟥	🟥	🟥	🟥	🟥	🟥	🟥	🟥	🟥
	1.30	🟥	🟥	🟥	🟥	🟥	🟥	🟥	🟥	🟥	🟥	🟥	🟥	🟥	🟥	🟥
	1.35	🟥	🟥	🟥	🟥	🟥	🟥	🟥	🟥	🟥	🟥	🟥	🟥	🟥	🟥	🟥
	1.40	🟥	🟥	🟥	🟥	🟥	🟥	🟥	🟥	🟥	🟥	🟥	🟥	🟥	🟥	🟥
	1.50	🟥	🟥	🟥	🟥	🟥	🟥	🟥	🟥	🟥	🟥	🟥	🟥	🟥	🟥	🟥

Table 4.10. Preliminary IHX results for shell coolant in cross-flow. Case with d_i=20mm.

		Helium velocity [m/s]														
		10.0	**12.5**	**15.0**	**17.5**	**20.0**	**22.5**	**25.0**	**27.5**	**30.0**	**32.5**	**35.0**	**37.5**	**40.0**	**45.0**	**50.0**
HITEC velocity [m/s]	**0.50**	🟥	🟩	🟥	🟥	🟥	🟥	🟥	🟥	🟥	🟥	🟥	🟥	🟥	🟥	🟥
	0.55	🟥	🟩	🟥	🟥	🟥	🟥	🟥	🟥	🟥	🟥	🟥	🟥	🟥	🟥	🟥
	0.60	🟥	🟩	🟥	🟥	🟥	🟥	🟥	🟥	🟥	🟥	🟥	🟥	🟥	🟥	🟥
	0.65	🟥	🟩	🟥	🟥	🟥	🟥	🟥	🟥	🟥	🟥	🟥	🟥	🟥	🟥	🟥
	0.70	🟥	🟩	🟩	🟥	🟥	🟥	🟥	🟥	🟥	🟥	🟥	🟥	🟥	🟥	🟥
	0.75	🟥	🟩	🟩	🟥	🟥	🟥	🟥	🟥	🟥	🟥	🟥	🟥	🟥	🟥	🟥
	0.80	🟥	🟩	🟩	🟥	🟥	🟥	🟥	🟥	🟥	🟥	🟥	🟥	🟥	🟥	🟥
	0.85	🟥	🟩	🟩	🟥	🟥	🟥	🟥	🟥	🟥	🟥	🟥	🟥	🟥	🟥	🟥
	0.90	🟥	🟥	🟩	🟥	🟥	🟥	🟥	🟥	🟥	🟥	🟥	🟥	🟥	🟥	🟥
	0.95	🟥	🟥	🟥	🟥	🟥	🟥	🟥	🟥	🟥	🟥	🟥	🟥	🟥	🟥	🟥
	1.00	🟥	🟥	🟥	🟥	🟥	🟥	🟥	🟥	🟥	🟥	🟥	🟥	🟥	🟥	🟥
	1.05	🟥	🟥	🟥	🟥	🟥	🟥	🟥	🟥	🟥	🟥	🟥	🟥	🟥	🟥	🟥
	1.10	🟥	🟥	🟥	🟥	🟥	🟥	🟥	🟥	🟥	🟥	🟥	🟥	🟥	🟥	🟥
	1.15	🟥	🟥	🟥	🟥	🟥	🟥	🟥	🟥	🟥	🟥	🟥	🟥	🟥	🟥	🟥
	1.20	🟥	🟥	🟥	🟥	🟥	🟥	🟥	🟥	🟥	🟥	🟥	🟥	🟥	🟥	🟥
	1.25	🟥	🟥	🟥	🟥	🟥	🟥	🟥	🟥	🟥	🟥	🟥	🟥	🟥	🟥	🟥
	1.30	🟥	🟥	🟥	🟥	🟥	🟥	🟥	🟥	🟥	🟥	🟥	🟥	🟥	🟥	🟥
	1.35	🟥	🟥	🟥	🟥	🟥	🟥	🟥	🟥	🟥	🟥	🟥	🟥	🟥	🟥	🟥
	1.40	🟥	🟥	🟥	🟥	🟥	🟥	🟥	🟥	🟥	🟥	🟥	🟥	🟥	🟥	🟥
	1.50	🟥	🟥	🟥	🟥	🟥	🟥	🟥	🟥	🟥	🟥	🟥	🟥	🟥	🟥	🟥

4.4.2 Detailed design calculations

The analysis of preliminary results has led to select the plate-baffled shell and tube exchanger. The range where it should be find the tube internal diameter has been defined in between 12 and 14 mm, as both values appear suitable to meet the selected design criteria, taking into account the thermal-hydraulic constrains and the characteristics of Helium and HITEC. In addition, a careful observation of Table 4.5 and Table 4.6 reveals that a molten salt average velocity of about 0.75÷0.8 m/s associated with an helium speed around 30÷35 m/s should help to keep the design in a “safe” zone, which means to have taken some margins against the approximations done in the first rough design. In fact, the choice of the two maximum velocities for the coolants would potentially allow to minimize the heat transfer area but, in a second, more pessimistic, scenario it might lead to fall outside the “green” border missing the fulfilment of one or more requirements. Further improvements of the design aimed at minimizing some quantities instead of others are a matter of the optimization process which is supposed to be performed in a more advanced phase of the BoP project. Nevertheless, in view of the several constrains and criteria that have been defined, this does not means that the heat exchanger design will not be a good starting point for additional developments.

To start the detailed design phase, a relatively complex, but still manageable set of input data are required. In particular, several geometrical parameters must be chosen to allow a complete sizing of the exchanger. These elements have been selected keeping in mind the target values that should be reached to be compliant with the preliminary results as well as envisaging the achievement of an easy-to-manufacture component. In order to do so, a step-by-step procedure has been followed. The main items are reported below.

4.4.2.1 Tubes characteristics and bundle layout

To definitely select the tubes diameter, a check of the nominal dimensions commonly available on the market has been done. The need of thousands tubes to equip 8 heat exchangers suggests the use of standard sizes, to avoid the order of uncommon pieces which would be not economically justifiable, unless particular conditions would occur.

Nominal dimensions, see Table 4.11, are usually referred to the external diameter, therefore to be compliant with the previously calculated internal diameter, a proper combination of wall thickness and standard diameter have to be selected.

Table 4.11. TEMA recommended tube dimensions (partial) [124].

Tube d_e [mm]	12.700	15.875	19.050	22.225	25.400
Wall thickness [mm]	0.889	0.899	0.889	0.889	-
	1.245	1.245	1.245	1.245	1.245
	-	1.651	1.651	1.651	1.651
	-	-	2.108	2.108	2.108
	-	-	2.769	-	2.769

The tube minimum thickness has been calculated by the proper formula drawn from ASME code [145]:

$$\begin{cases} t_{min} = \dfrac{p_{design} d_e}{2\left(S_m + p_{design} Y\right)} + A \\ \text{with } Y = 0.4 \end{cases} \tag{42}$$

where p_{design} is 9.2 MPa, as previously declared, and S_m is the maximum allowable stress intensity of the tube material at the design temperature, set to 530 °C. The A factor is an allowance that can be added to the minimum calculated value to consider any reason that could lead to a reduction of the material (e.g. corrosion, erosion, wall thinning do to treatments). Alloy 800H is the steel adopted due to the motivations already explained hence, as reported in Table 3.2, a corrosion rate lower than 10 micron per year can be expected. DEMO is supposed to operate for about 20 calendar years, but the load factor should be ~0.3 taking into account maintenance periods and pulsed operations, so that 7 full power year (FPY) of operation are foreseen [146]. However, although during long maintenances the exchanger will be drained, the salt will be kept into the IHX for both Pulse e Dwell periods meaning that a correction must be done. According to the actual DEMO phases, see section 2.1, approximating the ramp-up/ramp-down phases with linear functions, the total operating time of the exchanger can be written as follow:

$$T_{IHX} = 7FPY \frac{T_{Pulse} + T_{Dwell} + T_{Transitions}}{T_{Pulse} + \frac{T_{Transitions}}{2}} \tag{43}$$

This implies that an increment of about 10% has to be made respect to the 7 FPY resulting in 7.7 years of theoretical exchanger operation, thus the anticipated tube corrosion would be roughly 80 µm. Nevertheless, in line with the guidelines adopted in LMFBRs, an allowance of 0.1 mm has been employed.

Therefore, performing the calculations it has been seen that to lay within the optimal internal diameter region, a nominal d_e = 15.875 mm with a wall thickness of 1.245 mm must be used. It should be noticed that minimum tube thickness would be about 0.93 mm but this value has been rounded up to the nearest value recommended by TEMA.

As regard to the tube layout and the pitch, they determine the cross-flow area. In the preliminary evaluations it has been selected a square layout with variable pitches in order to obtain a ratio P/d_e of 1.4 in all the configurations. Of course, the smaller the pitch value is, the more tubes can be accommodated within a given shell diameter, however limitations are given by a minimum necessary “Webb thickness,” the distance between adjacent tube holes in the tubesheet, which is required for proper tube-to-tubesheet joint. So pitch values determining a $P/d_e < 1.1$ are basically forbidden [147]. *Taborek* [92] suggests to keep the tube pitch-to-tube diameter ratio between the values of approximately 1.25 as a minimum and 1.5 as a maximum, to reach both reasonable pressure drops and heat transfer coefficients on the shell side. The square pitch offers a bit lower effectiveness in terms of “pressure drop to heat transfer conversion” if compared to the triangular lattice, but for given pitch it has considerable lower pressure drops [128]. Furthermore, if mechanical cleaning is required on the shell side, a square layout with a gap between adjacent tubes of minimum 6.5 mm should be kept [91]. Although the definition of cleaning procedures for the DEMO exchangers seems too premature, it can be noticed that with an external diameter of 15.875 mm and a tube clearance of 6.5 mm, the ratio P/d_e is slightly above 1.4. Therefore, as at almost no price it would have been possible to prepare the IHX for a potential mechanical cleaning, this interspace has been selected, thus obtaining a square tube lattice with a pitch of 22.375 mm.

4.4.2.2 Bundle allocation, shell diameter, segmental baffles and clearances

According to the equation (28), with the selection of the tube internal diameter, the only parameter on which the number of tubes depend is the helium velocity (for the given boundary conditions). As found from the preliminary assessments, it should be in the range of

30÷35 m/s. However, regardless of the final helium speed, which has been set with a final tuning together with the HITEC velocity, the total number of tubes that will be allocated inside the shell must be defined taking into account some provisions. In particular, to cope with the occurrence of fouling, tube clogging and/or failures (which would enforce to plug it), it is very common in nuclear industry to assume that around 5 to 10 % tubes will be lost over the time [95] [130]. To ensure proper heat transfer capabilities also in the latest working period of the plant, in the so-called “End-of-Life” (EOL) conditions, an oversizing of the exchanger is usually envisaged. Therefore, in the assumption that 10% of the initial tubes will become progressively unavailable, the total amount must be calculated as follow:

$$N_{tot} = \frac{N_{min}}{0.9} \tag{44}$$

where the N_{min} is the minimum number of tube required to exchange the total power at the EOL conditions and calculated from the (28).

This means that the shell must be sized to allocate the total number of tubes even though the thermal-hydraulic design shall be performed neglecting such an “extra” surface. It should be intended that the component, at the beginning-of-life (BoL) would experience better performances.

It should be noticed that, for constructive reasons, the baffle are not welded to the shell, instead they are supported by some tie rods, which main scope is to hold together the bundle and keep located in the correct position the baffles. They are essentially circular metal rods screwed to one tubesheet and secured by lock nuts to the last baffle on the opposite side. The bundle is also comprehensive of them as they can be considered as part of the whole tubes lattice.

Therefore, in order to estimate the shell diameter, both tubes and tie rods must be taken into account. In addition, if the minimization of the shell diameter wants to be pursued, the bundle will be placed within the shell according to the most suitable position among the three possible solutions depicted in Figure 4.18. In fact, depending of the total numbers of circular elements, the best distribution of the tubes within the four quadrants can be obtained having: a) two central rows placed on the axes with a tube centred on the origin, b) only a tubes row placed on a Cartesian axis, say the x coordinate; c) no tubes rows passing through the centre.

Although the differences are very small when the bundle includes thousands of tubes and they could have been neglected in thermal-hydraulic calculations, the tubes must be properly allocated if a reasonable mechanical sizing of exchanger tubesheet is considered as part of the design activity.

The calculation of the circumference diameter through the centres of the outer tube rows has been done to be consistent with the following rules based on the circumference equation in Cartesian coordinates.

$$\begin{cases} \text{if } \dfrac{N_{tot}+N_{tie\,rods}}{4}-\left\lfloor \dfrac{N_{tot}+N_{tie\,rods}}{4}\right\rfloor = 0.25;0.75 \\ N_{tubes\ row\ 1} = 0.25+0.5\left\lfloor \dfrac{\sqrt{\left(\dfrac{D_{ctl}}{2}-\dfrac{d_e}{2}\right)^2-\left[(k-1)P\right]^2}}{P}\right\rfloor \quad \text{and} \\ N_{tubes\ row\ k} = 0.5+\left\lfloor \dfrac{\sqrt{\left(\dfrac{D_{ctl}}{2}-\dfrac{d_e}{2}\right)^2-\left[(k-1)P\right]^2}}{P}\right\rfloor \end{cases} \tag{45}$$

$$\begin{cases} \text{if } \dfrac{N_{tot}+N_{tie\,rods}}{4}-\left\lfloor \dfrac{N_{tot}+N_{tie\,rods}}{4}\right\rfloor = 0.5 \\ N_{tubes\ row\ k} = 0.5+\left\lfloor \dfrac{\sqrt{\left(\dfrac{D_{ctl}}{2}-\dfrac{d_e}{2}\right)^2-\left[(k-0.5)P\right]^2}}{P}\right\rfloor \end{cases} \tag{46}$$

$$\begin{cases} \text{if } \dfrac{N_{tot}+N_{tie\,rods}}{4}-\left\lfloor \dfrac{N_{tot}+N_{tie\,rods}}{4}\right\rfloor = 0 \quad \text{and if} \\ 0.5\left(\left\lfloor \dfrac{\left(\dfrac{D_{ctl}}{2}-\dfrac{d_e}{2}\right)}{P}-0.5\right\rfloor +1\right)-\left\lfloor 0.5\left(\left\lfloor \dfrac{\left(\dfrac{D_{ctl}}{2}-\dfrac{d_e}{2}\right)}{P}-0.5\right\rfloor +1\right)\right\rfloor = 0 \\ N_{tubes\ row\ 1} = 0.5\left\lfloor \dfrac{\sqrt{\left(\dfrac{D_{ctl}}{2}-\dfrac{d_e}{2}\right)^2-\left[(k-1)P\right]^2}}{P}\right\rfloor \quad \text{and} \\ N_{tubes\ row\ k} = \left\lfloor \dfrac{\sqrt{\left(\dfrac{D_{ctl}}{2}-\dfrac{d_e}{2}\right)^2-\left[(k-1)P\right]^2}}{P}\right\rfloor \end{cases} \tag{47}$$

Otherwise:

$$\left\{ N_{\text{tubes row k}} = \left\lfloor \left(\frac{\sqrt{\left(\frac{D_{ctl}}{2} - \frac{d_e}{2}\right)^2 - \left[(k-0.5)P\right]^2}}{P} - 0.5 \right) + 1 \right\rfloor \right. \tag{48}$$

$$\text{with } k = [1;Z],\ Z = \left\lfloor \frac{\left(\frac{D_{ctl}}{2} - \frac{d_e}{2}\right)}{P} \right\rfloor$$

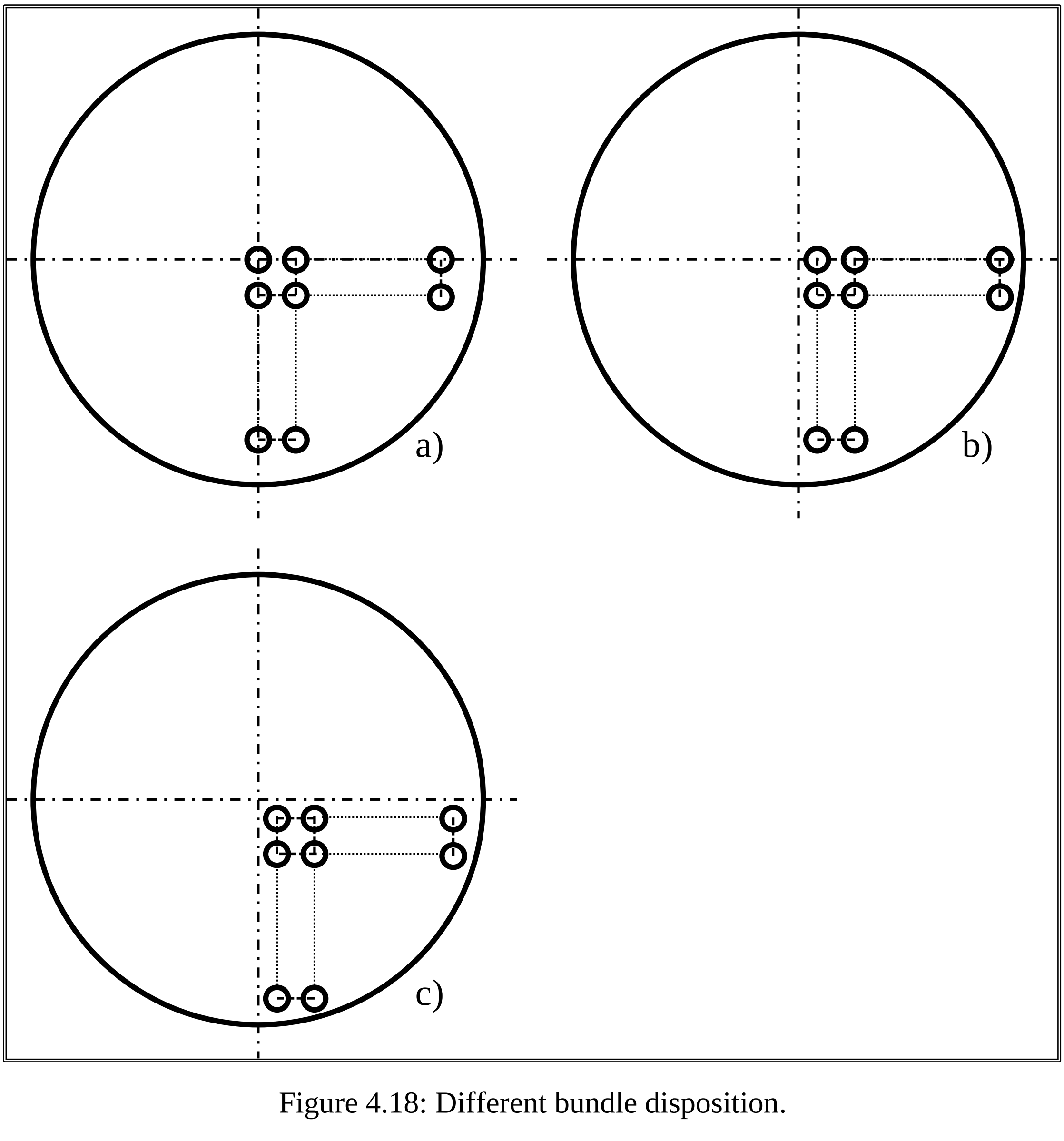

Figure 4.18: Different bundle disposition.

In the equations from (45) to (48) the quantity "$N_{\text{tube row k}}$" is referred to number of tubes in the row "k" within the forth quadrant. The rows counting starts from that closest to the x-axes proceeding downward in the bottom half of the circle. The calculation has been performed iteratively, selecting as initial value:

$$D_{ctl}^{tentative} = d_e \left(\frac{P}{d_e} \right) \sqrt{\frac{4\left(N_{tot} + N_{\text{tie rods}}\right)}{\pi}} \tag{49}$$

From the knowledge of the "outer tube limit" diameter, it is possible to establish the shell internal diameter via the addition of the "shell-to-bundle" clearance. This small gap between the last tubes surface and the inner shell diameter is needed for constructive reasons (e.g. welding of the shell to tubesheet with the minimum curvature radius). This value can be preliminary estimated according to the following equation [92]:

$$L_{BB} = 12.23 + 0.0051 D_S \tag{50}$$

with the dimensions in mm.

However, when large shells are used, the previous equation can lead to results which are too "optimistic", hence, a minimum value of 45 mm has been selected for this clearance in order to allow the use of joint curvature radii of at least 20 mm, thus avoiding sharp transition between the heads (or shell) and the top/bottom tubesheet [147].
Finally, shell internal diameter has been iteratively calculated considering the equations from (45) to (50) as:

$$D_S = D_{ctl} + L_{BB} \tag{51}$$

As regards to the segments baffles, they are perforated, circular disks having a segment removed. The function of the baffle is to direct the flow across the tube field as well as to mechanically support the tubes against sagging and possible vibration. The removed zone, known as the "baffle cut", creates a baffle window where the fluid can pass through to be redirected toward the downstream baffle compartment, see Figure 4.19. It is commonly expressed as a percentage of the shell inside diameter D_s:

$$B_c = 100 \frac{L_c}{D_s} \tag{52}$$

Heat transfer and pressure drops of crossflow bundles are greatly affected by the baffle cut, which generally is within 20%–25% but, depending on the application, it can also became larger. A baffle cut of about 20% usually manages to provide the highest heat transfer for a given pressure drop. For cuts smaller than 20% pressure losses become higher while as the baffle cut increases beyond 20%, the flow pattern deviates more and more from crossflow and can result in stagnant regions or areas with lower flow velocities, thus reducing the thermal effectiveness of the bundle, see Figure 4.19.

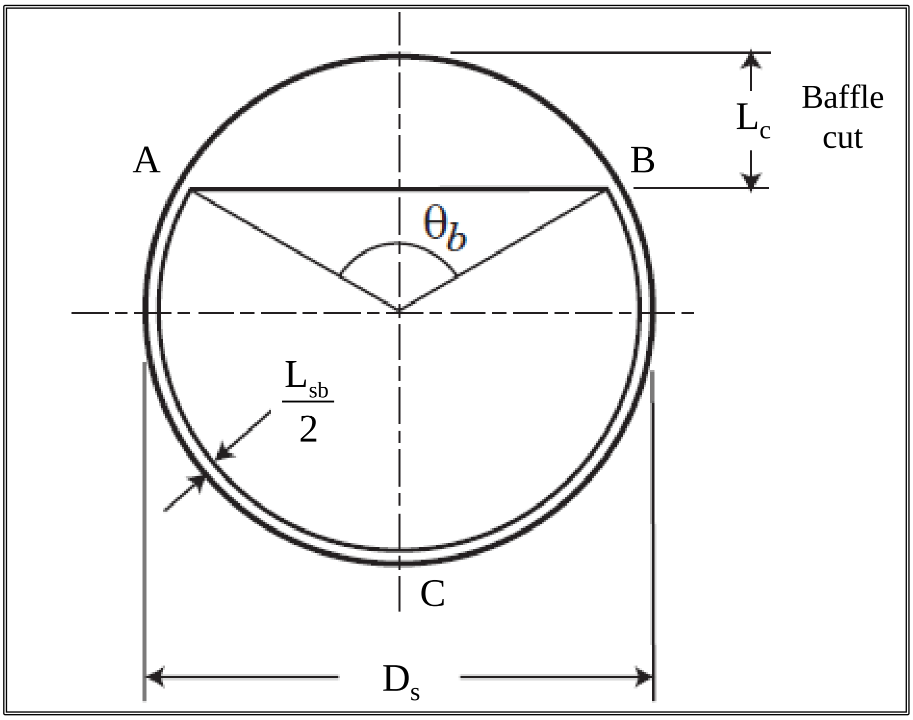

Figure 4.19. Baffle geometry showing baffle cut length and shell-to-baffle clearance.

The baffle spacing is another crucial design parameter for an efficient flow distribution (see Figure 4.20). Firmly established rules call for minimum baffle spacing equal to 20% of the shell and a maximum permissible distance between two consecutive baffle that should be limited to the shell dimeter length [128]. Summarizing, to achieve a steady flow pattern of the cross-flow and baffle window flow a baffle cut of around 20% and a baffle spacing within a range of 20÷100% of D_s should be ensured. For these reasons, these values have been considered as constrains for the final design of the exchanger.

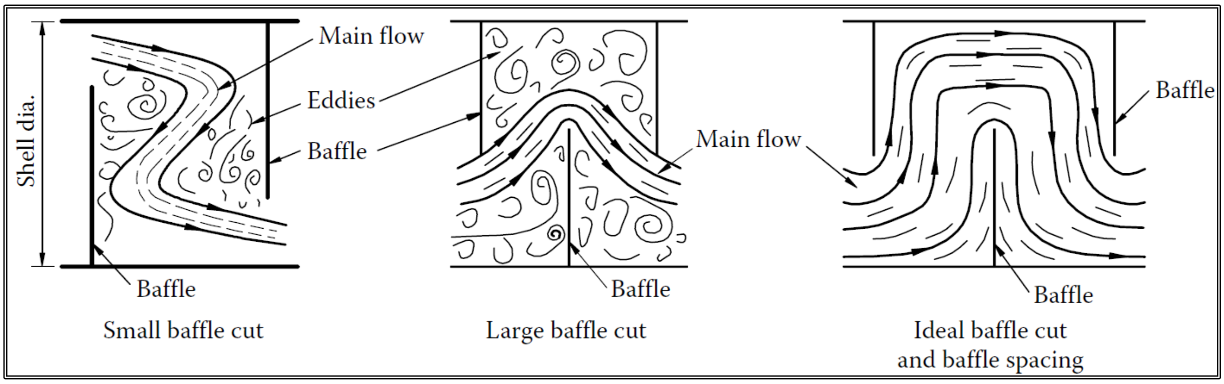

Figure 4.20. Shell-side flow distribution influenced by baffle cut and baffle spacing [125].

Furthermore, another guideline followed before starting with the thermal-hydraulic calculations has concerned the limitation of the liquid velocity when the shell-side stream is discharged into the tube bundle through a nozzle. If the flow velocity through the nozzle exceeds a certain maximum, the tubes can vibrate, and can be subjected to erosion and potential damage. TEMA specifies the maximum allowable shell-side nozzle velocity above which an impingement protection is required [124]:

$$u_{MS\,max} = \sqrt{\frac{2250}{\rho_{MS}}} \tag{53}$$

The employment of an impingement device would reduce the number of tubes that can be placed within a shell and should be respected in tube count estimations. However, this would imply the adoption of a larger shell for a given helium design velocity, therefore, it has been chosen to limit inlet HITEC velocity to the value calculated through the (53). Accordingly, the molten salt minimum inlet nozzle diameter has been calculated employing the $u_{MS\,max}$.

Once these main geometrical characteristics have been set, the calculation of the main thermal-hydraulic quantities has begun.

4.4.2.3 The Bell-Delaware method

In selecting the a proper method for a detailed thermal-hydraulic design of the plate-baffled heat exchanger, the Bell-Delaware approach, as modified by *Taborek* in [92], has been judged as the most suitable and indicated to complete the thermal-hydraulic methodology that has been developed so far. In fact, even though it is clear that the method has been originally made to be readily handled by hand-held calculators, progressing in a stepwise manner and making use of several auxiliary variables, it can be also programmed into even small programmable calculators, enhancing its performances, thus using it in the most effect way. For this purpose, the entire procedure has been implemented in the most widely used spreadsheet software package, namely Microsoft Excel®, thanks to its capabilities to apply numerical methods not only using the simple worksheets formulas, but also writing small programs in Excel's Visual Basic for Application programming language (the so-called Macros). This have allowed, for example, to obtain a working environment where the fluid properties functions or the heat transfer and pressure drop models have been embedded, in order to speed-up and automatize the calculations. Moreover, where necessary, iterative methods have been also implemented to solve the simplified steady-state conservation equations. Obviously this tool has not the presumption of being in "competition" with more sophisticated, complex computer programmes ad-hoc developed, however, it is worth to emphasise that the Bell-Delaware method is also the basic of some commercial codes, such as HEXTRAN [148], which deal with heat transfer processes. Moreover, it has been shown [149] that, in spite of its relatively simple implementation, the Bell method is able to provide results that are within respectable limits of accuracy for an exchanger that can be defined as "well-designed" [150]. Nevertheless, a verification of the heat transfer performances of the IHX has been done by using RELAP5-3D code. It will be discussed in the following, see paragraph 8.4.3.2.

The Bell-Delaware method is based on the calculation of a series of auxiliaries geometrical factors for the determination of the shell side heat transfer coefficients and pressure drops. These corrective factors are calculated in order to quantify those streaming paths that have been already discussed in the paragraph 4.3 and described in Figure 4.15. The parameters can be all estimated on the basis of the geometrical information described in the previous section because, as requirements, it has been assumed that the standards of TEMA are met with respect to various shell side constructional details. However, a rigorous description of all the geometrical items that have been calculated would be long, tedious and, in addition, it would not probably add particular value this dissertation. These factors are all listed in many handbooks, already cited, that deal with this topic. The interested reader can refer to manuals such as [92] or [128].

Nevertheless, as for the preliminary results, a brief description of the heat transfer and pressure drop models adopted will be given, then the results will are presented.

4.4.2.4 Heat transfer models

The Bell-Delaware belongs to that kind of methods developed only to predict the thermal-hydraulic behaviour of the fluid flowing on the shell side because in normal services there are not particular disturbing phenomena expected for the coolant inside tubes. For the helium, hence, it could have been possible to adopt the correlations as they have been already described in 4.4.1.4 however, some modifications have been done, so they will be re-introduced.

4.4.2.4.1 Tube side

In order to improve the predictability of the tool, in the detailed calculation phase some aspects which had been previously neglected now must be considered. Although the basic correlation used to calculate the Nusselt number, thus the heat transfer coefficient, has been kept the same, i.e. the *Gnielinski* correlation (33) with the aid of (34), the final Nusselt is corrected taking into account the effects of both tube roughness and fluid variable properties. Following the suggestions of *Saha* in [151] the relations adopted have been:

$$\mathrm{Nu}_{\mathrm{rough}} = \mathrm{Nu}_{\mathrm{smooth}} \left(\frac{\lambda_{\mathrm{rough}}}{\lambda_{\mathrm{smooth}}} \right)^{0.68\mathrm{Pr}_{\mathrm{bulk}}} \tag{54}$$

and

$$\mathrm{Nu}_{\mathrm{variable\ properties}} = \mathrm{Nu}_{\mathrm{rough}} \left(\frac{\mathrm{T}_{\mathrm{bulk}}}{\mathrm{T}_{\mathrm{wall}}} \right)^{0.36}_{\mathrm{for\ gases}} \tag{55}$$

where the Darcy coefficient for rough walls have been calculated according to the *Haaland*'s formula [143], which is a good approximation of the Colebrook-White equation [152]. It will be described in the paragraph 4.4.2.5.1.

4.4.2.4.2 Shell side

As said, the shell side heat transfer coefficient has been calculated in agreement with the Bell-Delaware method. Basically, it defines several coefficients (whose values are generally lower than 1) to modify the ideal heat transfer coefficient calculated in an indefinite tube banks. This, in principle, would allow to use whatever heat transfer model developed for ideal tube banks [92], therefore it would have been permitted to use the Zukauskas correlation (36), however to be fully coherent with the applied methodology also the ideal heat transfer coefficient have been according to the relation provided by Bell:

$$h_{\mathrm{ideal}} = j c_p G' \mathrm{Pr}^{-\frac{2}{3}} \left(\frac{\mu_{\mathrm{bulk}}}{\mu_{\mathrm{wall}}} \right)^{0.14} \tag{56}$$

with

$$\begin{cases} j = a_1 \left(\dfrac{1.33}{L_T / D_e} \right)^{\frac{a_3}{1+0.14\mathrm{Re}^{a_4}}} \mathrm{Re}^{a_2} \\ 10 \le \mathrm{Re} \le 10^5 \end{cases} \tag{57}$$

being j the Stanton number (in the form for graphical representation [92]) and G' the specific mass flow rate evaluated through the largest bundle row, namely at the diametral section of the shell in between two baffles. The coefficients in the equation (57) are reported in Table 4.12.

Once the ideal heat transfer coefficient has been calculated the procedure can continue modifying the ideal coefficient as follow:

$$h_{\mathrm{real}} = h_{\mathrm{ideal}} J_C J_l J_b J_S J_R \tag{58}$$

with J_C, J_l, J_b, J_S, J_S depending on geometry.

Usually, to define an exchanger as "well-design" and efficient, the overall product of those geometrical coefficients should be less than 0.7. Of course the upper boundary is defined by the unity but is very difficult to exceed a factor 0.9 without paying the price of very high pressure drops. With regard to the final design of the PHTS exchanger, a value of 0.83 has been reached. This value has been judged more than acceptable because it has allowed the molten salt to have a reasonable heat transfer performances while the criteria on the pressure drops have been preserved. On the contrary, attempting to further increase the heat transfer on the shell side would have led only minor improvements because the overall thermal resistance was already laid on the helium side.

Table 4.12. Bell-Delaware Stanton coefficients (partially from [128]).

Tube layout	**Re**	$\mathbf{a_1}$	$\mathbf{a_2}$	$\mathbf{a_3}$	$\mathbf{a_4}$
90° - square lattice	10^5-10^4	0.37	-0.395	1.187	0.370
	10^4-10^3	0.37	-0.266		
	10^3-10^2	0.408	-0.460		
	10^2-10	0.900	-0.631		

4.4.2.5 Pressure drop models

As in the preliminary calculation the distributed pressure drops have been calculated according to the (38). In this case, however, the length of tubes considered in the assessment consist not only of the tube heated length, but it takes into account the path of the bundle within two tubesheets.

Furthermore, in this phase the local pressure drops have been assessed accounting for the sudden expansion (contraction) that the fluids, in particular the helium, experience entering (exiting) into the exchanger head and, then, into the tube bundle.

The evaluation have followed the same criteria and relations that will be explained through the paragraph 5.1.1.

4.4.2.5.1 Tube side

As mentioned, the *Haaland*'s equation has been employed to evaluate the Darcy-Weisbach coefficient.

$$\lambda_{\text{rough}} = \left\{ -1.8\log_{10}\left[\frac{6.9}{\text{Re}} + \left(\frac{\varepsilon}{3.7} \right)^{1.11} \right] \right\}^{-2}$$

$$\begin{cases} 4000 \le \text{Re} \le 10^8 \\ 10^{-6} \le \varepsilon \le 0.05 \end{cases} \qquad (59)$$

with the absolute roughness of the exchanger tubes set to 5 μm due to the expected good surface treatment for these elements [153].

4.4.2.5.2 Shell side

The shell side pressure drop is calculated in the Bell method by summing the pressure drops for the inlet and exit sections and the internal sections after applying various correction factors.

The elements of pressure drop are shown schematically in Figure 4.21.

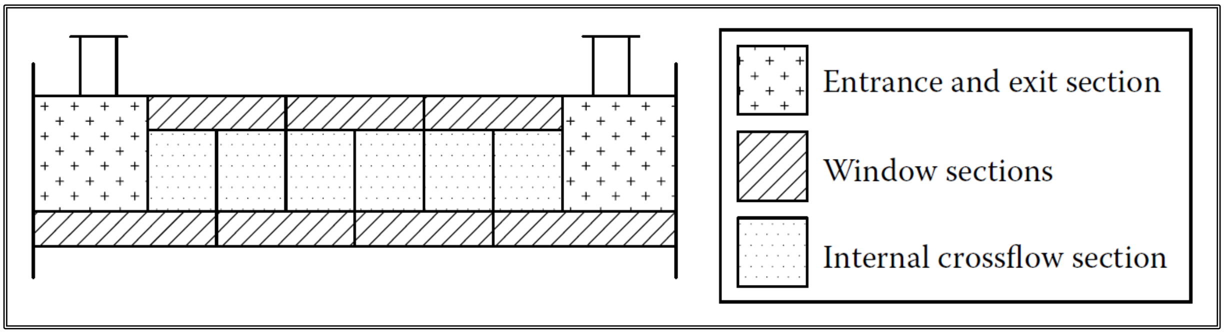

Figure 4.21: Shell side pressure drop regions of a TEMA E type shell [127].

The entrance and the exit losses may differ from the internal cross section when the first and the last baffle compartments are larger (or, rarely, smaller) than the central compartments. Therefore, if no requirements impose such a difference, the pressure drop regions become two as the entrance/exit sections behaves very similar to an internal cross-flow section.

The total pressure drop has been calculated as follow:

$$\Delta p_{tot} = \Delta p_{\text{baffle tip}} + \Delta p_{\text{windows}} + 2\Delta p_{\text{end zone}} \tag{60}$$

being the 3 terms defined as:

$$\begin{cases} \Delta p_{\text{baffle tip}} = \left[2\lambda_{\text{Bell}} N_{tcc} \dfrac{G'^2}{\rho} \left(\dfrac{\mu_b}{\mu_w} \right)^{-0.14} \right] (N_b - 1) R_b R_l \\ \Delta p_{\text{windows}} = \left[(2 + 0.6 N_{tcw}) \dfrac{G'^2_w}{2\rho} \right] N_b R_l \\ \Delta p_{\text{end zone}} = \left[2\lambda_{\text{Bell}} N_{tcc} \dfrac{G'^2}{\rho} \left(\dfrac{\mu_b}{\mu_w} \right)^{-0.14} \right] \left(1 + \dfrac{N_{tcw}}{N_{tcc}} \right) R_l \end{cases} \tag{61}$$

where N_{tcc} is the number of effective rows crossed between baffle tip (pure cross-flow section), N_{tcw} is the number of effective rows crossed in baffle window and N_b the number of baffles. In addition, G' and G'_w are cross and window specific mass flow rate, respectively. While R_b and R_l are those coefficients depending on the geometry that are used to consider the leakage streams discussed elsewhere in the precedent sections. The friction coefficient is calculated with an expression whose form resembles the relation (57):

$$\begin{cases} \lambda = b_1 \left(\dfrac{1.33}{L_T / D_e} \right)^{\frac{b_3}{1+0.14 Re^{b_4}}} Re^{b_2} \\ \text{with } b_1, b_2, b_3, b_4 \text{ depending on Re and lattice} \end{cases} \tag{62}$$

The coefficient are reported in Table 4.13.

Table 4.13. Bell-Delaware coefficients for friction factor (partially from [128]).

Tube layout	**Re**	a_1	a_2	a_3	a_4
90° - square lattice	10^5-10^4	0.391	-0.148	6.30	0.378
	10^4-10^3	0.0815	-0.022		
	10^3-10^2	6.0900	-0.602		
	10^2-10	32.1000	-0.963		

4.4.3 Final design data

Finally, in agreement with all the criteria and constrains described, a final design for the standard shell and tube IHX has been outlined. The exchanger layout and the coolant flow scheme are depicted in Figure 4.22. Helium coolant enters from the top the component in the upper head, here it is canalized in tube of the heating section through the holes drilled in the upper tubesheet. In the heating section the gas coolant flows downward and the molten salt travels on the shell side with an overall ascending motion while crossing the baffle compartments. At the outlet of the tube bundle, after being passed within the lower tubesheet, the primary fluid is collected into the lower head from which it exits and is carried to the circulator suctions via two pipes.

The heat transfer surfaces has been evaluated subdividing the calculation domain in 15 thermal regions applying the methodology discussed in the previous paragraphs. A further discretization of the exchanger zones has been also attempted but no sensible variations in the calculated quantities have been seen therefore, for the given coolants conditions, the choice of 15 nodes has been judged satisfactory. As a matter of fact, from the observation of the Figure 4.23 it can be understand that the variation of the overall heat transfer coefficient, thus of the global thermal-hydraulic behaviour of the exchanger, is weakly dependent on the coolant properties (see y-axes on the left).

It must be pointed out that the calculations have been run in parallel with those for pipework and circulators (see chapters 5 and 6) allowing to assess, though an iterative procedure, the inlet pressure of the exchanger as well as its outlet temperature.

The main thermal-hydraulic characteristics resulted from the assessments and some additional calculated mechanical data are summarized in Table 4.14 and Table 4.15.

Table 4.14. Main T/H features of the IHX. Shell&tube option with straight bundle.

	Helium	HITEC
Inlet pressure [MPa]	7.89	0.8
Inlet temperature [°C]	520.0	270.0
Outlet temperature [°C]	290.9	465.0
Mass flow rate [kg/s]	222.2	867.9
Number of tubes (BOL/EOL) [-]	10903	9812
Heat transfer surface (BOL/EOL) [m^2]	7454	6708
Tube external diameter [mm]	15.875	
Tube pitch [mm]	22.375	
Tube lattice [-]	square	
Tube thickness [mm]	1.245	
Tube active length [m]	13.71	
Tube material [-]	Alloy 800H	
Helium Volume [m^3]	30.2	
HITEC Volume [m^3]	49.0	
Helium mass [t]	0.16	
HITEC mass [t]	89.4	
Mean overall heat transfer coefficient [W/m^{2}K]	1117	
Helium ΔP [kPa]	60.7	
HITEC ΔP [kPa]	462.7	

Table 4.15. Additional mechanical data of the IHX. Shell&tube option with straight bundle.

Shell material [-]	316 SS
Tubesheet material [-]	316 SS
Other internals material [-]	316 SS
Overall height [m]	17.54
Shell external diameter (no discontinuities zones) [m]	2.758
Shell external diameter (reinforced zones) [m]	2.836
Shell thickness (no discontinuities zones) [mm]	28.00
Shell thickness (reinforced zones) [mm]	67.00
Head external diameter [m]	2.836
Head thickness [mm]	65.00
Lower/Upper tubesheet thickness [mm]	500.00
Reinforcement length (at tubesheet discontinuity) [mm]	755.9
Baffle spacing [mm]	721.4
Baffle thickness [mm]	19.1
Tube-to-baffle hole clearance (diametral) [mm]	0.4
Shell-to-baffle clearance (diametral) [mm]	12.4
Shell-to-bundle clearance (diametral) [mm]	45
Total metal mass [ton]	153

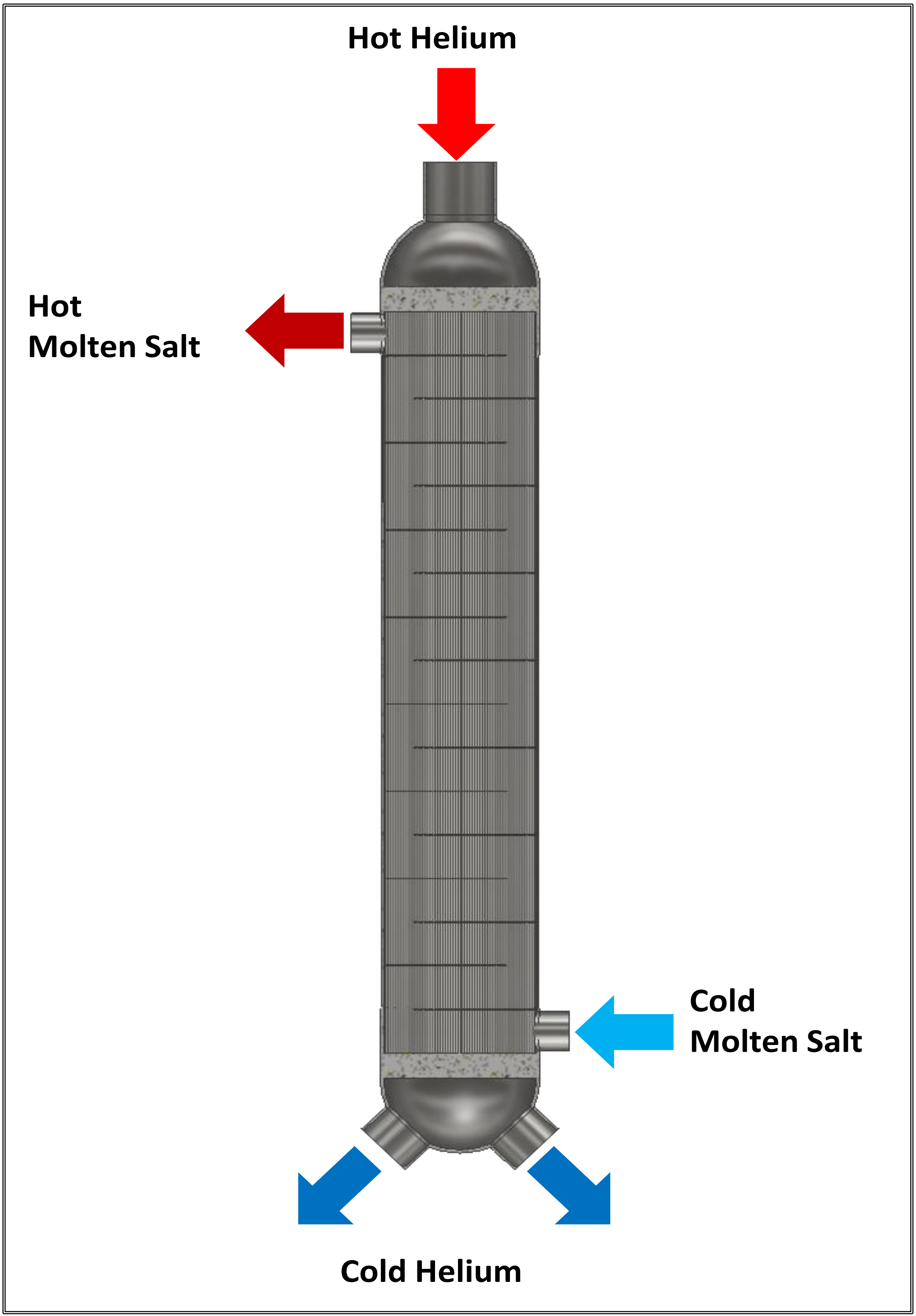

Figure 4.22. Preliminary sketch of the standard shell and tube option for the IHX.

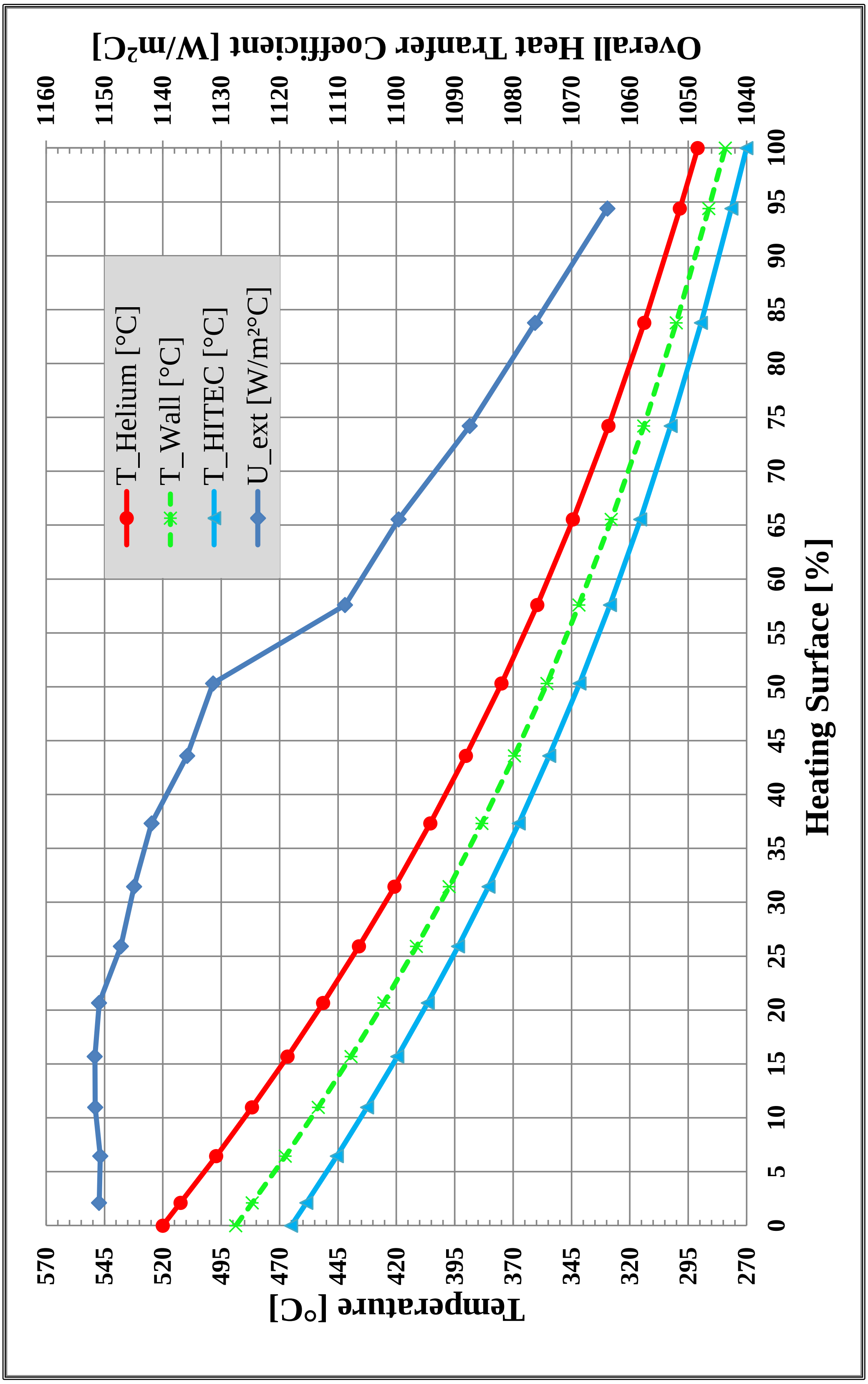

Figure 4.23. Profiles of temperatures and overall HTC in IHX option with straight bundle.

4.5 Helical coils shell and tube configuration

The helical coils heat exchangers show some potential advantages respect to the standard shell and tube heat exchangers. They have no internal baffle leakage problems and permit uninterrupted cross-flow through the tube banks for high local heat-transfer coefficients, providing a very effective terminal temperature distribution in the overall exchanger [154]. In spite of this claimed simplicity if compared to the baffled shell, the study and the discussion on this exchanger geometry might be as long as the standard tube shell has been. For sake of brevity the description of this type of heat exchanger will be reduced to the basic geometrical features.

An example of a typical helical coils heat exchanger geometry is shown in Figure 4.24.

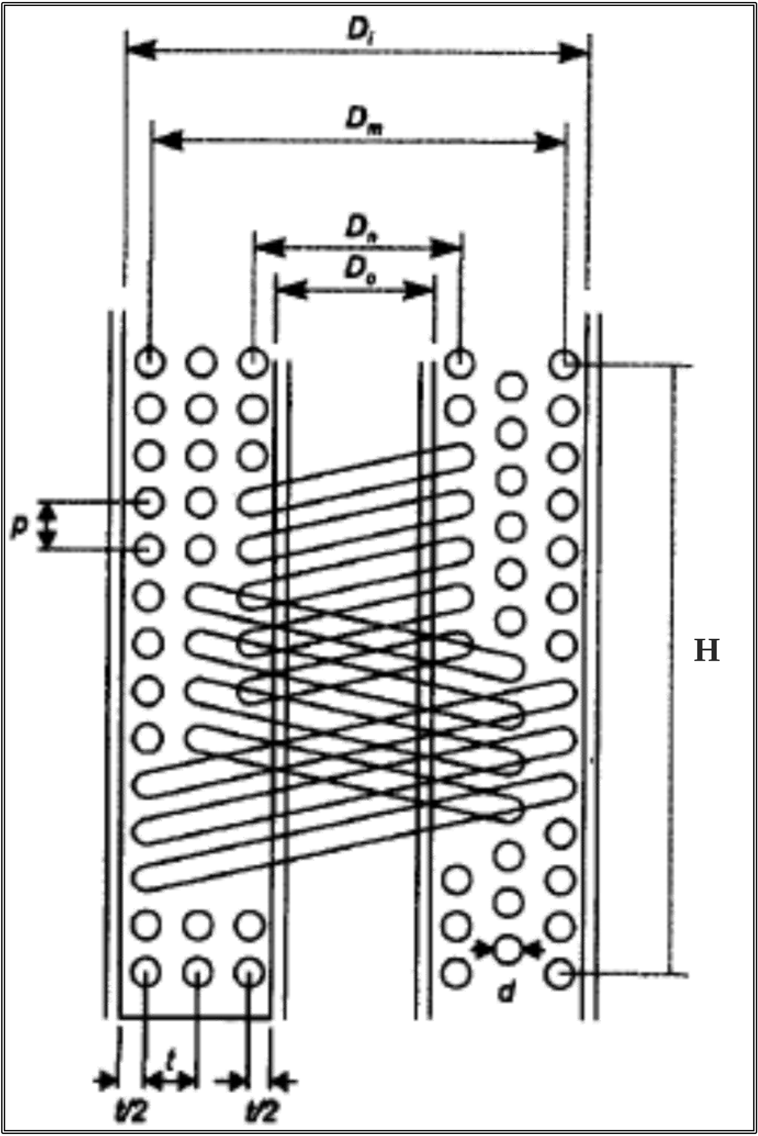

Figure 4.24. Typical geometrical parameters in helical-coil exchanger [154].

Generally, helical tube banks are composed of a multitude of cylindrical coils fitting into each other and consisting of helical tubes, in a multi-start arrangement, normally with uniform tube diameters and uniform longitudinal pitches. There are several distinct design possibilities of such banks of helical tubes. If the numbers of starts are equal in all coils, that is independent of coil diameter, then tube inclinations and therefore lengths of the tubes are by necessity unequal. On the other hand, if the numbers of starts increase proportionally to coil diameter, then uniform inclinations and uniform tube lengths are obtained all over the bundle. If, as first approximation, the effects of tube curvature are neglected, flow rates and heat loads per tube are also equal in all helical tubes, which is a really important feature from the flow distribution and flow stability point of view. Employing this particular bundle layout the longitudinal pitches are equal in all coils and so are the tube inclination angles, the so called helix angles. The design study has been focused on this latter option, which is the most commonly employed.

The simplest method of satisfying the above conditions is to adopt an annular arrangement where the central coil has one tube, the second coil has two tubes, the third coil three tubes and so on. The mean coil diameters are selected so that the shell-side fluid everywhere passes over exactly the same number of tube turns in traversing the bundle. This layout is very effective when a small flow area is required in the tube bundle compared with the shell-side flow area. Although the case already described is the simplest, it can be easily generalized if the number of tubes in all coils is multiplied by a constant factor “r”, which is an integer. This increases the number of tubes in the exchanger and the area for flow on the tube-side exactly by a factor “r”, thus allowing to reduce the length of the individual tube. This means that the general z-th coil will have nz tubes.

According to the Figure 4.25, it can be noticed that:

$$\begin{cases} \tan(\phi) = \left(\dfrac{p\mathrm{rz}}{\pi \mathrm{D_z}} \right) \\ \mathrm{D_z} - \mathrm{D_{z-1}} = 2\mathrm{t} \\ 2\mathrm{t} = \dfrac{p\mathrm{r}}{\pi \tan(\phi)} \\ \mathrm{D_z} = 2\mathrm{zt} \end{cases} \tag{63}$$

being ϕ the helix angle and D_z the z-th coil diameter and with $P > d_e/\cos\phi$ and $t > d_e$.

From the (63), it follows that:

$$\begin{cases} \mathrm{D_z} = 2\mathrm{zt} \\ \tan(\phi) = \dfrac{\mathrm{r}p}{2\pi \mathrm{t}} \end{cases} \tag{64}$$

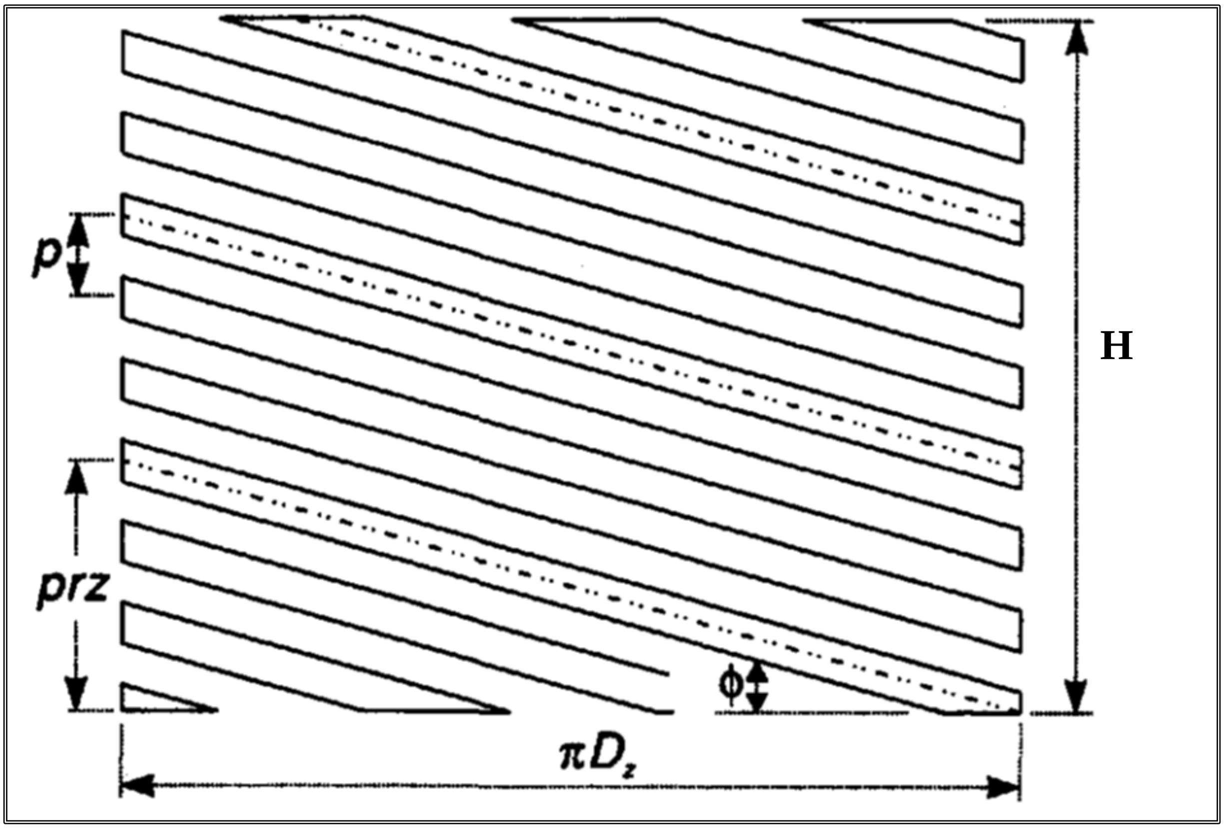

Figure 4.25. Developed z-th coil [154].

Moreover, always from the Figure 4.25 it can be see that for each tube into the exchanger the relation between the bundle height H and the tube length L is:

$$\sin(\phi) = \frac{H}{L} \tag{65}$$

which combined with the (64), gives:

$$\left(\frac{L}{H}\right)^2 = 1 + \left(\frac{2\pi t}{r p}\right)^2 \tag{66}$$

From this latter formula is possible to obtain the bundle height.

With regard to the previous expressions it is obvious that, although the final height and the final length will be the same in all tubes, the element placed on the larger coil diameter will have the bigger lead, meaning that they gain height more quickly than the inner tube with increasing azimuthal angle. This tube arrangement produces a continuous change from an ideal in-line cross flow configuration through irregularly (obliquely) staggered to regularly staggered configuration, see Figure 4.26. Moreover, as one can imagine, the helices can be wounded considering different possibilities: in fact the coils can be all right-handed, all left-handed or they can alternatively have both right-handed and left-handed helices.

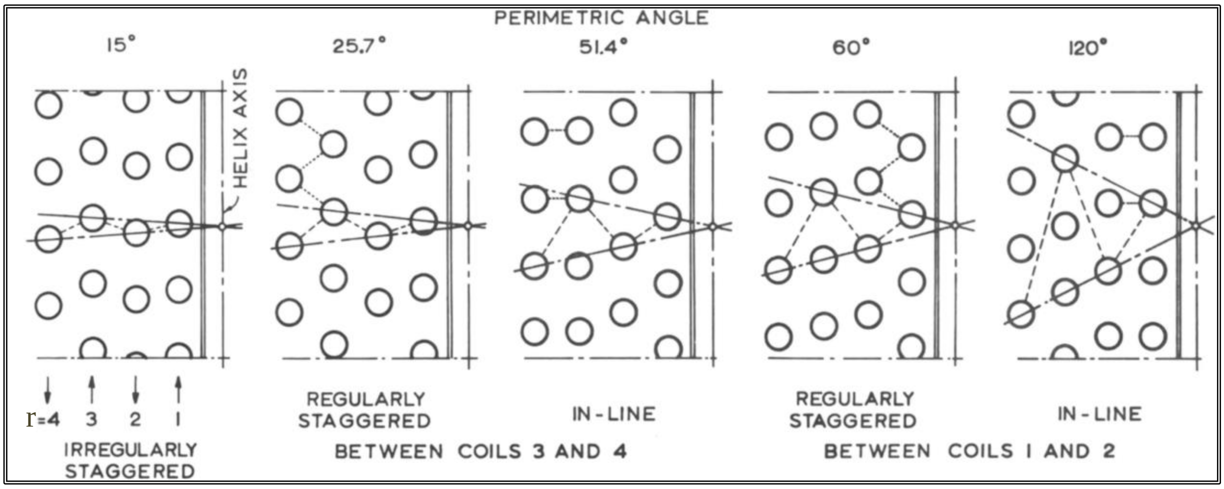

Figure 4.26. Exchanger with right-handed/left-handed helices: various azimuthal angles [155].

This further influence the tube pattern and the disposition of the lattice for given azimuth and bungle height.
In term of thermal-hydraulic effectiveness it might be even beneficial due to enhancement of the turbulence however, from the computational procedure point of view, it is more expensive because the net effect is that the shell flow area is continuously changing hence the evaluation of the shell fluid velocity is not so trivial.

Nevertheless, as the return of the same tube pattern occurs cyclically it is possible to correlate such a periodicity with the quantities that are needed to calculate thermal-hydraulic parameters like coolant speed, Reynolds number and so on. This quantities are defined as “effective” because they are evaluated according to an effective flow area, which is averaged in function of the tubes arrangement. This procedure has been followed but a detailed description will not be provided. The method is well described by *Gilli* in [155] and it has been taken as main reference for the calculation of the shell geometrical factors. A similar, more simple (but not less efficient), explanation can be found also in the more recent handbook of *Smith* [154]. Other quantities which could have been traced back to relations used for sizing the standard tube and shell exchanger have been calculated accordingly.

Furthermore, it is worth to underline that for practical calculations the approximation of an ideal in-line arrangement can be made however, if some correction factors are not applied, the likelihood of overestimate the heat transfer may be high [97].

As anticipated at the end of the survey on the main solutions adopted in nuclear industry (see par. 4.2), this exchanger option conceives HITEC and water as tube-side fluids in the two configurations where it acts as IHX and steam generator, respectively. For the reasons already explained, this layout is rather natural in case of the steam generator option because water is at higher pressure than helium.

On the other hand, it seems to go toward the opposite direction when it is employed as intermediate heat exchanger due to the lower pressure of HITEC compared to the helium coolant. However, in spite of the higher efforts to manufacture a pressure vessel which thicknesses must be compliant with the primary coolant pressure and temperatures, this configuration can help in minimizing the heating surfaces. In fact, being the gas the medium which offers the higher thermal resistance, the adoption of a flow configuration that enhances the thermal-hydraulic performances of the helium might improve the overall heat transfer coefficient experienced in the exchanger. In addition, from the results obtained for the standard shell and tube and at the given conditions imposed by the BB requirements, the number of tubes needed when the helium is put on the tube-side is in the order of ten thousand. This huge amount of tubes appears really unpractical for construction of a helical coil exchanger for both manufacturing and economic reasons therefore, if such a exchanger typology wants to be selected, the gas coolant has to flow across the tube bundle.

In this framework a careful literature review to choose the models that might realistically predict the heat transfer in helical coil heat exchangers has been made. A quick overview of the closure equations employed to calculate heat transfer and pressure drops is provided before showing the results.

4.5.1 Heat transfer models

An assessment of the heat transfer models has been needed to implement in the tool appropriate relations suitable for this particular geometry. Emphasis has been given to the two-phase models to be used in order to catch those complex phenomena proper of the flow boiling occurring in a once-through helical steam generator. A deep disquisition on the physics behind the selected models would probably need an entire chapter to achieve a satisfactory level of information. However, it would be beyond the topic of this thesis therefore in the following only a few attempts will be made with the aim of furnishing details to explain the relationships between the physical quantities that appear in the equations. Nevertheless, several reading to which it is possible to refer in order to have a more comprehensive view on this subject are reported.

The heat transfer modes expected on the tube side in case steam generator can be roughly subdivided in three main categories: single-phase liquid heat transfer, two-phase liquid/vapour heat transfer and single-phase vapour heat transfer. For the two-phase liquid/vapour heat transfer, additional sub-regions can be found: subcooled boiling, saturated boiling, post-dryout boiling.

It is worth to underline that single-phase liquid is the only heat transfer mode present on the tube side when the helical coil geometry is adopted as option for the IHX design.

4.5.1.1 Tube side – single-phase flow, liquid and vapour (steam)

A unique relation has been selected for the heat transfer mode involving single-phase fluids, either liquid or gas. Over the years, several models, both theoretical and experimental, have been developed for single phase medium in helical tubes. Authors generally agree on the suitability of the *Schmidt*'s model to be used in laminar regime [154], [156] while the *Ito*'s, *Mory and Nakayama*'s [154] and *Gnielinski*'s [156] correlations seem all suitable to be adopted in turbulent flow [157].

According to [156], *Schmidt* and *Gnielinski* models have been applied because their range of validity covers the Prandtl numbers expected for both subcooled water and HITEC as well as for the superheated steam. Therefore, the Nusselt number has been evaluated as follow:

$$\begin{cases} \text{if } \mathrm{Re} \le \mathrm{Re}_{\mathrm{Crit}} = 2300\left[1+8.6\left(\dfrac{d_i}{D_{coil}}\right)^{0.45}\right] \\ \mathrm{Nu}_{lam} = 3.66 + 0.08\left[1+0.8\left(\dfrac{d_i}{D_{coil}}\right)^{0.9}\right]\mathrm{Re}^{\left[0.5+0.2903\left(d_i/D_{coil}\right)^{0.194}\right]}\mathrm{Pr}^{1/3}\left(\dfrac{\mathrm{Pr}}{\mathrm{Pr}_{wall}}\right)^{0.14} \\ \text{if } \mathrm{Re} \ge 2.2\cdot 10^4 \\ \mathrm{Nu}_{turb} = \dfrac{(\lambda/8)\,\mathrm{Re}\,\mathrm{Pr}}{1+12.7(\lambda/8)^{1/2}\left(\mathrm{Pr}^{2/3}-1\right)}\left(\dfrac{\mathrm{Pr}}{\mathrm{Pr}_{wall}}\right)^{0.14} \\ \text{if } \mathrm{Re}_{\mathrm{Crit}} < \mathrm{Re} < 2.2\cdot 10^4 \\ \mathrm{Nu}_{transition} = \gamma \mathrm{Nu}_{lam}(\mathrm{Re}_{\mathrm{Crit}}) + (1-\gamma)\,\mathrm{Nu}_{turb}(2.2\cdot 10^4) \\ \text{with} \\ \gamma = \dfrac{2.2\cdot 10^4 - \mathrm{Re}}{2.2\cdot 10^4 - \mathrm{Re}_{\mathrm{Crit}}} \end{cases} \tag{67}$$

where λ is the Darcy-Weisbach turbulent friction factor for helical ducts as defined by *Mishra&Gupta* in [158] and slightly modified by *Gnielinski* [156] with the viscosities ratio to account for the property variation effects:

$$\lambda = \left[\frac{0.3164}{\mathrm{Re}^{0.25}} + 0.03\left(\frac{d_i}{D_{coil}}\right)^{0.5}\right]\left(\frac{\mu_{wall}}{\mu}\right)^{0.27} \tag{68}$$

4.5.1.2 Tube side – two-phase, subcooled and saturated flow boiling

The assessment of the flow boiling in helical coils has been developed since the '60s when *Owhadi* [159] and *Owhadi and Bell* [160] conducted the first pioneering experimental studies on forced convection boiling heat transfer of water in helical coiled tubes. It was found that the predicted results of *Chen*'s correlation [161], which is widely used to calculate boiling heat transfer coefficient in straight tubes, were within ±15% as long as the tube wall was completely wet. Basically, the centrifugal forces that occur in flow through bends give rise to secondary currents in the form of double vortices. In addition, the three-dimensional bends of helical coils, the direction of flow changes continuously, and a twist flow is superimposed on the double vortices. The vapour velocity that results from the high density ratio at moderate reduced pressures ensures that the double vortex and the twist flow suffice to wet the tube wall entirely in most of the applications that occur in engineering practice. In particular, in light of the results of *Owhadi and Bell,* at low pressures the perimeter averaged heat transfer coefficient can be estimated using models developed for vertical straight pipes. This approach can be applied at moderate and high pressures as well, unless the mass velocity is $G' \leq 500$ $kgm^{-2}s^{-2}$ because at very low values of the specific mass flow rate the risk of incomplete wetting of the tube perimeter is high [162]. The findings of *Owhadi and Bell* have been more recently confirmed by several authors in different independent assessments [163], [164].

In particular, the use of the *Steiner-Taborek* correlation [166] seems to ensure better heat transfer prediction in comparison with other models. The exploitation of this latter model allows to evaluate both the nucleate and the convective flow boiling heat transfer from the incipience of the first vapour bubbles, when the bulk of the fluid is still in subcooled conditions, to the occurrence of the boiling crisis. For these reasons, this model has been selected to be used in the design calculations.

Furthermore, as the Steiner and Taborek model is based on the knowledge of the dynamic flow quality $\dot{x}$, the actual quality profile and “onset of net vapour generation” (NVG) have been calculated as suggest in [143] and [162], according to the *Levy*’s model and the criterion of *Saha and Zuber,* respectively. The possibility to determine, in coiled tubes, the point of NVG by means of the above criterion was also confirmed in [167]. Specifically, when the bulk of the fluid is still subcooled, but near the wall its temperature is somewhat higher than the saturation temperature, nucleation occurs. This phenomenon is called “onset of nucleate boiling” (ONB). However, if the fluid mean temperature is still too low and/or the heat flux is not large enough, the bubbles do not detach but grow and collapse while attached to the wall, giving a small nonzero void that may be neglected. As the bulk of the coolant heats up, approaching the saturation, the bubbles can grow larger and the possibility that they will detach from the wall surface into the flow stream increases. The point along the axis z at which bubbles can depart from the wall before they suffer condensation is called Z_D, namely the location of net vapour generation. It is marked by a temperature of the fluid $T_{bulk,\,D}$. In this conditions, the bubbles detach regularly and condense slowly as they move through the coolant penetrating to the fluid bulk. Downstream this location the vapour presence cannot be neglected even though the thermodynamic equilibrium quality is still negative.

Levy demonstrated that, in almost all cases, the actual quality, $\dot{x}$, asymptotically approaches the equilibrium quality, x_e, with increasing z from the position of NVG.

The models are reported in the following.

$$\begin{cases} T_{bulk,D} = T_{sat} - 0.0022\left(\dfrac{q'' d_i}{k_L}\right) & \text{if } RePr < 7\cdot 10^4 \\ T_{bulk,D} = T_{sat} - 154\left(\dfrac{q''}{G' c_p}\right) & \text{if } RePr \geq 7\cdot 10^4 \end{cases} \tag{69}$$

$$\left\{ \dot{x}(z) = x_e(z) - x_e(Z_D)\exp\left[\frac{x_e(z)}{x_e(Z_D)} - 1\right] \right. \tag{70}$$

$$\left\{ \begin{array}{l} h_{TP} = \left[\left(h_{nb,of} F_{nbf}\right)^3 + \left(h_{LO} F_{TP}\right)^3\right]^{\frac{1}{3}} \\ F_{nbf} = F_{pf}\left(\dfrac{q''}{q''_{of}}\right)^{f(p_r)} \left(\dfrac{d_i}{d_o}\right)^{-0.4} f(M) \quad \text{if} \quad q'' \geq q''_{ONB} \\ \text{otherwise } F_{nbf} = 0 \\ F_{TP} = \left(\left[(1-\dot{x})^{1.5} + 1.9(\dot{x})^{0.6}(1-\dot{x})^{0.01}\left(\dfrac{\rho_L}{\rho_G}\right)^{0.35} \right]^{-0.2} + \right. \\ \qquad \left. + \left\{ \left(\dfrac{h_{GO}}{h_{LO}}\right)(\dot{x})^{0.01}\left[1 + 8(1-\dot{x})^{0.7}\left(\dfrac{\rho_L}{\rho_G}\right)^{0.67}\right] \right\}^{-2} \right)^{-0.5} \\ \text{with} \\ p_r = \dfrac{p}{p_{critical}} \\ F_{pf} = 2.816 p_r^{0.45} + \left(3.4 + \dfrac{1.7}{1-p_r^7}\right) p_r^{3.7} \\ f(p_r) = 0.8 - 0.1\exp\left(1.75 p_r\right) \\ f(M) = 0.377 + 0.199\ln\left(M\right) + 2.8427E - 5M^2 \\ q''_{ONB} = \dfrac{2\sigma T_{sat} h_{LO}}{r_{cr}\rho_G \Delta h_{lv}} \\ \\ q''_{of} = 150000\,[Wm^{-2}] \\ h_{nb,of} = 25580\,[Wm^{-2}K^{-1}] \\ d_o = 0.01\,[m] \\ r_{cr} = 0.3\cdot 10^{-6}\,[m] \end{array} \right. \tag{71}$$

4.5.1.3 Tube side – two-phase, dryout location and post-dryout heat transfer

It is well-known from the boiling heat transfer theory [168] that, even in low heat flux conditions, at some point of the heating section the liquid film on the wall becomes depleted due to vapour entrainment and evaporation and the dryout condition occurs.

In straight tubes, the transition from no dryout to total dryout of the tube occurs over a small length of tube, hence, it can be treated as a point transition under steady state conditions. However, due to the already mentioned secondary flows, in helical coils this transition spreads over a considerable portion of the tube, so that the assessment of the location of the boiling crisis through the adoption of models developed for a straight geometry might be insufficient and lead to a wrong evaluation of the dryout location.

Although several empirical correlations attempting to characterise the dryout phenomena in such a geometry have been proposed from different research teams, their utilization remains often confined in a narrow range of applicability related to the conditions in which the specific test has been conducted. In order to overtake this issue, in 1990 *Berthoud and Jayanti* [169] made a systematic investigation on the nature of dryout in helical coils that brought them to develop a mechanism-based model which manages to cover a wide range of thermal-hydraulic conditions, typical of those steam generators employed in nuclear reactors. This model was slightly enhanced in 2014 by *Hwang* and his group [165] that, thanks to a newer pool of experimental data, improved its reliability at low mass flux conditions.

The original *Berthoud and Jayanti*'s model has been also used as reference in the TRACE thermal-hydraulic system code [170] since the 2013 in the simulations of coiled tubes.

According to [157], the modifications presented in [165] allow to obtain better predictions than with its predecessor. Therefore the small changes suggested in [165] have been also implemented in the tool developed for this Ph.D thesis after the selection of the correlations from *Berthoud and Jayanti* as main reference.

Berthoud and Jayanti observed that in helical coil it exists a point, axial as well as circumferential, where dryout begins. Downstream this zone, it is present a region in partial dryout where the propagation of the dryout front continues in the circumferential direction until the total dryout occurs. Clearly, complete dryout occurs at a higher quality than the quality value corresponding to the occurrence of the first dryout. According to [169], complete dryout is predicted by the following equation:

$$x_{Tot} = \mathrm{Log}_{10}\left[\left(\frac{\rho_L}{\rho_G}\right)^{-1.61}\left(\frac{\mu_L}{\mu_G}\right)^{1.722}\left(\frac{G'd_i}{\mu_L}\right)^{0.494}\left(\frac{G'd_i}{\rho_L\sigma}\right)^{-0.381}\left(\frac{G'}{\rho_G\sqrt{gD_{coil}}}\right)^{0.08}\right] \tag{72}$$

If from one side the total dryout can be obtained through a unique relationship, on the other hand the first dryout may occur in one of three different regimes:

- Gravity zone, where high relative pressure, low mass flux, and large coil diameter results in stratified flow and low first dryout qualities;

- Redeposition zone, where low relative pressure, small coil diameters and high mass fluxes leads to an annular flow with a large redeposition rate and very high first dryout qualities;
- Entrainment zone where, high mass flux and large coil diameters lead to a case of high entrainment but relatively low redeposition and dryout qualities that are neither high nor low.

Determination of three regions of dominance is based on the following dimensionless parameters:

$$\begin{cases} x_0 = \dfrac{G'}{\rho_G \sqrt{gD_{coil}}} \\ y_0 = \dfrac{G' d_i}{\mu_L}\left(\dfrac{d_i}{0.02}\right)^{0.5} \end{cases} \tag{73}$$

The gravity zone for first dryout occurs when:

$$y_0 < 3.924 \cdot 10^5 x_0^{-1.71} \quad \text{if } x_0 \le 2 \tag{74}$$

The zone of redeposition is defined to be when:

$$y_0 < 6.46 \cdot 10^4 x_0^{0.893} \quad \text{if } x_0 > 2 \tag{75}$$

The zone of entrainment is defined to be when:

$$3.924 \cdot 10^5 x_0^{-1.71} < y_0 > 6.46 \cdot 10^4 x_0^{0.893} \tag{76}$$

Therefore, the first dryout quality has been calculated as follow:

$$\begin{cases} x_1^{Gravity} = 10^{7.068}\left[\left(\dfrac{\rho_L}{\rho_G}\right)^{-2.378}\left(\dfrac{G' d_i}{\mu_L}\right)^{-1.712}\left(\dfrac{q''}{G' h_{lv}}\right)^{-0.740}\left(\dfrac{G'}{\rho_G \sqrt{gD_{coil}}}\right)^{0.967}\right] \\ x_1^{Redeposition} = 3.223 + \mathrm{Log}_{10}\left[\left(\dfrac{\rho_L}{\rho_G}\right)^{0.101}\left(\dfrac{G' d_i}{\mu_L}\right)^{-0.785}\left(\dfrac{q''}{G' h_{lv}}\right)^{-0.43} \times \right. \\ \qquad \left. \times \left(\dfrac{G'}{\rho_G \sqrt{gD_{coil}}}\right)^{0.067}\left(\dfrac{q''}{\mu_L h_{lv}}\sqrt{\dfrac{\sigma}{g(\rho_L - \rho_G)}}\right)^{0.098}\right] \\ x_1^{Entrainment} = 10^{3.235}\left[\left(\dfrac{\rho_L}{\rho_G}\right)^{-0.267}\left(\dfrac{G' d_i}{\mu_L}\right)^{-0.984}\left(\dfrac{q''}{G' h_{lv}}\right)^{-0.428} \times \right. \\ \qquad \left. \times \left(\dfrac{G'}{\rho_G \sqrt{gD_{coil}}}\right)^{0.950}\left(\dfrac{q''}{\mu_L h_{lv}}\sqrt{\dfrac{\sigma}{g(\rho_L - \rho_G)}}\right)^{0.119}\right] \end{cases} \tag{77}$$

It should be noted that a complete thermodynamic equilibrium between the two phases in the partial dryout region was assumed in [169], thus the correlations are written in terms of equilibrium quality and not of actual quality. In the steam generators, dryout generally occurs at high steam quality therefore this hypothesis is easily understandable because, as can be seen from the (70), at high values actual and equilibrium qualities are almost coincident.

Furthermore, in the region that lies between the first dryout quality and the total dryout, the heat transfer regime begins a transition from nucleate boiling toward post-critical heat flux (post-CHF) heat transfer. In fact, in this zone the tube perimeter is only partially wetted hence the heat transfer suffers a gradual decrease of its efficiency. To account for this detrimental effect, the fraction of the surface that is wetted has been used as transition parameter. The fraction of the surface that is wetted is assumed to be a function of the normalized quality as defined in [169]:

$$\overline{x} = \frac{x - x_1}{x_{Tot} - x_1} \tag{78}$$

When the local quality exceeds the first dryout quality, then the local heat transfer coefficient have been given by:

$$\begin{cases} h_{trans} = f_{wetted} h_{TP} + \left(1 - f_{wetted}\right) h_{post-CHF} \\ \text{with} \\ f_{wetted} = \sum_{i=0}^{4} b_i \overline{x}^i \end{cases} \tag{79}$$

The values b_i for the estimation of the fraction of wetted surface, f_{wetted}, are reported in [169] and are based on experimental data.

With regard to the heat transfer coefficient in post-critical heat transfer regime, the correlation of *Slaughterbeck* [171] has been selected. This model improves the most famous *Groeneveld*'s equation [172], particularly at low pressures. As the basic model of *Groeneveld* is also suggested in [97] to be adopted in the design calculations of helium-heated steam generators, the use of an empirical law based on the thermal equilibrium between liquid and vapour phases has been judged suitable for the scope of this thesis work.

Therefore, according to [143], the Nusselt number in post-critical heat transfer mode has been calculated as follow:

$$Nu_{post-CHF} = 1.16 \cdot 10^{-4} \left\{ Re_G \left[x + \frac{\rho_G}{\rho_L}(1-x) \right] \right\}^{0.838} \left(Pr_G\right)^{1.81} \left(q''\right)^{0.278} \left(\frac{k_G}{k_{critical}} \right)^{-0.508} \tag{80}$$

4.5.1.4 Shell side

On the shell side, helium flows across the banks of helical tubes. As mentioned, according to [155], the dimensionless numbers for the heat transfer could be obtained from the model developed for the flow across straight-tube banks with the care of assessing the main flow quantities according the average effective free flow area of the shell.

With the use of this approach, any model suggested for the cross-flow heat transfer might be applied, however, as the original *Gilli* method was based on the *Grimison*'s formula [173], the same relation has been adopted to be fully in line with the procedure described in [155]. Therefore, the Nusselt number has been defined as:

$$\mathrm{Nu} = 0.338 F_{a,eff} F_i F_n \mathrm{Re}_{eff}^{0.61} \mathrm{Pr}^{1/3} \tag{81}$$

where $F_{a,eff}$, F_i and F_n are coefficients that take into account the tube arrangement as well as the entrance effects. Fluid properties are evaluated at the mean film temperature.

4.5.2 Pressure drop models

Similar procedures to those described in section 4.4.2.5 have been followed to calculate the pressure drops on both sides of the exchanger. In particular, local and distributed losses have been evaluated according to the geometry and the overall exchanger layout.

4.5.2.1 Tube side – single-phase flow

Owing to the tube curvature, centrifugal forces are initiated during flow and give rise to a secondary current in the form of a double vortex. The pressure drop is thus greater than that in a straight tube. In fact, both in laminar [154] and in turbulent flow [174] the ratio between coiled and straight Darcy's friction factors is higher than 1. The friction factor has been calculated according to [158] and considering the slight modification suggested by *Gnielinski* [156] to catch the effects of the non-isothermal flow in turbulent conditions:

$$\begin{cases} \text{if } \mathrm{Re} \le \mathrm{Re}_{Crit} \\ \lambda = \dfrac{64}{\mathrm{Re}}\left\{1 + 0.033\left[\mathrm{Log}_{10}\left(\mathrm{Re}\sqrt{\dfrac{d_i}{D_{coil}}}\right)\right]^4\right\} \\ \text{if } \mathrm{Re} > \mathrm{Re}_{Crit} \\ \lambda = \left[\dfrac{0.3164}{\mathrm{Re}^{0.25}} + 0.03\left(\dfrac{d_i}{D_{coil}}\right)^{0.5}\right]\left(\dfrac{\mu_{wall}}{\mu}\right)^{0.27} \\ \text{with} \\ \mathrm{Re}_{Crit} = 2300\left[1 + 8.6\left(\dfrac{d_i}{D_{coil}}\right)^{0.45}\right] \end{cases} \tag{82}$$

4.5.2.2 Tube side – two-phase flow

The method by which the pressure drop of a gas–liquid flow is calculated differs significantly to that of a single-phase flow. This is primarily due to the interaction of the two phases, which can be accounted for by applying the void fraction to the equations of mass, momentum, and energy conservation. It should be noticed that in case of boiling flow, the pressure profile has to be calculated taking into account also the pressure drops due to the acceleration and the gravity effect than cannot be neglected when huge changes of the coolant density are expected. Nevertheless, as they are basically part of the “reversible” losses, their description has been cut from this discussion and in the following only the model to calculate the friction pressure losses is reported.

Generally, the approach for formulating the two-phase friction factor (or the friction pressure gradient) is to relate it to friction factors and multipliers defined for a single-phase (either liquid or vapour) flowing at the same mass flux as the total two-phase mass flux and with a temperature corresponding to bulk conditions. Usually, in boiling channels the friction factor and the corresponding two-phase are referred to the “liquid-only” (LO) phase. Therefore, in a two-phase boiling channel, the friction pressure gradient is given by [143]:

$$\left.\frac{dp}{dz}\right|_{TP} = \lambda_{LO}\Phi_{LO}^2 \frac{1}{d_i}\frac{G'^2}{2\rho_L} \tag{83}$$

where the properties of the liquid-phase are calculated at the saturation condition, i.e. $x_e=0$.

Adiabatic two-phase flow experiments have shown that the ratio of two-phase to single phase pressure drop for a coil is approximately equal to that for a vertical straight tube with the same fluid at the same mass flow and quality [175]. For this reason, the model of *Friedel* [176], developed for straight tube in both vertical and horizontal flow, has been adopted as it is a frequently recommended correlation for the frictional two-phase pressure gradient [143]. It is written in terms of the total flow as liquid only and it has the following form :

$$\begin{cases} \Phi_{LO}^2 = \left[(1-\dot{x})^2 + \dot{x}^2 \dfrac{\rho_L \lambda_{VO}}{\rho_V \lambda_{LO}}\right] + \dfrac{3.24\dot{x}^{0.78}(1-\dot{x})^{0.224}\left(\dfrac{\rho_L}{\rho_V}\right)^{0.91}\left(\dfrac{\mu_V}{\mu_L}\right)^{0.19}\left(1-\dfrac{\mu_V}{\mu_L}\right)^{0.7}}{Fr^{0.0454}We^{0.035}} \\ \text{with} \\ Fr = \dfrac{G'^2}{g d_i \rho_{HEM}^2} \\ We = \dfrac{G'^2 d_i}{\sigma \rho_{HEM}} \\ \rho_{HEM} = \left(\dfrac{\dot{x}}{\rho_V} + \dfrac{1-\dot{x}}{\rho_L}\right)^{-1} \end{cases} \tag{84}$$

where the mean density, ρ_{HEM}, is presented according to the Homogeneous Equilibrium Model (HEM), which implies that: the velocity of the liquid equals that of the vapour, the two velocities are uniform within the area, the two phases are in thermodynamic equilibrium.

4.5.2.3 Shell side

A comprehensive review of available flow-friction correlations for helical-tube, multi-start coil heat exchanger bundles was given by *Le Feuvre* [177]. As conclusion of his work, the author provided a model to determine the pressure drops across a helical tube bank. This model has been used to calculate the helium pressure drop as follow:

$$\begin{cases} \Delta p = \lambda N_{rows} \dfrac{G'^2}{2\rho} \\ \lambda = 0.378\,\mathrm{Re}_{eff}^{-0.092} \left\{ \dfrac{[\cos(\phi)]^{-4} \left[\Gamma(S_T - 1)\right]^{0.59}}{(S_T S_L)^{0.5}} \right\}^{-1} \\ \text{with} \\ \Gamma = (S_T - 1)^{-1} \left\{ \dfrac{S_T^2}{S_L} \ln\left\{ \dfrac{S_L}{2S_T} + \left[\left(\dfrac{S_L}{2S_T} \right)^2 + 1 \right]^{0.5} \right\} + \dfrac{1}{2} \left[S_T^2 + \dfrac{1}{4} S_L^2 \right]^{0.5} - 1 \right\} \\ S_T = \dfrac{t}{d_e} \\ S_L = \dfrac{p}{d_e} \end{cases} \tag{85}$$

4.5.3 Final design and geometrical features of the helical coil exchanger

The outlined layout of the exchanger, both in IHX configuration that in case of steam generator option, envisages several coils assemblies that, together, contribute to provide the required heat transfer surface. In case of IHX configuration, the exchanger consists of 126 modules, while only 42 assemblies are needed for the steam generator. In both configurations, each assembly has a central column and five alternate concentric layers of tubes for a total amount of 20 helices with the same slope and the same effective length. On the innermost circumference 2 tubes finds place, then each layer has one more tube than the previous one. In each of the modular units, the gas flow on the shell side is limited in radial direction by an inner and an outer wall.

The sketch in Figure 4.27 shows a longitudinal section, with the overall flow scheme, of the entire modular-helical coil IHX/Steam generator; a particular of the bundle of a single assembly is also reported.

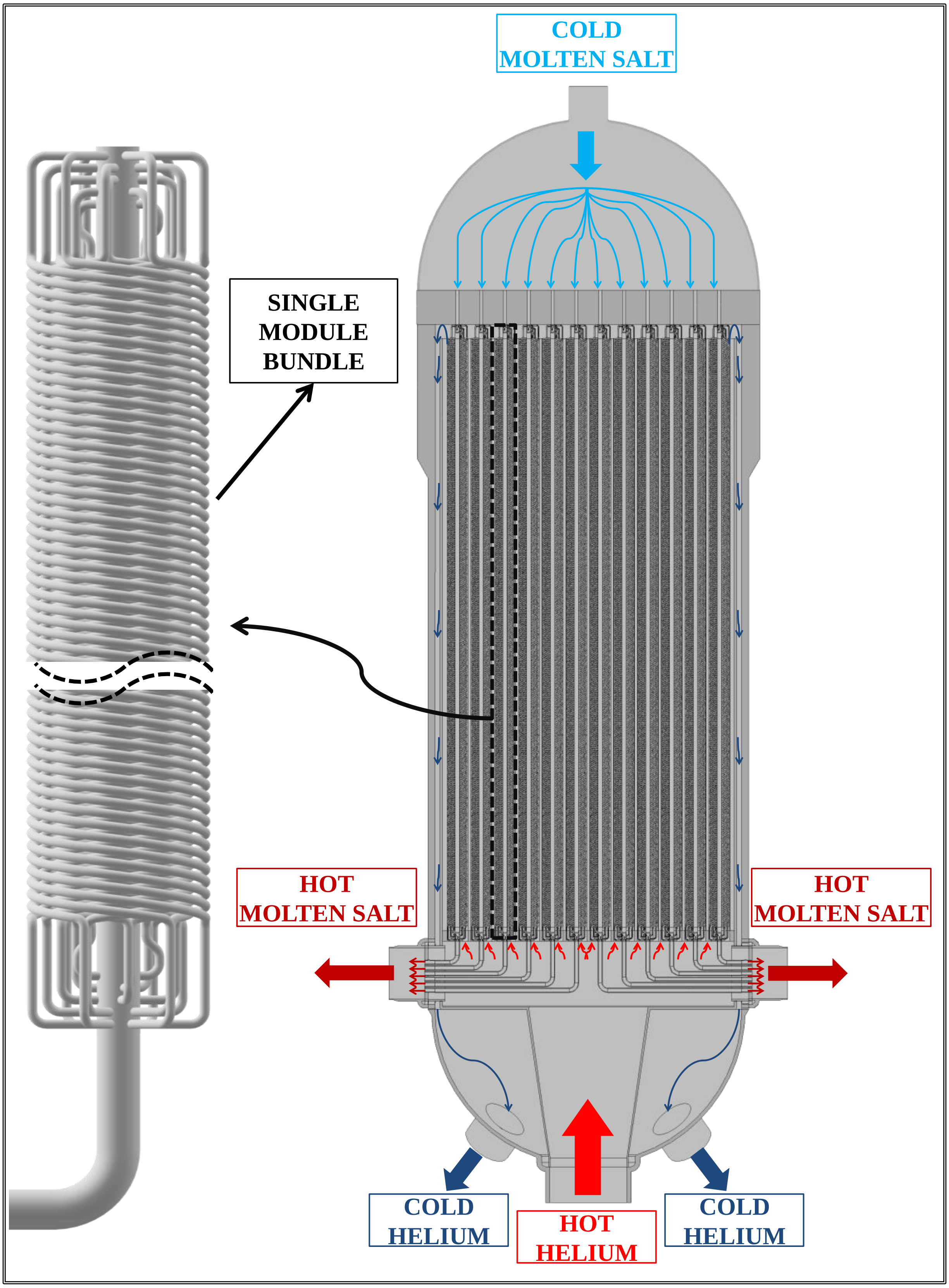

Figure 4.27: Modular-helical coil IHX/SG with general flow scheme and module’s bundle.

In the heating section, the helium flows across the tube banks in upward direction while the coolant on the tube side goes downward, generating a counter-current heat transfer path between primary and secondary fluids. The choice of this flow arrangement prevents the need of routing the large hot legs up to the top of the exchangers allowing to use the lower head only to let the helium goes in and out of the components. To do so, at the helium inlet, the hot coolant is channelled through a conical duct toward a hot distribution chamber from which it can be supplied to the different modules. Such an internal envelop keeps separate the hot helium zone from the cold one. Moreover, within this chamber, the outlet manifold of the secondary coolant are also located. Each manifold collects the fluid coming from the 20 helical tubes of a single assembly and brings it toward the two outlet pipes of the secondary coolant. The upper closure of the gas distribution chamber consists of a tubesheet where the outer wall of the modules are welded: the helium enters into the section of heating surfaces via the tubesheet holes that canalise it toward the banks of tubes.

Figure 4.28 depicts the main elements located in the bottom parts of the exchanger.

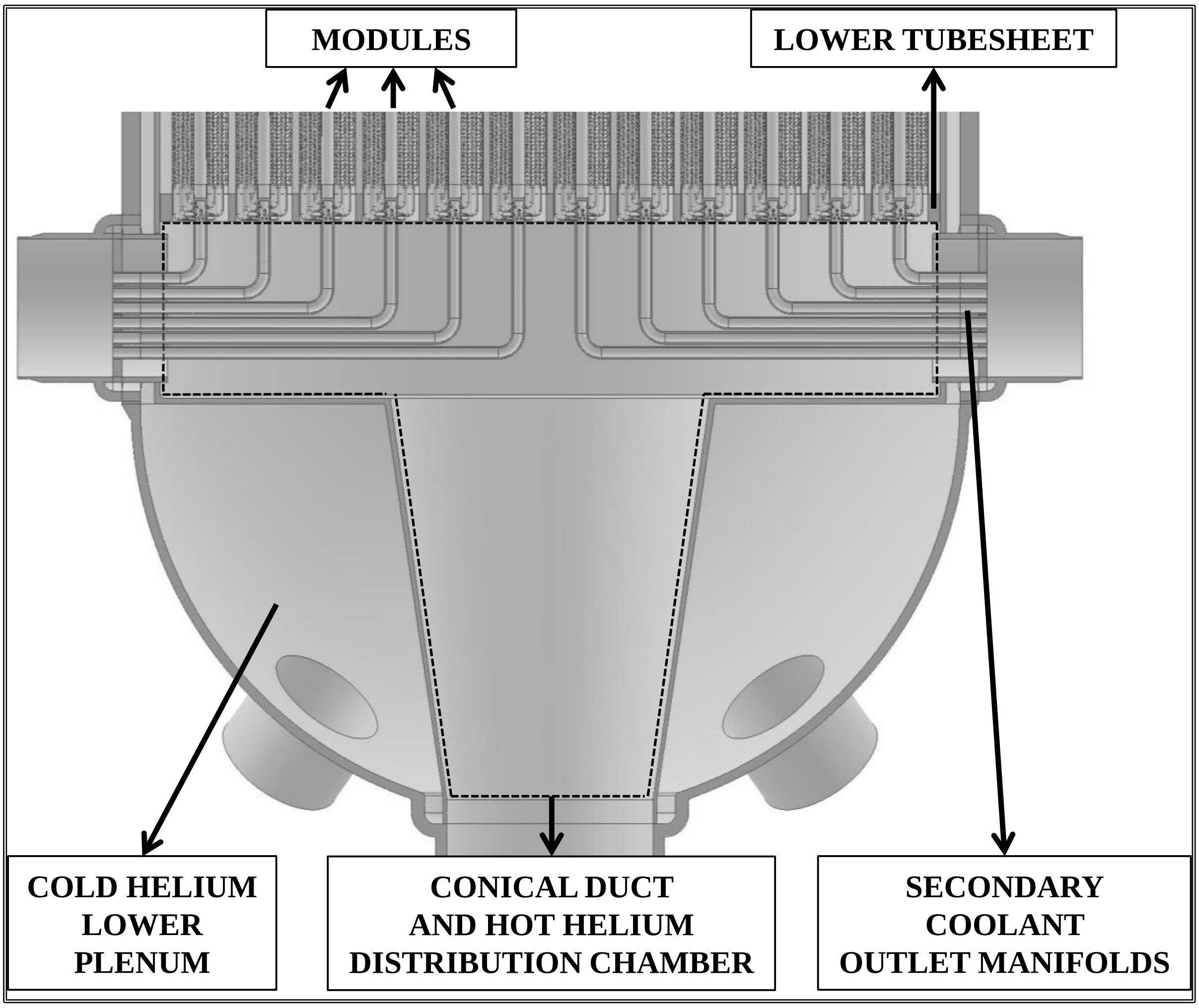

Figure 4.28: Features of the bottom part of the modular-heliacal coil exchanger.

After being cooled down, the helium leaves the modules, moves radially and is turned downward into the annulus between the outer shroud (containing the modules) and the wall of the pressure vessel (see Figure 4.29). Once the gas reaches the lower plenum in the bottom head, it exits from the two cold legs that carry it to the circulator suction (see Figure 4.28).

In the upper head, the cold secondary fluid (molten salt or water) is collected before being distributed among the different modules. The secondary coolant distribution is carried out by means of feeding tubes that penetrate an upper tubesheet that physically separates the upper head from the cylindrical part of the shell. Just below this separating plate, a cluster of 20 tubes comes off from each feeding tube with a form resembling the legs of a spider: from these "legs", the helical tubes bank takes shape running around a central column. The central column of each module is substantially a geometrical extension of the feeding tube that has an end cap immediately after the "spider". The main features above described are depicted in Figure 4.29.

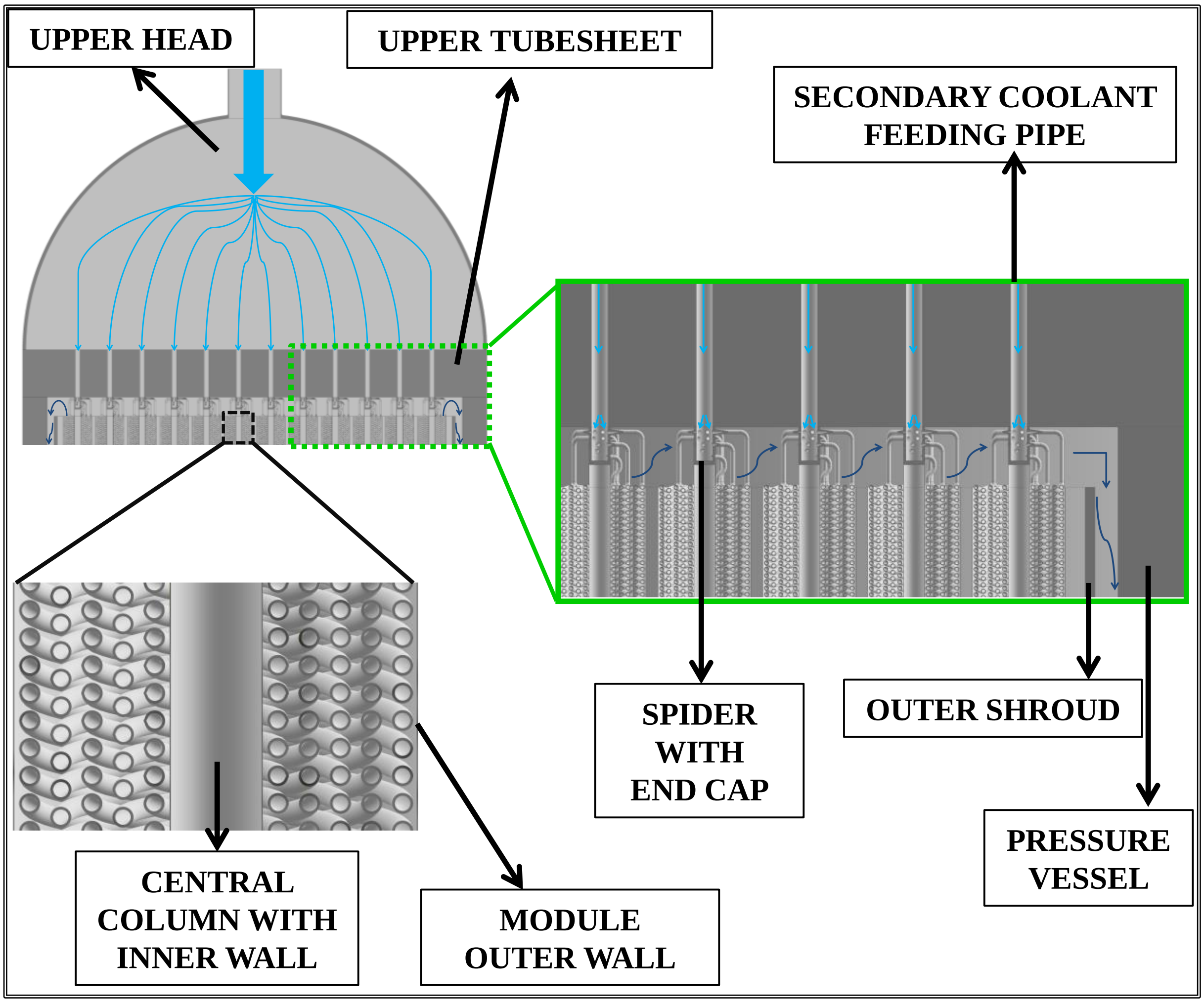

Figure 4.29: Upper part and module bundle features of the modular-helical coil exchanger.

It should be noticed that the same topological features (but with the geometry turned upside down) are used to collect the hot secondary coolant at the bottom of the exchanger from the 20 tubes to the outlet manifolds, see the bundle depicted on left side in Figure 4.27.

It is also worth to remark that, while flowing into the annular downcomer and in the bottom head, the helium keeps the shell at the cold temperature enabling the adoption of the same structural materials used in PWRs for the pressure retaining parts. This possibility is excluded if the straight tube layout is used because, due to its simplicity, that configuration has some zones of the shell which are in contact with the fluids in hot conditions.

This assembled structure calls to mind the arrangement of the steam generator of the HTR-PM reactor, see section 4.2. Such an architecture has been selected because it could make easier the processes of manufacturing and verification as well as the operation and maintenance services. Actually, as one of the main concerns in the construction of the helical coil exchanger is effectiveness of the winding-up operation, which needs a proper machinery to wound the tubes around the central channel, the adoption of small modules containing a few coils is more attractive than having an equivalent exchanger equipped with a single, larger helical bundle. In fact, due to the huge amount of tubes (basically imposed by the DEMO BoP fluid conditions currently selected), in both the IHX and the steam generator configuration there would have been a very large number of concentric layers if a layout similar to those employed in the Superphénix and in the THTR-300 reactors would have been chosen. Furthermore, due to the large variation between the innermost and the outermost coils, the effect of the curvature on the pressure drops, thus on the flow rates distribution, would have been more pronounced with all the tubes wounded around a single central tube.

These reasons have been the main drivers that have led to the preliminary selection of this exchanger architecture and its quantitative assessment.

As regard to the thermal-hydraulic assessment, a subdivision of the calculation domain into several nodes has been pursued to evaluate the total heat transfer surface. To compute the relevant quantities for the helium/HITEC IHX, the same number of nodes applied for the straight bundle configuration has been used, namely fifteen. In this case, the overall heat transfer coefficient experiences larger changes (~20%) however, due to the quasi-linear trend of its reduction in the majority of the exchanger moving from hotter to colder sections, a finer discretization has not implied substantial variations in the total heat transfer surface.

On the other hand, in view of the much more complicated thermal-hydraulic phenomena to be predicted, 56 calculation nodes have been adopted to assess the heating surface of the exchanger when a steam generator type is foreseen. Such a subdivision has allowed to achieve very good agreements in the benchmark calculations that will be described in the paragraph 4.7, hence, an equal number of control volumes have been used in the assessments relevant to DEMO design. Figure 4.30 and Figure 4.31 show the profiles of temperatures and the overall heat transfer coefficient as functions of the exchanger heating surface (in percentage).

The main data obtained are reported from Table 4.16 to Table 4.19.

Table 4.16. Main T/H features of the IHX. Shell and tube option with helical bundle.

	Helium	HITEC
Inlet pressure [MPa]	7.89	0.80
Inlet temperature [°C]	520.0	270.0
Outlet temperature [°C]	291.0	465.0
Mass flow rate [kg/s]	222.2	868.1
Number of tubes (BOL/EOL) [-]	2520	2268
Heat transfer surface (BOL/EOL) [m^2]	7218	6496
Number of modules [-]	126	
Layers per module [-]	5	
Module internal wall diameter [mm]	70.50	
Module external wall diameter [mm]	305.50	
Tube external diameter [mm]	15.875	
Tube transversal pitch [mm]	23.50	
Tube longitudinal pitch [mm]	21.40	
Helix angle [°]	8.25	
Tube thickness [mm]	2.00	
Tube active length [m]	57.4	
Bundle height [m]	8.24	
Tube material [-]	Alloy 800H	
Helium Volume [m^3]	98.1	
HITEC Volume [m^3]	43.7	
Helium mass [t]	0.6	
HITEC mass [t]	79.1	
Mean overall heat transfer coefficient [W/m^{2}K]	1149.6	
Helium ΔP [kPa]	58.3	
HITEC ΔP [kPa]	540.3	

Table 4.17. Additional mechanical data of the IHX. Shell and tube option with helical bundle.

Shell material [-]	SA-508 Gr3 Cl2
Upper tubesheet material [-]	SA-508 Gr3 Cl2 (SS cladding)
Lower tubesheet material [-]	9Cr1Mo-V
Other internals material [-]	9Cr1Mo-V
Overall height [m]	15.1
Shell external diameter (no discontinuities zones) [mm]	4748.0
Shell external diameter (reinforced zones) [mm]	5000.0
Shell thickness (no discontinuities zones) [mm]	104.0
Shell thickness (reinforced zones) [mm]	230.0
Lower head external diameter [mm]	4644.0
Lower head thickness [mm]	52.0
Upper head external diameter [mm]	5000.0
Upper head thickness [mm]	35.0
Shroud external diameter [mm]	4372.0
Shroud thickness [mm]	35.0
Lower tubesheet thickness [mm]	150.0
Upper tubesheet thickness [mm]	570.0
Reinforcement length (at upper tubesheet level) [mm]	1840.0
Hot/cold feeding tube thickness [mm]	8.4
Module pitch [mm]	342.0
Module lattice [-]	Triangular
Total metal mass [ton]	384

Table 4.18. Main T/H features of the modular-helical coil steam generator.

	Helium	Water
Inlet pressure [MPa]	7.89	13.82
Inlet temperature [°C]	520.0	235.4
Outlet temperature [°C]	290.7	480.0
Mass flow rate [kg/s]	222.2	117.3
Number of tubes (BOL/EOL) [-]	840	756
Heat transfer surface (BOL/EOL) [m^2]	4456	4012
Number of modules [-]	42	
Layers per module [-]	5	
Module internal wall diameter [mm]	100.50	
Module external wall diameter [mm]	435.50	
Tube external diameter [mm]	19.05	
Tube transversal pitch [mm]	33.50	
Tube longitudinal pitch [mm]	30.50	
Helix angle [°]	8.24	
Tube thickness [mm]	2.35	
Tube active length [m]	88.7	
Bundle height [m]	12.7	
Tube material [-]	Alloy 800H	
Helium Volume [m^3]	100.4	
Water Volume [m^3]	25.0	
Helium mass [t]	0.6	
Water mass [t]	17.4	
Mean overall heat transfer coefficient [W/m^{2}K]	1544	
Helium ΔP [kPa]	68.9	
Water ΔP [kPa]	335.5	

Table 4.19. Additional mechanical data of the modular-helical coil steam generator.

Shell material [-]	SA-508 Gr3 Cl2
Upper tubesheet material [-]	SA-508 Gr3 Cl2 (SS cladding)
Lower tubesheet material [-]	9Cr1Mo-V
Other internals material [-]	9Cr1Mo-V
Overall height [m]	18.6
Shell external diameter (no discontinuities zones) [mm]	4110.0
Shell external diameter (reinforced zones) [mm]	4350.0
Shell thickness (no discontinuities zones) [mm]	90.0
Shell thickness (reinforced zones) [mm]	210.0
Lower head external diameter [mm]	4020.0
Lower head thickness [mm]	45.0
Upper head external diameter [mm]	4350.0
Upper head thickness [mm]	245.0
Shroud external diameter [mm]	3745.0
Shroud thickness [mm]	35.0
Lower tubesheet thickness [mm]	140.0
Upper tubesheet thickness [mm]	510.0
Reinforcement length (at upper tubesheet level.) [mm]	1636.0
Hot/cold feeding tube thickness [mm]	12.0
Module pitch [mm]	486.0
Module lattice [-]	Triangular
Total metal mass [ton]	308

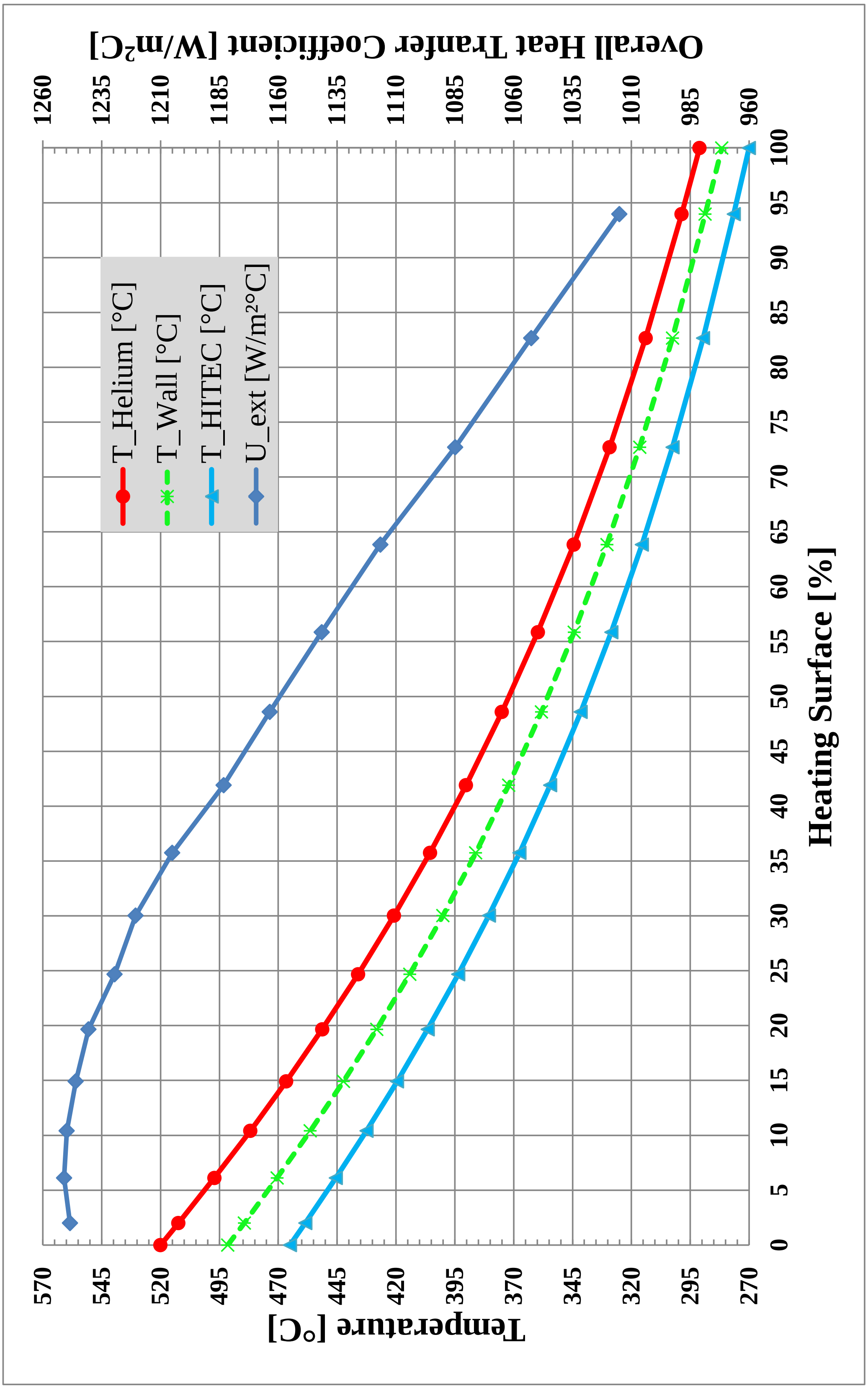

Figure 4.30: Profiles of temperatures and overall HTC in modular helical coil IHX.

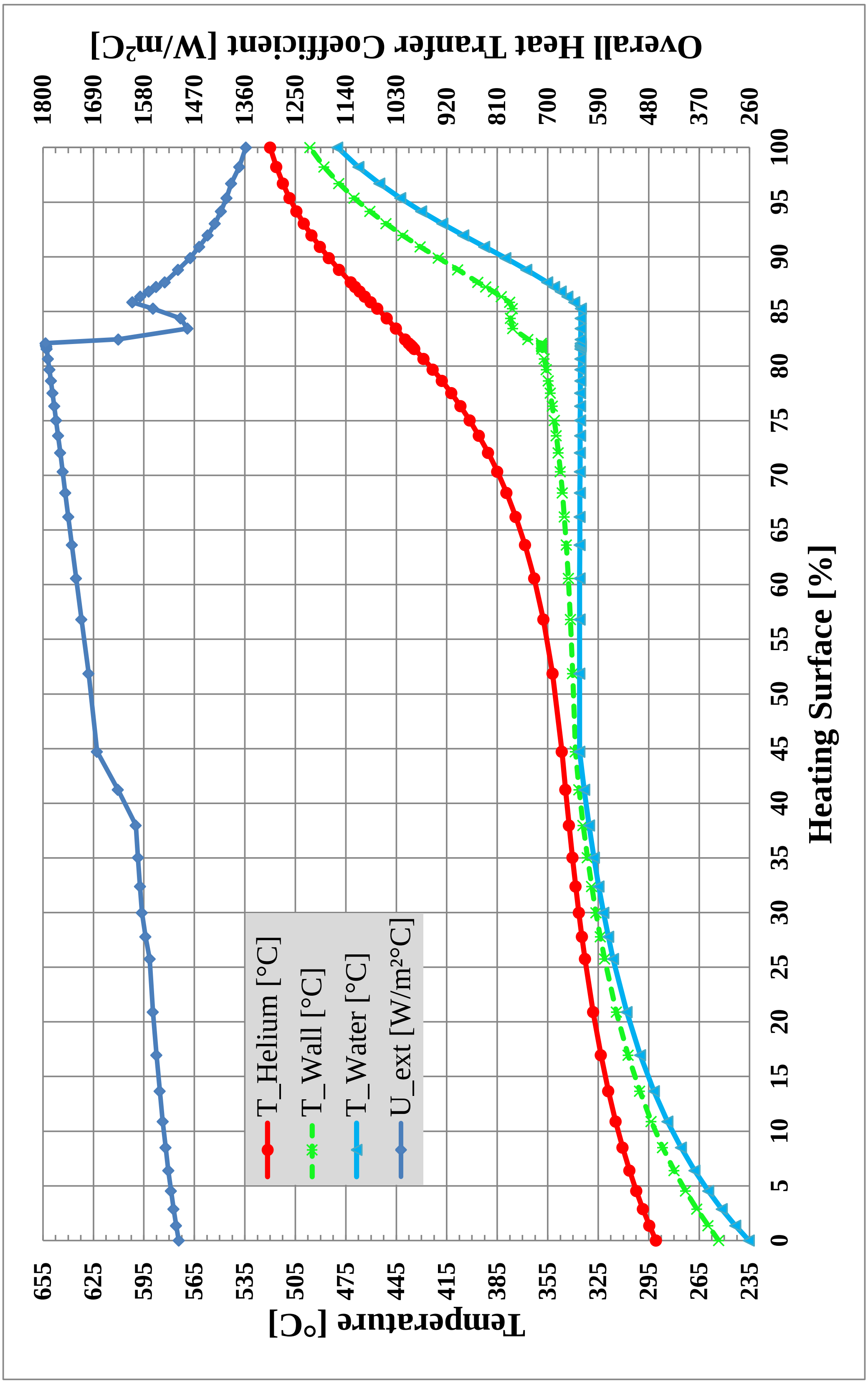

Figure 4.31: Profiles of temperatures and overall HTC in modular helical coil SG.

4.6 Assessment of the main thermal-hydraulic design uncertainties

The assessment of the probable range of error associated with the design calculations is often referred as the analysis of uncertainties. Since the fundamental output variable related to the thermal-hydraulic design of the heat exchanger is the heat transfer surface, a preliminary uncertainty study has been limited to this quantity.

The uncertainty in predicting heat transfer area might be defined as the statistical difference between estimated value and true value.

In principle, every variable involved in the design assessments can be source of uncertainty, from the correlations to calculate the thermo-physical properties of the materials, to the constitutive relationships adopted in the simplified forms of the conservative equations. The uncertainties on the material properties are often quite lower than those associated with heat transfer models, so that the predominant terms of errors are those connected to the latter correlations.

Nevertheless, when properties of coolants and structural materials are affected by a non-negligible uncertainty, they can play a role in the propagation of errors, therefore their evaluation has been usually taken into account.

Usually, in the uncertainty analysis, it is assumed that the individual errors have an equal probability of being positive or negative and, further, that the probability density function describing the uncertainty is normally distributed. This is mainly done for three reasons: first, these assumptions simplify the mathematical manipulations required; second, the existing knowledge regarding the uncertainty of the various errors does not allow a more sophisticated treatment; and finally, this allows convenient expression of the results [177].

A rigorous treatment of the statistical theory behind the uncertainty analysis is far beyond the purpose of this work, hence no attempt will be made to explain the mathematical and physical meaning of the different quantities that will be presented in the following. Further information about the topic can be found in several statistical textbook such as [178].

In general, assumed f to be a function of n statistically independent variables so that:

$$f = (\mathrm{x}_1, \mathrm{x}_2, \ldots, \mathrm{x}_\mathrm{j}, \ldots, \mathrm{x}_\mathrm{n}) \tag{86}$$

a mean value $\bar{\mathrm{x}}_\mathrm{j}$ and a standard deviation σ_j can be related to each of these random variables.

It can be demonstrated that the standard deviation of the function f can be estimated by means of the propagation formula of the standard deviations:

$$\sigma_f^2 = \sum_{\mathrm{j}=1}^{\mathrm{n}} \left(\frac{\partial f}{\partial \mathrm{x}_\mathrm{j}} \right)^2 \sigma_\mathrm{j}^2 \tag{87}$$

When the sample taken under consideration can provide a only a small statistic, the evaluation of the uncertainties due to the propagation of errors can be computed according to the following expression:

$$\Delta f^2 = \sum_{j=1}^{n} \left(\frac{\partial f}{\partial x_j} \right)^2 \Delta x_j^2 \tag{88}$$

The formula (88) for the uncertainty propagation, strictly speaking, is not exact as for the propagation of the standard deviations, however it is very practical and often gives values very close to the exact results [178].

Combining the equations (18) and (19) described in the paragraph 4.3, the external heat transfer area can be computed as:

$$S_e = \frac{\dot{Q}}{\Delta T_{LM}} R_{ov} \tag{89}$$

where R_{ov} is the overall thermal resistance (i.e. the inverse of the overall heat transfer coefficient) referred to the external heat transfer surface.

As the overall thermal resistance is the sum of the different thermal resistances associated with the two coolants, both primary and secondary, the tube wall and (eventually) the fouling factors, we can write:

$$R_{ov} = R_{He} + R_{foul_i} + R_{wall} + R_{foul_e} + R_{MS/H_2O} \tag{90}$$

In the hypotheses that:

- the thermal power as well as the temperatures of the fluids are not affected by uncertainties, being the fixed design values;
- the different thermal resistances have a very weak interdependence to one another, so that the any correlation between them can be neglected (at least as first approximation);

the uncertainty on the heat transfer surface can be calculated as:

$$\Delta S_e = \sqrt{\sum_{j=1}^{5} \left(\frac{\partial S_e}{\partial R_j} \right)^2 \Delta R_j^2} \tag{91}$$

Then, defining the relative uncertainty ε_x of a generic variable x as the ratio between the absolute uncertainty, Δx, and the mean (predicted) value, $\bar{x}$, so that:

$$\varepsilon_x = \frac{\Delta x}{\bar{x}} \tag{92}$$

with a proper manipulation of the equation (91), using the definition above, it follows that:

$$\varepsilon_{S_e} = \sqrt{\sum_{j=1}^{5} \left(\frac{R_j}{R_{ov}} \right)^2 \left(\frac{\partial S_e}{\partial R_j} \right)^2 \varepsilon_{R_j}^2} \tag{93}$$

where, according to the second hypothesis just stated, all the partial derivatives are equal to 1.

Therefore, expanding all the terms under the square root, the equation (93) can be rewritten as:

$$\varepsilon_{S_e} = \sqrt{\begin{aligned}&\left(\frac{R_{He}}{R_{ov}}\right)^2 \varepsilon^2_{R_{He}} + \left(\frac{R_{foul_i}}{R_{ov}}\right)^2 \varepsilon^2_{R_{foul_i}} + \left(\frac{R_{Wall}}{R_{ov}}\right)^2 \varepsilon^2_{R_{Wall}} + \\ &+ \left(\frac{R_{foul_e}}{R_{ov}}\right)^2 \varepsilon^2_{R_{foul_e}} + \left(\frac{R_{MS/H_2O}}{R_{ov}}\right)^2 \varepsilon^2_{R_{MS/H_2O}}\end{aligned}} \quad (94)$$

From the equation (94) it can be seen that the relative error associated with the heat transfer surface is weighted on the squares of the ratios between the individual thermal resistances and the overall one. This implies that:

- the overall relative uncertainty will tend to the individual relative error connected to the predominant thermal resistance;
- the relative error on the heat transfer surface/overall thermal resistance might be smaller than each relative error on the individual thermal resistance.

Although the first achievement might have been intuitively anticipated, the second achievement takes a while to be absorbed because, at a first glance, one may have naively thought that the overall relative uncertainty on the heat transfer surface would have been at least as large as the minimum among the individual relative errors.

However, it is worth to highlight that, in absolute terms, the error on the overall thermal resistance will be larger than each individual absolute error due to the propagation of the uncertainty.

Considering the equation (94) and the hypotheses upon which is grounded, each of the relative errors related to the individual thermal resistance can be independently estimated and, then, used in the equation.

In particular, to evaluate the uncertainties due to the thermal resistance of the coolants (errors on the heat transfer coefficients), it has been necessary to account not only for the uncertainties associated to the heat transfer models but also for the uncertainties on the fluid properties. Indeed, being the heat transfer constitutive laws dependent on the Reynolds and the Prandtl numbers, they are intrinsically related to the characteristics of the medium, thus any uncertainty on the thermo-physical quantities will be propagated to the heat transfer correlation.

Therefore, considering negligible the uncertainty on the geometrical data (no errors on the tube diameter) and single-phase heat transfer only, the uncertainties connected to thermal resistances of the coolants can be reduced as function of 4 independent variables, so that:

$$\Delta R_{coolant} = f\left(k_{coolant}, \mu_{coolant}, c_{p_{coolant}}, Nu\right) \quad (95)$$

It should be underlined that the thermal resistance of the coolant is basically the reciprocal of the heat transfer coefficient, hence the associated relative error will be the same whether it refers to the thermal resistance or its reciprocal. Since the heat transfer models are usually presented in form which is practical to evaluate the heat transfer coefficient, in the following the assessments will be referred to the relative uncertainties associated with this more familiar quantity, instead of its inverse value.

As done before, exploiting the equation (88) and the definition (92), it is possible to write a general expression to assess the relative error associated with the heat transfer coefficients:

$$\varepsilon_h = \sqrt{\left(\frac{\mathrm{k}}{h}\right)^2 \left(\frac{\partial h}{\partial \mathrm{k}}\right)^2 \varepsilon_{\mathrm{k}}^2 + \left(\frac{\mathrm{c_p}}{h}\right)^2 \left(\frac{\partial h}{\partial \mathrm{c_p}}\right)^2 \varepsilon_{\mathrm{c_p}}^2 + \left(\frac{\mu}{h}\right)^2 \left(\frac{\partial h}{\partial \mu}\right)^2 \varepsilon_{\mu}^2 + \left(\frac{\mathrm{Nu}}{h}\right)^2 \left(\frac{\partial h}{\partial \mathrm{Nu}}\right)^2 \varepsilon_{\mathrm{Nu}}^2} \tag{96}$$

Taking into account the relationship between the heat transfer coefficient and the typical expressions for the Nusselt number used in this work, the first three terms multiplying the relative errors related to the coolant properties are, in general, different from 1. On the contrary, the last term involving also the partial derivative of the function respect to Nusselt will be 1.

Therefore, the equation (96) can be rewritten in this simplified form:

$$\varepsilon_h = \sqrt{\mathrm{A}_{\mathrm{k}}^2 \varepsilon_{\mathrm{k}}^2 + \mathrm{A}_{\mathrm{c_p}}^2 \varepsilon_{\mathrm{c_p}}^2 + \mathrm{A}_{\mu}^2 \varepsilon_{\mu}^2 + \varepsilon_{\mathrm{Nu}}^2} \tag{97}$$

with the coefficients $\mathrm{A}_{\mathrm{k}}^2$, $\mathrm{A}_{\mathrm{c_p}}^2$, A_{μ}^2 to be evaluated according to the specific heat transfer model employed.

In particular, as discussed in the previous paragraphs, in both intermediate heat exchanger and steam generator calculations, the correlations adopted on the tube-side for single-phase flow are those suggested by *Gnielinski*. Despite the minor adjustments proposed by the author himself to modify his basic correlation when the tube type changes from straight to helical, the *Gnielinski*'s correlations share the main functional form which has facilitate the evaluation of the uncertainties on the tube side for single-phase heat transfer.

On the shell side, the correlations adopted are from different authors, however also in case the all the models can be brought back to a general form which maintains a common imprinting. In fact, the main structure of these heat transfer correlations might be written as follow:

$$\mathrm{Nu} = \mathrm{C}\,\mathrm{Re}^{\mathrm{b}}\,\mathrm{Pr}^{\mathrm{e}} \tag{98}$$

with C, b and e depending on the specific correlation.

Through the adoption of this general notation, it has been possible to compute a general symbolic form of the partial derivatives, then, according to the specific heat exchanger typology, the specific coefficients C, b and e have been substituted in the equations, thus allowing the calculation of the associated value of A_k^2, $A_{c_p}^2$, A_μ^2.

A different approach has been used for the two-phase heat transfer correlation, where the only term which has been considered in the uncertainty evaluation is that related to the correlation itself, neglecting the effects due to uncertainties on fluid properties. Although the *Steiner-Taborek* correlation involves a larger number of thermo-physical properties hence, in principle, higher uncertainties might be expected due to the propagation of the errors, it should be considered that the uncertainties related to the water properties are very small. In fact, as can be seen from the Table 4.20, for the single phase heat transfer models the relative error is almost coincident with the relative error of the correlation itself. Furthermore, taking into account that the uncertainty related to the two-phase heat transfer correlations is quite higher than those associated with single phase models, the assumption that the error caused by the correlation will play the dominant role has seemed well-grounded.

As regard to the relative errors related to the thermal resistance of the tube wall, it can be estimated as follow:

$$\varepsilon_{R_{wall}} = \sqrt{\left(\frac{k_{wall}}{R_{wall}}\right)^2 \left(\frac{\partial R_{wall}}{\partial k_{wall}}\right)^2 \varepsilon_{k_{wall}}^2} \tag{99}$$

Considering the functional dependence of this resistance from the wall conductivity (see equation (18)), it can be immediately written that:

$$\varepsilon_{R_{wall}} = \varepsilon_{k_{wall}} \tag{100}$$

Finally, concerning the relative uncertainty associated with the fouling factor, its value is independent of other variables, therefore it will be directly estimated from data available in literature or based on engineering judgement.

In agreement with the hypotheses, the equations described above, and the uncertainty data collected from literature for the different quantities involves in the calculation, the evaluation of the relative errors associated with the heat transfer surface of the different exchangers has been carried out.

Table 4.20 reports the uncertainty values used in this preliminary assessment.

It is worth to highlight that in comparison to helium and water, the properties of the molten salts are affected by a much higher uncertainties. In particular, the thermal conductivity data show dispersion around an average value [179], which is in any case different from that suggested by the Coastal Chemical Co [73] and adopted in this thesis. For this reasons, a conservative uncertainty of 20% has been assumed considering that measurements for the molten salt thermal conductivity can often show uncertainties in a range of 15÷20% [179].

The uncertainty associated to the fouling factor has been set to 50% following a conservative approach suggested in [180].

Results for the two intermediate heat exchanger configurations and the steam generator design are reported from Table 4.21 to Table 4.23.

As previously anticipated, the relative error associated with the total heat transfer surface is smaller than the individual relative errors related to the thermal resistances. This preliminary assessment shows encouraging results because, as can be seen from the last row of each table, the uncertainty on the estimated heat transfer area is all cases below 11%, which can be considered very satisfactory at this early stage of the design.

Table 4.20. Uncertainties values.

Quantity	**Unit**	**Helium** [54]	**Water** [56]	**HITEC** [179]
Density	%	$0.03\sqrt{p}$	0.05	2
Specific Heat capacity	%	0.02	0.3	5
Thermal conductivity	%	$3.5 \cdot 10^{-3} T$	2	20
Dynamic viscosity	%	$1.5 \cdot 10^{-3} T$	2	4
Tube wall thermal conductivity [139]	%	10		
Gnielinski model (straight tube) [150]	%	8		
Gnielinski model (helical tube) [155]	%	15		
Grimison model (cross-flow) [121]	%	15		
Bell-Delaware model (cross-flow) [91]	%	15		
Steiner-Taborek model (two-phase) [156]	%	30		
Fouling [180]	%	50		

Table 4.21. Heat transfer area uncertainty in IHX with straight bundle configuration.

Quantity	**Unit**	**Tube side**	**Shell side**
$A_{c_p}^2$	-	1.74	$7.29 \cdot 10^{-2}$
A_k^2	-	2.38	$4.1 \cdot 10^{-1}$
A_μ^2	-	1.74	$7.29 \cdot 10^{-2}$
ε_h tube side	%	9.0	
ε_h shell side	%	19.8	
ε_{S_e}	%	8.9	

Table 4.22. Heat transfer area uncertainty in IHX with helical bundle configuration.

Quantity	**Unit**	**Tube side**	**Shell side**
$A_{c_p}^2$	-	$4.4 \cdot 10^{-1}$	$7.7 \cdot 10^{-2}$
A_k^2	-	$5.7 \cdot 10^{-1}$	$4.4 \cdot 10^{-1}$
A_μ^2	-	$4.4 \cdot 10^{-1}$	$7.7 \cdot 10^{-2}$
ε_h tube side	%	21.7	
ε_h shell side	%	15.1	
ε_{S_e}	%	10.8	

Table 4.23. Heat transfer area uncertainty in modular helical coil Steam Generator.

Quantity	**Unit**	**Tube side**	**Shell side**
$A_{c_p}^2$ superheater	-	$5.5 \cdot 10^{-1}$	$7.7 \cdot 10^{-2}$
A_k^2 superheater	-	$8.1 \cdot 10^{-1}$	$4.4 \cdot 10^{-1}$
A_μ^2 superheater	-	$5.5 \cdot 10^{-1}$	$7.7 \cdot 10^{-2}$
$A_{c_p}^2$ boiler	-	0	$7.7 \cdot 10^{-2}$
A_k^2 boiler	-	0	$4.4 \cdot 10^{-1}$
A_μ^2 boiler	-	0	$7.7 \cdot 10^{-2}$
$A_{c_p}^2$ economizer	-	$2.7 \cdot 10^{-1}$	$7.7 \cdot 10^{-2}$
A_k^2 economizer	-	1.0	$4.4 \cdot 10^{-1}$
A_μ^2 economizer	-	$2.7 \cdot 10^{-1}$	$7.7 \cdot 10^{-2}$
ε_h tube side - superheater	%	15.2	
ε_h shell side - superheater	%	15.1	
ε_h tube side – boiler	%	30	
ε_h shell side – boiler	%	15.1	
ε_h tube side – economizer	%	15.2	
ε_h shell side – economizer	%	15.2	
ε_{S_e}	%	6.0	

4.7 Benchmarking of the thermal-hydraulic design methodology

To check the efficacy of the design methodology, procedures and models, a numerical benchmark of the developed tool has been performed. Although the thermal-hydraulic assessments have been done for both intermediate heat exchanger and steam generator, it has been judged that to have an global view of the tool capabilities, the verification through a comparison of a helium-heated steam generator design would have been sufficient. In fact, regardless the clear difficulties in finding data for an helium/molten salt heat exchangers (basically they do not exist), a thermal-hydraulic assessment of a exchanger where a fluid phase transition occurs is much more critical and challenging. Furthermore, it should be remarked that a helium/molten salt exchanger experiences just single-phase to single-phase heat transfer, which is a subcategory of the possible heat transfer modes already included in those proper of a helium-heated steam generator. Specifically, here there are both economizer and superheater that see gas/liquid and gas/gas heat transfer, respectively.

The verification has been performed on the THTR-300 steam generator, see Figure 4.12 in section 4.2. In particular, the geometrical data have been collected from [110] and [178] while the design calculations as well as the experimental values available have been found in [179]. The test has been led following the steps described in [179], where the owner of the power plant present their numerical calculations performed during the reactor commissioning phases to verify the predictability of computer programs developed for the design of the heat exchanger surfaces. At that time, the validation was made using the temperature measurements as well as the rest of the operating instrumentation to provide the input parameters to the codes. In addition, calculations did not consider the re-heater section because it was not part of the main helical bundle.

Taking the opportunity of benchmarking the tool developed for the DEMO design against both experimental and design values, the choice has immediately fallen on this exchanger.

The main geometrical data and the input conditions are reported in Table 4.24, while the results of the runs are reported in Table 4.25. Temperature profiles are plotted from Figure 4.32 to Figure 4.34, where they are compared with the experimental measurements. The design calculations made by the steam generator constructors are shown as well. Errors are relative to the experimental data. The calculation domain has been subdivided in 56 nodes.

Despite all the geometrical data of the exchanger were known, the fouling factor adopted for design calculations was not available. Therefore, as this parameter could have played an important role in the temperature profiles as well as in calculation of heat transfer surface, it has been decided to make three different assessments varying the fouling resistance on the water side. The value considered have been 0, 2.5E-5 and 5E-5 m^2K/W, being the first a sort of “best estimate” assumption, whereas the others two reasonable assumptions for the design calculations. They have been referred as Case 1, Case 2 and Case 3, respectively.

Generally, predictions coincide very well with the measurements and the design calculations, the measured temperatures being slightly below both calculated and design values. Furthermore, very good conformity is achieved for heat transfer area and helium pressure drops. The effects of the fouling factor on the mean wall temperatures can be catch from the graphs. Indeed, in case of no fouling condition, results more flattened to the water profile than in the design data. On the contrary, for the maximum fouling factor the calculated wall temperature results hardly higher than in the design data, especially in the zone of the departure of nucleate boiling. Nevertheless, the temperature discrepancies are usually less than 1% with a maximum difference of about 2%. The errors on calculated heat transfer area are within ~4% in all three cases, the Case 2 being almost coincident with the actual surface. Agreements can be found in the pressure drops too, despite they are slightly underestimated.

Table 4.24 Geometrical data and input boundary condition for the benchmark [178] [179].

	Helium	Water
Inlet pressure [MPa]	3.85	21.8
Inlet temperature (exp.) [°C]	665.0	183.9
Outlet temperature (exp.) [°C]	246.6	557.0
Mass flow rate [kg/s]	49.36	40.99
Number of tubes [-]	80	
Tube external diameter [mm]	25	
Tube longitudinal pitch [mm]	36	
Tube transversal pitch [mm]	38.33	
Tube thicknesses (from cold to hot parts) [mm]	2.6 to 5.0	
S_{ext} [m^2]	1190.85	

Table 4.25. Output results [179].

	Exp.	Design	Case 1	Case 2	Case 3
S_{ext} [m^2]	1190.85		1139.85	1191.33	1243.14
Helium Pressure Drop [kPa]	33.77	37.1	29.53	30.89	32.27
S_{ext} [Error %]	-	-	-4.28	0.04	4.39
Gas pressure Drop [Error %]	-	9.86	-12.56	-8.53	-4.43

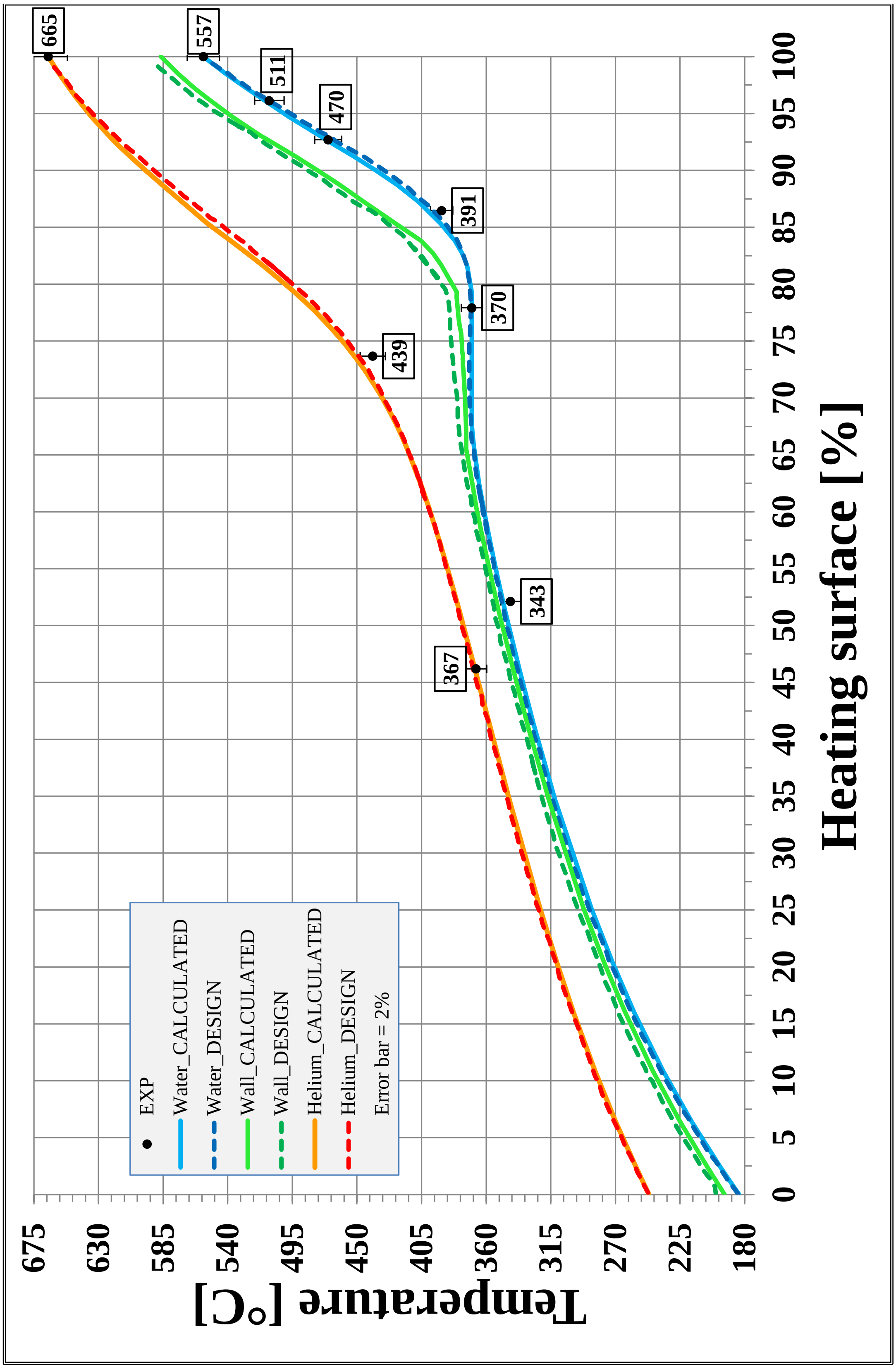

Figure 4.32. Temp. profiles of THTR-300 SG: exp., design and calculated values; Case 1.

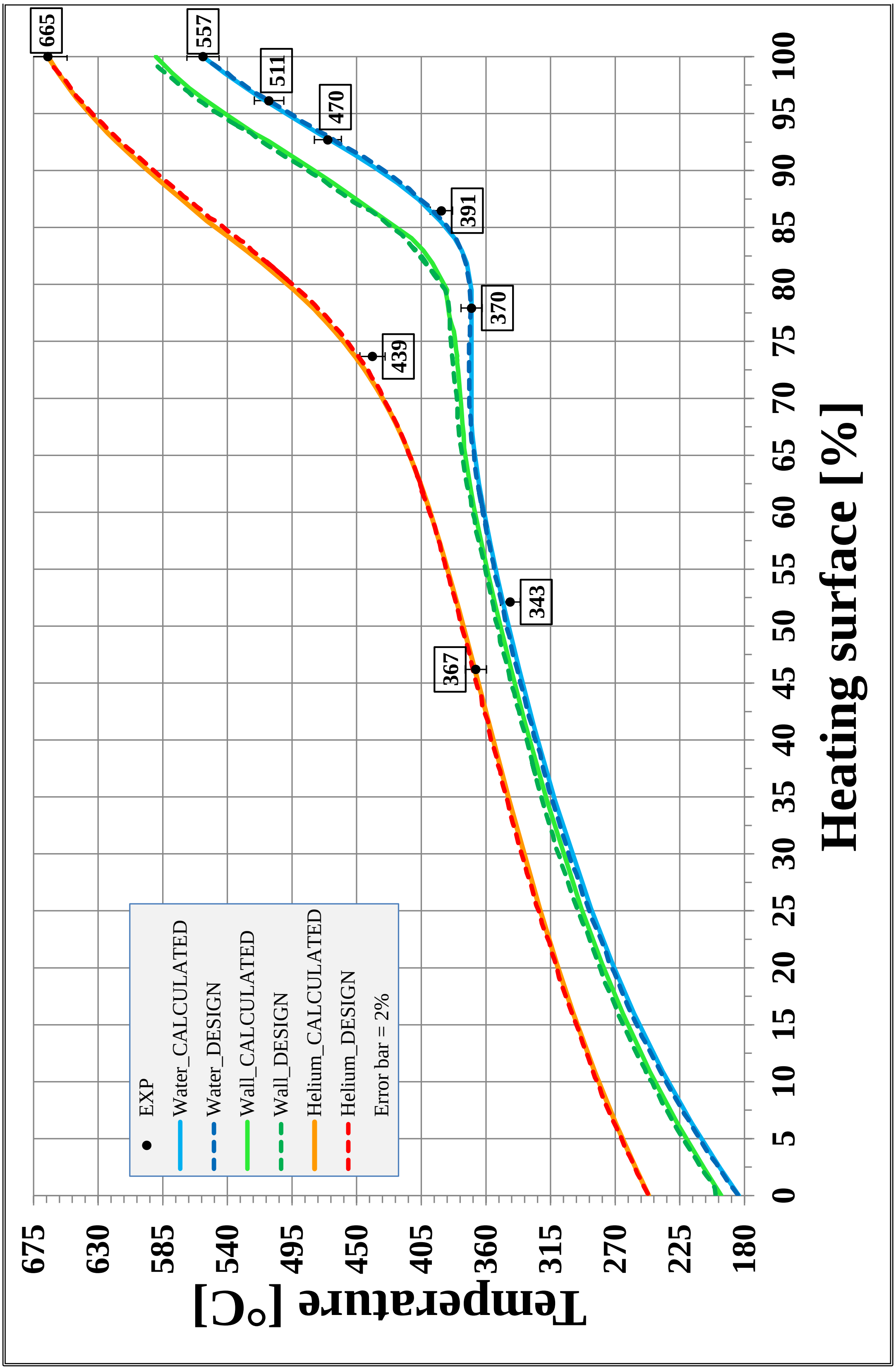

Figure 4.33. Temp. profiles of THTR-300 SG: exp., design and calculated values; Case 2.

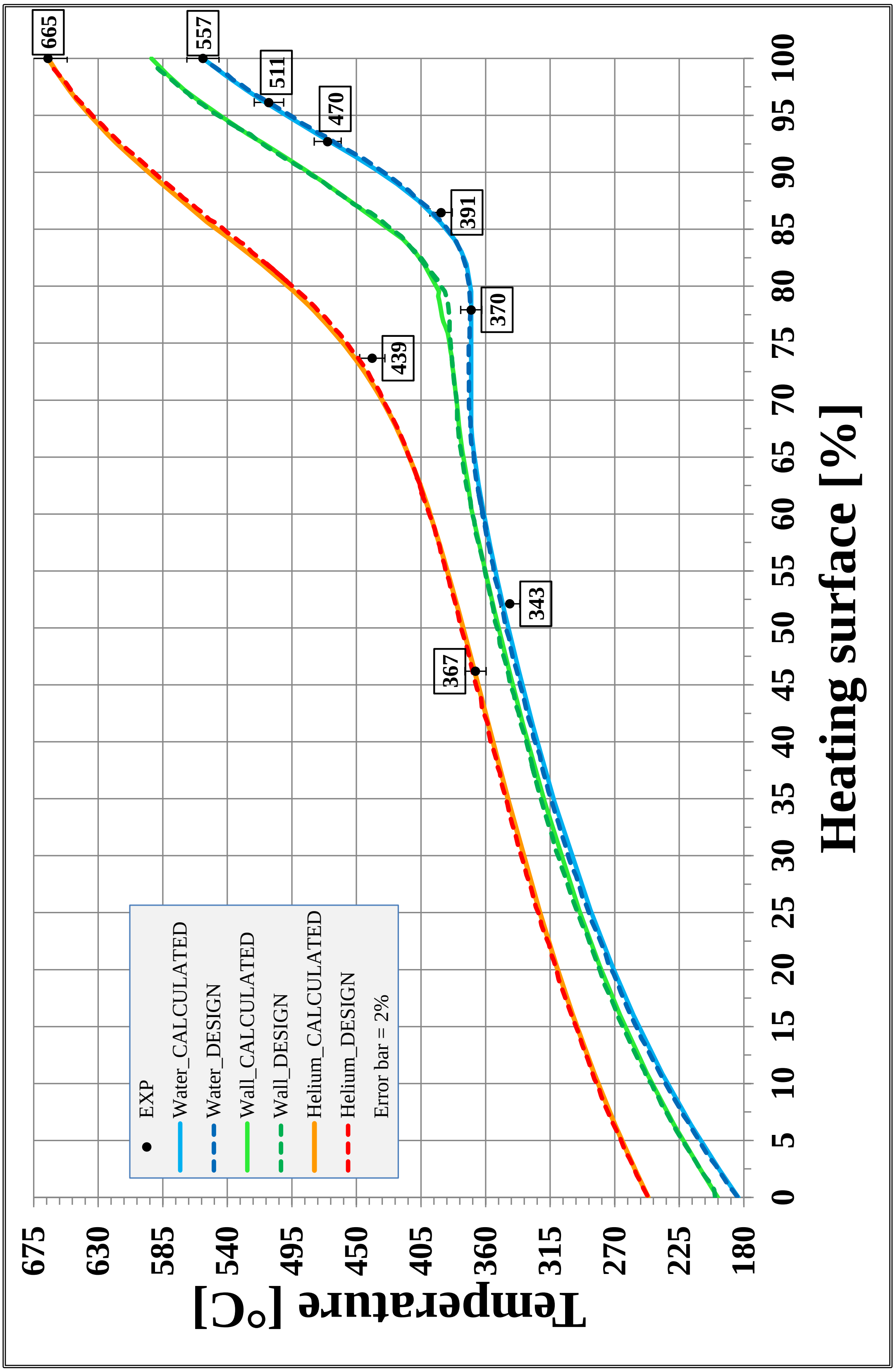

Figure 4.34. Temp. profiles of THTR-300 SG: exp., design and calculated values; Case 3.

4.8 Preliminary mechanical design of the exchanger

A preliminary assessment of the principal pressure retaining elements of the two exchanger configurations has been made. In particular, the thicknesses of the shell parts and the plates have been evaluated by means of the rules and the guidelines reported in the different sections of ASME Boiler and Pressure Vessel Code (BPVC), namely section III [145] [180] and section VIII [147], as well as in some textbooks related to this topic [181] [183].

Actually, the construction rules for the equipment employed in nuclear reactors are only reported in the section III of the ASME BPVC, however some parts of the exchangers have been preliminary sized following the ASME VIII rules because, often, the section III does not provide practical design equations for a first dimensioning of the main parts of a given component [182]. Although the ASME III code provides all those criteria of acceptance for the mechanical and thermal design of a nuclear system, they are generally applied according to the "design by analysis" approach. This method is usually pursued by means of suitable codes, developed with the aim of solving the elasticity problem via the numerical determination of stress, strain and displacement fields. Such codes (for ABAQUS or ANSYS Mechanical) adopt a finite element method to numerically assess the above quantities.

A detailed assessment made through a similar methodology has been judged beyond the scope of this work, therefore it has been preferred to exploit the methods described in those sections of the ASME BPVC that apply a "design by rules" approach, being confident that results obtained in such a way might give enough indications for a preliminary mechanical design of the component. As a matter of fact, is worth to point out that the ASME BPVC III itself provides some rules intended "*as an aid to the designer for determining a tentative thickness for use in the design*", although it also warns that the given relations "*are not to be construed as equations for acceptable thicknesses*" because, in principle, they do not exempt the user to check the thickness according to the "design by analysis" rules [145].

Nevertheless, the approach adopted in this work has meant to determine the preliminary thicknesses within the main elements of the exchanger following good engineering practices or, in other words, it can be seen as the first attempt to define a reasonable sizing of the component before starting a deeper investigation via the tools which are in need dedicated.

Table 4.26 shows pressures and temperatures employed as reference for design purposes.

Table 4.26. Design pressures and temperatures for primary and secondary circuits.

	Helium	HITEC	Water
Design pressure [MPa]	9.2	2.0	15.6
Design temperature in cold part [°C]	375.0	375.0	375.0
Design temperature in hot part [°C]	525.0	500.0	500.0

The main mechanical properties of the materials, in the range of temperatures relevant to the design, are reported from Table 4.27 to Table 4.30. Data is collected from [140] and [180].

Table 4.27. Mechanical properties of austenitic stainless steel 316L.

	Temperature [°C]								
	350	375	400	425	450	475	500	525	550
S_m [MPa]	114	112	111	110	108	108	107	101	88
S_y [MPa]	127	125	123	122	121	120	118	117	116
E [GPa]	172		169		165		160		156
ν [-]	0.31								
α [mm/mm°C]	17.9	18	18.1	18.2	18.3	18.4	18.4	18.5	18.6

Table 4.28. Mechanical properties of Alloy 800H.

	Temperature [°C]								
	350	375	400	425	450	475	500	525	550
S_m [MPa]	110	108	105	105	104	103	101	99	89
S_y [MPa]	123	120	118	115	113	112	110	108	108
E [GPa]	179		176		173		170		167
ν [-]	0.31								
α [mm/mm°C]	16.4	16.5	16.5	16.6	16.7	16.8	16.8	16.9	17

Table 4.29. Mechanical properties of low alloy steel 9Cr1Mo-V.

	Temperature [°C]								
	350	375	400	425	450	475	500	525	550
S_m [MPa]	187	184	178	172	165	154	133	117	102
S_y [MPa]	371	366	358	348	337	322	306	288	269
E [GPa]	191		187		183		179		174
ν [-]	0.3								
α [mm/mm°C]	11.9	11.9	12	12.1	12.2	12.3	12.3	12.4	12.5

Table 4.30. Mechanical properties of low alloy steel SA-508 Gr3 Cl2.

	Temperature [°C]								
	350	375	400	425	450	475	500	525	550
S_m [MPa]	207	207	Not allowable under nominal condition						
S_y [MPa]	370	364	357	347	335	319	298	270	250
E [GPa]	171		167		163		158		153
ν [-]	0.3								
α [mm/mm°C]	13.6	13.7	13.8	14	14.1	14.2	14.4	14.5	14.6

4.8.1 Heat exchanger parts under internal and external pressures

In accordance with the above preconditions, being the circular and spherical products the elements which cover the majority of the exchanger geometry, a suitable set of equations to assess the minimum required thicknesses for these components has been identified and drawn from the pertaining parts of the ASME code.

The relations used to deal with the main elements of the exchangers, when they are under internal and/or external pressure loads, are reported in the following.

In particular, for the cylindrical and spherical shell parts subjected to internal pressure and far from discontinuities, equations of the same kind of the (42) have been employed:

$$\begin{cases} \text{Cylindrical shell} \\ t_{min} = \dfrac{p_{design} D_i}{2\left(S_m - 0.5 p_{design}\right)} + A \quad \text{or} \quad t_{min} = \dfrac{p_{design} D_e}{2\left(S_m + 0.5 p_{design}\right)} + A \\ \text{Spherical shell} \\ t_{min} = \dfrac{p_{design} D_i}{2\left(2S_m - p_{design}\right)} + A \quad \text{or} \quad t_{min} = \dfrac{p_{design} D_e}{4S_m} + A \end{cases} \tag{101}$$

with the quantities having the same meaning of those described in the subsection 4.4.2.1.

A corrosion allowance of 0.1 mm has been used in those parts in contact with molten salt or water, whereas no corrosion has been considered on the primary side.

For the cylindrical shell parts subjected to external pressure, according to ASME rules, the assessment of the minimum thickness requires the calculation of some quantities which evaluation has to be performed either through charts or by reading the values in tabular form. Furthermore, the procedure to define the maximum allowable external pressure is iterative. For sake of brevity, a summary of the method applied is reported below. The interested reader can find all the details elsewhere [140] [145].

$$
\left\{
\begin{array}{l}
\text{if} \quad \dfrac{\mathrm{D_e}}{\mathrm{t_{min}}} > 10 \\
\text{calculate the ratios} \\
\dfrac{\mathrm{D_e}}{\mathrm{t_{min}}} \quad \text{and} \quad \dfrac{\mathrm{L_o}}{\mathrm{D_e}} \\
\text{then, evaluate} \\
A = \mathrm{f}\left(\dfrac{\mathrm{D_e}}{\mathrm{t_{min}}}, \dfrac{\mathrm{L_o}}{\mathrm{D_e}}\right) \\
B = \mathrm{f}\left(A, \mathrm{T}\right) \\
\text{calculate the maximum allowable pressure } \mathrm{p_a} \\
\text{either } \mathrm{p_a} = \dfrac{4B}{3\left(\dfrac{\mathrm{D_e}}{\mathrm{t_{min}}}\right)} \quad \text{or} \quad \mathrm{p_a} = \dfrac{4A\mathrm{E}}{3\left(\dfrac{\mathrm{D_e}}{\mathrm{t_{min}}}\right)} \\
\text{depending on } A \\
\text{if} \quad 4 < \dfrac{\mathrm{D_e}}{\mathrm{t_{min}}} < 10 \\
\text{procede as above but} \\
\mathrm{p_a} = \min\left[\left(\dfrac{2.167}{\dfrac{\mathrm{D_e}}{\mathrm{t_{min}}}} - 0.0833\right)B; \ \dfrac{2\min\left(1.5\mathrm{S_m}; 0.9\mathrm{S_y}\right)}{\dfrac{\mathrm{D_e}}{\mathrm{t_{min}}}}\left(1 - \dfrac{1}{\dfrac{\mathrm{D_e}}{\mathrm{t_{min}}}}\right)\right] \\
\text{therefore if } \mathrm{p_a} > \mathrm{p_{design}} \Rightarrow \text{OK} \\
\text{otherwise increase } \mathrm{t_{min}}
\end{array}
\right.
\tag{102}
$$

Where $\mathrm{L_o}$ is the unsupported length of the tube, E is the modulus of elasticity, $\mathrm{S_m}$ and $\mathrm{S_y}$ are the stress intensity and the yield strength, respectively, at the design temperature. *A* and *B* are values that must be calculated according to the tables and figures reported in [140].

In practice, due to the relatively low design pressure of the molten salt, the verification of the cylindrical parts under external pressure has been necessary only for the helical-coil exchangers. Specifically, the assessment has been made for the secondary coolant tubes and manifolds where the helium pressure acts as external wall load. The calculation has been performed in the hypothesis that, for whatever reason, in the secondary circuit the pressure has been brought to the atmospheric condition while the primary system has reached the design pressure (e.g. depressurization of the secondary circuit and consequent loss of heat sink for the primary circuit). The estimated allowable pressures are reported in Table 4.31.

Table 4.31. Allowable external pressure in helical-coil exchangers.

	p_a [MPa]
IHX helical tubes	9.42
Steam generator helical tubes	9.21
IHX – HITEC hot/cold feeding tubes	9.34
Steam generator – water hot/cold feeding tubes	9.38

4.8.2 Heat exchanger tubesheets

As said, the majority of the pressure retaining parts consists of cylindrical and spherical shells, however there is at least another element that is usually fundamental in the construction of a heat exchanger, namely the tubesheet.

The tubesheet of an exchanger, by virtue of being drilled, is a flat, porous plate, very prone to stresses when exposed to differential pressure [184]. If the shell would not being used as stiffeners and supports for the tubesheet, its thickness could become much higher. The most common tubesheets typologies that can be found in nuclear industry are the “fixed” tubesheet and the “U-tube” tubesheet.

The term fixed tubesheets apply to those heat exchangers in which two tubesheets are used with the tubes acting as stays and shell acting as a support at the outside circumference. The design of such tubesheets is based on the theory of plates on elastic foundation and is more complicated than that for tubesheets in U-tube construction which, instead, relies on the classical theory of the bending of a circular plate subjected to pressure.

As regard to the BB PHTS exchangers, the theoretical treatment and analysis of their tubesheets can be attributed at either “fixed” or “U-tube” typology, in dependence on the bundle layouts. In particular, in the intermediate heat exchanger with the straight bundle, both upper and lower tubesheets are fixed to the shell and they are pressure retaining boundary. The two perforated plates are put in close mechanical interaction by the tubes which directly transmits forces and displacements between the two closure ends (different thermal expansions between the shell and the tubes etc). This exchanger geometry is clearly compliant with the “fixed” tubesheet configuration.

Figure 4.35 shows the details of the lower tubesheet separating the primary and secondary coolant environments in the half bottom of the IHX with straight tube bundle.

On the other hand, the design of the two perforated plates of the helical-coil exchanger is characterized by features that enables the use of the sizing methodology typical of the “U-tube” configurations. As a matter of fact, the whole design of the helical-coil exchanger has been though to make the mechanical coupling of the two tubesheets as weak as possible, ideally reaching a total decoupling between them.

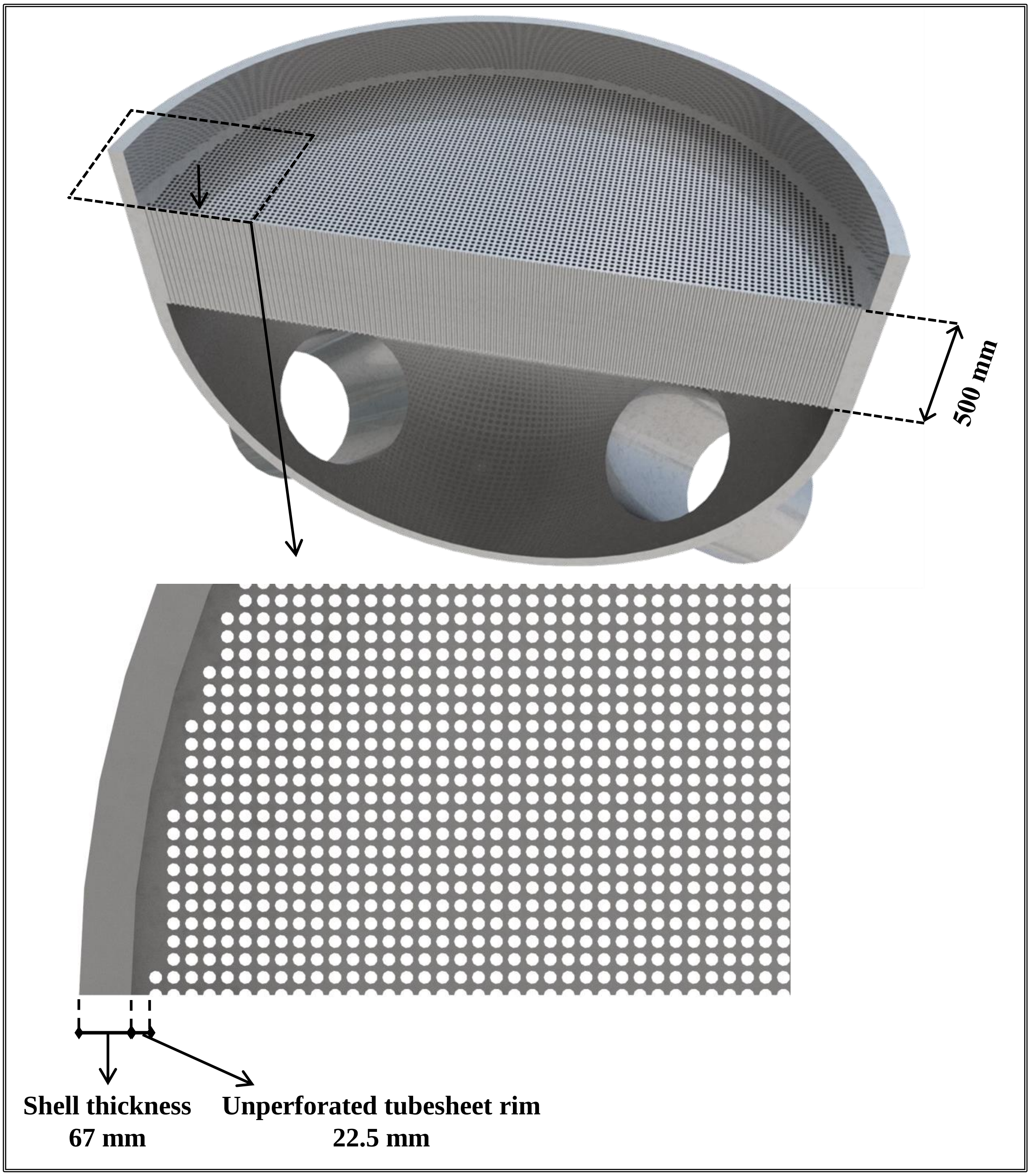

Figure 4.35. Details of the lower tubesheet region in the IHX with straight tube bundle.

Specifically, the lower tubesheet supports only the external walls of the module channels. These channels are not joint to the upper tubesheet owing to the existing gap above the heating section that let helium move radially and reach the downcomer.

In a similar fashion, the clusters containing the helical bundles are “suspended” to the upper tubesheet to which the central columns are welded. With such a layout, bundles and central columns are virtually allowed to glide within the module channels if different thermal expansions occur, without any transferring of forces between the upper and lower tubesheets.

Clearly, some supports will be employed to hold up the tubes, keep the lattice pitches in the right positions, prevent vibrations and partially unload the central columns from the bundle weight. Therefore, if the supporting elements will be connected to the external wall of the module, then some reacting forces might be theoretically spread between the two tubesheets. However, considering a non-stiff nature for those supports and the inherent vocation of the coiled tubes to self-compensate for the imposed displacements caused, for instance, by thermal expansions, the interconnection between the two perforated plates can be assumed much weaker respect to that occurring with a straight tube configuration.

In addition, it is also worth to remark that with this exchanger architecture, the two plates are subjected to totally different pressure loads. The upper tubesheet acts as a pressure retaining boundary because on its two circular faces the pressure gradient between primary and secondary circuits is applied, whereas the lower tubesheet is surrounded by a helium environment on all its sides, therefore it is basically subjected to the very small pressures, coming up from the friction losses. Owing to these preliminary considerations, as first approximation, each of the two plates has been analysed as stand-alone, adopting the same equations applied for the “U-tube” configurations.

As regard to the practical design calculations, according to the method proposed in the ASME code, a trial-and-error approach has been followed to size the components. Tentative thicknesses for tubesheets and adjacent zones are set, then an assessment of the stresses in key locations of the structure is made: if all the calculated values are within the maximum allowable limits the design is considered satisfactory, otherwise the process re-starts considering higher thicknesses.

Although the procedures to design both typologies of tubesheets are somehow straightforward, their application is very lengthy because a lots of auxiliary quantities and steps are needed to accomplish all the required calculations. For this reason, the methodology will not be described.

Since the results of the sizing calculations have been already provided into the pertaining tables of the previous sections (thickness of tubesheets, reinforcements etc.), the information that will be given below will concern the verification of the stress state in the key locations of the domain. It should be noticed that the loading condition that would cause the maximum stresses in the structures cannot be evaluated a-priori. Hence, as suggested in the ASME BPVC VIII-Division 1 [147], the assessments have been performed for various loading conditions conceiving several combinations of primary and secondary pressures (and temperatures). Four design loading cases must be analysed for both “fixed” and “U-tube” type tubesheet: the cases are set considering all the possible combinations between maximum and minimum design pressure of both primary and secondary side, see Table 4.32. The maximum design pressures have been evaluated according to the Table 4.26 while the minimum design pressure has been always assumed 0.1 MPa. Properties of the material have been evaluated at the maximum design temperature as prescribed

Table 4.32. Design loading combinations .

Case	**Tube side pressure p_t**	**Shell side pressure p_s**
1	$p_{t_{max}}$	$p_{s_{max}}$
2	$p_{t_{max}}$	$p_{s_{min}}$
3	$p_{t_{min}}$	$p_{s_{max}}$
4	$p_{t_{min}}$	$p_{s_{min}}$

The IHX configuration with fixed tubesheet requires additional verifications which account for operating conditions. Besides the pressure loads, in each operating condition "*i*", the thermal loads caused by the different thermal expansion between tubes and shell must be considered too. In these evaluations, the material properties can be taken at the operating condition under exam. Table 4.33 provides an example of load combinations to evaluate the operating condition "*i*".

Table 4.33. Operating load combinations.

Case	**Tube side pressure p_t**	**Shell side pressure p_s**	**Tube wall axial mean temperature T_t**	**Shell wall axial mean temperature T_s**
1	$p_{t_{max,i}}$	$p_{s_{max,i}}$	$\bar{T}_{t_i}$	$\bar{T}_{s_i}$
2	$p_{t_{max,i}}$	$p_{s_{min,i}}$	$\bar{T}_{t_i}$	$\bar{T}_{s_i}$
3	$p_{t_{min,i}}$	$p_{s_{max,i}}$	$\bar{T}_{t_i}$	$\bar{T}_{s_i}$
4	$p_{t_{min,i}}$	$p_{s_{min,i}}$	$\bar{T}_{t_i}$	$\bar{T}_{s_i}$

In principle, such an assessment must be repeated for each anticipated operating case, thus including normal, start-up, shutdown, cleaning, and upset operating conditions. However, because of the pre-conceptual phase in which the DEMO project is being, the majority of the cases have not been defined yet, therefore the assessment has been preliminary limited just to the normal operating conditions.

Showing the results for all cases investigated would be undoubtedly boring and, probably, even useless, therefore the data reported are limited to the most relevant and worst conditions.

The selected results for the intermediate heat exchanger with straight tube bundle and fixed tubesheets are summarized from Table 4.34 to Table 4.36. These analyses have pointed out that, due to the relatively long bundle, as shell material it should not be used a steel which thermal expansion features are quite different from the tube alloys. In fact, establishing that the tubes will be made of Alloy 800H for the reasons explained in the first paragraphs of this chapter, as first attempt the material selected for the shell has been the 9Cr1Mo-V, which has been already envisaged as pressure retaining material in high temperature reactors (see paragraph 4.2) and it is also suggested in the section of the ASME code dealing with these kind of power plants, namely the BPVC III – Division 5 [180]. However, such a material is characterized by a low thermal expansion coefficient (in comparison with other steels suitable for DEMO purpose), so that the preliminary assessments have shown scarce compatibility with the specific exchanger layout, tube material and thermal-hydraulic design conditions. In particular, it has been seen that, during normal operation, the huge differences in the thermal expansion of the structures would have led the tubes to be under excessive axial compressive loads. Adding some expansion joints or intensifying the stiffness of the tubes through an increase of their thicknesses might have improved the response of the component as concern to this aspect, but it would have had many drawback on the overall exchanger architecture. Moreover, even though the effects of axial compression would have been somehow relaxed, the presence of phenomena that might have caused axial instability in the tubes should be avoided or, at least, limited as much as possible in the design of these elements. Therefore, it has been chosen to move toward another material for the construction of the shell and the tubesheets. Taking into account that in many liquid metal fast breeder reactors, where the shell is generally at low pressure, the 316 stainless steel is used for the exchanger structures, the choice has fallen on this material. The 316 SS has still reasonable mechanical properties at high temperatures, is compliant with the Division 5 of the ASME III, and shows an optimal resistance against the corrosion of molten salts at the conditions foreseen in the DEMO BoP.

Table 4.34. Straight bundle IHX with fixed tubesheets. Design conditions.

Primary calculation pressure [MPa]	9.2 (max)	
Secondary calculation pressure [MPa]	0.1 (min)	
Stress type	|σ| [MPa]	Stress limit [MPa]
Tubesheet maximum bending moment	121.9	1.5S$_m$ = 147.6
Tube axial stress	29.6	S$_m$ = 97.0
Shell axial stress in thin part (membrane)	18.0	S$_m$ = 107.0
Shell axial stress at tubesh. junction(membr+bend)	125.0	1.5S$_m$ =160.5
Head axial stress at tubesh. junction(membr+bend)	97.3	1.5S$_m$ =147.6

Table 4.35. Straight bundle IHX with fixed tubesheet. Operating condition 1 – Pulse.

Primary calculation pressure [MPa]	8.4	
Secondary calculation pressure [MPa]	0.2	
Tube wall mean axial temperature [°C]	365.5	
Shell wall mean axial temperature [°C]	350.6	
Stress type	|σ| [MPa]	Stress limit [MPa]
Tubesheet maximum bending moment	128.5	$1.5S_m\|_T = 153.3$
Tube axial stress	39.2	$2S_m = 194.0$
Shell axial stress in thin part (membrane)	8.5	$1.5S_m\|_T = 162.0$
Shell axial stress at tubesh. junction(membr+bend)	126	$1.5S_m\|_T =162.0$
Head axial stress at tubesh. junction(membr+bend)	107	$1.5S_m\|_T =153.3$

Table 4.36. Straight bundle IHX with fixed tubesheet. Operating condition 2 – Dwell like.

Primary calculation pressure [MPa]	8.4	
Secondary calculation pressure [MPa]	0.2	
Tube wall mean axial temperature [°C]	350.6	
Shell wall mean axial temperature [°C]	350.6	
Stress type	|σ| [MPa]	Stress limit [MPa]
Tubesheet maximum bending moment	149.1	$1.5S_m\|_T = 153.3$
Tube axial stress	53.3	$2S_m = 194.0$
Shell axial stress in thin part (membrane)	39.0	$1.5S_m\|_T = 162.0$
Shell axial stress at tubesh. junction(membr+bend)	161.3	$1.5S_m\|_T =162.0$
Head axial stress at tubesh. junction(membr+bend)	130.0	$1.5S_m\|_T =153.3$

The values of S_m in the different table cells can vary to one another because they depend on the material of the element considered and, in addition, on its design temperature. Moreover, in when in the operating scenarios the allowable stress has been calculated considering the actual temperature of the material (set equal to the maximum coolant temperature with which the component is in contact), the notation $S_m|_T$ has been adopted.

As can be seen from the reading of the tables, the worst case can be identified in the "Operating condition 2 – Dwell like". It is worth to underline that such a case is a conservative approximation of what generally happens in the exchanger during the Dwell. In particular, at the end of the Pulse phase the tube wall is hotter than the shell, with a mean axial temperature difference of about 15 °C. When the Dwell starts, the reactor is shut down and the generated power drops faster than the transferred power to the heat exchanger. The net effect is a cooling of the helium which temperature profile in the exchanger tends to lay down upon the one of the molten salt. Moreover, looking at the behaviour on the whole exchanger on a global scale, an overall decrease of the average temperatures should be experienced by the structures because a small flow rate of cold salt must be ensured at the inlet of the exchanger. In agreement with this qualitative scenario, it has been chosen to set-up an operating condition which would be the most challenging for the component. In fact, in the (quite realistic) hypothesis of considering the inertia of both shell structures and molten salt much more higher than those of tubes and helium, the overall decrease of the molten salt temperature might be neglected while a considerable narrowing of the temperature differences between the coolants would occur bringing the tube wall temperature to approach the shell temperature. Taking into account the differences in the thermal expansion coefficient of the two materials, the worst case happens if the tube temperature become equal to that of the shell (an inversion of the temperatures of the coolants is a very unlikely event). Therefore, this extreme, conservative case has been selected as good candidate to verify reliability of the tubesheets under conditions can be considered as an extension of normal operation.

Since the stresses are below the allowable limits, the preliminary design of the "fixed" type tubesheet has been considered acceptable.

As regard to the design of the tubesheets for the helical-coil exchanger, the verification procedures are simpler than those necessary for the fixed type configuration [132]. In this case the assessments have been needed at the design conditions only because of the hypothesis of no-interactions between the two tube plates.

The results are reported from Table 4.37 to Table 4.40.

It should be noticed that for the lower tubesheet the primary and secondary design pressures have been set as 3 times the maximum pressure drop expected on the two sides of the plate. Due to the large radial dimension of the helical-coil exchangers and the high pressure loads, in particular in the steam generator option, huge (maybe prohibitive) thicknesses would have been expected if it would have not been chosen a proper combination of materials and coolant flow paths. Therefore, as already discussed in the paragraph 4.5.3, the overall exchanger envelope has been conceived to maintain the pressure vessel and its fundamentals pressure retaining parts at the cold temperature, enabling the use of materials compliant with ASME nuclear sections for the component with temperature below 371°C.

In this way it has been possible to adopt those well-proven low alloy steels that commonly finds application in nuclear equipment heavy industry for the manufacturing of large plates and forged pieces.

To this purpose, in order to avoid any kind of extrapolation from the state-of-art technology described in paragraph 4.2, it has been put as further design constrain to not exceed the range of thicknesses present in large PWR steam generators for shell parts and the tubesheets.

Table 4.37. Helical-coil IHX – Lower tubesheet at the worst design condition.

Primary calculation pressure [MPa]	7.89 (max)	
Secondary calculation pressure [MPa]	7.72 (min)	
Stress type	σ [MPa]	Stress limit [MPa]
Tubesheet maximum bending moment	211.3	$2S_m$ = 228.0
Shell axial stress at tubesh. junction(membr+bend)	123.4	$1.5S_m$ = 171.0
Head axial stress at tubesh. junction(membr+bend)	156.3	$1.5S_m$ = 171.0

Table 4.38. Helical-coil steam generator – Lower tubesheet at the worst design condition.

Primary calculation pressure [MPa]	7.89 (max)	
Secondary calculation pressure [MPa]	7.69 (min)	
Stress type	σ [MPa]	Stress limit [MPa]
Tubesheet maximum bending moment	215.1	$2S_m$ = 228.0
Shell axial stress at tubesh. junction(membr+bend)	105.9	$1.5S_m$ = 171.0
Head axial stress at tubesh. junction(membr+bend)	139.1	$1.5S_m$ = 171.0

Table 4.39. Helical-coil IHX – Upper tubesheet at the worst design condition.

Primary calculation pressure [MPa]	9.2 (max)	
Secondary calculation pressure [MPa]	0.1 (min)	
Stress type	σ [MPa]	Stress limit [MPa]
Tubesheet maximum bending moment	113.7	$2S_m$ = 414
Shell axial stress at tubesh. junction(membr+bend)	309.6	$1.5S_m$ = 310.5
Head axial stress at tubesh. junction(membr+bend)	72.6	$1.5S_m$ = 310.5

Table 4.40. Helical-coil steam generator – Upper tubesheet at worst design condition.

Primary calculation pressure [MPa]	0.1 (min)	
Secondary calculation pressure [MPa]	15.6 (max)	
Stress type	σ [MPa]	Stress limit [MPa]
Tubesheet maximum bending moment	125.8	$2S_m = 414$
Shell axial stress at tubesh. junction(membr+bend)	78.5	$1.5S_m = 310.5$
Head axial stress at tubesh. junction(membr+bend)	308.7	$1.5S_m = 310.5$

5 Pipework design and arrangement of the cooling loops

The main task of PHTS pipework is to transport the helium from the BB segments to the intermediate heat exchangers (steam generators) and bring it back once the thermal power has been transferred to the secondary circuit.

For this part of the primary cooling system, a comparison with the architectures adopted in nuclear systems is much more difficult in this case respect to what it has been done for the exchangers.

In common PWRs, indeed, the steam generators are placed near by the reactor pressure vessel in order to cover a length of about a hundred of meters for the whole pipework network. As regard to the latest HTR designs, then, differences are much more marked because the reactor vessel and the steam generator(s) are connected to one another through a co-axial, straight duct inserted in the gap between them. The duct is generally 10÷20 meters long and, due to its layered architecture, allows the passage in both direction of the coolant; this makes possible a further decrease of the total piping length to a few tens of meters [185].

In DEMO, these configurations are basically inapplicable because the shape and the inherent dimensions of the tokamak, as well as the architecture of the In-Vessel components, make almost impossible the application of a piping arrangement similar to those of other nuclear reactors; just think that the diameter of the Bio-shield is over 40 meters long that it is trivial to understand that several kilometres of pipes will be needed to join all the BB segments with the heat exchangers.

In spite of these innate layout differences between the PHTSs of fission and fusion power plants, some further guidelines can the gather from the NPPs experiences and practices.

As stated in the paragraph 3.3, a coolant average velocity between 40 m/s and 50 m/s should be kept within the larger pipework as a trade-off value between the need to limit system pressure drop (hence pumping power) and coolant total inventory [186]. However, the main hot leg collects the helium coming from the segments through a complex network of pipes, which dimensions might not always be compliant with such a speed range. The feeding pipes of the segments, indeed, have to respect further specifications and constrains enforced by other DEMO tasks, hence it could be difficult to meet all the thermal-hydraulic criteria if they would be too strict. For example, due to the reasons explained in the section 1.3.1, the sizes of the segments feeding pipes routed through the upper port have been already fixed, therefore from those portions of pipework may potentially arise a conflict between the different requirements. To avoid this happening, an additional investigation has been conducted with the aim of discovering whether the requirement on the helium maximum velocity might be somehow relaxed.

The main concerns about a fluid which passes through a pipeline with a high velocity are related to the possibility of causing both vibrations and erosion. If the gas speed exceeds the so-called “erosional velocity” in a given transmission line, the erosion of the pipe wall can overtake the acceptable rates, thus causing a significant reduction of the pipework lifetime. Moreover, an increase of the erosion rate might lead to an intolerable presence of eroded particles within the circuits that could induce impingement damages in their most vulnerable parts like the circulator blades and the heat exchangers tubes.

In addition, being subjected to neutron irradiation, the carried particles can get activated during their paths inside the In-Vessel components and, following their subsequent deposition in some Ex-vessel parts of the PHTS, could finally increase the radiation exposure of the workers [20]. This potential effect must be absolutely prevented and minimized as much as possible [42].

According to the results obtained during the ‘80s in the framework of the tests performed in the German Component Testing Facility (KVK) [187] a helium velocity of about 60 m/s in a hot (~900 °C) duct of about 700 mm can be sustained without any evidence of undue vibrations or erosions in the components.

It is intuitive to understand that the erosion process is closely related to the force with which a fluid particle impacts the pipe walls, thus to the fluid density. In fact, both Menon [188] and Mohitpour et al. [189] suggest the following formula to calculate the erosional velocity for single-phase compressible fluids:

$$u_e = 1.22 \frac{C}{\rho^{0.5}} \tag{103}$$

where, u_e is the erosional velocity, ρ is the fluid density and C is a constant depending on the coolant service conditions (as the original formula is given in British units, the 1.22 has been applied to allow the use of SI units).

The equation (103) is derived from the American Petroleum Institute recommended practice 14E (API RP 14E) [190]. These recommendations state that “industry experience to date indicates that for solid-free fluids values of C=100 for continuous service and C=125 for intermittent service are conservative”. In agreement with this statement, at the PHTS relevant conditions, during normal operation the erosional helium velocity would be about 56 m/s in the hot piping and 47 m/s in the cold parts.

However, it should be highlighted that these guidelines are commonly adopted in the sizing of pipes transporting heavy gas streams and/or two-phase fluids on production platform located off-shore, where combined corrosion-erosion effects are very likely to occur, at least in comparison with a “clean” system as the helium-cooled PHTS is expected to be.

In fact, the very conservative origin of the previous statement, which is meant to cover corrosive fluids, is brought to light by a specific statement of the 14E (API RP 14E) where a more precise definition of a so-called clean service is given: “for solid-free fluids where corrosion is not anticipated or when corrosion is controlled by inhibition or by employing corrosion resistant alloys”, a higher C-factor of 150–200 is recommended for continuous service and up to 250 for discontinuous operations.

Appearing this latter situation closer to the DEMO one, a minimum factor of 150 is strongly suggested so that the previously estimated speeds would now become about 84 and 71 m/s, respectively.

The decision to choice the latter values in place of those more conservative is also strengthened if similar recommendations and rules-of-thumb are taken from other independent standards. As a matter of fact, for the single-phase gas lines where pressure drops are not critical, the NORSOK P-001 standard [191] suggest to adopt the following formula to avoid exceeding the limits which may create noise or vibration problems:

$$u_{max} = \frac{175}{\rho^{0.5}} \tag{104}$$

where the meaning of the parameters are basically identical to those used in (103).

From an easy comparison of (103) and (104), it is possible to notice that the value of 175 used in the NORSOK standard is very close to the number obtain with the API formulation when a C-factor of 150 is employed.

Obviously, the values obtained with the equations above have not been used as driving design equations for the BB PHTS pipework, instead they have been intended as boundary values which encompass the “safe” region for the pipework design. Therefore, if coolant velocities in non-major mainlines or laterals (feeding pipes) exceed the 50 m/s, but being still within the maximum speed limits, they should not cause concerns.

As regard to the pipe dimension, a nominal diameter of DN 1300 has been considered as the maximum allowable size for the PHTS piping, see paragraph 3.3. This size is in line with previous works performed by Siemens on a helium-cooled fusion reactor. In particular, depending on the reactor power and the specific coolant working conditions, DN1200 [50] and DN1400 [186] were selected for the hot legs. In the latter design the wall thickness could achieve 83 mm owing to the reference pressure and temperature which were set to 90 bar and 560 °C, respectively.

Furthermore, similar dimensions have also been adopted in the Combustion Engineering type PWR, where hot legs with an external diameter about 1260 mm and a wall thickness of about 91 mm are used [192], while in the latest helium-cooled HTR designs the internal diameter of the cross-duct connecting the reactor pressure vessel to the steam generator vessel can reach 1565 mm with the consequent need of a 92 mm thick wall [193].

In DEMO, the combination of loads are expected to require smaller wall thicknesses also for a DN1300 pipe therefore, taking into account the state-of-art in nuclear field, the manufacturing of such a pipe seems reasonably feasible.

Once the criteria for the thermal-hydraulic design of the PHTS piping have been defined, the nominal dimensions and the relevant quantities have been calculates for those pipe and fitting elements needed to connect the 10 blanket segments of each of the 8 cooling loops with their own exchanger. Then, a proper arrangement of the cooling loops has been pursued with the support of the CREATE consortium whose design team has provided the pipework CAD models of both “direct” [195] and “indirect” [194] coupling BoP options, afterward used to perform the thermal-hydraulic assessments.

Two separate layouts have been outlined taking into account the differences in the two heat exchanger options. They are depicted from Figure 5.1 to Figure 5.4 with hot and cold zones of piping marked in red and blue colours, respectively.

As can be recognized from the pictures, the two system layouts are very similar. The only remarkable variance is represented by the hot legs routing, which must be compliant with the exchanger architecture.

In particular, for the IHX configuration with the straight tube bundle, the hot legs is routed up to the top of the exchanger to let helium enters from the upper head of the intermediate heat exchanger. On the contrary, in case of helical-coil IHX/SG, the paths of the hot legs are quite shorter because the exchanger inlet nozzle is placed in the lower head. This aspect denotes a good advantage of the latter architecture in comparison with the former because it allows to minimize the length the largest pressure pipes of plant, thus reducing the complexity due to their manufacturing and installation.

Nevertheless, with the exclusion of the hot legs length, the two designs are coincident, therefore it has been possible to adopt the same methodology and relations to study the pipework of both options.

Moreover, a careful observation of the overall loops disposition around the tokamak and the respective pipes routing highlights how from the 8 parallel BB PHTS circuits it is possible to gather together the loops which are characterized by the same pipework topology. Actually, 2 loops can be recognized as each one representatives of 4 equal circuits. The 4 external and 4 internal circuits are called “longest loops” and “shortest loops”, respectively.

Figure 5.5 provides an insight into these features, while the main data related to these two characteristic loops are summarized in Table 5.1 and Table 5.2.

As can be seen from the two tables, pipe sizes and thicknesses have been chosen in order to limit the helium speed in the main hot and cold legs below 50 m/s and to withstand the design loads. The OB hot and cold feeding pipes provide an exception respect to the preferable velocity due to the small pipe diameters imposed by integration and remote maintenance constrains already explained. Nevertheless, the speed is kept below the limit imposed by the equations (103) or (104) so that no operational issues should be expected for this pipework.

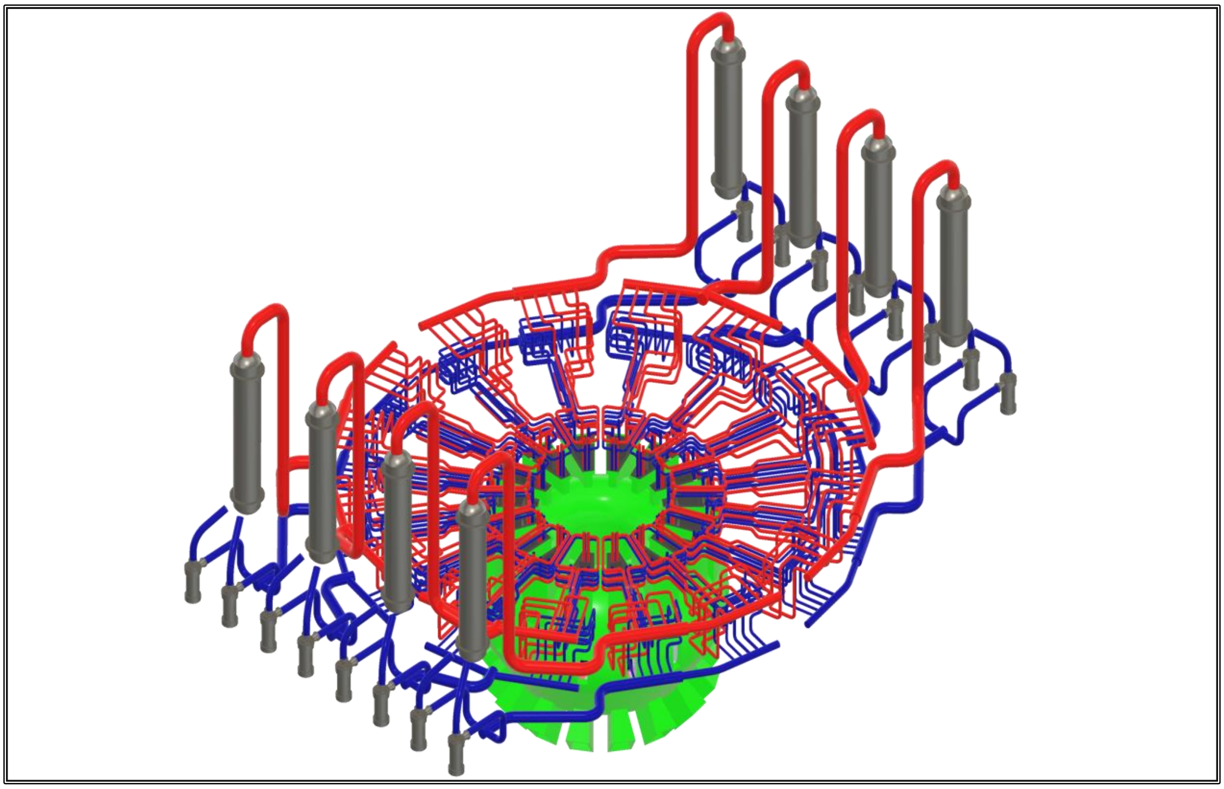

Figure 5.1. Isometric view of BB PHTS layout - straight tube IHX configuration.

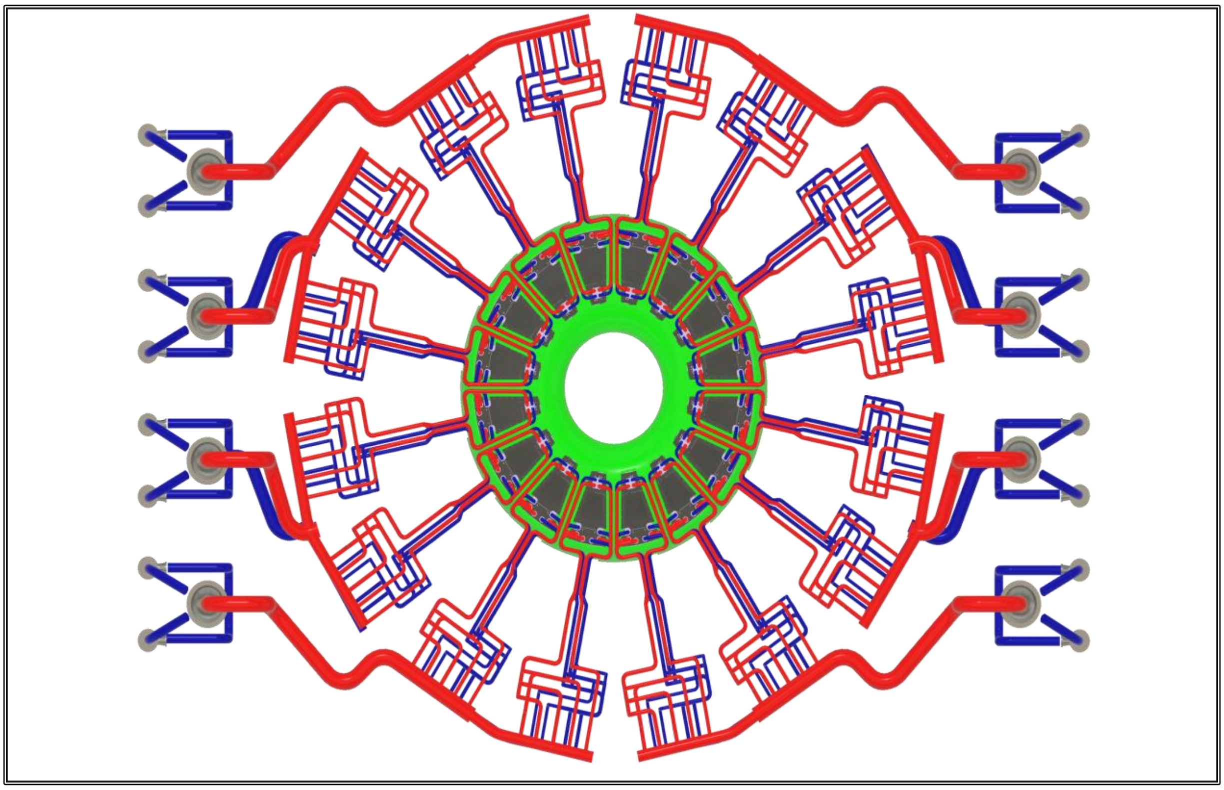

Figure 5.2. Top view of the BB PHTS layout - straight tube IHX configuration.

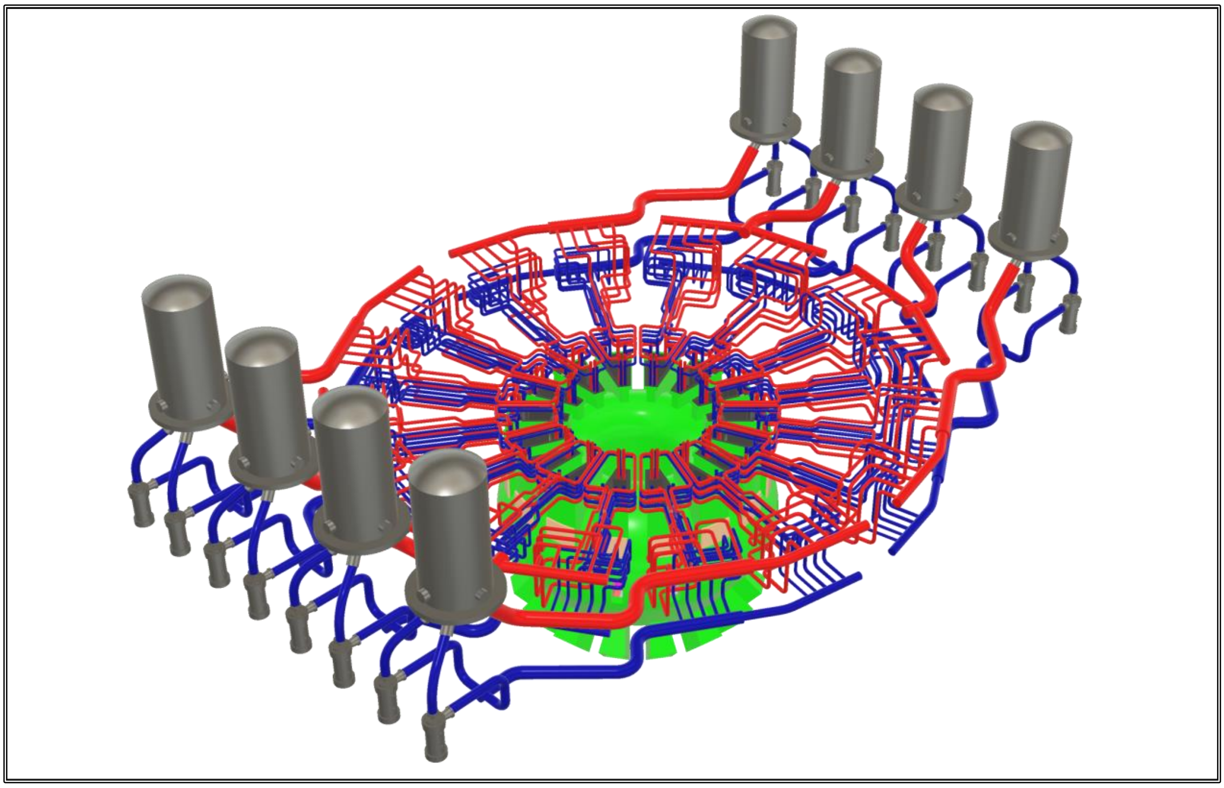

Figure 5.3. Isometric view of the BB PHTS layout – helical-coil IHX/SG configuration.

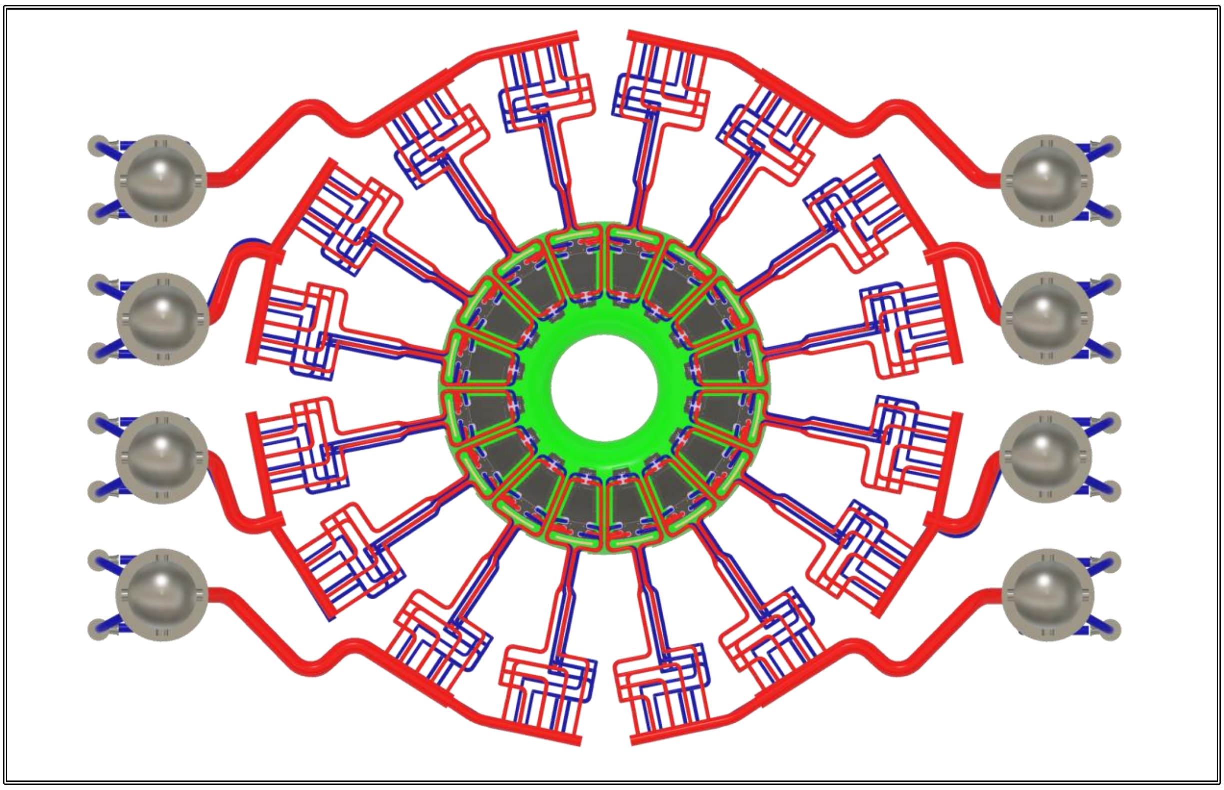

Figure 5.4. Isometric view of the BB PHTS layout – helical-coil IHX/SG configuration.

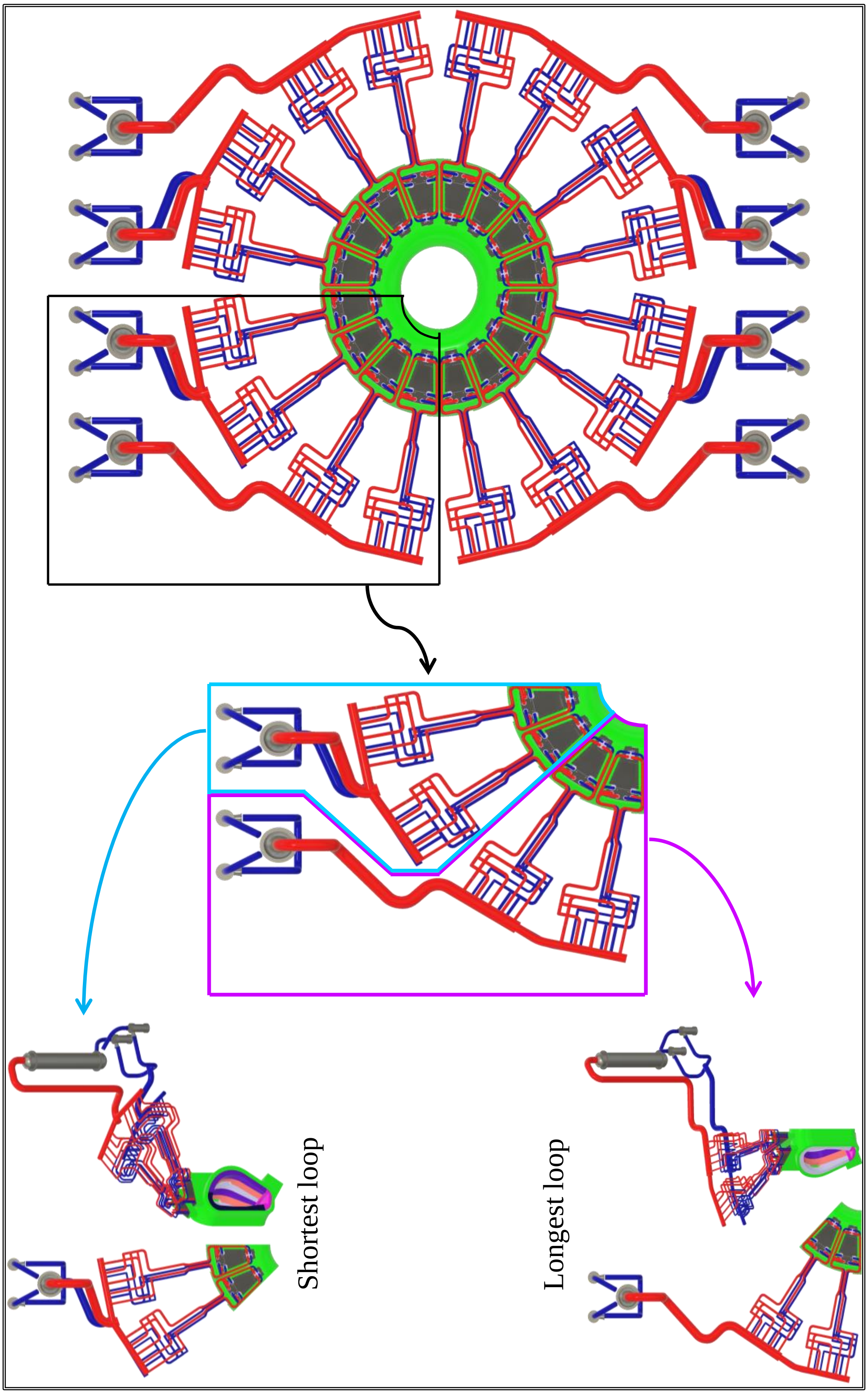

Figure 5.5. The 2 characteristic loops and their arrangement – standard S&T configuration.

Table 5.1. PHTS pipes data. Longest loop.

Element	**Number per loop**	**DN**	D_e [mm]	Thick. [mm]	G_{max} [kg/s]	u [m/s]
OB hot feeding pipe	6	350	355.60	17.48	26.54	69.2
IB hot feeding pipe	4	300	323.80	15.88	15.76	49.6
OB cold feeding pipe	6	300	323.80	14.27	26.54	58.4
IB cold feeding pipe	4	250	273.00	11.13	15.76	48.2
Hot collector (sector 1)	1	900	914.00	45.00	111.12	44.0
Hot collector (sector 2)	1	1300	1321.00	65.00	222.24	42.1
Main hot leg	1	1300	1321.00	65.00	222.24	42.1
Cold circulator suction	2	750	762.00	32.00	111.12	44.0
Cold C-shaped header	1	750	762.00	32.00	222.24	43.5
Main cold leg	1	1100	1118.00	45.00	222.24	40.1
Cold distributor (sector 2)	1	1100	1118.00	45.00	222.24	40.1
Cold distributor (sector 1)	1	750	762.00	32.00	111.12	43.5

Table 5.2. PHTS pipes data. Shortest loop.

Element	**Number per loop**	**DN**	D_e [mm]	Thick. [mm]	G_{max} [kg/s]	u [m/s]
OB hot feeding pipe	6	350	355.60	17.48	26.54	69.2
IB hot feeding pipe	4	300	323.80	15.88	15.76	49.6
OB cold feeding pipe	6	300	323.80	14.27	26.54	58.4
OB cold feeding pipe	4	250	273.00	11.13	15.76	48.2
Hot collector	2	900	914.00	45.00	111.12	44.0
Main hot leg	1	1300	1321.00	65.00	222.24	42.1
Cold circulator suction	2	750	762.00	32.00	111.12	44.0
Cold C-shaped header	1	750	762.00	32.00	222.24	43.5
Main cold leg	1	1100	1118.00	45.00	222.24	40.1
Cold distributor	2	750	1118.00	45.00	111.12	43.5

5.1 Thermal-hydraulic design

Usually the layouts envisaged in NPPs are very simple and the piping system connecting the reactor vessel to the steam generators is regularly made up of a number of elements that are arranged in series, so that the fluid can continuously flow through one element and then another.

In DEMO, instead, for the reasons already discussed, the exchangers are inevitable placed far away from the centre of the reactor and, due to the topology and the amount of the blanket segments, several parallel flows are present.

In parallel flow, two or more series combinations of piping elements diverge from a distributor and then come together again downstream into a collector. Such a type of flow can be extremely complicated to analyse because the pressure difference (driving factor) is the same at the ends of the sections in parallel (between distributor and collector), but the flow resistances of the parallel branches might differ to one another, therefore the mass flow rates distribution may not meet the desired value.

In order to study the overall hydraulic behaviour of the system, an assessment of the pressure drops along the different paths of the cooling circuit has been made. Furthermore, with the aim of ensuring the required mass flow rate in each segment, a proper balance of the helium pressure losses has been pursued assuming that dedicated zones of the loops will be equipped with devices suitable for this scope.

To this purpose, the evaluations have followed the approach usually suggested in the reference handbooks on this topic, such as the *Idelchik*'s "Handbook of Hydraulic Resistance" [196] or "Pipe Flow" by *Rennels* and *Hudson* [197].

In the following, a brief description of the basic equations adopted is reported before showing the final results.

5.1.1 Pressure drops calculation methodology

From the generalized Bernoulli equation [152], which related the specific loss of energy of a fluid flowing from a general section "0" to another arbitrary section "1" over a duct, in the hypothesis of a steady-state, incompressible fluid flow, to which gas at small flow velocities (practically up to u ≈150 m/s) can also be referred, and negligible internal energy variations ($U_0 \approx U_1$), it is possible to write:

$$g\rho_0 z_0 + p_0 + N_0 \frac{\rho_0 u_0^2}{2} = \left(g\rho_1 z_1 + p_1 + N_1 \frac{\rho_1 u_1^2}{2} \right) \frac{\rho_0}{\rho_1} + \Delta p_{tot} \tag{105}$$

or

$$\Delta p_{tot} = g\rho_0 z_0 + p_0 + N_0 \frac{\rho_0 u_0^2}{2} - \left(g\rho_1 z_1 + p_1 + N_1 \frac{\rho_1 u_1^2}{2} \right) \frac{\rho_0}{\rho_1} \tag{106}$$

with N_0 and N_1 characterizing the degree of the non-uniformity of kinetic energy and velocity distributions over the sections “0” and “1”.

In the case of a small pressure drop (practically equal to about 10^4 Pa), $\rho_0 = \rho_1 = \rho$; then instead of equation (106) we have:

$$g\rho z_0 + p_0 + N_0 \frac{\rho u_0^2}{2} = \left(g\rho z_1 + p_1 + N_1 \frac{\rho u_1^2}{2} \right) + \Delta p_{tot} \tag{107}$$

and with uniform flow velocity profile, i.e. $N_0 = N_1 = 1$,

$$g\rho z_0 + p_0 + \frac{\rho u_0^2}{2} = \left(g\rho z_1 + p_1 + \frac{\rho u_1^2}{2} \right) + \Delta p_{tot} \tag{108}$$

or

$$\Delta p_{tot} = \left(g\rho z_0 + p_0 + \frac{\rho_0 u_0^2}{2} \right) - \left(g\rho z_1 + p_1 + \frac{\rho u_1^2}{2} \right) \tag{109}$$

Two types of the total pressure (hydraulic resistance) losses in the pipeline are considered:

- Pressure losses resulting from friction (frictional drag), Δp_{fr};
- Local pressure losses (local resistance), Δp_{loc}.

The fluid friction loss is due to the viscosity (both molecular and turbulent) of real liquids and gases in motion, and results from momentum transfer between the molecules (in laminar flow) and between the individual particles (in turbulent flow) of adjacent fluid layers moving at different velocities [196].

The local losses of total pressure are caused by the following:

- local disturbances of the flow;
- separation of flow from the walls;
- formation of vortices and strong turbulent agitation of the flow at places where the configuration of the pipeline changes or fluid streams meet or flow past obstructions (entrance of a fluid into the pipeline, expansion, contraction, bending and branching of the flow, flow through orifices, grids, or valves, filtration through porous bodies, flow past different protuberances, etc.).

All of these phenomena contribute to the exchange of momentum between the moving fluid particles (i.e., friction), thus enhancing energy dissipation.

The two kinds of losses, frictional and local, are summed according to the principle of superposition of losses and consist of the arithmetic sum them:

$$\Delta p_{tot} = \Delta p_{fr} + \Delta p_{loc} \tag{110}$$

In fact, the value of Δp_{fr} should be taken into account only for relatively long fittings or only for elements (branch pipes, diffusers with small divergence angles, etc.), or when this value is commensurable with Δp_{loc}.

Usually, hydraulic calculations use the dimensionless coefficient of fluid resistance, which conveniently has the same value in dynamically similar flows, that is, flows over geometrically similar regions and with equal Reynolds numbers or other pertinent similarity criteria, irrespective of the kind of fluid or of the flow velocity (at least up to Ma = 0.8–0.9) and transverse dimensions of the segments being calculated.

The fluid resistance coefficient is defined as the ratio of the total energy lost over the given segment (0-0)–(1-1) to the kinetic energy in the section taken (for example, 0-0) or (which is the same) the ratio of the total pressure lost over the same segment to the dynamic pressure in the section taken, so that on the basis of equations (107) or (109) if the density is invariable along the flow ($\rho_0 = \rho_1 = \rho = \text{const}$) and for the case of uniform distribution of static pressure, it is possible to write:

$$\zeta \equiv \frac{\Delta p_{tot}}{\frac{\rho u^2}{2}} \tag{111}$$

In accordance with the accepted principle of superposition of losses, through a simple manipulation of (110) and (111), it is possible to write:

$$\zeta_{tot} = \zeta_{fr} + \zeta_{loc} \tag{112}$$

where ζ_{fr} is the friction loss coefficient in the given element of pipe and ζ_{loc} is the coefficient of local resistance of the given element of pipe.

The friction loss coefficient of the element considered is defined through the well-known Darcy-Weisbach friction factor of hydraulics, λ, already presented in the sections dealing with the heat exchanger assessment. Here, in agreement with the definition of friction fluid resistance coefficient, it can be write :

$$\begin{cases} \Delta p_{fr} = \zeta_{fr} \rho \dfrac{u^2}{2} \\ \text{with} \\ \zeta_{fr} = \lambda \dfrac{L}{D_h} \end{cases} \tag{113}$$

where D_h is the hydraulic diameter of the element considered. It is worth to point out that for circular component, the (113) becomes identical to the equation (38), used to calculate the distributed pressure drop in the tubes of the exchangers.

The Darcy-Weisbach coefficient has been assessed by means of *Haaland*'s formula (see equation (59)).

For the pipework roughness, the value has been selected after a review of several sources, which report data that are not always in perfect agreement. In fact, according to Idelchik [196], new seamless steel ducts for commercial use can have an absolute roughness in a range of 20 to 100 µm; these values can fall in a window of 15 to 40 microns if the conduits are manufactured to be used in electric power station. Rennels and Hudson [197] suggest a value of 45 µm for seamless steel pipes, regardless to their specific applications. Mohitpour et al. [189], instead, state that for new, uncoated steel pipes adopted in gas transmission pipelines, an effective roughness in a range of 16÷19 µm is generally measured; moreover, due to operations reasons (erosion, corrosion, deposits), these authors affirm that an the roughness can be increased with an annual rate between 0.8-1.3 µm/year. Finally, as regard to the fusion related applications, in the already mentioned Siemens' study of the '92 [50], a roughness of exactly 50 µm was suggested for the calculation of the pressure drops in the primary heat transfer system. This number is definitely higher than the data reported by Mohitpour, but it is also above the values recommended by Rennels and Idelchik (if one refers to applications for electric power production).

Considering the helium conditions and the pipe sizing of the BB PHTS, it has been preliminary estimated that the differences (reduction) in the pressure drops would be between 11÷16 % when, for instance, an absolute roughness of 15 µm is adopted in place of 50 µm

Although it is clear that the roughness can have a non-negligible effect on the distributed pressure drops, it has been decided to apply in any case the value reported by Siemens for conservative reasons. Nonetheless, it is worth to remark that the uncertainties on the wall roughness weight basically on the distributed pressure drop because the local frictions have a quite weak dependence on the pipe asperities. In the BB PHTS, due to the massive presence of fitting, bends the distributed pressure losses should affect less than 50% of the total losses, therefore the roughness is generally expected to influence the assessment for less than 10%.

For what concern the local resistance coefficient, it is mainly a function of the geometric parameters of the component under investigation and also of some general factors of motion. In particular it is affected on the velocity distribution and the degree of turbulence at the entrance of the element considered; this velocity profile, in turn, depends on the flow regime, the shape of the inlet, the shape of various fittings and obstacles, and their distance upstream from the element considered, as well as the length of the preceding straight pipe.

Usually, the basic local resistance coefficients are measured in isolated components having sufficiently long inlet and outlet lengths of straight pipe to ensure that fully developed flow exists at the inlet to the component and redevelops again downstream of the component. This simplifies the experimental campaigns set-up and allows to achieve more reliable data to be used in correlating the phenomena through practical equations.

However, in a fusion reactor, the PHTSs are characterized by complex pipes installation, which has to meet strictly space constrains due to the building integration issues. When the piping elements are close to each other, the mutual interaction (coupling effects) may appreciably affect their hydraulic performances. Coupling effects may not completely disappear unless the components are separated by a straight pipe section of 20÷30 pipe diameters or more; in practice, 4 or 5 pipe diameters may be often sufficient to reduce coupling effects to a level reasonably low. Generally, the method adopted to account for the close coupling of two pipe components is to multiply the sum of their loss coefficients by a correction factor. The correction factors are frequently less than unity, thus ignoring them leads to an overestimation of pressure loss. However, exceptions to this usual trend exist: for example a bend located upstream of a diffuser causes an increase of the non-uniformities of velocity profile at the diffuser inlet preventing the normal pressure recovery [197].

A complete overlooking of these aspects might have led to high discrepancies in the thermal-hydraulic assessments compared to the real case. Hence, to improve the reliability of the calculation, where possible, data available in literature have been used to account for the consequences of the close interaction of pipes elements. Nevertheless, to test and verify the accuracy of the methods adopted in the thermal-hydraulic design phase, a numerical assessment of the pipework pressure drops has been carried out through a fully 3-D CFD code. The results and comparisons will be discussed in the next chapter.

The basic equations for the local losses as well as the corrective factors for the coupling effects of bends and elbows have been taken mainly from [196]. Because of the tabular form in which the corrective factors are normally reported in the reference handbooks, they will not be further described nor reported below. On the contrary, the basic relations for the local resistances in different geometries are written in the following.

5.1.1.1 Bends

The local pressure drop in a bend mainly depends on the its angle and the relative curvature of radius. According to the geometry depicted in Figure 5.6, and for the specific values in which the main helium flow quantities range, the flow resistance coefficient has been calculated as follow:

$$\begin{cases} \zeta_{\mathrm{loc}} = \mathrm{f}(\varepsilon) A_1 \dfrac{0.21}{\sqrt{\dfrac{\mathrm{R}_0}{\mathrm{D}_\mathrm{h}}}} \\ \text{with} \\ A_1 = 0.9\,\mathrm{sen}(\delta) \ \text{ if } \ \delta < 70° \\ A_1 = 1 \ \text{ if } \ \delta = 90° \\ A_1 = 0.7 + 0.35\dfrac{\delta}{90} \ \text{ if } \ \delta > 100° \\ \mathrm{f}(\varepsilon) = \dfrac{\lambda_{\mathrm{rough}}}{\lambda_{\mathrm{smooth}}} \ \text{ if } \ \mathrm{Re} < 2 \cdot 10^5 \\ \mathrm{f}(\varepsilon) = \left(1 + \varepsilon \cdot 10^3\right) \ \text{ if } \ \mathrm{Re} \geq 2 \cdot 10^5 \end{cases} \tag{114}$$

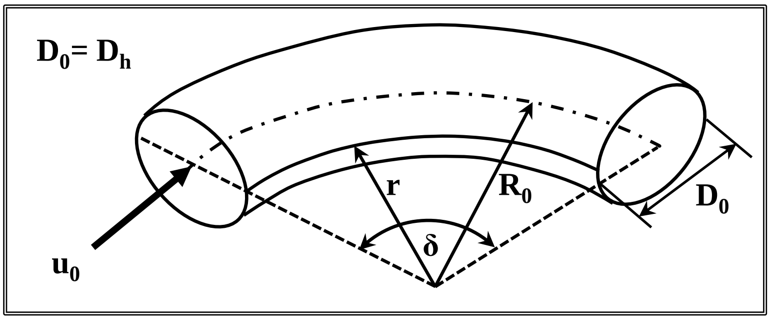

Figure 5.6. Bend main geometrical characteristics.

5.1.1.2 Conical diverging and converging nozzles

The transition from a smaller (larger) section to a larger (smaller) one through a smoothly diverging (converging) element is usually followed by irreversible losses of total pressure. The resistance mainly depends on the transition angle α, see Figure 5.7, and can be written as follow (reference kinetic energy is calculated for the smallest flow area, i.e. at D_0) :

$$\begin{cases} \text{Diverging and converging sections} \\ \zeta_{\text{fr}} = \dfrac{\lambda}{8\,\text{sen}(\frac{\alpha}{2})}\left[1-\left(\dfrac{D_0}{D_1}\right)^4\right] \\ \text{Diverging section} \\ \zeta_{\text{loc}} = 3.2\tan^{1.15}(\frac{\alpha}{2})\left[1-\left(\dfrac{D_0}{D_1}\right)^4\right] \\ \text{Converging section} \\ \zeta_{\text{loc}} = \left[-0.0125\left(\dfrac{D_0}{D_1}\right)^8 + 0.0224\left(\dfrac{D_0}{D_1}\right)^6 - 0.0723\left(\dfrac{D_0}{D_1}\right)^4 + 0.0044\left(\dfrac{D_0}{D_1}\right)^2 - 0.00745\right]\times \\ \qquad \times\left[(0.01745\alpha)^3 - 2\pi(0.01745\alpha)^2 - 10(0.01745\alpha)\right] \\ \text{with } \alpha \text{ in degree} \end{cases} \tag{115}$$

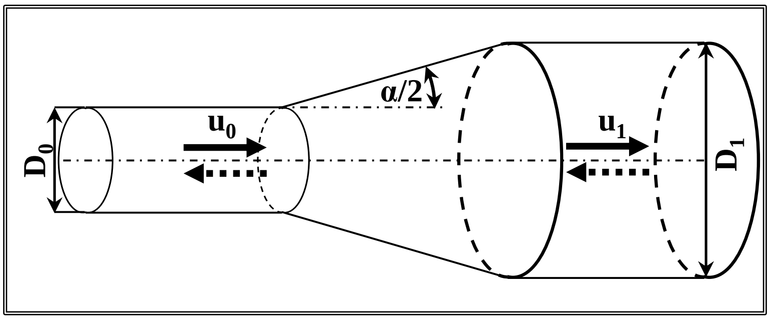

Figure 5.7. Diffuser (converging nozzle) main geometrical characteristics.

5.1.1.3 90° Tee-junction: merging, diverging and symmetrical converging flows

The 90° tee-junction, see Figure 5.8, is the basic geometry that composes the helium collectors, distributors and C-shaped header in the BB PHTS. In converging tees, a secondary stream from a lateral pipe enters into a main (usually bigger) leg and is merged with the main coolant stream. Conversely, a diverging tee distributes the coolant from the main stream to a secondary pipe. In a symmetrical tee-junctions, instead, 2 (usually equivalent) flow streams converge into a single pipe. Due to the PHTS cooling circuits segmentation, the loop collectors and distributors are normally made up of 5 tee-junction. The C-shaped header is characterized, from the hydraulic point of view, by a single, symmetrical converging flow.

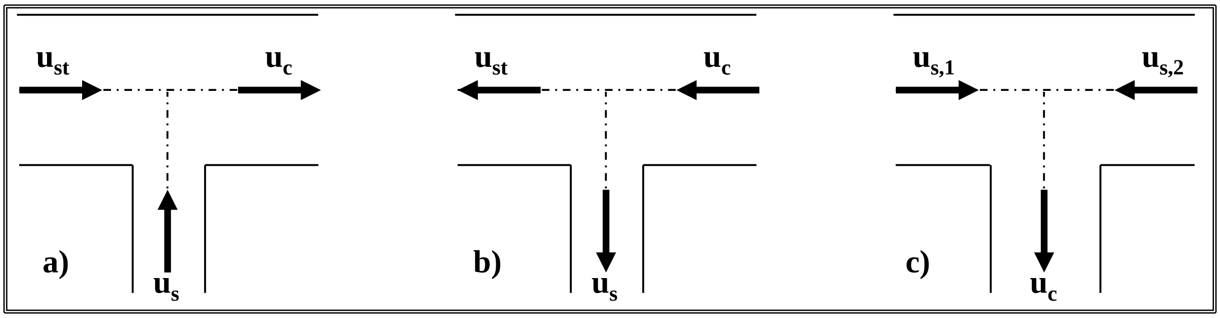

Figure 5.8. 90° Tee-junction: a)merging, b) diverging and c) symmetrical converging flows.

The resistance coefficients for both straight passage and side passage in the merging tees have been assessed according the equations below.

$$\begin{cases} \text{Side passage} \\ \zeta_{loc} = 1 + \left(\dfrac{u_s}{u_c} \right)^2 - 2\left(1 - \dfrac{\rho_c G_s}{\rho_s G_c} \right)^2 \\ \text{Straight passage} \\ \zeta_{loc} = 1.55\left(\dfrac{\rho_c G_s}{\rho_s G_c} \right) - \left(\dfrac{\rho_c G_s}{\rho_s G_c} \right)^2 \end{cases} \tag{116}$$

The resistance coefficients for both straight passage and side passage in the diverging tees have been assessed in agreement with the following equations:

$$\begin{cases} \text{Side passage} \\ \zeta_{loc} = 1 + \left(\dfrac{u_s}{u_c} \right)^2 \\ \text{Straight passage} \\ \zeta_{loc} = 0.4\left(\dfrac{\rho_c G_s}{\rho_s G_c} \right)^2 \end{cases} \tag{117}$$

The resistance coefficient for symmetric converging tees has been assessed as follow:

$$\zeta_{loc} = 1.25\left\{1+\left(\frac{A_c}{A_s}\right)^2 + 3\left(\frac{A_c}{A_s}\right)^2\left[\left(\frac{\rho_c G_s}{\rho_s G_c}\right)^2 - \left(\frac{\rho_c G_s}{\rho_s G_c}\right)\right]\right\} \tag{118}$$

In all cases the subscripts “s” and “c” denotes quantities that are calculated in the “side” and in the “common” branches, respectively. Moreover, the reference kinetic energy to estimate the pressure drops is always calculated in the common branch, where the total mass flow rate exists.

5.1.2 Pressure drops results

Pressure drops in the various sections of the 2 loops representative of the PHTS cooling circuits have been assessed in agreement with the equations just presented.

Clearly, the work has been repeated for both the two heat exchanger designs. Slight discrepancies in the pressure drops distribution can be noticed due to the small changes of the piping arrangement; nevertheless, a comparison between the cooling circuits of similar topology shows that the differences in total pressure drops are kept within a range of about 0.1 bar, with a the helical-coil design attaining the minor losses.

For the helical-coil exchanger architecture, in turn, the evaluations have been carried out taking into account the IHX and the steam generator configurations. However, for these two latter option, no differences are appreciable in the pipework pressure losses. This could have been anticipated because the piping layout is identical and, in spite of the non-equivalent pressure drop of the components itself, the small changes occurring in the helium density downstream the exchanger are “immediately” corrected by the circulators that restore the pressure and temperature level at the required value in the cold leg.

It must be remarked that as consequences of the 10 parallel paths, each circuit has needed a fine balancing of the pressure drops in order to deliver to right mass flow rate in each segments. In fact, due to the differences in lengths of feeding pipes and their number of bends, helium velocities and behaviour of the tee junctions of collectors and distributor distributors, it would have been rather difficult to have a self-balanced PHTS. Therefore, a small additional pressure drop has been added to equalise each single parallel flow, assuming that in the upper pipe chase, before crossing the Bioshield, the cold feeding pipes will be equipped with a valve that, during the plant commissioning phase, will be properly set to achieve the helium distribution. A similar approach will be used in ITER to balance the flows [198].

Table 5.3 through Table 5.6 report the pressure drops calculated in across the different regions of the circuits. The data for the helical coil IHX and SG are provided through the same tables. Figure 5.9 through 5.16 illustrate the various “pressure probing sections” to aid in reading the tables.

The “tuning valves” are placed in position 4→5, in all the loop typologies.

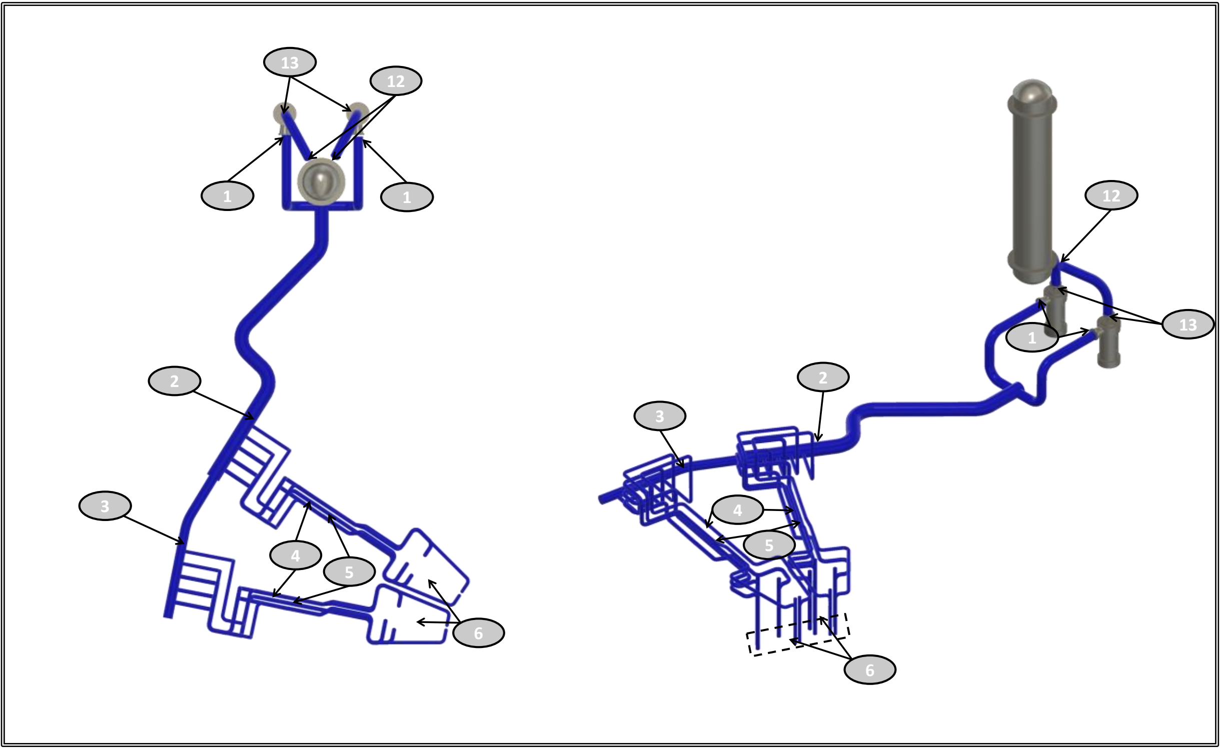

Figure 5.9. Cold piping for straight IHX option – longest loop. Pressure probing sections.

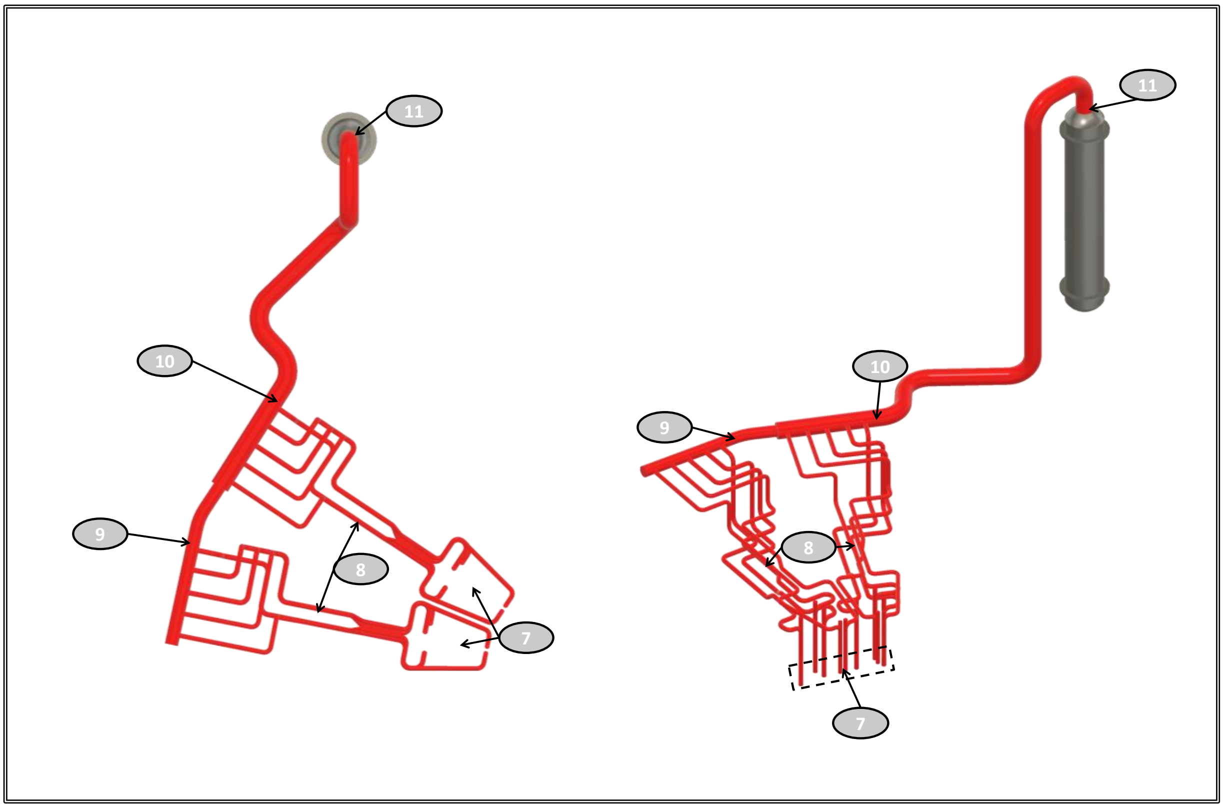

Figure 5.10. Hot piping for straight IHX option – longest loop. Pressure probing sections.

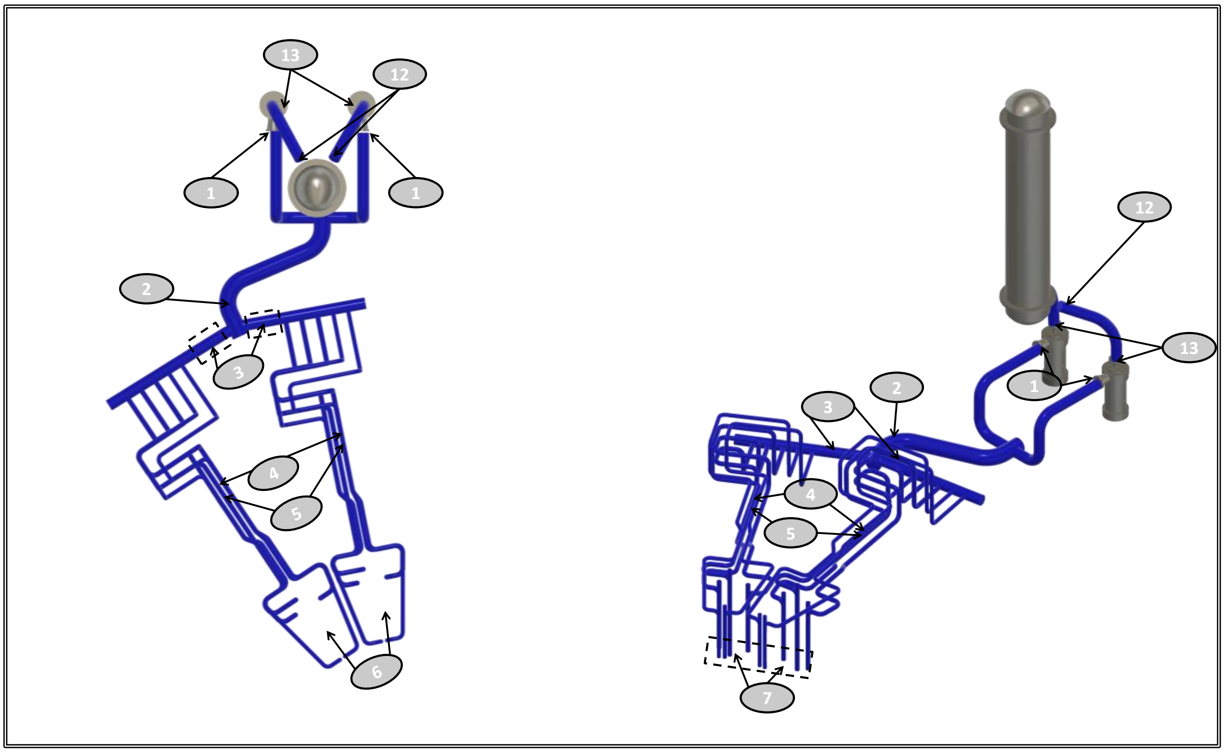

Figure 5.11. Cold piping for straight IHX option – shortest loop. Pressure probing sections.

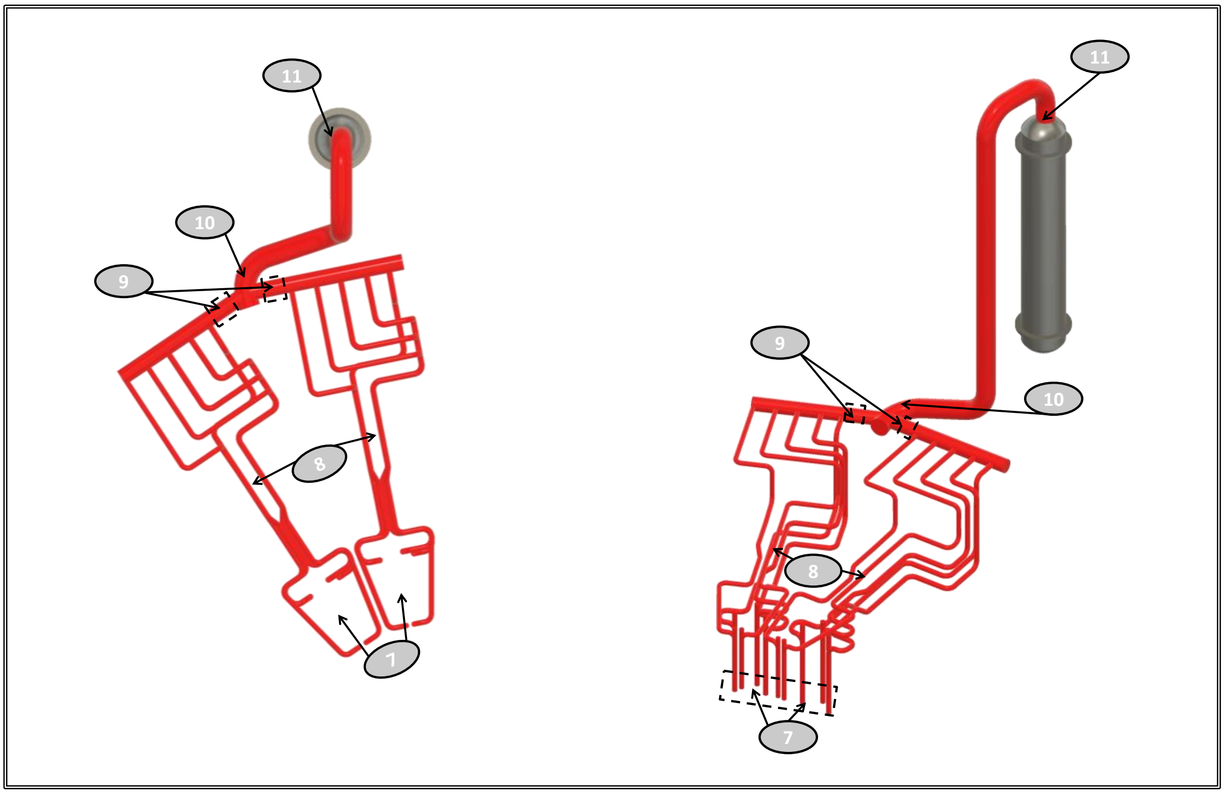

Figure 5.12. Hot piping for straight IHX option – shortest loop. Pressure probing sections.

Table 5.3. Longest loop pressure drops. Layout for standard S&T IHX.

[kPa]	**Sector 1**					**Sector 2**				
	OUTBOARD			**INBOARD**		**OUTBOARD**			**INBOARD**	
	OBL 1	**OBC 1**	**OBR 1**	**IBL 1**	**IBR 1**	**OBL 2**	**OBC 2**	**OBR 2**	**IBL 2**	**IBR 2**
1→2	12.9									
2→3	1.1					-	-	-	-	-
3→4;2→4	36.5	39.0	33.7	33.3	31.6	35.3	38.1	32.2	31.5	31.0
4→5 (valve)	2.5	0.0	9.4	25.6	31.1	11.8	8.9	18.6	34.8	38.6
5→6	16.4	14.9	17.2	14.1	14.0	16.5	14.9	17.2	14.1	14.0
6→7	79.9	79.9	79.9	79.9	79.9	79.9	79.9	79.9	79.9	79.9
7→8	15.4	15.4	15.3	9.6	9.6	15.4	15.4	15.3	9.6	9.6
8→9	31.3	32.8	26.5	19.7	15.9	-	-	-	-	-
9→10; 8→10	3.3					27.6	29.3	23.3	16.6	13.4
10→11	4.4									
11→12	60.7									
12→13	1.3									
1→13 (TOTAL)	**265.8**									

Table 5.4. Shortest loop pressure drops. Layout for standard S&T IHX.

[kPa]	**Sector 1**					**Sector 2**				
	OUTBOARD			**INBOARD**		**OUTBOARD**			**INBOARD**	
	OBL 1	**OBC 1**	**OBR 1**	**IBL 1**	**IBR 1**	**OBL 2**	**OBC 2**	**OBR 2**	**IBL 2**	**IBR 2**
1→2	12.1									
2→3	7.3									
3→4	34.1	37.6	30.9	32.5	31.2	36.2	36.2	36.5	26.8	27.4
4→5 valve	3.6	0.2	11.0	25.0	30.3	0.0	2.6	1.3	34.5	39.6
5→6	16.4	14.9	17.2	14.1	14.0	16.4	14.9	17.2	14.1	14.0
6→7	79.9	79.9	79.9	79.9	79.9	79.9	79.9	79.9	79.9	79.9
7→8	15.4	15.4	15.3	9.6	9.6	15.4	15.4	15.3	9.6	9.6
8→9	31.3	32.8	26.6	19.7	15.9	32.9	31.8	30.7	16.0	10.4
9→10	5.9									
10→11	2.9									
11→12	60.7									
12→13	1.3									
1→13 (TOTAL)	270.9									

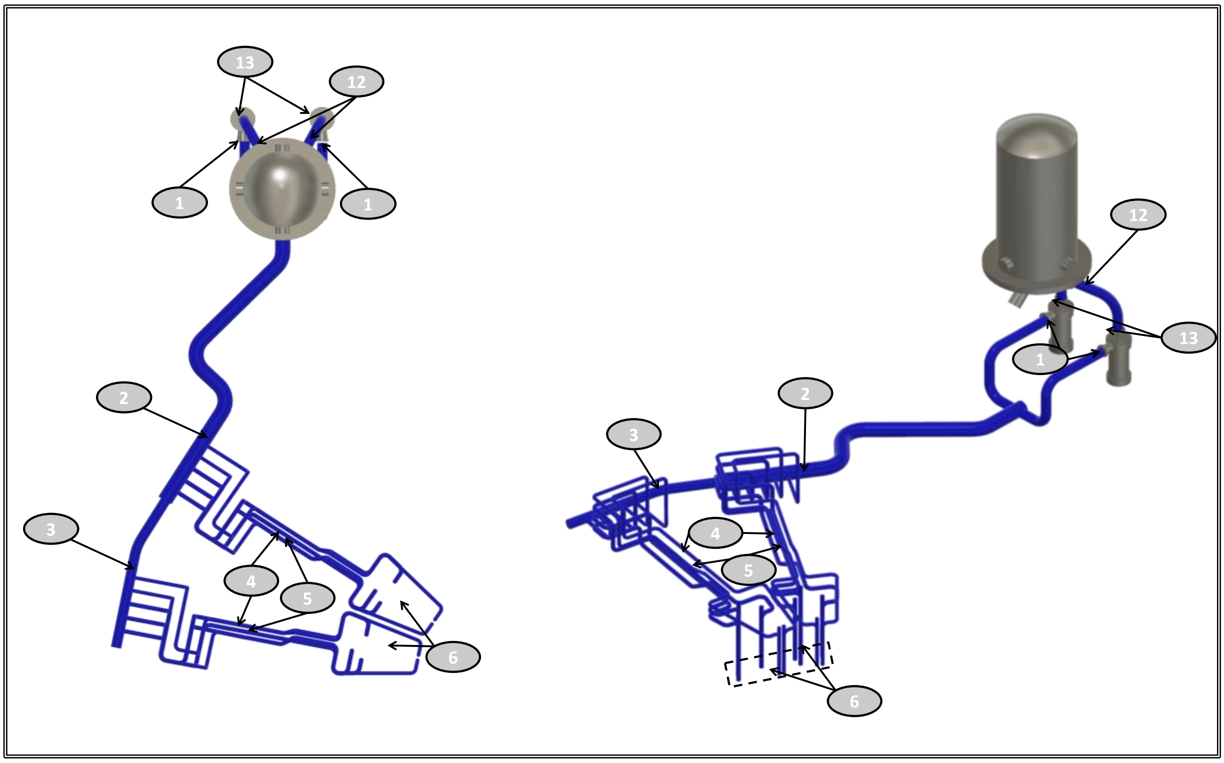

Figure 5.13. Helical IHX/SG options - Cold pipes - Longest loop. Pressure probing sections.

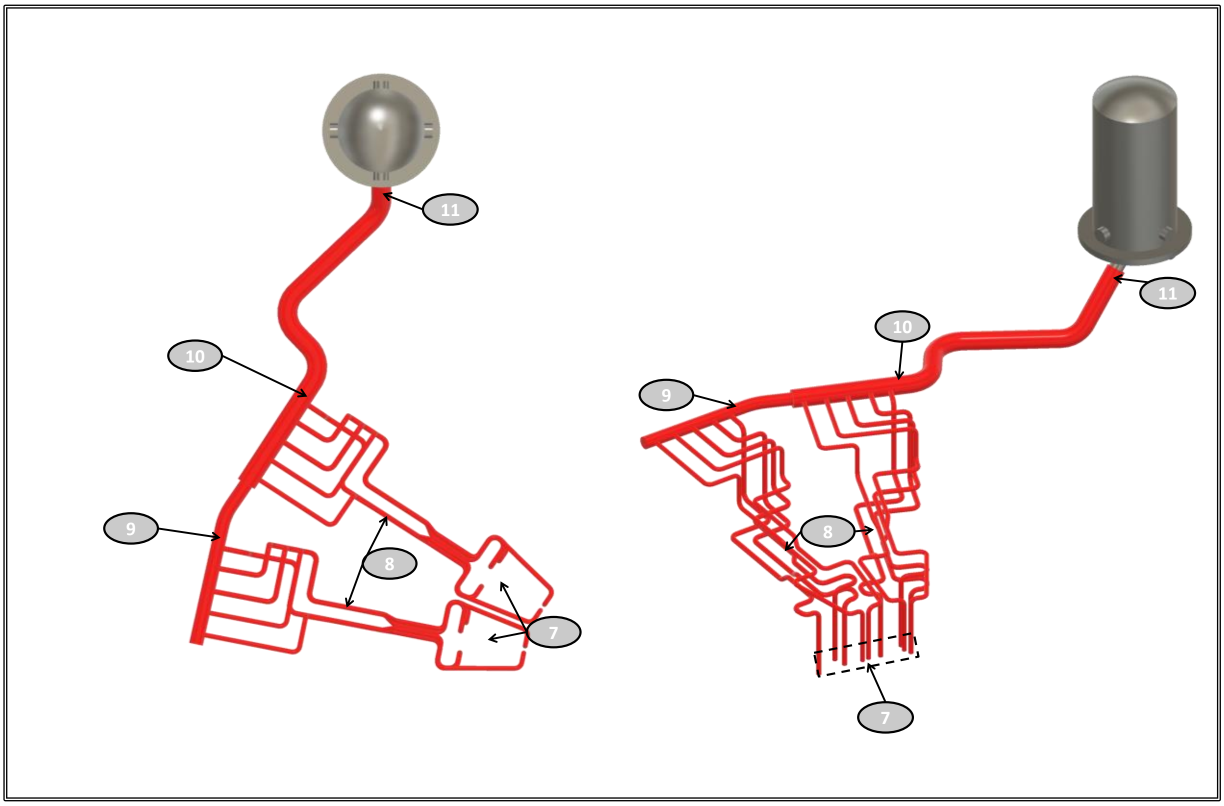

Figure 5.14. Helical IHX/SG options - Hot pipes – Longest loop. Pressure probing sections.

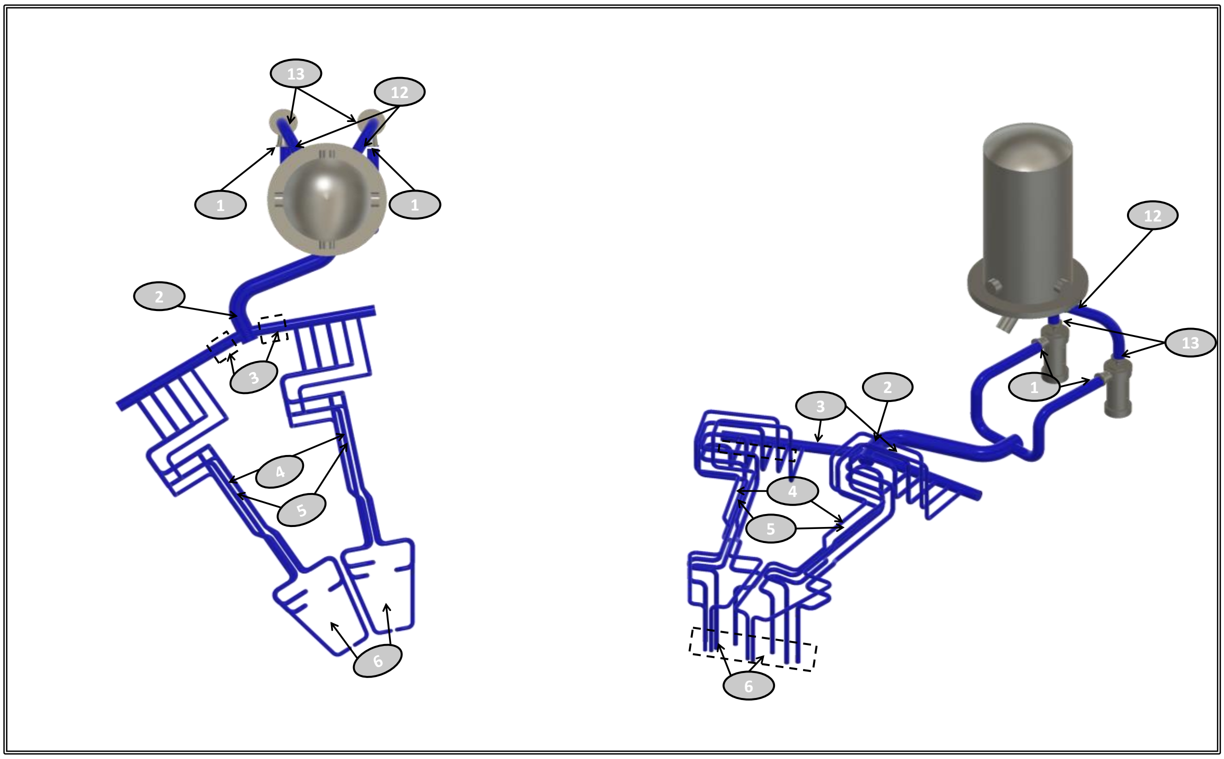

Figure 5.15. Cold piping for helical IHX option – shortest loop. Pressure probing sections.

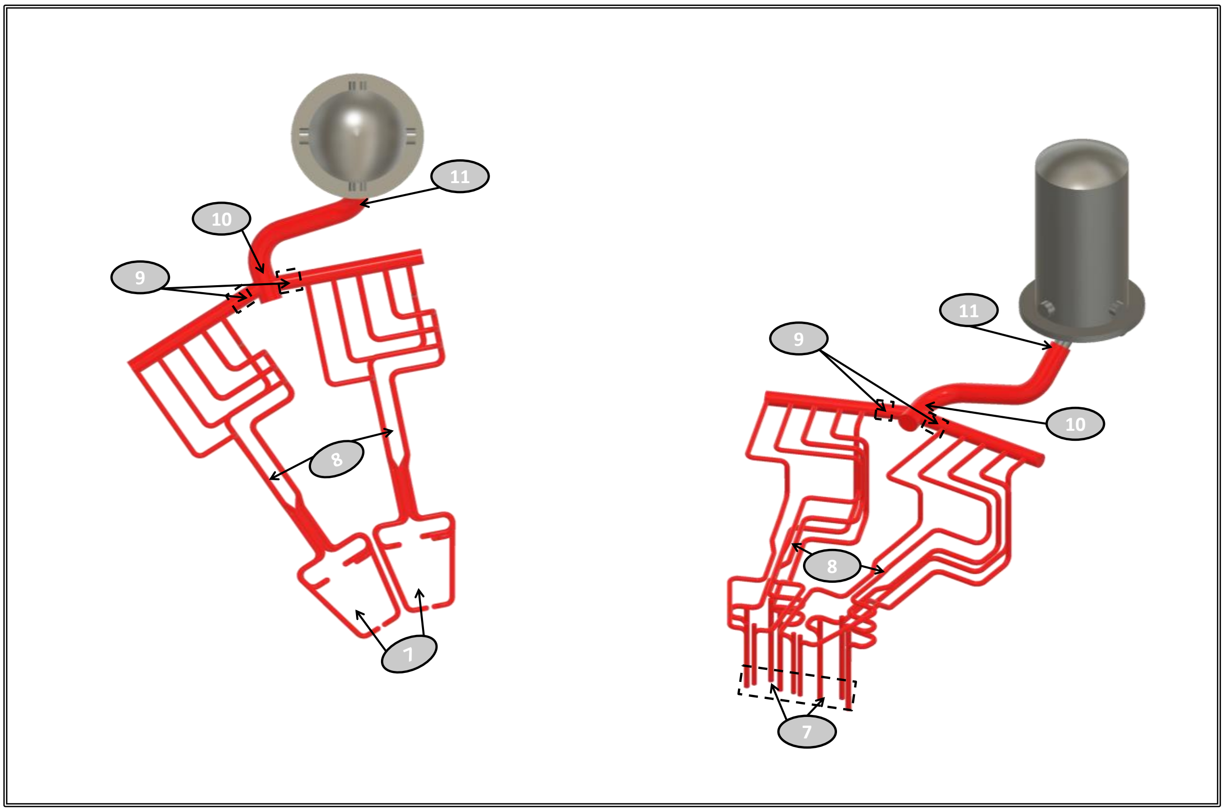

Figure 5.16. Hot piping for helical IHX option – shortest loop. Pressure probing sections.

Table 5.5. Longest loop pressure drops. Layout for helical coil IHX and SG.

[kPa]	**Sector 1**					**Sector 2**				
	OUTBOARD			**INBOARD**		**OUTBOARD**			**INBOARD**	
	OBL 1	**OBC 1**	**OBR 1**	**IBL 1**	**IBR 1**	**OBL 2**	**OBC 2**	**OBR 2**	**IBL 2**	**IBR 2**
1→2	12.9									
2→3	1.1					-	-	-	-	-
3→4;2→4	36.5	39.0	33.7	33.3	31.7	35.3	37.9	32.0	31.3	30.8
4→5	2.5	0.0	9.4	25.5	31.0	11.8	9.1	18.8	35.0	38.8
5→6	16.4	14.9	17.2	14.0	13.9	16.4	14.9	17.2	14.0	13.9
6→7	79.9	79.9	79.9	79.9	79.9	79.9	79.9	79.9	79.9	79.9
7→8	15.3	15.2	15.1	9.5	9.5	15.3	15.2	15.1	9.5	9.5
8→9	31.2	32.7	26.5	19.6	15.8	-	-	-	-	-
9→10; 8→10	3.3					27.5	29.2	23.3	16.5	13.4
10→11	2.3									
11→12	58.3 (IHX) / 68.9 (SG)									
12→13	1.3 (IHX) / 1.3 (SG)									
1→13 (TOTAL)	**261.1 (IHX) / 271.6 (SG)**									

Table 5.6. Shortest loop pressure drops. Layout for helical-coil IHX and SG.

[kPa]	**Sector 1**					**Sector 2**				
	OUTBOARD			**INBOARD**		**OUTBOARD**			**INBOARD**	
	OBL 1	**OBC 1**	**OBR 1**	**IBL 1**	**IBR 1**	**OBL 2**	**OBC 2**	**OBR 2**	**IBL 2**	**IBR 2**
1→2	12.1									
2→3	7.3									
3→4	34.1	37.6	30.9	32.5	31.2	36.2	36.2	36.5	26.8	27.4
4→5	3.6	0.2	11.0	25.0	30.2	0.0	2.6	1.3	34.4	39.5
5→6	16.4	14.9	17.2	14.0	13.9	16.4	14.9	17.2	14.0	13.9
6→7	79.9	79.9	79.9	79.9	79.9	79.9	79.9	79.9	79.9	79.9
7→8	15.3	15.2	15.1	9.5	9.5	15.3	15.2	15.1	9.5	9.5
8→9	31.2	32.8	26.5	19.6	15.9	32.8	31.7	30.6	16.0	10.4
9→10	5.9					5.8				
10→11	1.5									
11→12	58.3 (IHX) / 68.9 (SG)									
12→13	1.3 (IHX) / 1.3 (SG)									
1→13 (TOTAL)	**266.9 (IHX) / 277.5 (SG)**									

6 Preliminary circulator sizing and typology selection

In the paragraph 4.4.1 we have already explained the laws of perfect gases can be applied for helium in the temperature and pressure region which is relevant for the DEMO plant. The uncertainties caused by the correction for the ideal gas helium which has been indicated before are relatively small and in the order of 1–2%. Therefore, the equations (25) and (26) can be applied to obtain results with an reasonable degree of confidence.

However, in the previous chapters the focus has been on the power that, in the end, the circulator transfer to the helium to let it circulate. If the electrical power required by the circulator and its drive needs to be calculated, it is necessary to considers both mechanical and electrical efficiencies of the whole circulator assembly. The circulator assembly is comprehensive of turbomachinery, motor and mechanical elements that allow the coupling between the first two main components. These two efficiencies are usually higher than the isentropic one [111] so that assuming a product of the two yields of about 0.9 it is likely that conservative results are achieved. For instance, the electrical drives can have an electrical efficiency of 96÷98% [199], thus in the hypothesis of adopting the same value for the mechanical coupling efficiency, the global yield might be 0.92 as minimum.

Nevertheless, using the more conservative assumptions, the total circulator electrical consumption has been, hence, calculated from the relation:

$$W_{\mathrm{Circulator}}^{\mathrm{elect}} = \frac{G_{\mathrm{He}} c_{p_{\mathrm{He}}} T_{\mathrm{in}}^{\mathrm{Circulator}}}{\eta_{\mathrm{mech/elect}} \eta_{\mathrm{is}}} \left(\beta^{\frac{\gamma-1}{\gamma}} - 1 \right) \tag{119}$$

Taking into account the thermal-hydraulic features of the PHTS previously described, the power per circulator is still kept below 6 MW in all the possible BoP options investigated. However, due to the large amount of turbomachinery present in the circuits, namely sixteen, the whole power that must be provided to the electrical drives is slightly above 90 MW, see from Table 6.1 to Table 6.3, which is in the order of the 10% of the turbine gross electrical power [47].

Such a percentage is quite high if one considers that, normally, the power of the circulators corresponds to 3÷5 % of the net electrical power of a gas-cooled reactor with steam cycle. However it is worth to remember that in gas reactors the temperature rise is at least 2 times larger than in the current DEMO design conditions. Therefore, in the hypotheses of an equal plant gross output and similar pressure drops, if a comparable temperature rise would be applied to the DEMO BB PHTS, a decrease of the circulators power by a factor 2 might be reasonably expected, thus obtaining a values with are in line with the fission industry. Unfortunately, the occurrence of this situation is not currently possible due to the strict operating limits of the low activation structural steel adopted for the In-vessel components.

Table 6.1. Circulator characteristics and electrical consumption – standard S&T IHX option.

	T_{in} [°C]	p_{in} [bar]	Pressure ratio [-]	Volumetric flow [m^3/s]	η_{mech}/η_{is} [-]	Motor power [MW]
Longest Loop Circulator	291.08	78.21	1.034	16.92	0.90/0.85	5.72
Shortest Loop Circulator	290.91	78.19	1.035	16.92	0.90/0.85	5.82
Total electrical power (16 circulators) [MW]	92.31					

Table 6.2. Circulator characteristics and total electrical consumption – helical IHX option.

	T_{in} [°C]	p_{in} [bar]	Pressure ratio [-]	Volumetric flow [m^3/s]	η_{mech}/η_{is} [-]	Motor power [MW]
Longest Loop Circulator	291.24	78.35	1.033	16.91	0.90/0.85	5.61
Shortest Loop Circulator	291.04	78.33	1.034	16.91	0.90/0.85	5.74
Total Power	90.79					

Table 6.3. Circulator characteristics and total electrical consumption – helical IHX option.

	T_{in} [°C]	p_{in} [bar]	Pressure ratio [-]	Volumetric flow [m^3/s]	η_{mech}/η_{is} [-]	Motor power [MW]
Longest Loop Circulator	290.88	78.25	1.035	16.93	0.90/0.85	5.84
Shortest Loop Circulator	290.69	78.23	1.035	16.92	0.90/0.85	5.97
Total Power	94.45					

As regard to the circulator configuration, in the latest modular HTR designs, the circulator unit consists of a one-stage radial compressor driven by an electrical motor which is controlled by changing the speed. The motor is cooled by helium, which in turn is cooled by water in a closed cycle. The unit is arranged in vertical position at the top of the steam generator heating section.

On the side of gas intake there is a flap, which can regulate the gas flow. The shaft of the motor has two bearings; the single-stage radial rotor is mounted on the motor shaft in an overhang position. The shaft bearings are lubricated and cooled by oil. The total unit can be removed with special devices without air ingress to the primary circuit. Both components, circulator and drive, are integrated into a separate primary enclosure, which is flanged to the vessel of the steam generator. Therefore, relatively easy access to the components allows for the repair and/or the replacement of the unit [111].

In DEMO the principle of inserting the compressor into the exchanger is currently not foreseen because the need of 2 circulators per loop makes the option of placing the component into the upper head of heat exchanger/steam generator vessel hard to be implemented.

However, regardless to the location in which circulator shall be placed, the experience maturated over the years in gas-reactor power plant might provide some useful information for the DEMO circulators design.

Some important characteristics of the circulator built and operated in the helium-cooled fission reactors are briefly reported below. This summary cannot be comprehensive of all the aspects that should be kept in mind during the design of such a turbomachinery but it can be a good starting point to reach a preliminary selection of the component type. To obtain more details on these devices it is suggested the reading of [129] or [201].

Until now, helium circulators have been built and operated in the HTR plants, AVR, THTR-300 [200], Dragon, Peach Bottom, Fort St. Vrain, HTTR, and HTR-10 reactors.

The AVR had two helium circulators arranged in the bottom part of the reactor pressure vessel. Each circulator consists of an asynchronous motor, which can vary the rotor speed via a frequency converter, in oil-lubricated bearings and a fan wheel in overhung position on the motor shaft. The machines are arranged in horizontal position, and they are accessible from the inner containment. Labyrinths and a barrier gas system prevented the oil from malting its way into the cooling gas circuit and the cooling gas from penetrating the motor housing. The circulators were designed for maintenance-free operation however special devices allowed the entire replacement. Apart from a bearing change in 1979, which made necessary to dismount one of the two circulators, these equipment run without any maintenance problems for 20 years. The speed change of the blowers allowed a reduction from 100 to 50% within two minutes.

In the THTR-300 reactor, the helium coolant gas was circulated by six parallel flow coolant circulators, each connected to a steam generator. The circulators were anchored firmly to each steam generator via holes in the cylindrical PCRV wall. Though one of these holes, equipped with a liner flange, the system lines for coolant water, oil, gas, power, and measuring instruments were passed. The circulator rotor, the drive motor with coolers, and the shutoff and control valve, including the drive of each of the components, were integrated into one global circulator unit. The motor operated in a helium atmosphere under the respective reactor pressure of around 4 MPa. The single-stage radial wheel were mounted on the motor shaft in an overhung position. The shaft bearings are lubricated and cooled by oil. A sealing gas system supplied with pure helium prevented oil from leaking into the primary coolant circuit as well as activated coolant gas from leaking into the oil circuit. The shutoff and control valve located on the intake side of the circulator had a hydraulic drive mechanism. It serves for individual control of the delivery of the coolant gas circulator and ensures the functions reported in the following.

- Setting of a minimum coolant gas flow during start-up of an individual steam generator circulator unit during operation of the other units;
- Plugging of a shutoff steam generator circulator unit on the coolant gas side, with the possibility of setting a reusable backflow of cold coolant gas through the shutoff steam generator;
- Throttling to a lower coolant gas flow rate through a steam generator at constant circulator speed, e.g., during removal of decay heat.

Apart from the helium circulators, a proven example of gas circulators operated in nuclear environment with large power is the component in the last build AGR plants. They are still being operated with good availability since decades in the large AGR power plants so that they form a useful basis for the technology of circulators of helium-cooled reactors. Especially, the large electrical power which has been realized in CO_2-cooled reactors demonstrates the feasibility to build large machines for helium cycles too [203].

Each compressor has a motor of about 6 MW that allows the centrifugal impeller to circulate the CO_2 through the reactor. The inlet gas temperature is around 300 °C, the pressure in many cases 4 MPa and the pressure rise in the order of 3 bar. In AGRs, the circulators are arranged in vertical position at the bottom of the vessel. They are completely enclosed with an electrical, induction motor and control gear in a penetration at the vessel bottom. The CO2 inlet is at the top of the component and the outlet on the side. The normal operation speed of the machine is 3000 rpm and the gas flow is varied by inlet guide vanes, which also control the reverse gas flow, when the machine is operating in a stationary mode. However, a variable frequency supply of the motor via a separate circuit breaker enables the operation at low speeds: the circulator speed can drop under trip conditions to around 450 rpm. The guide vanes, links, drive shafts, and associated gears are located within the pressure vessel penetration, which houses each circulator unit. The drive motor gearbox and the equipment for position indication are arranged outside the penetration. The machine has shaft bearing seals and a shaft labyrinth system to control the gas flow between the reactor gas circuit and the motor compartment and to prevent the ingress of oil into the reactor gas circuit.

The main design features that characterize the circulators just described are given in Table 6.4.

As can be seen, although some constructive differences exist, the components discussed until now share several analogies. Moreover, many important features that characterize both helium (THTR-300 and HTR-PM) and CO_2 (Hartlepool) circulators are comparable with the data that distinguish the DEMO BB turbomachinery, namely the volumetric flow, power, and pressure rise. From the Table 6.4, in addition, it can also be gathered that use of axial circulator might become necessary only if the flow rate would be very high [202], like in the Fort Saint Vrain reactor, whose data have been put as basis for comparison respect to the other blower types.

Table 6.4. Main characteristics of the gas-cooled reactor circulators.

Reactor	AVR	THTR-300	HTR-PM	Fort St. Vrain	Hartlepool
Coolant	He	He	He	He	CO_2
Type	Centrifugal	Centrifugal	Centrifugal	Axial	Centrifugal
Motor power [kW]	220	2297	4500	3954	5400
Vol. flow [m^3/s]	5.8	15.2	15.0	32.2	13.0
Inlet press. [bar]	10.9	36.7	70.0	43.7	38.1
Inlet temp. [°C]	200	250	243	394	282
Pressure rise [kPa]	8.3	122.7	200	96.7	328.2
Pressure ratio [-]	1.008	1.033	1.029	1.020	1.086
Impeller diam. [m]	0.71	0.90	1	0.81	0.86
Nom. Speed [rpm]	3500	5600	3750	9550	2970
Speed range [%]	11÷125	47÷107	20÷105	10÷113	15÷100

It is obvious that the design of any compressor must be based upon detailed aerodynamic and stress calculations, well-supported by developmental test data. During the early design phases, however, it is often useful to use simplified methods in order to rough in the compressor characteristics. For instance, exploiting the methodology of Balje [204], the most promising design parameters for a circulator can be determined. According to the Balje curves, developed through similarity considerations, it is possible to compute the optimal design geometry to obtain the maximum achievable efficiency, as function of the specific speed and the specific diameter of the turbomachine. The angular speed and the rotor diameter are related to the specific speed and the specific diameter by the following expressions:

$$N_s = N \frac{\sqrt{\dot{V}_{in}}}{\left(\frac{144 \Delta p}{\rho_{in}}\right)^{0.75}} \tag{120}$$

$$D_s = D\frac{\left(\frac{144\Delta p}{\rho_{in}}\right)^{0.25}}{\sqrt{\dot{V}_{in}}} \tag{121}$$

where N is the rotational speed, D the rotor diameter, $\dot{V}_{in}$ is the inlet volumetric flow and the term in the bracket defines the adiabatic head of the circulator. All the quantities in British Units as depicted in .

By means of these two simple relations, 4 possible configurations for the DEMO circulators have been assessed with the aim of outlining the boundaries within which the design of the circulator should be kept to ensure an operation in the high efficiency regime. Adopting the useful gas-reactor circulator data collected in [129] and [199], it has been estimated the range in which the couples angular speed-impeller diameter should vary to strive for a good design.

The calculation has proceeded as follow.

- Selection of 3000 rpm and 10000 rpm as minimum and a maximum values for the rotational frequency of the impeller. Intermediate speeds have been then chosen to make available a more comprehensive array of values for the investigation. The choices of maximum and minimum velocities have been mainly driven by the literature review and some general considerations about mechanics and safety, considering the quadratic dependence on the angular velocity of the stresses in rotating equipment.
- Calculation of the specific speeds, N_s, for all the options to be investigated.
- Use of the Balje graph, see Figure 6.1, to find the specific diameters, D_s, that intersect the pertaining specific speed curve in the zone of maximum achievable efficiency.

The results are directly reported on top of the Figure 6.1, where a portrayal of many circulator data are also given. The data related to the gas circulator taken as examples during the previous discussion are highlighted too.

In agreement with the expectations, the centrifugal circulators are all located in the area of maximum efficiency for the radial geometries, while the Fort St. Vrain compressor finds place in the sphere of interest for achieving a maximum efficiency with an axial typology.

As regard to the assessment for the DEMO PHTS, the first point that comes to light is the unlikelihood to adopt an axial flow compressor to let helium circulate through the cooling circuits. In fact, even for the highest angular speed investigated, the geometry of the impeller could not reproduce a purely axial flow, instead the component should be chosen among the so called mixed flow machines.

With the minimum angular velocity, dimensioning the whole machine for an high efficiency regime could be problematic because the size of the rotor would be rather larger than those commonly employed in compressors with similar powers and volumetric flows.

The assessment has hence suggested that the range of values encompassed by the two intermediate couples of values selected for the angular speed and the rotor diameter, namely 4500rpm/1.18m and 6000rpm/0.92m, might be suitable to achieve a reasonable design of the circulator, being the dimensions of the component as well as the specific numbers very close to those of the HTR-PM and THTR-300 compressors, respectively.

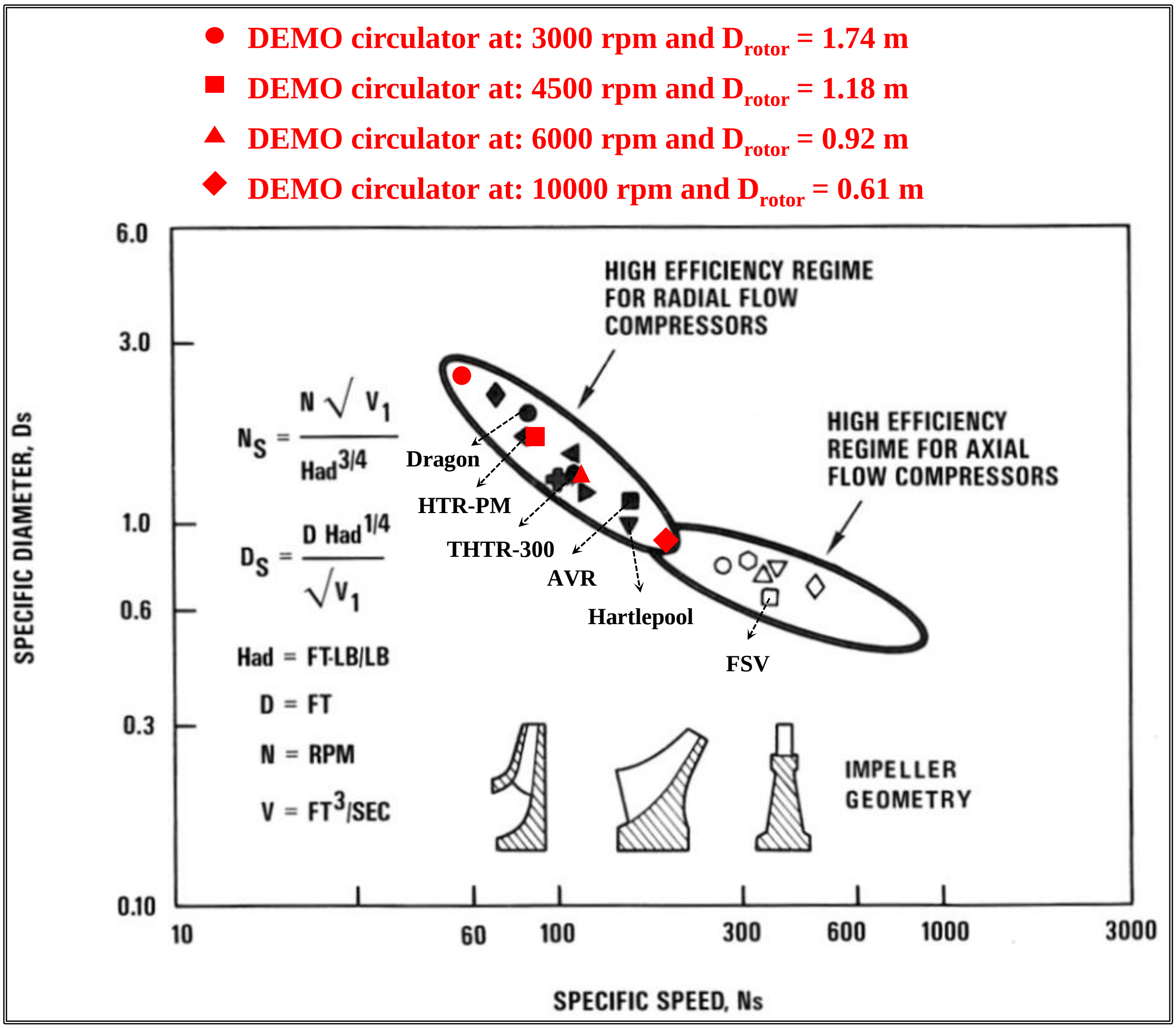

Figure 6.1. High efficiency regions for BB PHTS helium circulators.

7 Brief summary on the PHTS design and integration

The layout of the HCPB BoP systems has been outlined, developed and integrated in a 3D-CAD model of the DEMO baseline 2017. The BB primary system have been sized with a highly degree of segmentation of its cooling loops which are 8. These circuits are completely independent, from mechanical point of view, in order to limit some common mode failures.

Each cooling circuit provides helium to all ten segments of 2 blanket sectors. The main equipment of the PHTS have been preliminary sized in order to meet not only the needs of the BoP but even to satisfy the requirements of the integrations and safety.

Table 7.1 through Table 7.4 provide a brief summary the overall data characterizing the system for the different BoP options.

The global arrangement of the PHTS within the tokamak building is depicted from Figure 7.1 to Figure 7.4.

Table 7.1. BB PHTS – Main components per loop.

Piping elements	
Hot feeding pipe	10
Cold feeding pipe	10
Hot collector	2
Cold distributor	2
Hot leg	1
Cold leg	1
Main hot leg	1
Cold header	1
Main equipment	
Heat exchanger/Steam Generator	1
Circulator	2

Table 7.2. BoP with ESS – BB PHTS with standard S&T exchanger option.

BB Thermal Power [MW]	2029.1
Circulator power [MW]	92.3
Total helium volume (with In-vessel inventory) [m^3]	1812.5
Total pipework length [m]	6838.4
Total internal piping surface [m^2]	8389.5
Total external piping surface [m^2]	9237.9
Number of cooling circuits [-]	8

Table 7.3. BoP with ESS – BB PHTS with helical S&T exchanger option.

BB Thermal Power [MW]	2029.1
Circulator power [MW]	90.79
Total helium volume (with In-vessel inventory) [m^3]	2127.3
Total pipework length [m]	6633.1
Total internal piping surface [m^2]	7621.6
Total external piping surface [m^2]	8386.2
Number of cooling circuits [-]	8

Table 7.4. BoP without ESS – BB PHTS with helical-coil steam generator.

BB Thermal Power [MW]	2029.1
Circulator power [MW]	94.5
Total helium volume (with In-vessel inventory) [m^3]	2145.5
Total pipework length [m]	6633.1
Total internal piping surface [m^2]	7621.6
Total external piping surface [m^2]	8386.2
Number of cooling circuits [-]	8

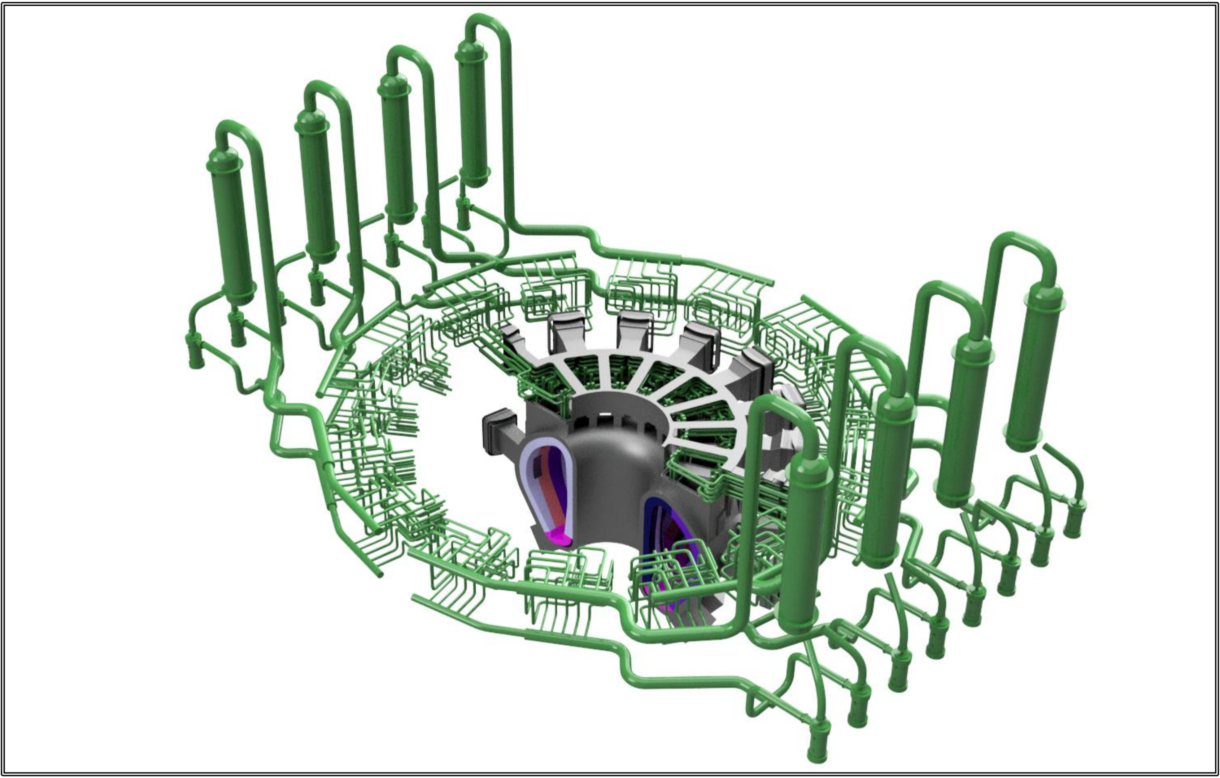

Figure 7.1. PHTS with standard S&T layout

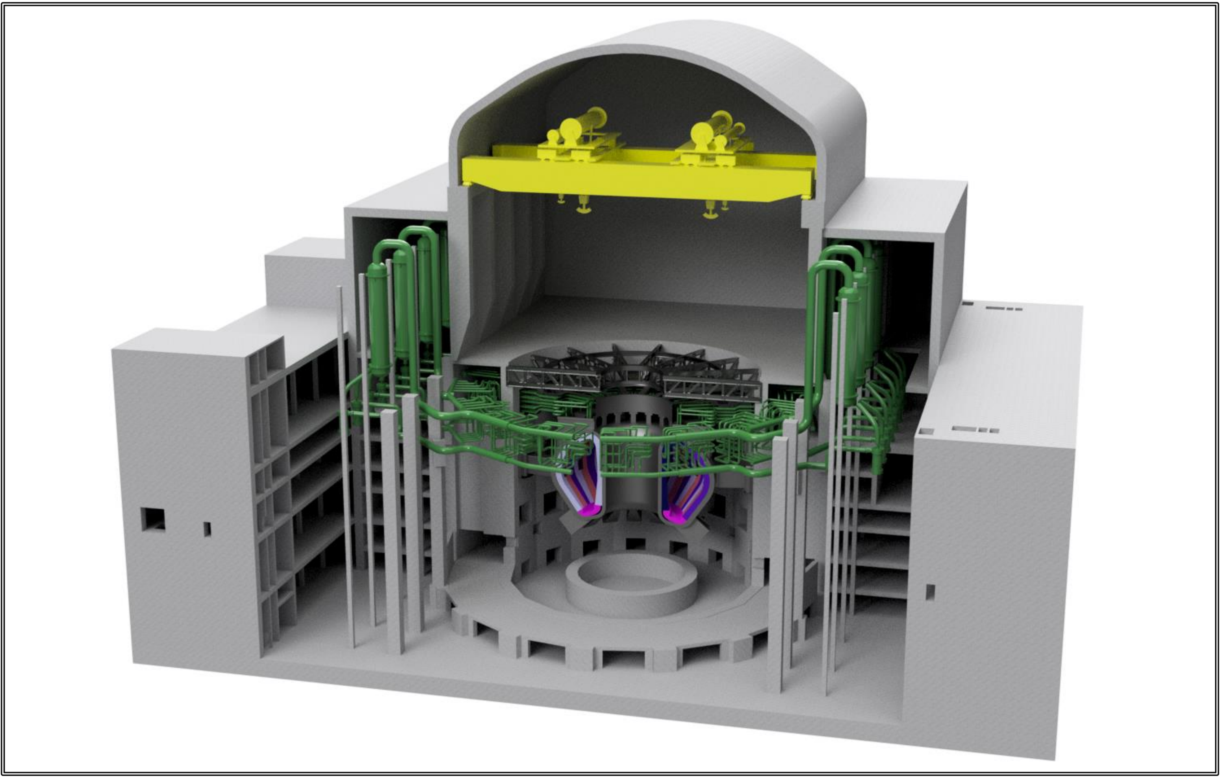

Figure 7.2. PHTS with standard S&T layout – integration into Tokamak building

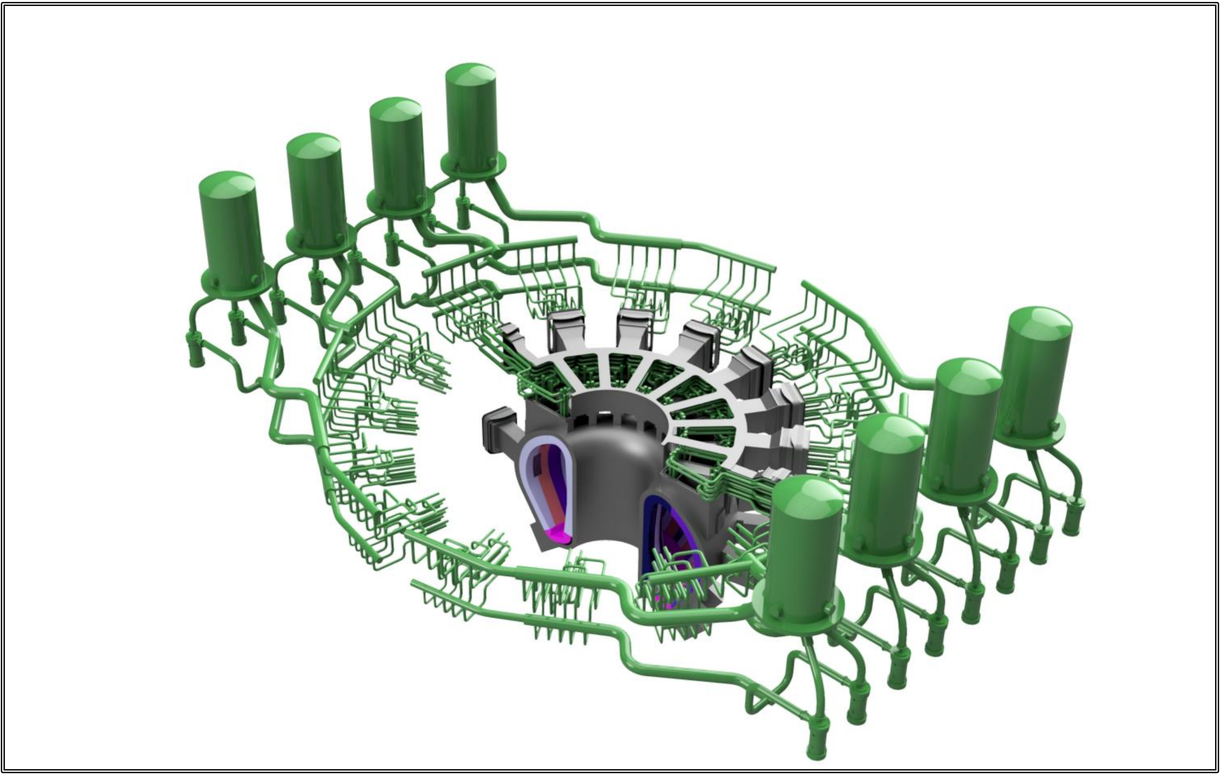

Figure 7.3. PHTS with helical-coil exchanger layout

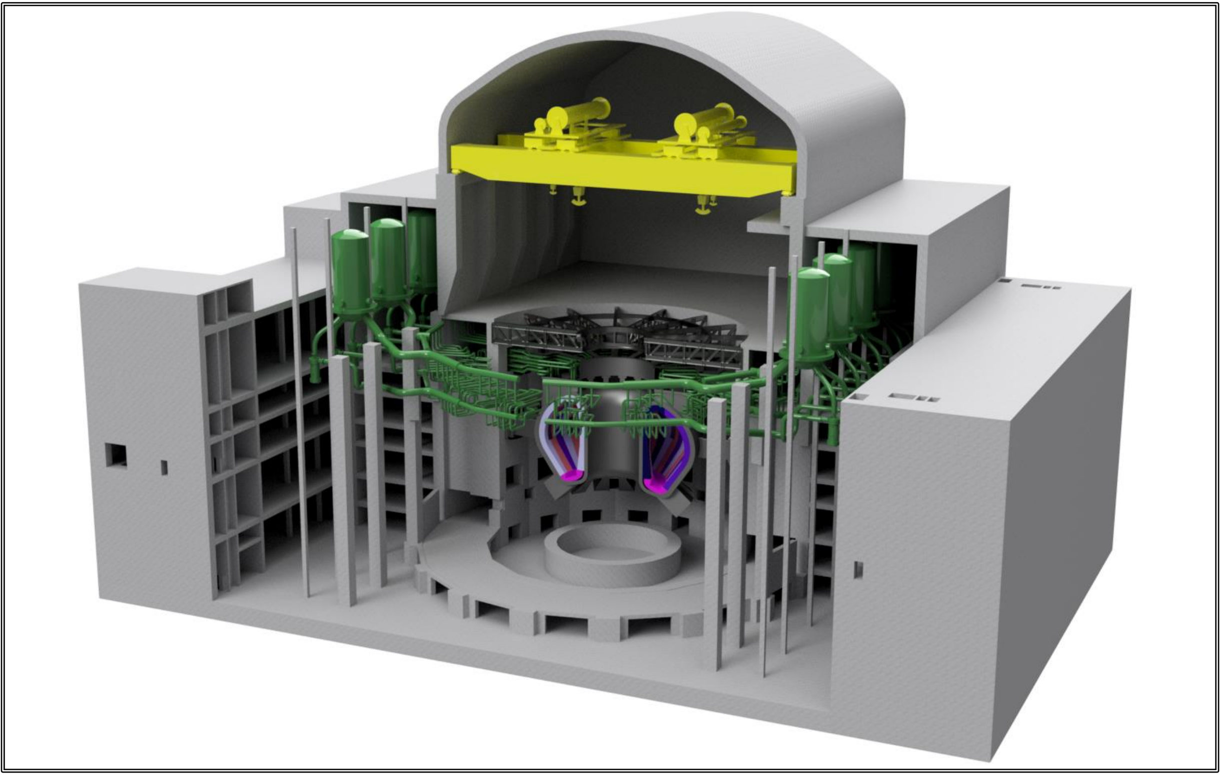

Figure 7.4. PHTS with helical-coil exchanger layout – integration into Tokamak building.

8 Thermal-hydraulic assessment of BB PHTS performances

8.1 Introduction

The procedures described in the previous chapter have been developed with the aim of obtaining a conceptual design of the main BB PHTS equipment which have been outlined, sized and integrated within the Tokamak cooling rooms. Their thermal-hydraulic features appear compliant with the fixed criteria and the overall cooling capabilities of the primary system should be ensured keeping the overall electrical power consumption of the circulators within acceptable value for a first-of-a-kind fusion power reactor.

The methodology adopted so far has been meticulously expanded upon the specific thermal-hydraulic aspects of the components, with the purpose of limiting the deviations from the reality, however, in spite of this, it has been judged appropriate to assess the thermal-hydraulic performances of the system with an higher degree of detail. This choice has been needed in order to understand if the “reference design values” have been found with a reasonable level of confidence. In fact, should the previous results fall within a range of uncertainties typical of the constitutive models and the correlations which must be unavoidably employed as closure equations, the whole approach might be positively evaluated, thus being also used obtain a thermal-hydraulic design of other parts of the Balance of Plant, such as the Divertor and VV PHTSs, as well as the whole IHTS.

Therefore, it has been decided to verify the robustness of some relevant calculations by means of well-established computational tools. In particular, a Computational Fluid Dynamic code has been used to assess the pressure drops in the pipework of one loop representative of the 8 PHTS parallel circuits. The circuit investigated contains all those features that can be a sources of error in a (semi-)analytical calculation of the head losses in a complex network of pipes. Indeed, as previously mentioned, the presence of closely spaced elements such as tee-junctions, collectors/distributors, bends, can dramatically affect the results obtained unless a great care has been taken in the evaluations of each single disturbance that the fluid stream may encounter.

However, in spite of the code capabilities and the continuous improvements in the computational methods and numerical algorithms, a fully 3-D approach is viable to study only some portions of the entire circuit, at least for what concerns a single simulation with a unique flow domain. Basically, due to the massive amount of calculations required by a CFD tools for unit of volume, the thermal-hydraulic study of a whole primary circuits of a fusion reactor is still out of reach for computational resources commonly available in the majority of the research centres and the universities.

Hence, in order to assess the global thermal-hydraulic behaviour of an entire loop, a RELAP5-3D model has been developed. In particular, the activity carried out though the adoption of this code has been articulated in two steps.

During the first part, the model has been devoted to evaluate the thermal-hydraulic behaviour of the main equipment of the BB PHTS under hypothetical steady-state conditions. This has allowed to verify the thermal-hydraulic performances of the intermediate heat exchanger and to assess whether the cooling capabilities of the loop are sufficient to fulfil the requirements of all the segments that the circuit feeds. In the second step, the investigations have dealt with the DEMO actual normal operation: the total duty cycle of the Tokamak, namely Pulse, Dwell and Ramp-up/down phases, have been simulated. The aim has been to understand the response of the system during nominal operational transients and begin the definition of the strategies to be followed in order to minimize the thermal fluctuations due to the power oscillation.

8.2 Methodology

As mentioned, due to the extreme complexity of the flow domain of the entire PHTS to be investigated, the research activity has been carried out following a theoretical-computational approach based on the finite volume method and adopting a suitable release of the ANSYS CFX Computational Fluid-Dynamic (CFD) code and the RELAP5-3D thermal-hydraulic system code. In the following, a brief description of the two codes is provided.

8.2.1 CFD code

ANSYS CFX is the CFD code that has been adopted to perform such a kind of analyses. It is widespread CFD code intended to simulate in a fully 3D approach the thermofluid-dynamic behaviour of fluid flows, taking into account passive scalars (temperature, enthalpy, concentration, etc.) convective/diffusive transport phenomena and including other related physical processes. In particular, it numerically solves the thermofluid-dynamic equations governing the fluid flow over the region of interest with the prescribed boundary conditions by adopting an element-based Finite Volume Method (FVM), resulting to be suitable to realistically predict especially the thermofluid-dynamic behaviour of single-phase, single-component flows, both in laminar and fully turbulent regimes.

It is typically employed in the numerical simulation of fluid flows in nuclear and chemical industrial plant, in gas turbine engines as well as in aircraft or high-speed vehicles aerodynamics and it has been already adopted for the numerical modelling of the thermal-hydraulic behaviour of a wide variety of fusion reactor components under steady-state conditions [205] [206].

The recent progress in the meshing algorithms implemented, particularly those oriented to free-meshing applications suitable for the discretization of complex 3D flow domains, the wide library of qualified turbulence models implemented and validated, the complete database of “wall functions” (to be adopted in order to save calculation time avoiding the simulation of complex transport processes taking place in the thermofluid-dynamic boundary layer), the robustness of the numerical techniques adopted and the flexibility in convergence control settings as well as the high level of post-processing capabilities make of this code an excellent tool for the numerical assessment of the steady-state thermal-hydraulic behaviour of the DEMO PHTS pipework. Ansys guide [207] provides the complete list of the equations employed by the code. A short summary of equations relevant to the Ph.D. activity is reported in this paragraph, the interested reader can refer to books such as [208] or to [209] for further details. The typical partial differential conservation equations, which describe the behaviour of a Newtonian fluid and are solved by ANSYS CFX, may be written as:

$$\frac{\partial \rho}{\partial t}+\frac{\partial\left(\rho u_j\right)}{\partial x_j}=0 \qquad \text{continuity equation} \qquad (122)$$

$$\frac{\partial\left(\rho u_i\right)}{\partial t}+\frac{\partial\left(\rho u_i u_j\right)}{\partial x_j}=-\frac{\partial p}{\partial x_i}+\frac{\partial \tau_{ij}}{\partial x_j}+f_i''' \qquad \text{momentum equations} \qquad (123)$$

$$\frac{\partial\left(\rho\, c_p T\right)}{\partial t}-\frac{\partial\left(\rho u_i c_p T\right)}{\partial x_i}=\frac{\partial}{\partial x_i}\lambda\frac{\partial T}{\partial x_i}+q''' \qquad \text{energy equation} \qquad (124)$$

with ρ referring to the fluid density, t to the time, u_i to the ith-component of vector of velocity, p to the static thermodynamic pressure, T to the static thermodynamic temperature, μ to the dynamic viscosity, c_p to the specific heat capacity, f_i''' to the momentum source, λ to the thermal conductivity (which, in the most general case, is more properly expressed as a tensor λ_{ij}) and q''' to the energy source. If the following “Boussinesq hypothesis” is applied, the viscous stress tensor (τ_{ij}) may be expressed as:

$$\tau_{ij}=\mu\left[\left(\frac{\partial u_i}{\partial x_j}+\frac{\partial u_j}{\partial x_i}\right)-\frac{2}{3}\delta_{ij}\frac{\partial u_k}{\partial x_k}\right] \qquad (125)$$

Consequently, combining equation (123) with equation (125), the momentum equations become the Navier-Stokes equations:

$$\frac{\partial\left(\rho u_i\right)}{\partial t}+\frac{\partial\left(\rho u_i u_j\right)}{\partial x_j}=-\frac{\partial p}{\partial x_i}+\frac{\partial}{\partial x_j}\left[\mu\left(\frac{\partial u_i}{\partial x_j}+\frac{\partial u_j}{\partial x_i}\right)-\frac{2}{3}\mu\delta_{ij}\frac{\partial u_k}{\partial x_k}\right]+f_i''' \qquad (126)$$

Since $\delta_{ij} = 1$ when i = j and is equal to 0 in the other cases, defining a modified pressure (p^*) as:

$$p^* = p + \frac{2}{3}\mu\frac{\partial u_k}{\partial x_k} \tag{127}$$

equation (126) can be written as:

$$\frac{\partial(\rho u_i)}{\partial t} + \frac{\partial(\rho u_i u_j)}{\partial x_j} = -\frac{\partial p^*}{\partial x_i} + \frac{\partial}{\partial x_j}\mu\left(\frac{\partial u_i}{\partial x_j} + \frac{\partial u_j}{\partial x_i}\right) + f_i''' \tag{128}$$

The conservation equations describe respectively the processes of mass, momentum and energy transfer. Since they can be analytically solved only in a limited range of simple cases, they are generally discretized and solved numerically.

Additionally, the code allows to solve other equations in order to describe other processes (i.e. combustion or diffusion of scalar quantities) as well as to use approximating models, such as the ones devoted to describe turbulence phenomena. The general form of the transport equation for an additional scalable variable Φ is:

$$\frac{\partial(\rho\Phi)}{\partial t} + \frac{\partial(\rho u_i \Phi)}{\partial x_i} = \frac{\partial}{\partial x_i}\Gamma\frac{\partial\Phi}{\partial x_i} + S_\Phi \tag{129}$$

where Γ is the diffusivity and S_Φ the variable source.

The transport equations must be coupled with constitutive equations of state for density and for enthalpy, so to form a closed system. State equations are characterised by the general form:

$$\rho = \rho(p, T) \tag{130}$$

with:

$$c_p = c_p(p, T) \tag{131}$$

Naturally, the form of the state equations depends on the fluid type. For example, for incompressible fluids, density is constant and c_p is at most a function of temperature:

$$\rho = \rho_{const} \tag{132}$$

$$c_p = c_p(T) \tag{133}$$

For an ideal gas, c_p is at most a function of temperature and density is calculated from the ideal gas law:

$$\rho = \frac{w\,p_{abs}}{R_0 T} \tag{134}$$

where w is the molecular weight, p_{abs} is the absolute pressure and R_0 is the universal gas constant. For real gas, instead, cubic EOS are a convenient means for predicting real fluid behaviour. Finally, in a more general case, for fluid such as water, the equation of state for its properties can be provided by the IAPWS-IF97 library, already implemented in the code. Particularly, the IAPWS database considers five distinct thermodynamic regions for water and steam, namely subcooled water (1), supercritical water/steam (2), superheated steam (3), saturation data (4) and high temperature steam (5). During the calculation, water properties are transferred into tabular form and they are evaluated as functions of pressure and temperature.

The turbulent flows behaviour might be directly described by the conservation equations. Nevertheless, since they are characterised by many length and time scales phenomena, prohibitively fine meshes should be set-up in order to describe them effectively. Consequently, statistical turbulence models have been developed.

As far as statistical turbulence models are concerned, each variable describing a turbulent flow is considered as the sum of a variable, fluctuating component and an average (smoothly varying) component. For example, a velocity component may be decomposed as follows:

$$u_i = \overline{u}_i + u'_i \tag{135}$$

into a time varying component (u'_i) and an average component ($\overline{u}_i$). The latter is obtained as:

$$\overline{u}_i = \frac{1}{\Delta t}\int_t^{t+\Delta t} u_i\,dt \tag{136}$$

where Δt is a time scale that is large if compared to turbulent fluctuations, but small if compared to the analysed transient time scale.

Introducing this division in averaged and fluctuating quantities inside the original Navier-Stokes equations in equation (128) and time averaging these equations, the RANS (Reynolds Averaged Navier-Stokes) equations are obtained ($\overline{p}^*$ has been substituted simply with $\overline{p}$):

$$\frac{\partial(\rho\overline{u}_i)}{\partial t} + \frac{\partial(\rho\overline{u}_i\overline{u}_j)}{\partial x_j} = -\frac{\partial\overline{p}}{\partial x_i} + \frac{\partial}{\partial x_j}\left[\mu\left(\frac{\partial\overline{u}_i}{\partial x_j} + \frac{\partial\overline{u}_j}{\partial x_i}\right)\right] - \frac{\partial\left(\rho\overline{u'_i u'_j}\right)}{\partial x_j} + \overline{f}_i''' \tag{137}$$

Once deriving the RANS equations, their system needs to be closed, since Reynolds stresses, defined as $-\rho\overline{u'_i u'_j}$, have introduced new variables.

The closure relations used to evaluate the additional Reynolds stresses define the type of turbulence model. Specifically, RANS turbulence models can be broadly divided into two classes: eddy viscosity models and Reynolds stress models.

The SST k-ω model belongs to the eddy viscosity turbulence models, which are based on the assumption that in a turbulent flow small eddies are continuously forming and dissipating and that Reynolds stresses can be considered proportional to mean velocity gradients. The following equation illustrates the “eddy viscosity hypothesis”, highlighting the relationship between Reynolds stresses and mean velocity gradients as well as μ_t , which represents the turbulent viscosity (also called eddy viscosity):

$$-\rho\overline{u'_i\,u'_j} = -\frac{2}{3}\rho k\delta_{ij} + \mu_t\left[\left(\frac{\partial\overline{u_i}}{\partial x_j}+\frac{\partial\overline{u_j}}{\partial x_i}\right)-\frac{2}{3}\delta_{ij}\frac{\partial\overline{u_k}}{\partial x_k}\right] \tag{138}$$

where k is the turbulent kinetic energy, defined as:

$$k=\frac{1}{2}\overline{u'^{2}_i} \tag{139}$$

Substituting equation (138) into the RANS equations (137), they become:

$$\frac{\partial\left(\rho\overline{u_i}\right)}{\partial t}+\frac{\partial\left(\rho\overline{u_i}\,\overline{u_j}\right)}{\partial x_j}=-\frac{\partial p}{\partial x_i}+\frac{\partial}{\partial x_j}\left[\left(\mu+\mu_t\right)\left(\frac{\partial\overline{u_i}}{\partial x_j}+\frac{\partial\overline{u_j}}{\partial x_i}\right)\right]+\overline{f}'''_i \tag{140}$$

where:

$$p=\overline{p}+\frac{2}{3}\rho k+\frac{2}{3}\left(\mu+\mu_t\right)\frac{\partial\overline{u_k}}{\partial x_k} \tag{141}$$

Likewise, the Reynolds averaged energy equation and the generic Reynolds averaged transport equation may be expressed respectively as:

$$\frac{\partial\left(\rho\, c_p\overline{T}\right)}{\partial t}+\frac{\partial\left(\rho\overline{u_i}\,c_p\overline{T}\right)}{\partial x_i}=\frac{\partial}{\partial x_i}\left[\left(\lambda+c_p\frac{\mu_t}{\sigma_t}\right)\frac{\partial\overline{T}}{\partial x_i}\right]+\overline{q}''' \tag{142}$$

$$\frac{\partial\left(\rho\overline{\Phi}\right)}{\partial t}+\frac{\partial\left(\rho\overline{u_i}\,\overline{\Phi}\right)}{\partial x_i}=\frac{\partial}{\partial x_i}\left[\left(\Gamma+\frac{\mu_t}{\sigma_t}\right)\frac{\partial\overline{\Phi}}{\partial x_i}\right]+S_\Phi \tag{143}$$

where σ_t is the Prandtl turbulent number.

Eddy viscosity models are distinguished by the manner in which eddy viscosity (μ_t) is derived. Among them, the two-equation turbulence models are widely used, since they offer a good compromise between numerical effort and computational accuracy.

In particular, the k-ε and the k-ω two-equation models define the turbulent viscosity as the product of a turbulent velocity and turbulent length scale. In two-equation models, the turbulence velocity scale is computed from the turbulent kinetic energy, which is provided from the solution of its transport equation. The turbulent length scale is estimated from two properties of the turbulence field. The k-ε model introduces two new variables into the system of equations. k is the turbulence kinetic energy, it is defined as the variance of the fluctuations in velocity, as shown in equation (139), and it has the dimensions of (L^2 T^{-2}). ε is the rate at which the velocity fluctuations dissipate (the turbulence eddy dissipation) and has dimensions of k per unit time (L^2 T^{-3}).

The k-ε model assumes that μ_t is linked to the turbulence kinetic energy and dissipation via the Prandtl-Kolmogorov relation:

$$\mu_t = C_\mu \rho \frac{k^2}{\varepsilon} \tag{144}$$

where C_μ is a k-ε turbulence model constant (amounting to 0.09).

The values of k and ε are derived from their differential transport equations:

$$\frac{\partial(\rho k)}{\partial t} + \frac{\partial\left(\rho \overline{u_i} k\right)}{\partial x_i} = \frac{\partial}{\partial x_i}\left[\left(\mu + \frac{\mu_t}{\sigma_k}\right)\frac{\partial k}{\partial x_i}\right] + P_k - \rho\varepsilon \tag{145}$$

$$\frac{\partial(\rho \varepsilon)}{\partial t} + \frac{\partial\left(\rho \overline{u_i} \varepsilon\right)}{\partial x_i} = \frac{\partial}{\partial x_i}\left[\left(\mu + \frac{\mu_t}{\sigma_\varepsilon}\right)\frac{\partial \varepsilon}{\partial x_i}\right] + \frac{\varepsilon}{k}\left(C_{\varepsilon 1} P_k - C_{\varepsilon 2}\rho\varepsilon\right) \tag{146}$$

where $C_{\varepsilon 1}$, $C_{\varepsilon 2}$, σ_k and σ_ε are k-ε turbulence model constants (amounting respectively to 1.44, 1.92, 1.0 and 1.3) and P_k is the turbulence production due to viscous forces.

The k-ε model effectively describes the behaviour of a turbulent flow in a wide range of applications. Nevertheless, it is not applicable to the fluid in near-wall regions, especially in the viscous laminar sub-layer. This problem could be overcome, for example, adopting the k-ω model or by means of the so-called wall functions. In particular, the latter have been devised as analytical expressions which describe the fluid thermal and velocity profile in near-wall regions. One of the major drawbacks of the classical wall-function approach is that the predictions depend on the location of the point nearest to the wall and are sensitive to the near-wall meshing. This problem has been overcome by ANSYS CFX developing a scalable wall function, which can be applied on arbitrarily fine meshes and allows to perform a consistent mesh refinement independent of the Reynolds number of the application.

As regard to the k-ω model, along with the turbulence kinetic energy k, introduces the transport equation of the turbulent frequency ω, which has the dimensions of (T^{-1}) since it could be assumed proportional to ε/k. k and ω transport equations result:

$$\frac{\partial(\rho k)}{\partial t}+\frac{\partial\left(\rho\overline{u_i}k\right)}{\partial x_i}=\frac{\partial}{\partial x_i}\left[\left(\mu+\frac{\mu_t}{\sigma_k}\right)\frac{\partial k}{\partial x_i}\right]+P_k-\beta'\rho k\omega \tag{147}$$

$$\frac{\partial(\rho\omega)}{\partial t}+\frac{\partial\left(\rho\overline{u_i}\omega\right)}{\partial x_i}=\frac{\partial}{\partial x_i}\left[\left(\mu+\frac{\mu_t}{\sigma_\omega}\right)\frac{\partial\omega}{\partial x_i}\right]+\frac{5}{9}\frac{\omega}{k}P_k-\beta\rho\omega^2 \tag{148}$$

where P_k is still the turbulence production due to viscous forces and β’, σ_k, β and σ_ω are k- ω turbulence model constants (amounting respectively to 0.09, 2, 0.075 and 2 in the Wilcox model formulation). Also, the Prandtl-Kolmogorov relation in equation (144) is substituted by:

$$\mu_t=\frac{\rho k}{\omega} \tag{149}$$

On the other hand, results of this model tend to be dependent on the assumed free stream value of ω which is a serious problem, in particular for external aerodynamics applications where free stream boundary conditions are used as a matter of routine. Depending on the value specified for at the inlet, a significant variation in the results of the model can be obtained. In order to overcome the problem, a blending between the k-ω model near the surface and the k-ε model in the outer region was developed by Menter [210]. As can be imagined, this method tries to merge the pros of both the models previously developed being virtually more flexible in managing situations and single fluid domains where different flow fields are expected.

Since the SST k-ω model offers a good compromise in terms of accuracy and robustness, it is widely indicated for general industrial purposes [208], therefore, as far as the calculations described in the following chapters of this thesis are concerned, the SST k-ω model has been adopted.

8.2.2 RELAP5-3D

The RELAP5-3D (Reactor Excursion and Leak Analysis Program—Three Dimensional) code is the state-of-the art member of a series of computer programs developed at Idaho National Laboratory (INL) for modelling nuclear power plants [211]. As can be gathered from the name, the main feature that distinguishes this last code from its forerunners is the capability to simulate full three-dimensional hydrodynamics with rectangular, cylindrical, and spherical geometries. Nevertheless, the core of the tool is based on a quasi-2D approach to simulate the behaviour of a fluid system. In particular, it is adapt to well describe the thermal-hydraulics of a single-component, two-phase system, in presence of a non-volatile solute and a non-condensable gases. For many decades, the RELAP codes family has been typically employed in the numerical simulation of light water fission reactor thermal-hydraulic transients however, since the creation of RELAP5-3D and thanks to the implementation of several working fluids, it also finds application in the studies upon molten salt reactors, liquid metal reactors, high-temperature gas-cooled reactors, and supercritical fluid reactors. Furthermore, recently has been used outside the nuclear industry, from commercial steam flow to cryogenic storage and delivery systems [211].

Its generic modelling philosophy permits RELAP5 to be a very versatile program, which manages to simulate a variety of thermal hydraulic systems making it available to be used also in fusion relevant applications.

The two-fluid equations of motion that are used as the basis for the RELAP5-3D hydrodynamic model are formulated in terms of volume and time-averaged parameters of the flow. The system model is solved numerically using a semi-implicit finite-difference technique. Phenomena that depend upon transverse gradients, such as friction and heat transfer, are formulated in terms of the bulk properties using empirical transfer coefficient formulations. In situations where transverse gradients cannot be represented within the framework of empirical transfer coefficients, such as subcooled boiling, additional models specially developed for the particular situation are employed. The RELAP5 thermal-hydraulic model solves eight field equations. The primary dependent variables are pressure, phasic specific internal energies, vapour volume fraction, phasic velocities, non-condensable quality, and boron density. The independent variables are time and distance. The secondary dependent variables used in the equations are phasic densities, phasic temperatures, saturation temperature and non-condensable mass fraction in non-condensable gas phase for the i-th non-condensable species.

Properties of fluids are calculated from thermodynamic tables that tabulate saturation properties as a function of temperature, saturation properties as a function of pressure and single-phase properties as a function of pressure and temperature. The properties and derivatives in the tables are saturation pressure, saturation temperature, specific volume, specific internal energy and three derivatives (i.e. the isobaric thermal expansion coefficient, the isothermal compressibility, and the specific heat at constant pressure). The constitutive relations include models for defining flow regimes and flow-regime-related models for interphase drag and shear, the coefficient of virtual mass, wall friction, wall heat transfer, interphase heat and mass transfer and direct (sensible) heat transfer. The constitutive relations, in general, include flow regime effects for which simplified mapping techniques have been developed to control the use of constitutive relation correlations. The detailed description of code equations, models and procedures is out of the scope of this thesis and may be found in its manuals [214].

8.3 CFD Analysis of the BB PHTS pipework

According to the description of the methodology selected to carry out the activity, in order to numerically investigate the nominal steady-state hydraulic behaviour of the DEMO BB PHTS pipework, fully 3D steady-state CFD analyses have been run for the different portion of the primary loop under consideration. In particular, it has been decided to perform the analyses only on the longest circuit because it already encompasses those geometries that are worth to investigate to make available a sufficient number of elements to be compared with the design values.

To this purpose specific 3D Finite Volume Models have been set-up, realistically reproducing the layout of the loop of the DEMO BB PHTS under consideration. In particular, the development of each Finite Volume Model has been articulated in the following steps:

- flow domain discretization;
- constitutive model definition;
- loads and boundary conditions definition;
- turbulence model definition.

These points will be discussed and better explained in the following paragraph.

8.3.1 Assumptions and operative procedures

The flow domain discretization has been carried out importing, by means of the ANSYS Design Modeler tool, the CAD file representing the coolant flow domain of the circuit to be analysed. Since calculation time strongly depends on the mesh size and, on the other hand, a poor mesh may result in un-realistic predictions, sensitivity analysis campaigns have been carried out in order to select a mesh fine enough to give stable predictions with a further increase of its density without inducing too long calculation times. Moreover, since the volume of the pipework is extremely large, it would be really dared to attempt to generate a single calculation grid which manages to catch in detail the relevant aspects of the fluid flow. For these reasons it has been chosen to split the flow domain in several parts to be separately studied allowing to find a good compromise between results accuracy and calculation time.

Figure 8.1 depicts the whole flow domain to be investigated and the 10 regions in which it has been subdivided. Typically, a proper trade-off is obtained generating meshes with a node density ranging between 10^6 and 10^8 nodes/m^3 however, it has to be underlined that geometry deeply affects mesh dimensions, so mesh complexity should be defined on a base case. Actually, although the specific fluid domains present the mentioned difficulties to be handled with analytical procedures, their topology is quite simpler than those that can be found in the In-Vessel cooling circuits or in the heat exchangers.

Nevertheless, due to huge inventory to be treated, efforts are needed to achieve a reasonable amount of nodes in order to not penalize the prediction capabilities of the code.

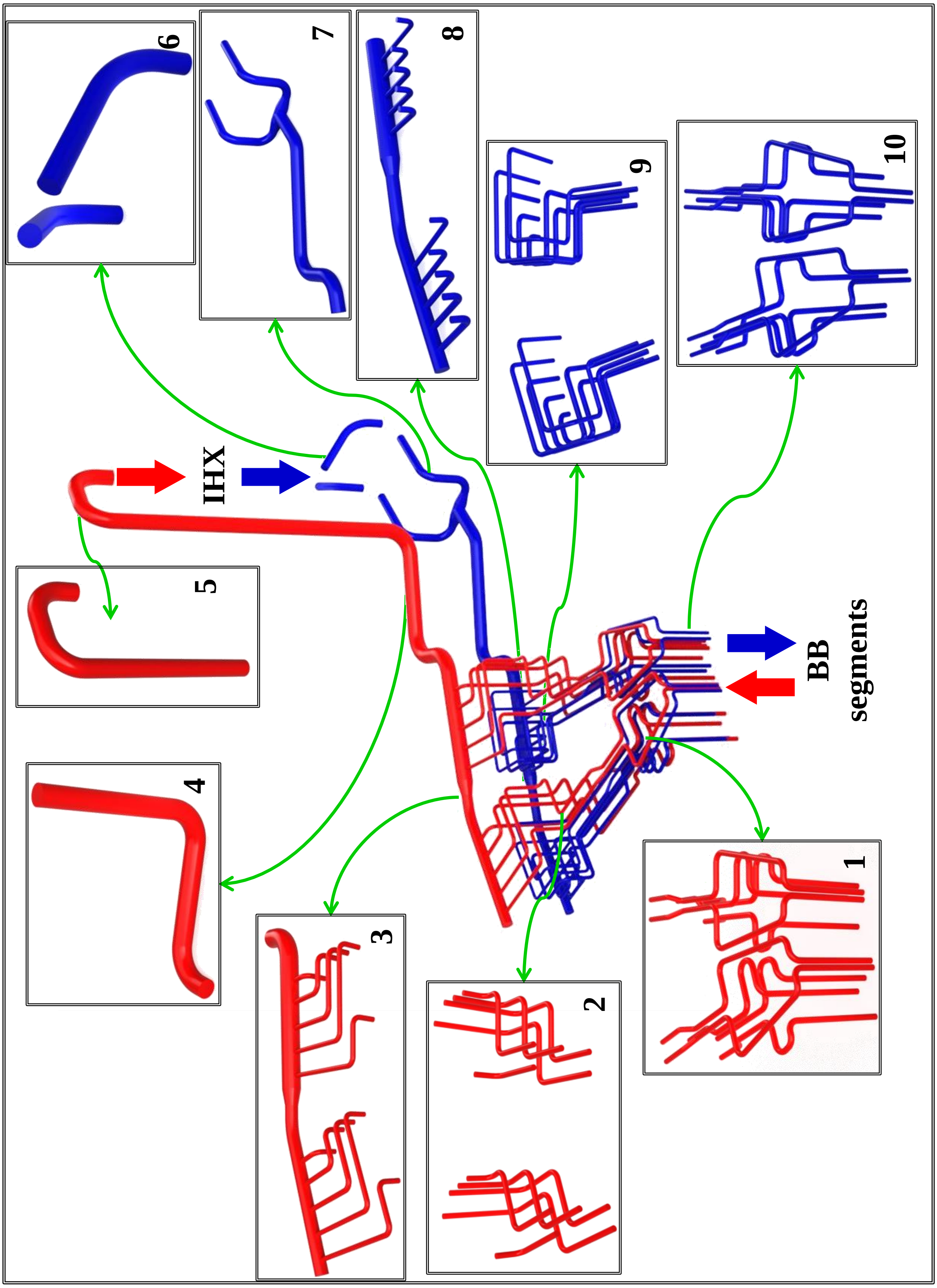

Figure 8.1. The 10 domain subdivisions. Red/blue colours mark hot/cold parts, respectively.

Concerning the constitutive model, helium coolant thermofluid-dynamic properties defined by the Aungier modified Redlich Kwong model have been adopted. The model is already implemented in the code and it is suggested as default cubic equation for a real gas law [207].

As to the loads and boundary conditions definition, a proper combination of inlet and outlet conditions have been imposed case by case with the aim of following the fluid behaviour and the pressure profile along the separated fluid domains from the BB to the IHX and vice-versa. In particular, although the flow domain have been subdivided in different parts and the analyses have run in different times, it has been possible to exploit a particular function of ANSYS that let the users apply as inlet boundary condition of one calculation, the output results coming from another analysis. This has enabled to follow the procedure herewith summarized.

- Three groups of analyses have been performed in series. One group has been comprehensive of the flow domains in which the hot helium flows, from 1 to 5 in Figure 8.1. The second group has consisted of the two parallel pipes between the heat exchanger and the circulators, namely the domain 6. The last analyses have been done on all those pipe downstream the circulators, from 7 to 10.
- For both first and third group of pipes the analyses have begun from the domain 1 and 7, respectively, setting the target mass flow rates as inlet boundary conditions. The “section averaged static pressure” condition has been adopted at the outlet boundaries. This coupling of BCs is very common in CFD analyses. The same type of BCs have been employed also for the two pipes of the second group because they are basically isolated from the other flow domains under investigation.
- In the subsequent analyses, to catch the influence of the upstream conditions, the inlet boundary conditions have been imported from the outlet sections of the previous runs. Of course, this approach has been possible because the inlet section(s) of the downstream domain is(are) coincided with the outlet sections of the upstream pipes.
- With the exclusion of one case, the total pressure profile and the velocity directions at the outlet(s) of the downstream domain have been taken as the inlet conditions of the domain under investigation. Then, the target mass flow rate has been set in the outlet section(s). This virtually allows to set a single reference pressure in all the fluid domains of one group and follow exactly the pressure distribution
- The exclusion consists of the domain 3, namely the hot collector. In fact, if in such a domain the mass flow rate is set at the common outlet section, it is very likely that the flow distribution resulting from the calculation will not suit the requirements of each single pipe that composes the branch in exam. Therefore, to overtake this potential issue, as inlet condition a velocity vector has been imposed importing the profiles from the previous calculation. In addition, to be compliant with the required mass flow rate, the reference pressure (on which the coolant density depends) has been corrected respect to the upstream

case taking into account the pressure losses.

As a matter of fact, since ANSYS CFX solves the CFD equations in terms of relative pressure and the absolute pressure is simply calculated as the sum of the relative and the reference pressures, it is common practice to set the reference pressure to a value close to the average absolute pressure in circuit, in order to reduce round-off errors and pressure wiggles. Nevertheless, it is worth to remark that in the neighbourhood of 80 bars, as the pressure drops experienced in each flow domain are in the order of 10÷20 kPa, the helium could have been considered almost incompressible.

At the interface between the coolant and the circuit steel walls a no-slip condition has been assumed together with a proper "wall function" algorithm, that allows to effectively model the fluid-wall interaction effects in the overall pressure drop, simplifying the simulation of complex transport processes taking place in the thermofluid-dynamic boundary layer and, consequently, saving calculation time. Moreover an absolute wall roughness of 50 µm has been adopted, to be completely in line with the design calculations, see section 5.1.1.

Finally, isothermal flow conditions have been assumed, setting the coolant temperature to its design temperatures, namely 520 °C in the hot parts and 300 °C in the cold part, excepting for the circulator suctions where the temperature is about 290° for the reasons already discussed. In this way, since the ducts are well-insulated and appreciable temperature variations are not expected, energy equation has not been solved because it should not affect the pressure drops. In this way it has been possible to reduce the calculation time without incurring in un-realistic predictions.

Once set-up the Finite Volume Model, analysis settings have been properly defined. In particular, the typical steady-state analysis under nominal conditions has been simulated by the ANSYS CFX code adopting the "false transient" algorithm to speed-up the convergence of steady-state numerical simulations. Initial values can be set automatically if a good initial guess is not known or is not required. Although accurate initial values may not always be available, a good approximation can reduce the time to solve a steady-state simulation and reduce the chance that the solution fails to converge due to diverging residuals. The more complicated the simulation and models used, the more important it becomes to start the solution process with sensible initial values. For this reason, it is highly suggested to get an initial solution with an approximate model and to successively impose it as initial condition for a more accurate final solution. As to the calculation time, it has depended mainly on the number of nodes and on whether and how the ANSYS High Performance Computing (HPC) has been used. Increasing the number of mesh nodes obviously rises the calculation time. On the other hand, ANSYS HPC supports parallel processing, so it has been used to numerically speed-up large numerical analyses.

Finally, once defined analysis settings and convergence controls, the analysis is launched and, once finished, results are easily post-processed with a particular reference to flow velocity field (v), static (p_S) and total pressure (p_T) fields and mass flow rate distribution (G).

In particular, the following variables are typically calculated with reference to a generic cross section, A, of the flow domain:

$$u = \frac{1}{A}\iint_A \underline{v}\cdot\underline{n}\,dA \qquad \text{average flow velocity} \qquad (150)$$

$$G = \iint_A \rho\underline{v}\cdot\underline{n}\,dA \qquad \text{mass flow rate} \qquad (151)$$

$$p_T = p_S + \frac{1}{2}\rho\underline{v}\cdot\underline{v} \qquad \text{local total pressure} \qquad (152)$$

$$p = \frac{1}{A}\iint_A p_T\,dA \qquad \text{average total pressure} \qquad (153)$$

where ρ is the coolant density. It hence follows that the total pressure drop of the coolant between the two sections i and j has to be calculated as follows:

$$\Delta p_{ij} = p_i - p_j \qquad \text{total pressure drop} \qquad (154)$$

representing the variation in volumetric density of energy that the coolant experiences flowing between the aforementioned sections due to friction and non-reversible (turbulence) processes, deprived of the gravitational contribution due to the assumption of no gravity loads.

8.3.2 Preliminary analyses and sensitivity on the mesh grid parameters

The overall dimensions of one PHTS circuit could make questionable the use of a fully 3-D approach to simulate these huge flow domains. Therefore, validation and sensitivity analyses have been preliminarily carried out aiming to assess the predictive potential of the code in fusion-relevant application, checking with reference to a peculiar flow condition of the DEMO blanket primary cooling system. Furthermore, the minimum node density together with the best mesh topology and inflation layers arrangement (in terms of layers number, first layer thickness and layers growth rate) have been settled in order to obtain realistic and reliable numerical predictions without incurring in too long calculation time.

Specifically, a portion of an OB hot feeding pipe has been investigated, namely the one that is routed through the Upper port, from the BB to the Bioshield. Its characteristic dimensions and flow conditions are reported in Table 8.1.

Numerical results obtained in terms of total pressure drop across pipes, and pressure gradient in fully developed flow conditions have been compared with those calculated during the design calculations.

Attention has been devoted to the assessment of the best mesh configuration to be implemented for the calculation campaign. In fact, although it is a common agreement that “inflation layers” should be used to well predict the velocity radial profile, thus obtaining a reliable flow prediction, the wall treatment is actually a tricky point that must be handled with care: in fact, the first layer height has to be chosen in accordance with the turbulence model and the near-wall treatment in use.

The adopted SST k-ω model, with its hybrid near-wall treatment implemented in ANSYS CFX, allows a great freedom in the choice of the first layer thickness, determining no lower bounds for the first cell height, and an upper bound that, in wall units, can be expressed as y^+ around 500 [215].

Since the constraints related to the near-wall treatment are weak, the analyses have been focussed on the effects of grid clustering close to the wall in terms of grid independency, instead of assessing the effects of y^+ distribution on the final solution. However, the y^+ values have been examined in every configuration, to check its compliancy with the chosen model

Table 8.1. Main characteristic of the investigate portion of the OB hot feeding pipe.

D_i [mm]	320.64
L_{tot} [m]	15.30
N_{bends}	6
Mass flow rate [kg/s]	26.54
Velocity [m/s]	68.93
Reynolds number [-]	2.68E6
Wall roughness [μm]	50
ΔP_{Design} [kPa]	15.43

To this purpose, the first parametric studies have been performed varying those grid parameters that affect the node density of the pipe cross-section. In particular, to assess the effects that a roughness of 50 micron might induce on the turbulent wall scales, 7 cross-section meshing configurations have been tested. Starting from a grid with the thickness of first inflation layer set to 200 μm, finer grids have been gradually made, up to reaching a first layer thickness of 2 micron. This choice has been followed in order to obtain data both from calculation grids whose first layer has fallen within the radial zone enclosed by the wall asperities, as well as from those coarser meshes in which the code would have adopted automatic wall functions to grab the flow behaviour in the wall region.

Furthermore, depending on the considered first layer height, the total number of layers and their growth rates have been suitably imposed to avoid a sharp transition between the last inflation layer and the element size characterizing the core of the calculation grid.

Then, as pipe topology allows to adoption of hexahedral mesh, the grid constructed upon the pipe cross-section has been extruded along the pipe axis, exploiting the sweep option foreseen in the “multizone” method.

Table 8.2 summarizes the parameters used in this first set of analyses, while the details of the finest and the coarsest grids are illustrated in Figure 8.2 and Figure 8.3, respectively.

Table 8.2. Mesh features for the first parametric analysis.

Case	**First layer’s thickness [μm]**	**Number of layers [-]**	**Growth rate [-]**	**Element size [mm]**	**Sweep size [mm]**
1	2	28	1.38	14	14
2	3	27	1.38	14	14
3	4	26	1.38	14	14
4	10	23	1.39	14	14
5	20	20	1.405	14	14
6	100	15	1.415	14	14
7	200	14	1.415	14	14

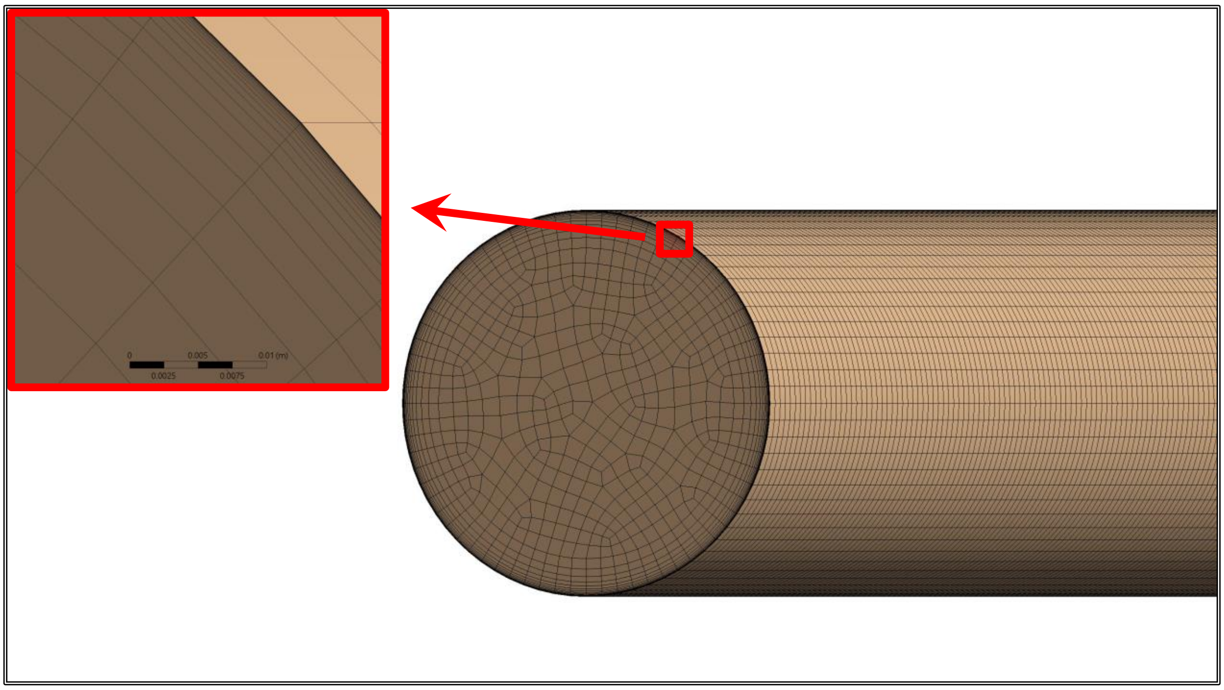

Figure 8.2. Detail of the finest mesh for sensitivity analysis 1 – Case 1

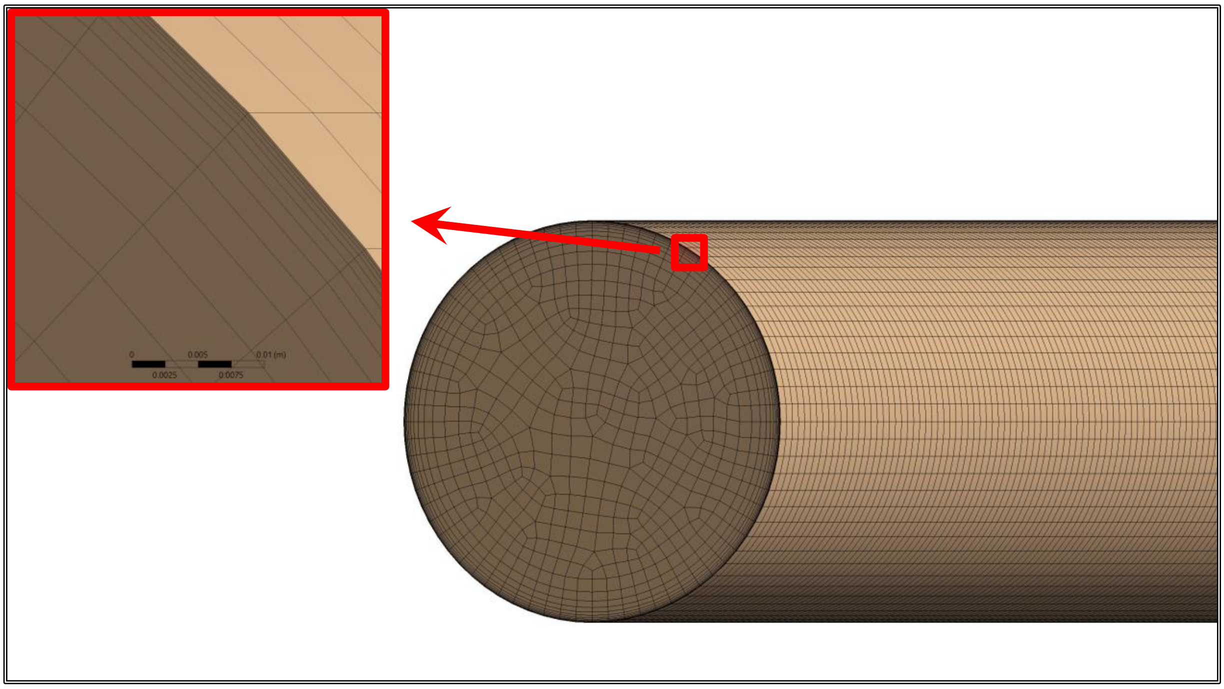

Figure 8.3. Detail of the coarsest mesh for sensitivity analysis 1 – Case 7

The results have shown that the trend of estimated pressure drop is increasing going from a small number of inflation layers (thicker first layer) to larger values, see Figure 8.4.

It has to be noted that it is not easy to quantify with some errors estimators the quality of the chosen mesh: in fact, all the methodologies based upon the Richardson extrapolation require the convergence to be strictly monotonic [216] and, as visible in Figure 8.4, the finer grids exhibit an oscillating behaviour.

Despite that, the calculated losses tend to stabilize around a values of 12.5 kPa, where the first 3 cases with a first layer height of 2, 3 and 4 microns, respectively, feel relative maximum variations below 1%, being the case 1 and 3 almost identical. The maximum relative error of 1% has been chosen as an indication of the error related to the choice of the inflation layers.

A similar analysis has been performed looking at the sensitivity with respect to the element size at the pipe cross section. The results, here not explicitly reported, are similar to those of the layer analyses and the results are not monotonically converging to an asymptotic value. The error in the oscillating part of the convergence plot have a maximum relative error of the order of 1%. Furthermore, as can be noticed from the Figure 8.5, the dimensionless wall scale is practically unchanged for all the cases which first inflation layer falls below the wall roughness, namely from Case 1 to Case 5. In view of these results, to minimize the number of nodes (and elements) in the calculation grid while keeping characteristic sizes that might have ensure both “grid independency” and accuracy, the mesh parameters pertaining to the Case 3 have appeared a good trade-off choice to be further used.

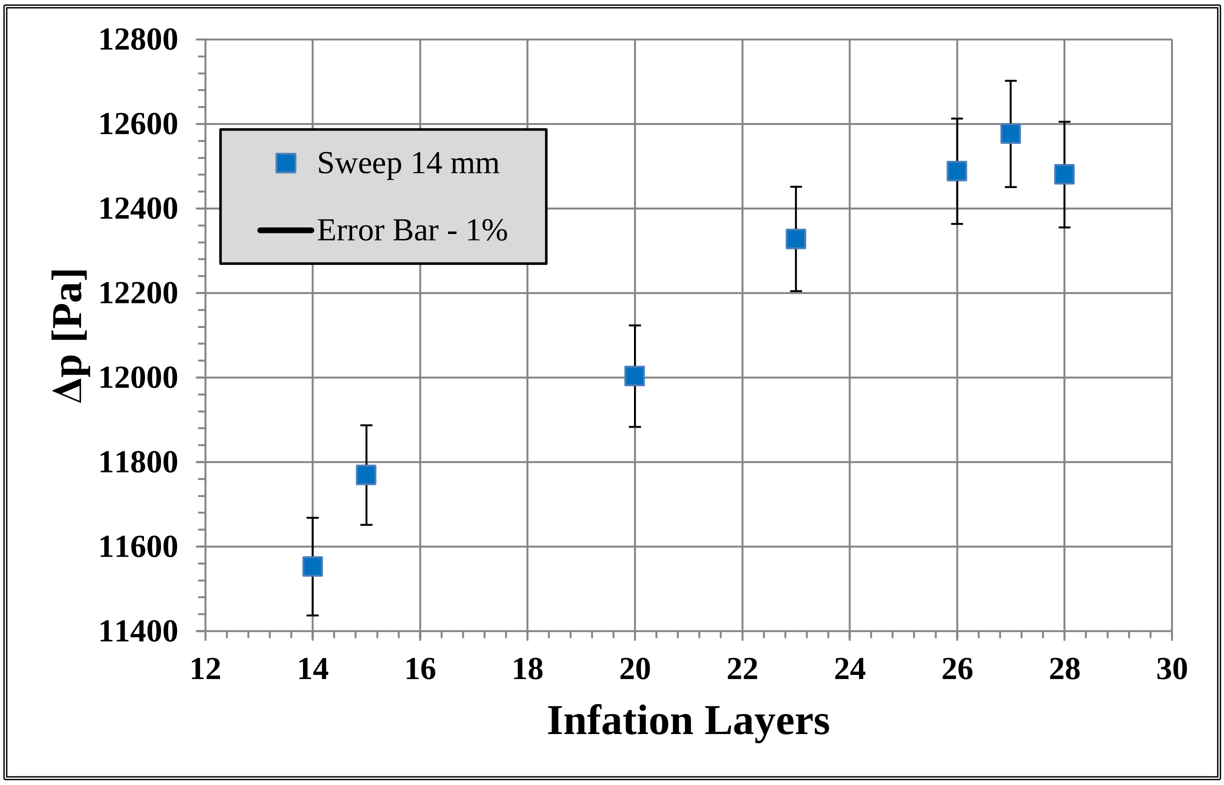

Figure 8.4. Sensitivity analysis 1 – Pipe pressure drop vs inflation layers.

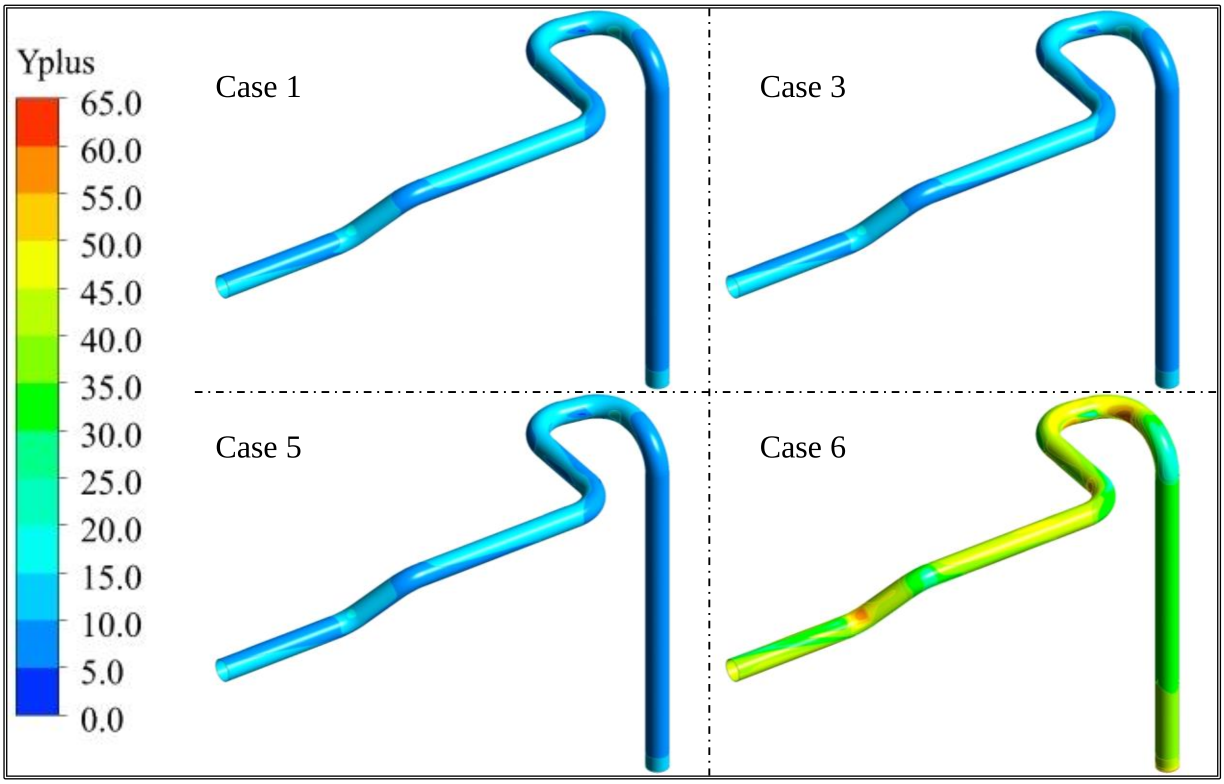

Figure 8.5. Sensitivity analysis 1 – Y-plus for different cases.

Once the mesh in the radial direction has been set, a second investigation has started in order to understand whether a better mesh sweeping could have been selected.

In fact, taking into account the huge dimensions of the whole cooling circuit pipework, every little gain in the longitudinal size of the hexahedrons could give a very good aid to simplify the analyses and speed-up the calculations.

Therefore, fixing the cross-section grid at the values previously founded, 14 sweep sizes have been checked, ranging the longitudinal length of the hexahedrons from 100 mm to 10 mm.

Table 8.3 summarizes the characteristics of the grids used in the second parametric runs.

Table 8.3. Mesh features for the second parametric runs

Case	**First layer's thickness [μm]**	**Number of layers [-]**	**Growth rate [-]**	**Element size [mm]**	**Sweep size [mm]**
3a	4	26	1.38	14	100
3b	4	26	1.38	14	75
3c	4	26	1.38	14	55
3d	4	26	1.38	14	40
3e	4	26	1.38	14	30
3f	4	26	1.38	14	25
3g	4	26	1.38	14	21
3h	4	26	1.38	14	18
3i	4	26	1.38	14	16
3j	4	26	1.38	14	14
3k	4	26	1.38	14	13
3l	4	26	1.38	14	12
3m	4	26	1.38	14	11
3n	4	26	1.38	14	10

The second parametric assessment have demonstrated the capability of a coarser sweep size to simulate the hydraulic behaviour of the pipes without any losing of degree of accuracy and/or "grid independency". As a matter of fact, the Figure 8.6 shows how the total pressure drop in the pipe is kept substantially constant for all the calculations conceiving a pipe axial subdivision above 500, with the abscissa defined as pipe length over sweep size.

In practice, this has meant that any sweep size smaller than 30 mm would have been applicable in the assessments since the maximum variations from Case 3e to Case 3n has been within 0.2%. Nevertheless, a final sweep size of 20 mm has been adopted in all calculations because of the still reasonable computational demands.

Starting from the results of this latter sensitivity analysis, an error estimation related to the grid size has been performed, according to the methodology described in [216].

First of all, using a couple of results previously calculated, it is evaluated the Richardson extrapolation value of the pressure drop, as following:

$$\Delta p_{RE} = \Delta p_{fine} + \frac{\Delta p_{fine} - \Delta p_{coarse}}{r^{p} - 1} \tag{155}$$

where the fine and coarse are referred to the results obtained with the finer and the coarser gids, r is the refinement ratio, defined as:

$$r = \frac{h_{fine}}{h_{coarse}} \tag{156}$$

where h is equal to the sweep size and p is the order of accuracy of the spatial discretization scheme. This latter parameter is equal to 2, since a second order scheme has been chosen for all the calculations.

The Richardson extrapolation has to be intended as an higher order approximation of the exact solution of the fluid-dynamics equations. It is related to the exact solution by the following expression:

$$\Delta p_{exact} = \Delta p_{RE} + \text{H.O.T.} \tag{157}$$

where H.O.T. represents the higher order terms, that can be usually considered negligible.

Selecting simulations 3h and 3n, in order to have a refinement ratio higher than 1.3, as suggested by [216], the extrapolated pressure drop is estimated to be around 12.4 kPa.

Is then calculated the Grid Convergence Index (GCI), a suitable estimator of the error against the exact solution, in order to quantify the uncertainty related to the mesh refinement; it is expressed as:

$$GCI_{coarse\,grid} = F_S \left| \frac{\Delta p_{fine} - \Delta p_{coarse}}{\Delta p_{fine}} \right| \frac{r^{p}}{r^{p} - 1} \approx \left| \frac{\Delta p_{exact} - \Delta p_{coarse}}{\Delta p_{exact}} \right| \tag{158}$$

where *Fs* is a safety factor, whose suggested value is 1.25 for results in the asymptotic range [216].

Performing the calculations, the GCI value for the chosen sweep size is estimated to be around 1.8%, confirming that the results obtained are only marginally dependent on the spatial discretization in use.

Summing up the terms related to the uncertainties of the sweep, the element size in the cross-section, and the layer distribution, it is possible to give a conservative estimation of the overall mesh error, evaluated to be around 3.8%

Hence, for a further confirmation, a CFD analyses with the selected mesh discretization has been run to verify the mesh capabilities to predict the pressure losses in fully developed flow conditions. This choice has been made to allow an easy comparison with the values calculated through an highly reliable analytical approximation of the Moody’s chart.

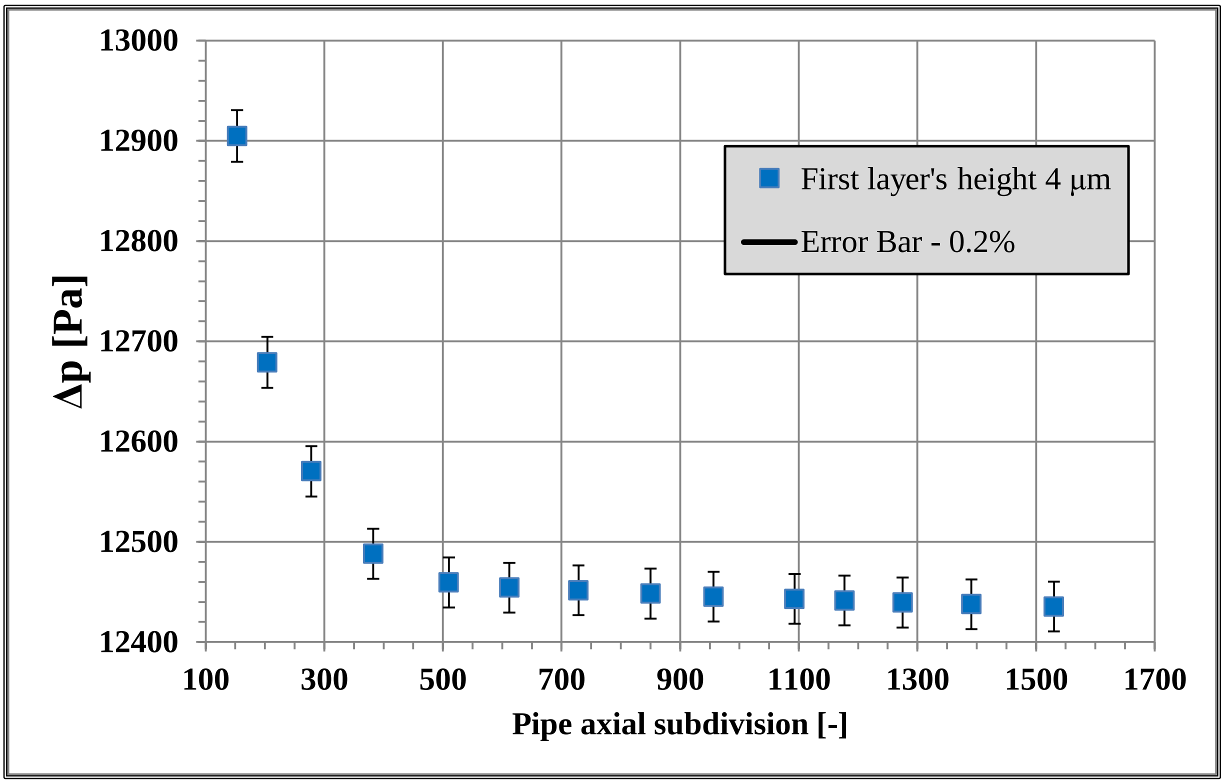

Figure 8.6. Sensitivity analysis 2 – Pipe pressure drop vs pipe curvilinear abscissa divisions.

In this respect, Figure 8.7 shows the numerical prediction of the pressure gradient within the straight section of the OB hot feeding pipe, downstream the outlet of the BB segment. The entrance effects cause larger friction losses in the developing flow; then, as can be expected from the theory [199], the inlet perturbations decrease up to around 10÷12 diameters where they completely disappear and the flow conditions become fully developed. From that point on, the pressure gradient oscillates imperceptibly around a mean value. In the graph, the numerical results are compared with the analytical pressure gradient obtained through the *Haaland*’s formula for the fully developed flows, already used in the design assessments to estimate the distributed pressure drops, see sections 4.4.2.5.1 and 5.1.1. A good agreement have been achieved between numerical and analytical results as they are within 5%, thus demonstrating the nice performances of the calculation grid.

The numerical campaign has therefore started taking into account the set of above parameters investigated. However, it is worth to underline that the radial dimension of the OB feeding pipe are not perfectly representative of all the PHTS piping. For instance, it is about 4 times smaller than that of the main hot leg. For this latter pipe, a first layer height of 4 µm might result excessively small, therefore according to the wall treatment theory and the relative Reynolds number, a proper scaling factor has been applied in those pipes where high differences in the dimensionless numbers where expected. Nevertheless, the maximum layer height set during the calculations has been 10 µm, which is widely within the wall roughness.

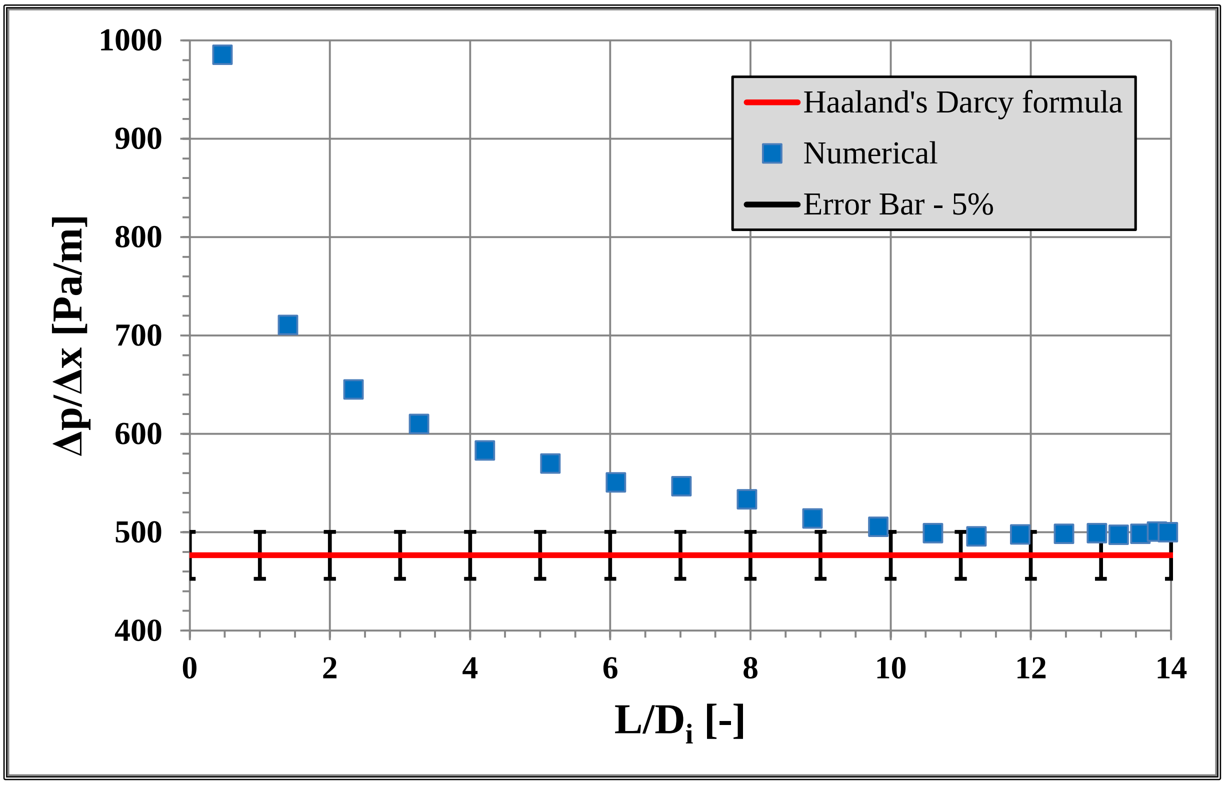

Figure 8.7. Pressure gradient in developing and fully developed flow conditions.

8.3.3 Comparison between CFD results and design values

The estimation of the pressure drops has proceeded according the methodology described in the section 8.3.1 with the aim of testing the approach followed during the thermal-hydraulic design phases. In particular, being the subject of this numerical benchmark the design assessment concerning the piping pressure drops shown in the paragraph 5.1.2, with specific reference to those reported in Table 5.3, the results have been reported in a similar form that makes use of the same numbering of Figure 5.9 and Figure 5.10. It is worth to highlight that the local pressure drop due to the control valve to have a fine balancing of the mass flow rate has not been taken into account. The reason behind such a choice is that its simulation has been judged useless for this kind of analysis which main scope has been to estimate the accuracy of the design models and if they would be suitable to be employed in the future for design purpose. Hence, the assessment of an “imposed” pressure drop would have not added any particular value to the work.

The pressure drops calculated via ANSYS CFX code are reported in Table 8.4, while Table 8.5 and Table 8.6 illustrate the percentage differences between the design data and the numerical assessments via CFD code.

The relative difference is defined as:

$$\frac{\Delta p_{CFD} - \Delta p_{design}}{\Delta p_{design}} \tag{159}$$

It should be noticed that, the pressure drops of BB and IHX have not been considered in the tables because they have not been part of the assessment

With regard to the results, as it has been expected, the design approach confirms its conservative nature, being the design data always higher than those numerically estimated though a fully 3-D tool. The differences can be mainly attributed to the impossibility to consider all the coupling effects among the different geometrical discontinuities, such as Tee-junctions. In particular, the zone of the cold distributors, namely 3→4; 2→4, present the largest discrepancies between design and numerical calculations, with a maximum difference of about 35%, see Table 8.5.

Table 8.4. CFD calculated pressure drops in pipework. Longest loop for standard S&T IHX.

[kPa]	**Sector 1**					**Sector 2**				
	OUTBOARD			**INBOARD**		**OUTBOARD**			**INBOARD**	
	OBL 1	**OBC 1**	**OBR 1**	**IBL 1**	**IBR 1**	**OBL 2**	**OBC 2**	**OBR 2**	**IBL 2**	**IBR 2**
1→2	12.0									
2→3	1.0					-	-	-	-	-
3→4;2→4	23.6	27.6	21.5	26.4	25.1	24.8	27.2	20.7	24.8	23.8
4→5	Control valve pressure drop not considered									
5→6	13.4	13.6	13.9	12.5	12.9	13.7	13.4	14.1	12.5	12.9
6→7	BB segment pressure drop not considered									
7→8	12.5	13.0	12.2	8.1	8.1	12.4	13.0	12.1	8.1	8.1
8→9	24.7	26.0	19.1	15.9	14.3	-	-	-	-	-
9→10; 8→10	3.2					23.2	23.8	19.3	13.4	11.2
10→11	2.9									
11→12	IHX pressure drop not considered									
12→13	1.1									

On the other hand, it must be pointed out that in some portions of the system a very good agreement is found with values that differ less than 10% (minimum error of about 3%). Nevertheless, as general trend, it can be stated that usually the results lie in the neighbourhood of -20%. In fact, when the difference are reported in terms of entire cooling path that the coolant can follow, see Table 8.6, the total pressure drops of the pipework numerically assessed vary within -14% and -25% of the design data.

Table 8.5. Pressure drop comparison between design and CFD data.

[%]	Sector 1					Sector 2				
	OUTBOARD			INBOARD		OUTBOARD			INBOARD	
	OBL 1	OBC 1	OBR 1	IBL 1	IBR 1	OBL 2	OBC 2	OBR 2	IBL 2	IBR 2
1→2	-6.93%									
2→3	-13.47%					-	-	-	-	-
3→4;2→4	-35.4%	-29.2%	-36.3%	-20.5%	-20.7%	-29.8%	-28.8%	-35.6%	-21.4%	-23.4%
4→5	Control valve pressure drop not considered									
5→6	-18.4%	-9.3%	-19.3%	-11.0%	-7.3%	-16.8%	-10.5%	-18.3%	-11.4%	-7.9%
6→7	BB segment pressure drop not considered									
7→8	-19.3%	-15.5%	-20.4%	-15.5%	-15.5%	-19.5	-15.6%	-20.6%	-15.5%	-15.4%
8→9	-21.1%	-20.9%	-28.1%	-19.0%	-9.9%	-	-	-	-	-
9→10; 8→10	-3.1%					-15.9%	-18.9%	-17.4%	-19.4%	-16.1%
10→11	-33.8%									
11→12	IHX pressure drop not considered									
12→13	-15.1%									

Table 8.6. Pressure drops comparison between design and CFD data. Entire cooling paths.

[%]	Sector 1					Sector 2				
	OUTBOARD			INBOARD		OUTBOARD			INBOARD	
	OBL 1	OBC 1	OBR 1	IBL 1	IBR 1	OBL 2	OBC 2	OBR 2	IBL 2	IBR 2
1→13 (Total)	-23.1%	-19.9%	-25.1%	-16.5%	-14.3%	-20.5%	-19.8%	-22.9%	-17.3%	-16.8%

As can be seen from these results, the discrepancies generally fall in a range that can still considered typical of uncertainties of the correlation adopted, therefore the design approach seems suitable to be also employed in the futures works where a certain degree of conservativism if requested.

Figure 8.8 and Figure 8.9 show additional CFD results.

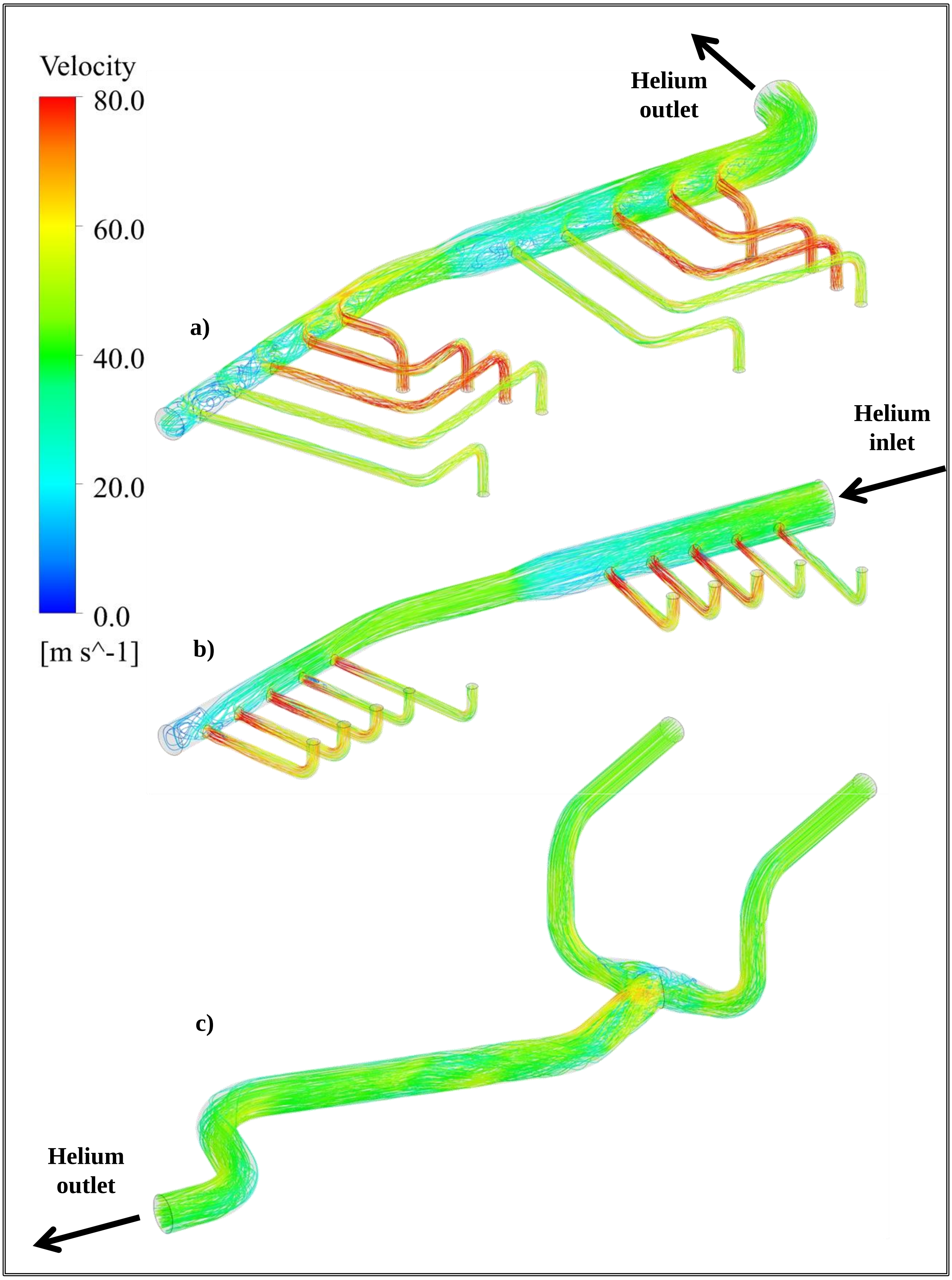

Figure 8.8. Streamlines in T-junctions :a) hot collector; b) cold distributor; c) cold header.

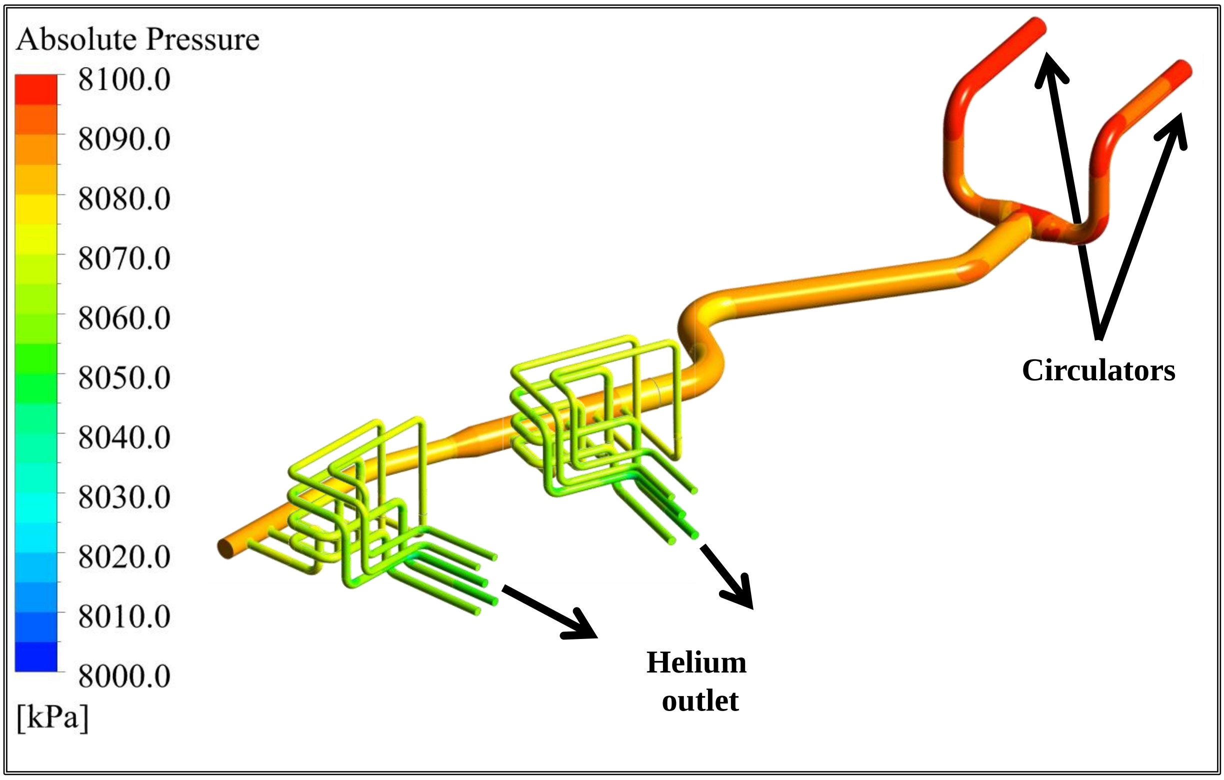

Figure 8.9. Pressure distribution from circulators to cold feeding pipes.

8.4 RELAP5-3D Analysis of the dynamic behaviour of BB PHTS

A computational model of the HCPB BB PHTS relevant cooling loop has been developed for the RELAP5-3D system code in order to support the thermal-hydraulic design activities assessing the normal operational conditions and to verify the design evaluations.

8.4.1 RELAP5-3D basic structures

The RELAP5-3D flow model includes a one-dimensional, stream-tube formulation option in which the bulk flow properties are assumed to be uniform over the fluid passage cross-section. The control volumes are finite increments of the flow passage and may have a junction at the inlet or outlet (normal junctions) or at the side of a volume (crossflow junctions) [215].

The basic two-fluid model is applied uniformly to all volumes and junctions. Thus, the programming design of the hydrodynamic calculation is primarily organized on volumes and junctions. Components are organized collections of volumes and junctions and, to a lesser extent, the program is organized on components. Components are designed for either input convenience or to specify additional specialized processing. A pipe component is an example of a component designed for input convenience, since by taking advantage of typical features of a pipe, several volumes and junctions can be described with little more data than for one volume. Pump (compressor) and valve components are examples of components requiring additional processing. A pump component includes data defining pump head and torque characteristics for single-phase and two-phase conditions as a function of pump angular velocity. A pump (compressor) component requires additional processing to advance the differential equation defining pump (compressor) angular velocity. A valve component requires additional data defining its characteristics and additional processing to calculate the junction flow area as a function of valve position [215].

The main hydrodynamic components that have been adopted for the modelling of the HCPB BB PHTS are herein briefly introduced.

8.4.1.1 Time-Dependent Volume

A time-dependent volume must be used wherever fluid can enter or leave the system being simulated. The geometry data required are similar to system volumes, but during input processing the volume’s length, elevation change, and volume are set to zero. With the staggered mesh, the pressure boundary would be applied in the centre of the time-dependent volume. Setting these quantities to zero moves the boundary to the edge of the system volume.

A time-dependent volume is used to model mass sources/sinks and pressure boundaries. The state conditions as a function of time or some time-advanced quantity may be entered as a table, with time or the time-advanced quantity as the independent or search variable. If constant state values are desired, only one set of data consisting of any search value and the associated constant data needs to be entered. Step changes can be accommodated by entering two adjacent sets of data with the same time or an extremely small time difference.

8.4.1.2 Time-Dependent Junction

Time-dependent junctions can be used whenever the phasic velocities or phasic mass flow rates are known as a function of time or other time-advanced quantity. Time-dependent junctions can connect any two system volumes, or a system volume and a time-dependent volume. Phasic mass flow rates are converted to phasic velocities using the upstream phasic densities and upstream phasic volume fractions.

Examples of their use would be to model a constant displacement pump in a fill system, a pump or a valve (or both), by using an associated control system or measured experimental data. Time-dependent junctions are also used frequently in test problems to check code operation.

The phasic velocities or phasic mass flow rates in the time-dependent junction as a function of time or the time-advanced quantity may be entered as a table, with time or the time-advanced quantity as the independent or search variable.

The capability of using time-advanced quantities as search arguments can be used to model pressure-dependent liquid injection systems. If the injection flow is a function of the pressure at the injection point, the volume pressure at that point is used as the search argument.

8.4.1.3 Single-Volume

A single-volume component is simply one system volume. A single-volume can also be described as a pipe component containing only one volume. This single-volume component uses fewer input cards and fewer data items than does a pipe component.

8.4.1.4 Single-Junction

A single-junction component is simply one system junction. It is used to connect other components such as two pipes. Initial junction conditions can be phasic velocities or phasic mass flow rates.

8.4.1.5 Pipe

A pipe component is a series of volumes and interior junctions, the number of junctions being one less than the number of volumes, and the junctions connect the outlet of one volume to the inlet of the next volume. Pipe components can be used for those portions of the system without branches. Pipe components offer input conveniences, since most characteristics of the volumes and junctions in a pipe are similar or change infrequently along the pipe, and input data requirements can be reduced accordingly. Because of the sequential connection of the volumes, junctions are generated automatically rather than being individually described. Although the input is designed to assume considerable similarity in volume and junction characteristics, any of the volume and junction features (such as flow area, orientation, pipe roughness, or control flags) can be changed at each volume or junction.

8.4.1.6 Compressor

The compressor component model can be separated into models for hydrodynamics, compressor-fluid interaction, and compressor driving torque. The compressor component input provides information for the hydrodynamic and compressor-fluid interaction models. A compressor can be connected to a shaft that is a specialized component within the control system. A shaft component is used when the compressor is driven by a turbine or by an electric motor with a control system to regulate speed. The compressor also may optionally include input for an electric motor to drive the compressor.

8.4.1.6.1 Compressor Model Description

The hydrodynamic model of a compressor component consists of one volume and one or two associated junctions. One junction is connected to the inlet and is called the suction junction; and must be supplied with the compressor component. Optionally, a second junction can be specified with the compressor component, which is connected to the outlet and is called the discharge junction. The compressor head, torque, and angular velocity are computed using upstream junction mass flow rate, density, and sound speed. The head developed by the compressor is treated like a body force in the momentum equations for the inlet junction.

With the exception of the head term, the hydrodynamic model for the compressor volume and junctions is identical to that for normal volumes and junctions.

The compressor head curve specification is formulated as pressure ratio and the compressor torque is calculated based on the compressor characteristic curves and the stage adiabatic efficiency.

8.4.1.6.2 Compressor Performance Modeling

Interaction of the compressor and the fluid is described by empirically developed performance maps relating compressor pressure ratio and efficiency to the mass flow rate and compressor angular (rotational) velocity. The performance map is an xy representation that has a mass flow rate parameter (e.g. u) as the abscissa and a head-related parameter (e.g. pressure ratio) as the ordinate. Lines of constant speed and lines of constant efficiency are represented parametrically on the compressor performance map.

In RELAP5-3D, compressor performance maps are read in as a series of tables, one for each value of angular velocity. Each table consists of triplets of numbers for mass flow rate, pressure ratio, and efficiency.

8.4.1.7 Heat structures

Heat structures represent the selected, solid portions of the thermal-hydrodynamic system. Being solid, there is no flow, but the total system response depends on heat transferred between the structures and the fluid, and the temperature distributions in the structures are often important requirements of the simulation. System components simulated by heat structures include fuel rods, pipe walls, core barrels, pressure vessels, and heat exchanger tubing.

8.4.2 Description of the RELAP5-3D model

The model nodalization has been developed to realistically predict the overall thermal-hydraulic behaviour of the selected loop demanding admissible computing time. Indeed, it reproduces accurately the current design of the system reported in [7] and [9] by using 211 thermal-hydraulic components, being 110 PIPEs, 4 MULTIPLE JUNCTIONs, 90 SINGLE JUNCTIONs, 2 SINGLE VOLUMEs, 1 COMPRESSOR, 2 TIME DEPENDENT VOLUMEs, 2 TIME DEPENDENT JUNCTIONs and 93 HEAT STRUCTUREs. In addition, 1031 CONTROL BLOCKs, 167 SIGNAL VARIABLEs and 125 TABLEs complete the model.

Figure 8.10 shows the nodalization scheme adopted for the cold (a) and hot (b) legs and that adopted to simulate each of the segments (c) related to the analysed loop along with their CAD geometrical model.

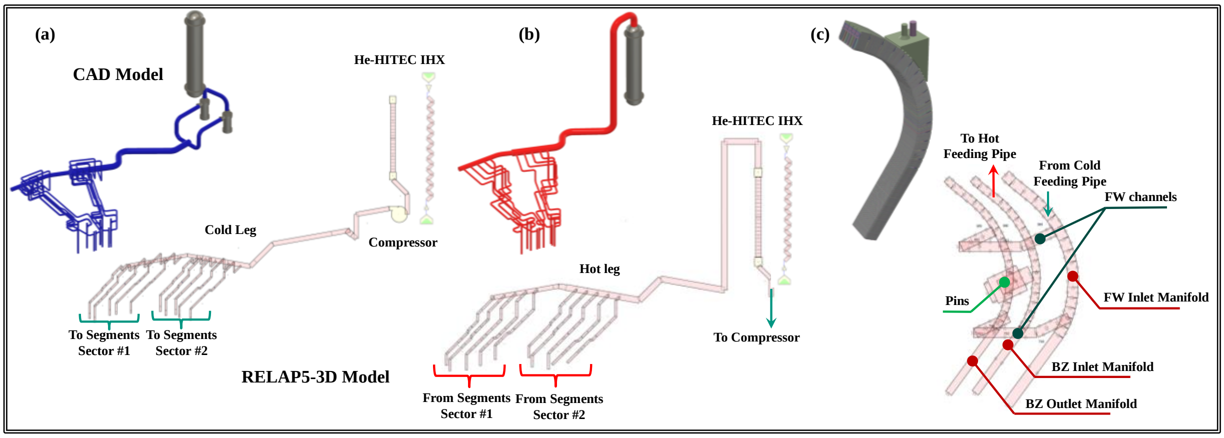

Figure 8.10. PHTS code nodalization for cold part (a), hot parts (b) and in-VV circuits (c)

In point of fact, the computational model consists of four main sub-models: (i) the flow domain model, reproducing in a quasi-2D approximation the lay-out of the cooling circuit; (ii) the constitutive models, provided by the system code to describe the thermo-dynamic behaviour of the helium circulating inside the cooling system; (iii) the hydraulic model, intended to simulate the fluid flow along the cooling system and the (iv) thermal model articulated in different sub-patterns aimed at realistically reproducing the heat transfer phenomena which take place along the cooling system.

In order to better reproduce the hydraulic performance of the analysed system, it has been developed a specific procedure to integrate the RELAP5-3D system code aptitude to synthetically simulate the thermal-hydraulic performances of complex systems with the highly realistic predictive potential guaranteed by ANSYS CFX in the assessment of the fluid-dynamic behaviour of coolant flowing through deeply 3-D circuits. In particular, with reference to the in-vessel components, the model implements hydraulic functions which relate the total pressure drops experienced by the main In-Vessel components, namely “fuel pin” channels, FW channels and the manifolds, to the mass flow rate according to a law of the type $\Delta p = \alpha G^{\beta}$. The characterization of the functional dependence of their total pressure drop for different mass flow rates has been performed by the KIT laboratories through detailed parametric analyses for the COB. These functions have been kindly provided to the University of Palermo to be implemented within the RELAP5-3D code [213] [214].

As concerns the thermal modelling, the heat transfer phenomena have been reproduced implementing the thermo-physical properties of all the structural materials involved and by adopting the properly selected heat transfer models. The Gnielinski correlation, already implemented in the RELAP5-3D models package, has been adopted for the helium convective heat transfer; on the molten salt side, in order to be fully consistent with the design data, the Bell-Delaware procedure for evaluating the heat transfer coefficient has been used. In particular, since it is not directly available into the system code, it has been implemented by using proper CONTROL FUNCTIONs which allow to evaluate the heat flux as boundary conditions for the HEAT STRUCTUREs simulating the heating surface of the IHX.

With regard to the IHX and its model, since the solar molten salt HITEC has been foreseen as working fluid for the Intermediate Heat Transfer System, a dedicated binary file has been generated to implement its thermo-physical properties into the code fluid libraries. The model reproduces accurately the shell side of the heat exchanger, while the inlet and outlet boundary conditions have been simulated by adopting TIME DEPENDENT VOLUMEs and JUNCTIONs, see Figure 8.10. Moreover, the thermal modelling approach here adopted has been assessed by performing a benchmark with the experimental data coming from the experiences conducted on the HETRA facility [215]. The thermal power adopted for simulating the normal operational scenario including the ramp-up /down takes into account both the FW heat flux and the nuclear heating as reported in [216]; the latter is re-scaled to according to [39]. Figure 8.11 shows the thermal power profile for adopted for the cases under investigation. It follows the DEMO duty cycle already described in the paragraph 2.1

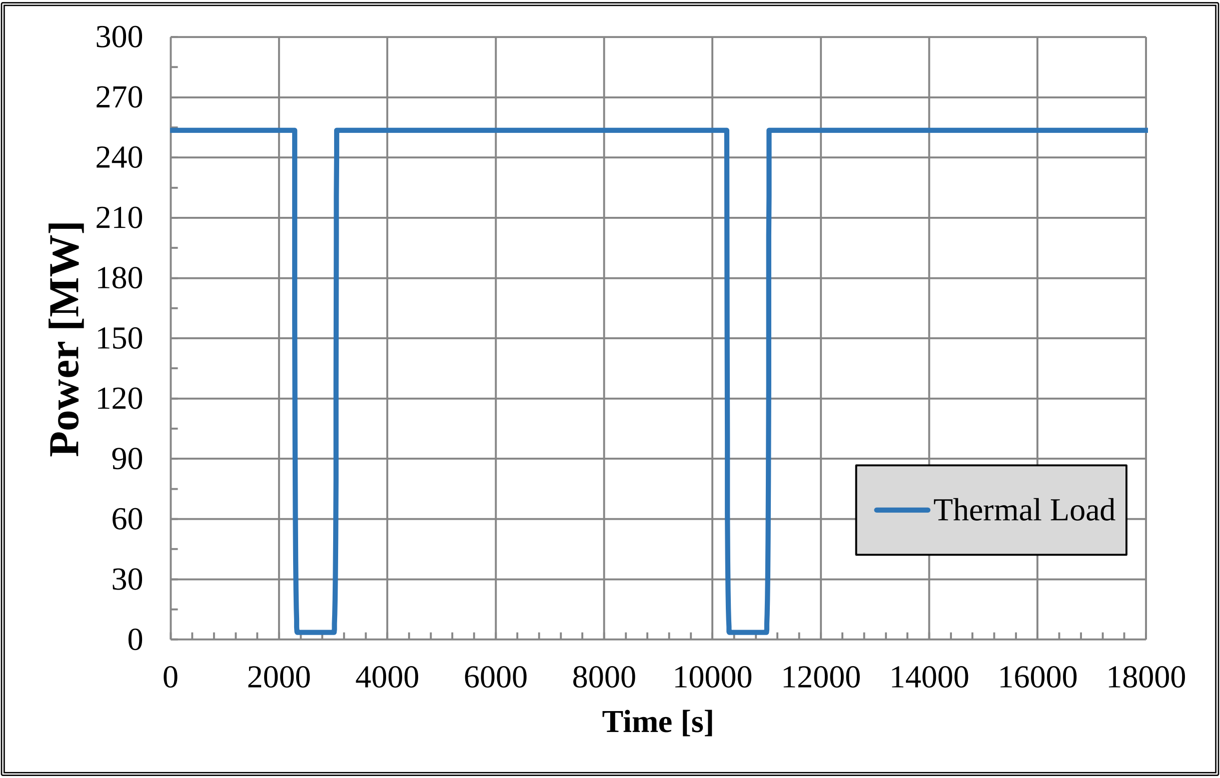

Figure 8.11.Thermal power profile

8.4.3 Comparison of the RELAP5-3D results against the PHTS design values

The simulation of the normal operational conditions has been mainly intended to investigate the capability of the model to predict the thermal-hydraulic phenomena occurring into the system. The final scope has been to study a possible strategy to control both the helium and HITEC mass flow rates in order to maintain the inlet temperature to the BB equal to 300 °C, as required in [37]. However, before the beginning of the simulation campaign with the reference to the nominal DEMO duty cycle, it has been set-up an analysis to preliminary assess the response of the PHTS under hypothetical steady-state conditions (e.g. a DEMO reactor which manages to operate in Pulse mode for an indefinite time span).

The main steady-state parameters calculated through RELAP5-3D are summarized in Table 8.7. As can be seen, the steady-state behaviour of the systems is well predicted by the RELAP5-3D code, with the calculated main thermal-hydraulic parameters of the PHTS being very close to the design values. The maximum deviation occurs in the secondary coolant mass flow rate, which results about 3% higher than the design value. This is mainly due to a slight underestimation of the heat transfer rate in the exchanger. To ensure the transfer of the whole thermal power the flow control on the secondary coolant acts increasing the mass flow. As consequence, the outlet HITEC temperature is a bit below the design value.

Table 8.7. Comparison between design data and RELAP5-3D calculated values.

	Design	**RELAP5-3D**	**Error [%]**
Loop thermal power [MW]	253.63	253.63	0.00
Helium mass flow rate [kg/s]	222.24	222.24	0.00
HITEC mass flow rate [kg/s]	868.23	895.74	3.17
Helium hot/cold temperature [°C]	520.00/300.00	520.58/300.00	0.11/0.00
HITEC hot/cold temperature [°C]	465.00/270.00	460.88/270.04	-0.89/0.02
Helium pressure drop [kPa]	265.81	270.96	1.93

8.4.3.1 Pressure drops and hot temperature distributions

In order to qualify the developed nodalization, the pressure drops and the segments outlet temperatures calculated by the code have been compared to the theoretical ones.

The results show a very good accordance between theoretical and RELAP5-3D data; in particular, as can be seen from the two curves depicted in Figure 8.12, the developed model manages to simulate the pressure distribution along the circuit with a high degree of accuracy.

In fact, up to the blanket outlet both design and RELAP5 values are almost coincident, then small differences are appreciable but the maximum variance is kept within 2%. As already described in Table 8.7, the differences in the overall estimated pressure drop are about 5 kPa, which is a deviation of almost negligible if compared to the total pressure losses.

As regard to the helium hot temperature at the blanket outlet, also in this case optimal results have been achieved both in terms of mean hot leg temperature, well as in the outlet temperatures distribution among the different blanket segments. The former is about half degree above the design value whereas the outlet BB temperatures show very little differences from the hot leg bulk temperature, falling all within -0.89/+1.10 °C (see Figure 8.13).

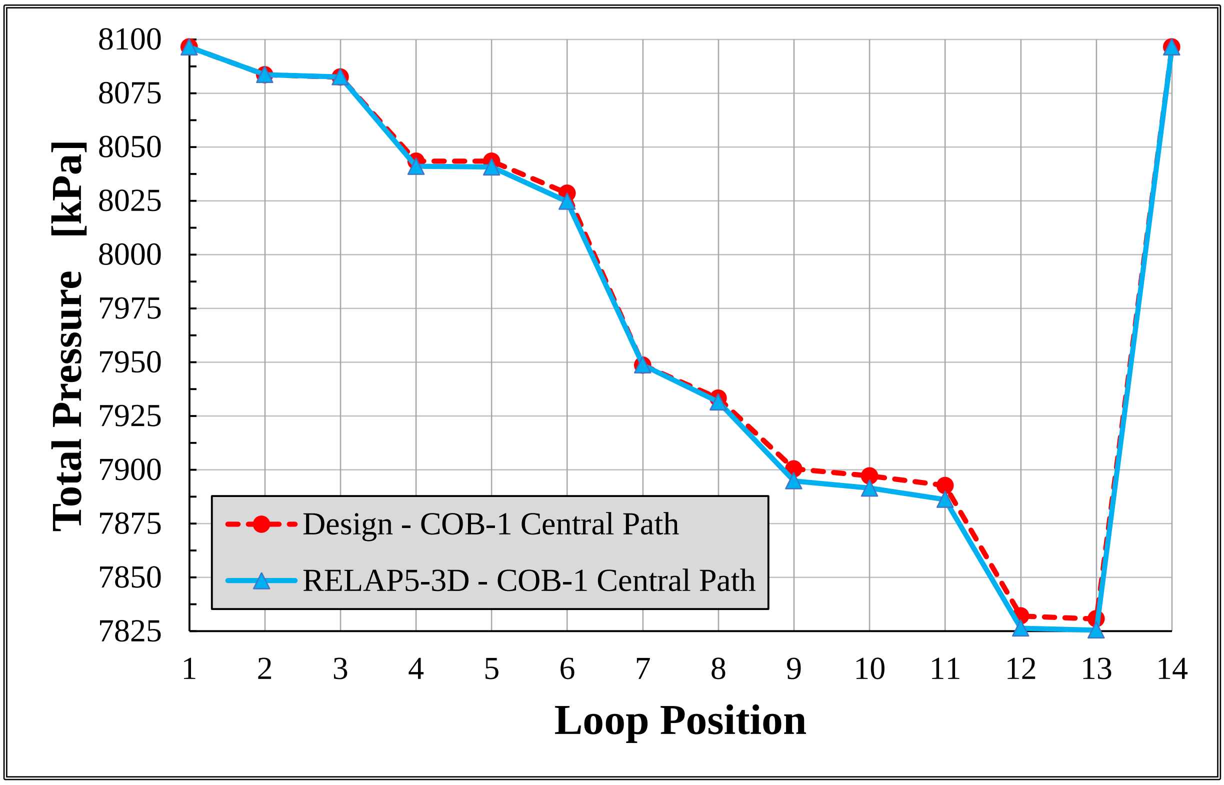

Figure 8.12. Pressure distribution along the OBC-sector 1 path – Design vs RELAP5-3D data.

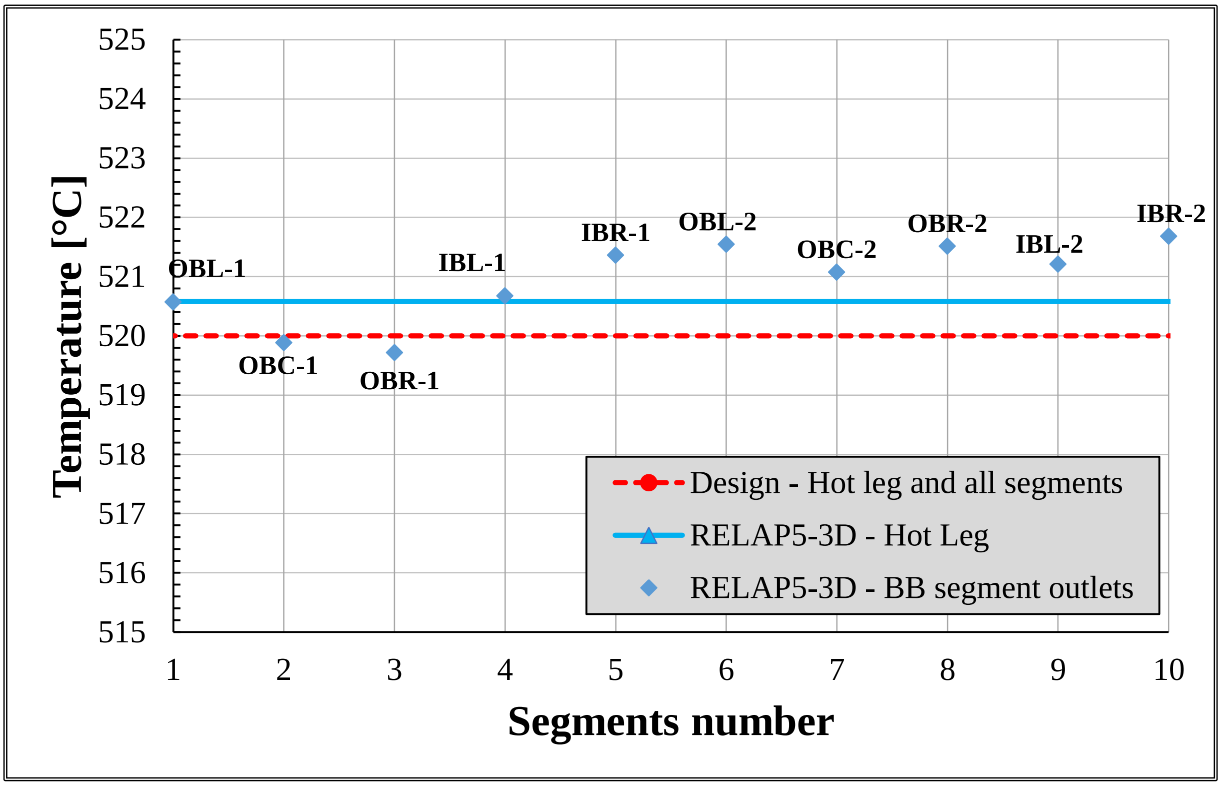

Figure 8.13. Pressure distribution along the OBC-sector 1 path – Design vs RELAP5-3D data

8.4.3.2 IHX thermal-hydraulic behaviour

A better understanding of the behaviour of the exchanger can be gather from Figure 8.14, where both design and RELAP5 calculated temperature profiles are depicted.

In spite of the small differences (about 4°C) in the HITEC outlet temperature, the coolant temperature profiles calculated through the RELAP5-3D code match very well the design data. This is a further confirmation of the effectiveness of the methodology used during the early design phase to size the component. Moreover, it can be noticed that the wall temperature predicted by the system code is slightly below the design values; this is mainly due to the higher secondary mass flow rate which tends to pull down the wall temperature toward the coolant.

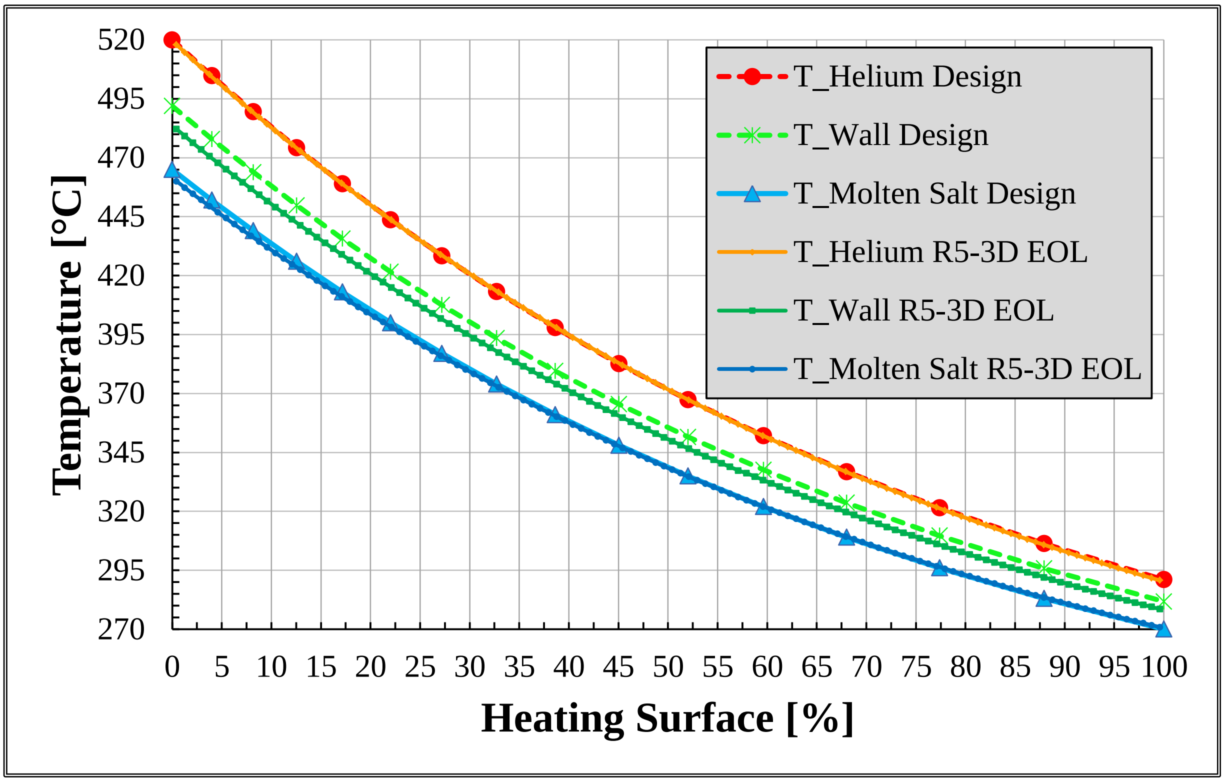

Figure 8.14. IHX temperature profiles – Design data vs RELAP5-3D values.

8.4.4 Thermal-hydraulic behaviour of the BB PHTS during Pulse/Dwell transition

A parametric study has been thereafter performed analysing the normal operational conditions. The main objective of this preliminary study has been to assess the dynamic response of the system when it switches from pulse to dwell and vice-versa.

In particular, 4 cases involving a combination of different mass flow rates on both helium and HITEC sides have been set-up with the aim of understanding the potential maximum variations that relevant quantities such as pressure and temperatures can experience for a given Balance of Plant control. To this purpose, it has been initially assumed that a fine regulation of the coolant mass flow rates might not be possible, so that helium and HITEC flows can only pass from their maximum to their minimum values.

Such a control of the flow rates could appear too restrictive, however before studying a proper regulation strategy aimed at minimizing pressure and temperature excursions that might occur in the system, it has been judged opportune to analyse these somewhat limiting cases.

Therefore, the 4 cases that has been identified are:

- Case I, both the helium and the HITEC mass flow rate are kept constant at the nominal pulse value during the entire period;
- Case II, the helium flow rate is the same that in Case I, while the HITEC one follows the same functional shape of the BB thermal power;
- Case III consists in changing the helium mass flow rate according to the same functional shape of the BB thermal power, while the molten salt mass flow does not change;
- Case IV, both the helium and the HITEC mass flow rates evolve like the power functional shape.

Figure 8.15 and Figure 8.16 depict helium and HITEC mass flow rates, respectively.

The trend of the temperatures in cold and hot legs is shown in Figure 8.17 and Figure 8.18, respectively; whilst in Figure 8.19 the cold leg pressure is displayed.

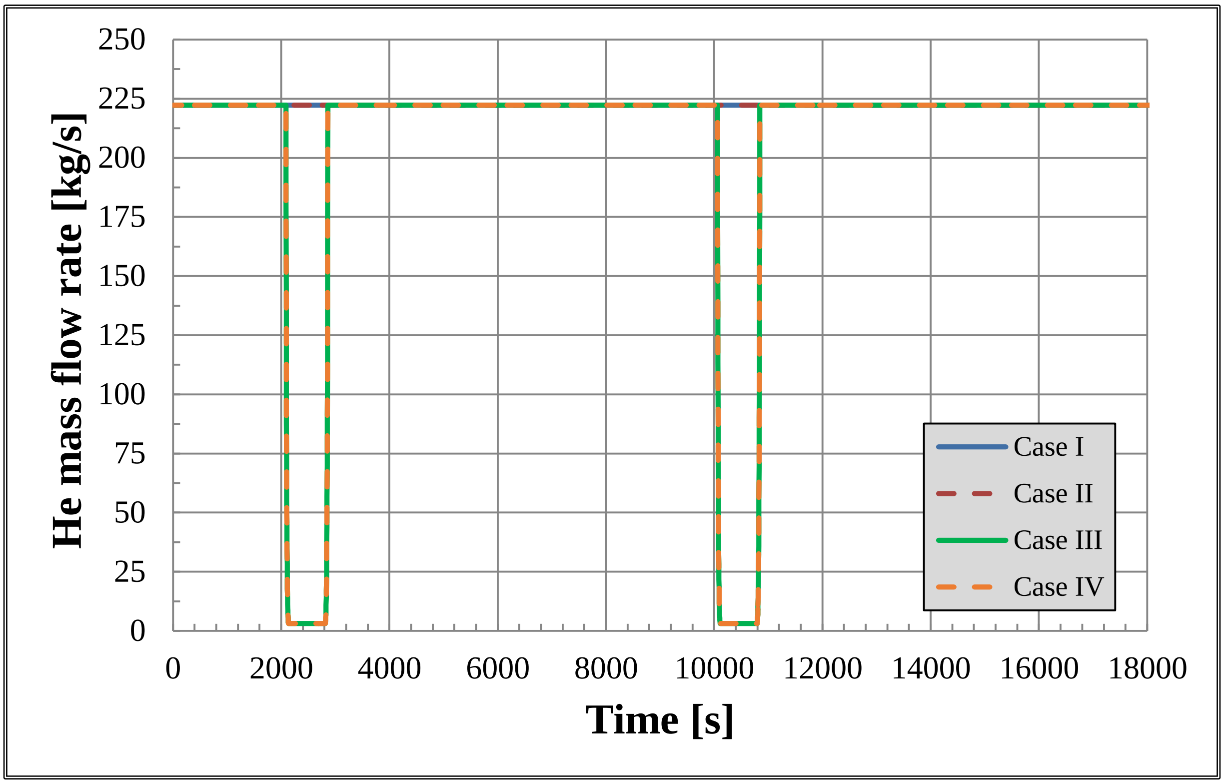

Figure 8.15. Helium mass flow rate

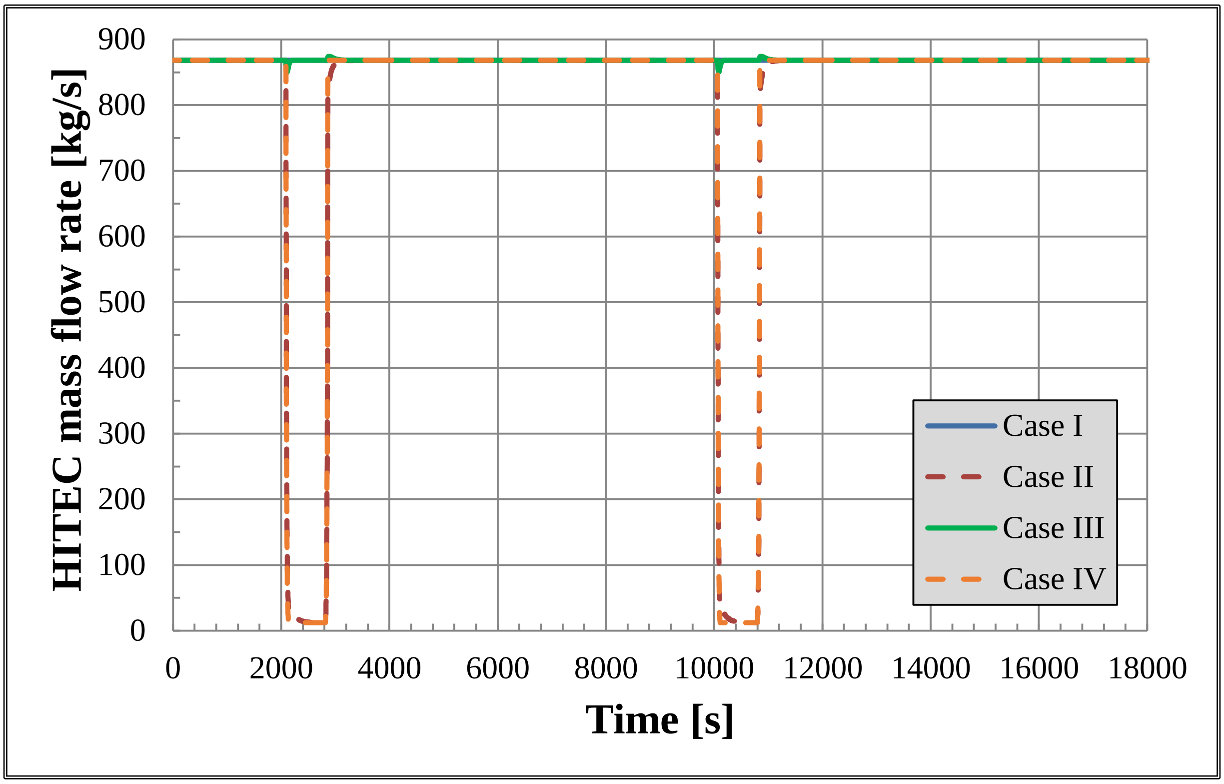

Figure 8.16. HITEC mass flow rate

In both Cases I and II, when the dwell starts, temperatures and/or pressure show high and fast changes. In particular the former presents too large increase of the pressure, while in the latter case the huge thermal-hydraulic variations affect the whole dwell phase as well as the following pulse period. Indeed, the system is able to recover the design values just before the beginning of the next dwell. This is due to the control of PHTS that, keeping the helium mass flow rate at its maximum value, extends the time needed to heat up again the BB structures.

Cases III and IV present less marked deviation of the relevant quantities thanks to the helium mass flow rate control which basically follows the BB thermal load profile. However, such regulation seems to be very challenging since it implies a quick and fast variation of the primary mass flow rate.

Starting from these outcomes, another case has been simulated in which the helium mass flow rate evolves assuming a viable rate of change of 12.5% per minute, reaching the minimum value of 83.34 kg/s during the dwell (37.5% of the nominal value). Such ramp-up/down of the circulator seems feasible as it is still in line with the state-of-art of helium compressor technology (chapter 6). On the secondary side, the regulation strategy might be more flexible because it is assumed that HITEC mass flow rate can be regulated through active control valves as well as variation of the speed of the feed pumps. For these reasons the molten salt mass flow rate is evaluated by the system code with a dedicated proportional-integral controller aimed at maintain the required BB inlet temperature to 300 °C.

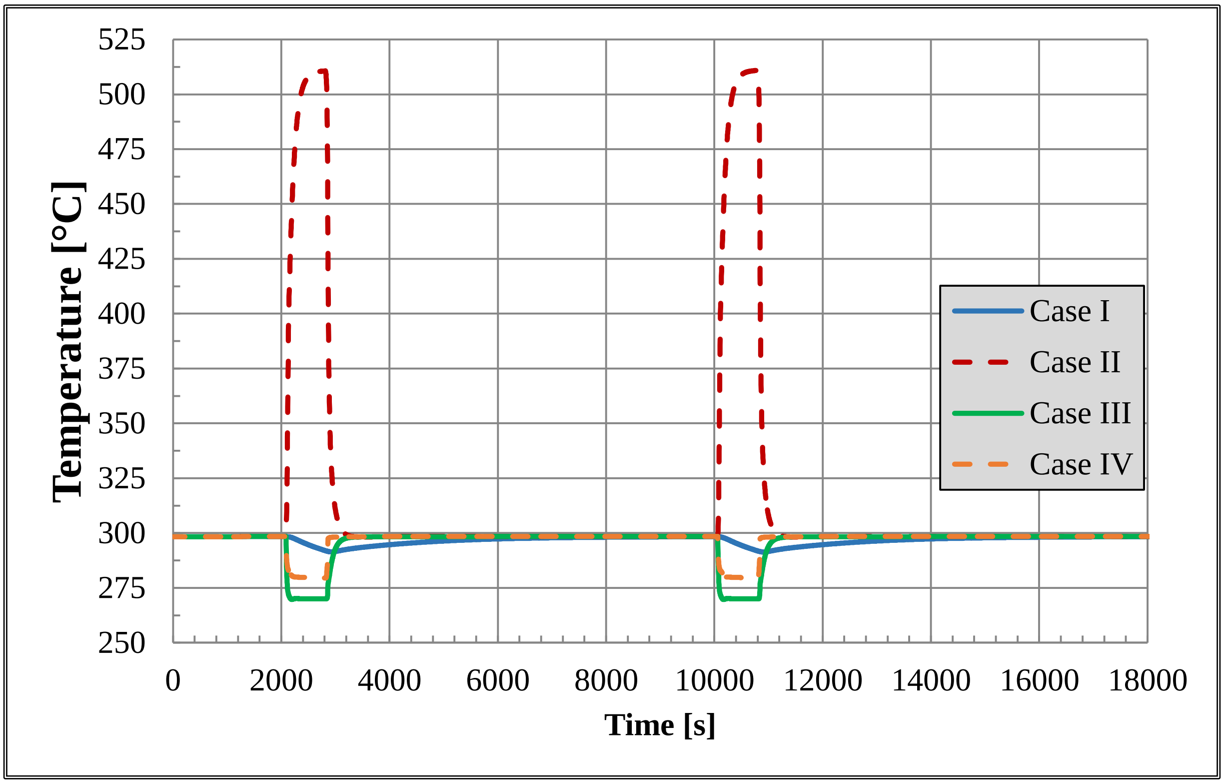

Figure 8.17. Cold Leg temperature

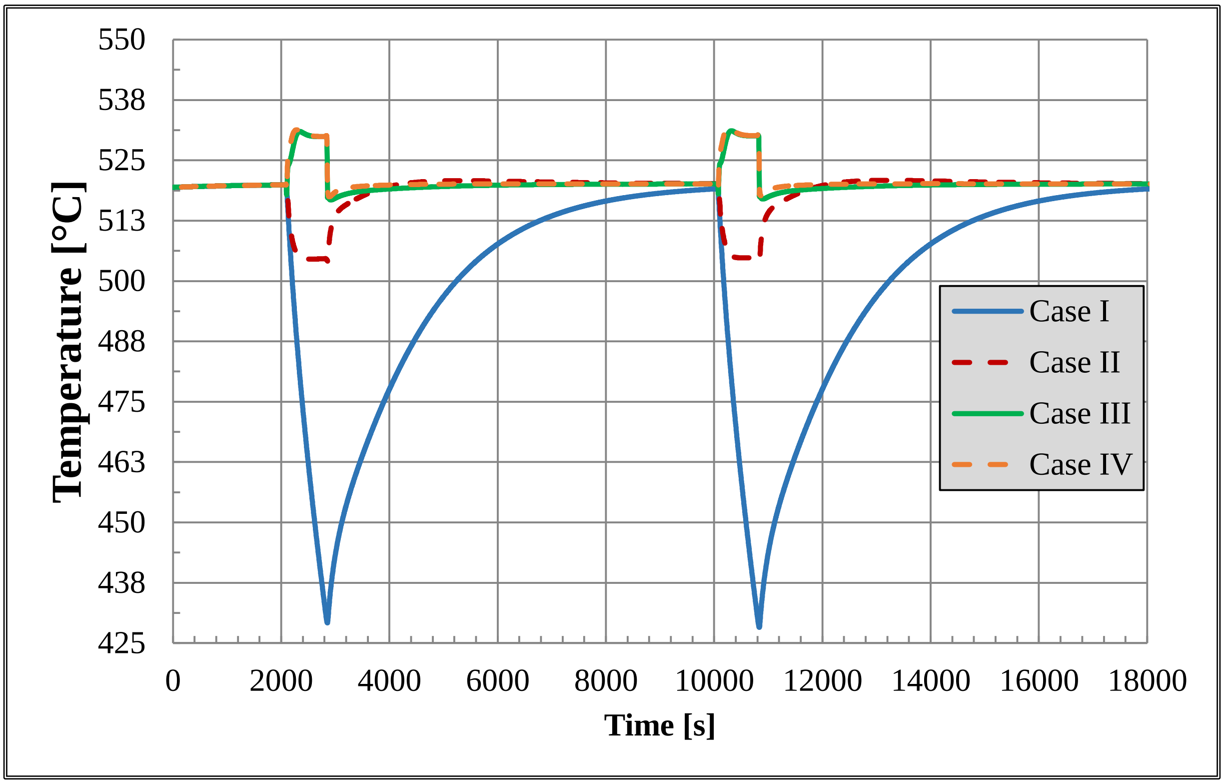

Figure 8.18: Hot Leg temperature.

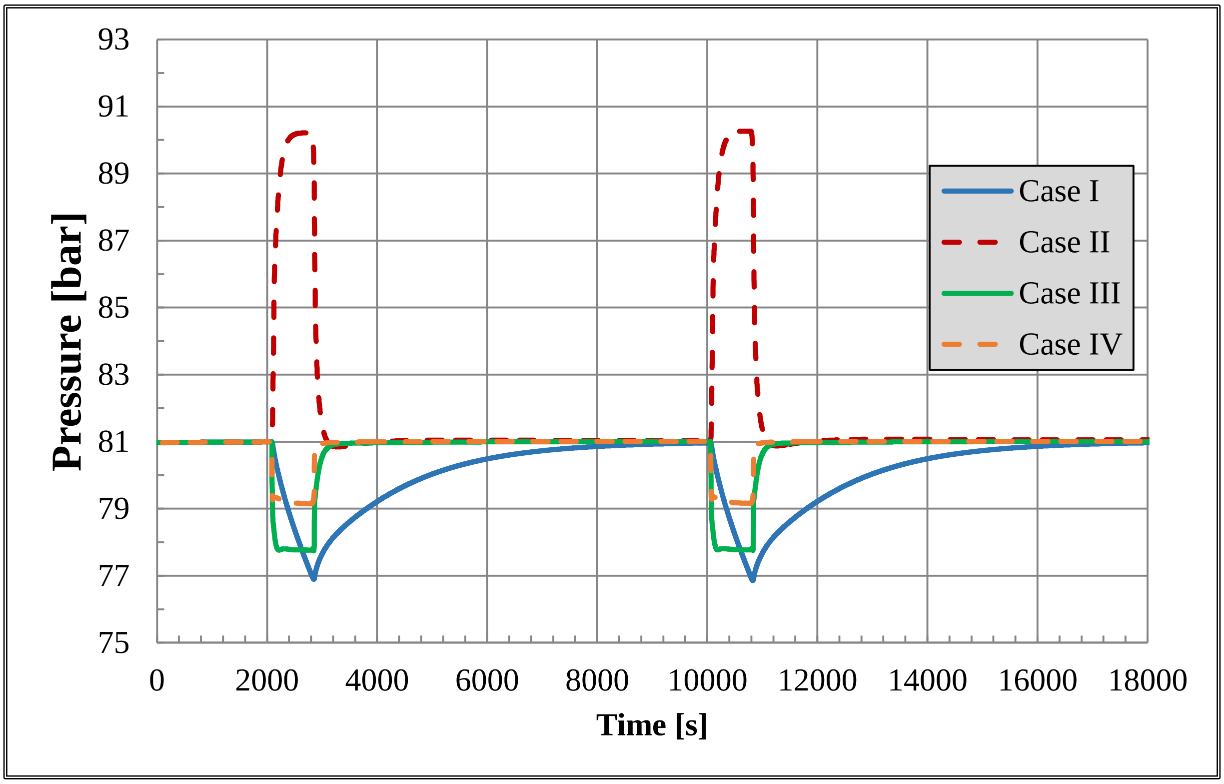

Figure 8.19. Cold leg inlet pressure.

Figure 8.20 reports the mass flow rate behaviour both Helium and HITEC while the primary coolant temperatures and pressure are depicted in Figure 8.21 and Figure 8.22.

The PHTS control simulated in this last case allows to reduce the excursion of the main thermal-hydraulic quantities when the reactor switches from one operational phase to another.

The variations of pressure does not seem a critical issue because helium experiences a maximum variation of about 2 bar due to the global cooling of the primary fluid.

However, what causes concerns is: 1) the helium temperature drop in hot leg (about 60°C) and 2) the need of the entire following Pulse period to reach the nominal temperature value at the blanket outlet.

In fact, as regard to the first point, considering the large number of cycles foreseen during the whole operating period of DEMO, the fast and sharp temperature drops could excessively challenge the components in the “hot” part of the PHTS due to the thermal cycling.

On the other hand, since the helium in hot leg takes the whole Pulse period to reach again its nominal temperature, the effectiveness of the overall Balance of Plant operations and controls may be questionable.

According to these preliminary results, further investigations on the most suitable system control strategy seems, hence, needed with the support of the Balance of Plant expert and relevant industries involved into this DEMO task.

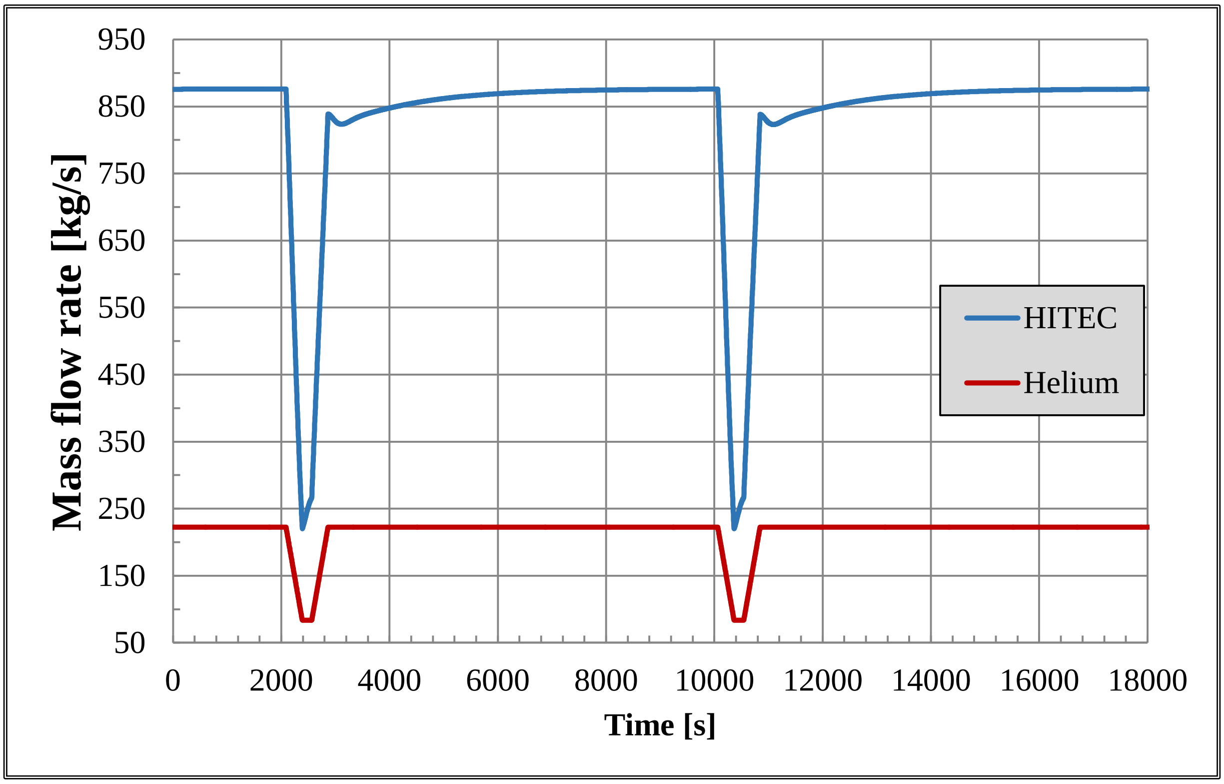

Figure 8.20. Helium and HITEC mass flow rate.

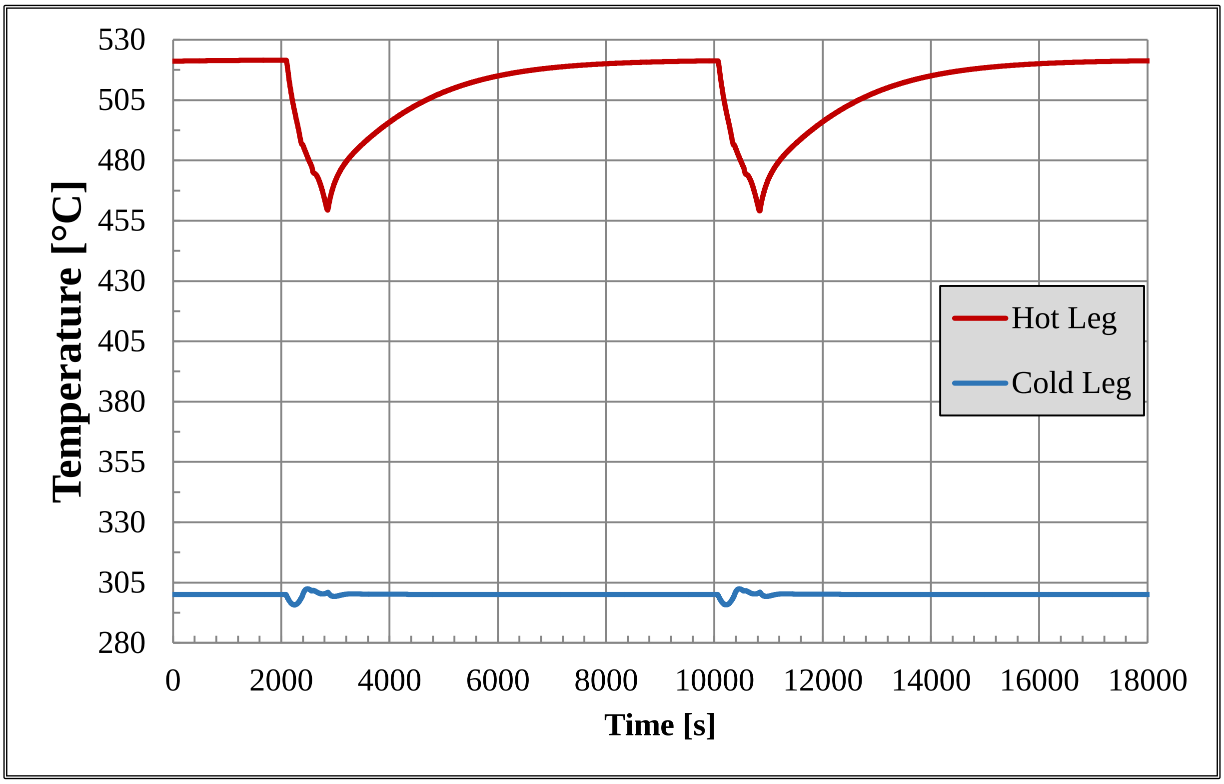

Figure 8.21. Hot and cold leg temperature.

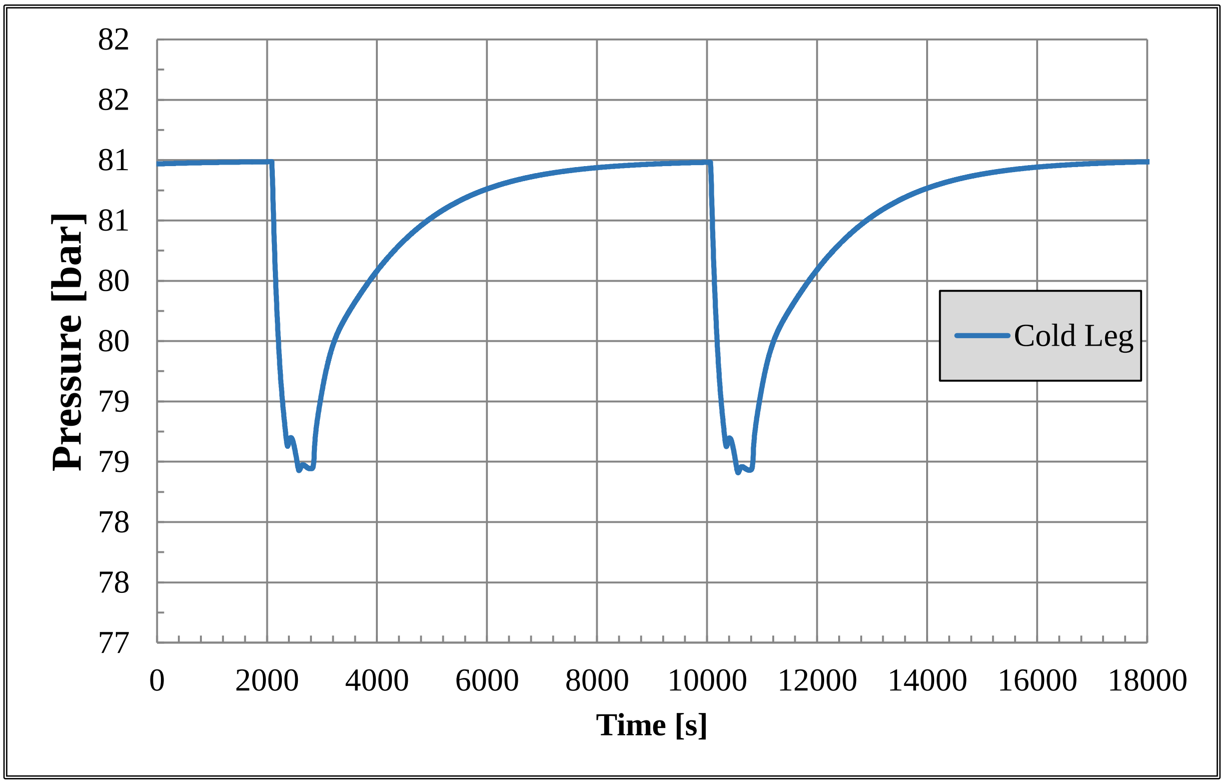

Figure 8.22. Cold leg inlet pressure.

Conclusions

The Ph.D. work, held at University of Palermo, has been carried out within the framework of the R&D activities, promoted by EUROfusion, relevant to the DEMO power plant.

The aim of the thesis has been to study the thermal-hydraulic challenges of the DEMO Balance of Plant equipped with a Helium-Cooled Breeding Blanket concept. A conceptual design of the Primary Heat Transfer System of Helium-Cooled Pebble Bed Breeding Blanket has been developed establishing criteria and thermal-hydraulic procedures to be followed in order to outline a system compatible with the DEMO requirements, with particular attention to the safety and integration needs.

The activity has been always conducted considering the global status and the past achievements of the nuclear industry, with particular regard to those solutions envisaging high temperatures and gaseous coolants. The objective to be pursued has been the transfer of knowledges, lessons learnt and technologies commonly used in fission reactors to the systems of the DEMO Balance of Plant, in order to achieve a feasible thermal-hydraulic and mechanical design of the main cooling equipment. For this purpose, the assessments have been made through a stepladder methodology, which has consisted in the application of a series of numerical tools with a growing grade of evolution and thermal-hydraulic prediction capabilities. An early development of analytical and semi-analytical procedures has, in fact, allowed to strengthen the engineering "feel" for the design processes proper of a helium cooling system placed in a nuclear fusion environment.

Finally, the most promising layout of the HCPB BB PHTS has been outlined, developed and integrated in a 3D-CAD model of the DEMO baseline 2017. The BB primary system have been sized with an highly degree of segmentation of its cooling loops which are 8. These circuits are completely independent, from mechanical point of view, in order to limit some common mode failures. Each cooling circuit provides helium to all ten segments of 2 blanket sectors.

Particular care has been paid to the design of the heat exchangers. In fact, in the BoP of DEMO, these components have a key role because their thermal-hydraulic performances and responses are fundamental to ensure a safe plant operation. Moreover, being them the largest elements of the primary cooling circuit to be placed within the tokamak building are probably the most challenging components from the BoP integration point of view.

The definitions of the best design options for the primary exchanger has been pursued after preliminary assessments on a range of several alternatives.

The final selected configurations are aimed at fulfil the demands of the 2 main BoP options envisaged in the pre-conceptual design phase of DEMO.

A thoroughly assessment of the pipework size and their hydraulic performances has been also made in order to obtain a reliable estimation of the total pressure drops of the circuits. The knowledge of the pressure drops and their distribution among the cooling paths has allowed to evaluate the electrical power required by the circulators to let helium flow within the PHTS.

A preliminary investigation on the most suitable characteristics and the requirements that helium circulators should meet to work in high efficiency regimes has been made.

Then, further investigations of the whole system thermal-hydraulic performances have been performed exploiting the features of well-established and robust computer programmes such as Ansys CFX, a fully 3-D CFD tool, and the RELAP5-3D system code, a truly state-of-the-art program for the nuclear thermal-hydraulics.

The numerical campaign has allowed to partially test the equipment of the PHTS, whose pre-conceptual design has been developed during the first period of activities.

In particular, the procedure to deal with the pressure losses in a rather complex piping network applied during the design phase has been also verified by means of a 3D fluid dynamic tool. The results are encouraging as they show a general agreement of the design data with the numerical assessments, being commonly the differences in the order of 20%. In particular, the conservative approach of the thermal-hydraulic design calculations has been confirmed by the computational runs, providing some margins to envisage a further optimization of the design.

A thermal-hydraulic model of a whole loop, representative of the 8 circuits in parallel, has been developed in RELAP5-3D environment. The model has been devoted to evaluate the thermal-hydraulic behaviour of the PHTS under hypothetical steady-state conditions as well as during the normal operation foreseen in DEMO, thus considering the total duty cycle of the Tokamak, namely Pulse, Dwell and Ramp-up/down phases. Different strategies to control the primary and the secondary mass flow rates have been investigated with the aim of minimizing the thermal transients in the structures due to the power oscillations.

The results obtained simulating the normal operational scenario are in good agreement with the design data calculated for the Pulse phase, however the hot leg temperature fluctuations seems still too large to let the system operate in a very reliable and safe mode.

Further investigations on the most suitable system control strategy seems, hence, needed with the support of the Balance of Plant expert and relevant industries involved into this DEMO task. Nevertheless the model itself appears suitable and robust enough to investigate both operational and, in future, also accidental transients.

Developments are on-going to implement within the model all the remaining components needed to simulate the intermediate system as well as the turbine loop.

Acknowledgements

I would like to offer special thanks to Dr.s Luciana Barucca, Gianfranco Federici and Sergio Ciattaglia for the expertise and competence with which they have kindly supported and cooperated to the realization of this work.

I wish to take this opportunity to sincerely thank my Professor and Tutor, Pietro Alessandro Di Maio, and my Co-Tutor Pierluigi Chiovaro for their high quality contributions, the scientific excellent hints, and the curtesy.

I also wish to express my infinite gratefulness to my colleagues and, above all, friends, who always supported and helped me to improve this present thesis with their precious assistance and contributions: Salvatore, Eugenio, Andrea, Ruggero.

Finally, I wish to especially express my heartfelt gratitude to my beloved girlfriend, Sabrina, who was so patience and allowed me to spend so much extra time on my favourite hobbies of thermal-hydraulics, heat exchangers and many other “boring” things.

References

[1] T. Donné and W. Morris, European Research Roadmap to the Realisation IN BRIEF of Fusion Energy, EUROfusion, 2018.

[2] G. Federici and al., “Overview of EU DEMO design and R&D activities,” *Fusion Engineering and Design,* vol. 89, pp. 882-889, 2014.

[3] G. Federici and al., “Overview of the design approach and prioritization of R&D activitiestowards an EU DEMO,” *Fusion Engineering and Design,* Vols. 109-111, p. 1464–1474, 2016.

[4] G. Federici and al., “Overview of the DEMO staged design approach in Europe,” *Nuclear Fusion,* vol. 59, no. 6, 2019.

[5] C. Gliss, “DEMO Reference Configuration model,” EFDA_D_2N4EZW, 2017.

[6] G. Federici and al., “DEMO design activity in Europe: Progress and updates,” *Fusion Engineering and Design,* vol. 136, p. 729–741, 2018.

[7] C. Bachmann, S. Ciattaglia, F. Cismondi, G. Federici, G. Keech, F. Maviglia and M. Siccinio, “Critical design issues in DEMO and solution strategies,” *Fusion Engineeting and Design,* vol. 146, pp. 178-181, 2019.

[8] F. Maviglia, A. R., R. Ambrosino, W. Arter, C. Bachmann and al., “Wall protection Strategies for DEMOplasma transients,” *Fusion Engineering and Design,* vol. 136, pp. 410-414, 2018.

[9] D. Stork, P. Agostini, J. Boutard, D. Buckthorpe, E. Diegele and e. al., “Developing Structural, High-heat flux and Plasma Facing Materials for a near-term DEMO Fusion Power Plant: the EU Assessment,” *Journal of Nuclear Material,* vol. 455, pp. 277-291, 2014.

[10] F. Cismondi and al., “Progress in EU Breeding Blanket design and integration,” *Fusion Engineering and Design,* vol. 136, pp. 782-792, 2018.

[11] H. Reimerdes and al., “Assessment of alternative divertor,” in *Proceedigns of 2018 IAEA Fusion Energy Conference,* Gandhinagar, India, 2018.

[12] R. Kembleton and al., “Engineering and integration risks arising from advanced magnetic divertor configurations,” *Fusion Engineering and Design,* vol. 146, pp.

2281-2284, 2019.

[13] R. Ambrosino, A. Castaldo, S. Ha, V. Loschiavo, S. Merriman and H. Reimerdes, “Evaluation of feasibility and costs of alternative magnetic divertor configurations forDEMO,” *Fusion Engineering and Design,* vol. 146, pp. 2717-2720, 2019.

[14] C. Bachmann and al., “Overview over DEMO design integration challenges and their impact oncomponent design concepts,” *Fusion Engineering and Design,* vol. 136, pp. 87-95, 2018.

[15] G. Keech and al., “Issues of the vertical blanket segment architecture in DEMO: Current progress and resolution strategies,” *Fusoin Engineering and Design,* vol. 146, pp. 1408-1412, 2019.

[16] L. Barucca and al., “Status of EU DEMO heat transport and power conversion systems,” *Fusion Engineering and Design,* vol. 136, pp. 1557-1566, 2018.

[17] I. Moscato and al., “Preliminary design of EU DEMO helium-cooled breeding blanket primary heat transfer system,” *Fusion Engineering and Design,* vol. 136, pp. 1567-1571, 2018.

[18] E. Martelli and al., “Study of EU DEMO WCLL breeding blanket and primary heat transfer system integration,” *Fusion Engineering and Design,* vol. 136, pp. 828-833, 2018.

[19] C. Gliss and al., “Initial layout of DEMO buildings and configuration of the main plant systems,” *Fusion Engineering and Design,* vol. 136, pp. 534-539, 2018.

[20] S. Ciattaglia and al., “Key EU DEMO Plant and Building Layout Criteria,” in *14th International Symposyum on Fusion Nuclear Technology*, Budapest, 2019.

[21] C. Gliss and al., “Integration of DEMO hazard piping into the tokamak building,” in *14th International Symposyum on Fusion Nuclear Technology*, Budapest, 2019.

[22] C. Day and T. Giegerich, “The Direct Internal Recycling concept to simplify the fuel cycle of a fusion power plant,” *Fusion Engineering and Design,* vol. 88, no. 6-8, pp. 616-620, 2013.

[23] C. Day and T. Giegerich, “The KALPUREX-process – A new vacuum pumping process for exhaust gases in fusion power plants,” *Fusion Engineering and Design,* vol. 89, no. 7-8, pp. 1476-1481, 2014.

[24] T. Giegerich, “Advanced design of the Mechanical Tritium Pumping System for JET DTE2,” *Fusion Engineering and Design,* Vols. 109-111, pp. 359-364, 2016.

[25] B. Peters and C. Day, “Analysis of low pressure hydrogen separation from fusion exhaust gases by the means of superpermeability,” *Fusion Engineering and Design,* vol. 124, pp. 696-699, 2017.

[26] M. Siccinio and al., “Development of a plasma scenario for the EU-DEMO: current

activities and perspectives," in *27th IAEA Fusion Energy Conference (FEC 2018),* Ahmedabad, 2018.

[27] G. Federici and al., "Assessment of erosion of the ITER divertor target during type-I ELMs," *Plasma Physics and Controlled Fusion,* vol. 45, no. 9, pp. 1523-1547, 2003.

[28] L. V. Boccaccini and al., "Objectives and status of EUROfusion DEMO blanket studies," *Fusion Enginnering and Design,* Vols. 109-111, pp. 1199-1206, 2016.

[29] G. Federici and al., "An overview of the EU breeding blanket design strategy as an integral part of the DEMO design effort," *Fusion Enginnering and Design,* vol. 141, pp. 30-42, 2019.

[30] A. Del Nevo and al., "Recent progress in developing a feasible and integrated conceptual design of the WCLL BB in EUROfusion project," *Fusion Engineering and Design,* vol. 146, pp. 1805-1809, 2019.

[31] F. Hernández and al, "Consolidated Design of the HCPB Breeding Blanket for the pre-Conceptual Design activities of the EU DEMO and Harmonization with the ITER HCPB TBM Program," in *14th International Symposyium on Fuison Nuclear Technology,* Budapest, 2019.

[32] F. Hérnandez and al, "Advancements in the Helium Cooled Pebble Bed Breeding Blanket for the EU DEMO: Holistic Design Approach and Lessons Learned," *Nuclear Science and Technology,* vol. 75, pp. 352-364, 2019.

[33] F. Hérnandez and al., "HCPB Design Report 2018," EFDA_D_2NUTXK, 2019.

[34] I. Moscato and al., "On the thermal dynamic behaviour of the helium-cooled DEMO fusion reactor," *Journal of Physics: Conference Series,* vol. 1224, no. 1, 2019.

[35] E. Bubelis and H. W., "Conceptual Design Definition for an Intermediate Cooling Loop Configuration and Coolant," EFDA_D_2HDVN9, 2014.

[36] F. Maviglia and al., "Wall protection strategies for DEMO plasma transients," *Fusion Engineering and Design,* vol. 136, pp. 410-414, 2018.

[37] F. Hérnandez, «DDD 2015 for HCPB (Update of DDD 2014),» EFDA_D_2MRQ4E, 2016.

[38] I. Moscato e al., «Progress in the design development of EU DEMO helium-cooled pebble bed primary heat transfer system,» *Fusion Engineering and Design,* vol. 146, pp. 2416-2420, 2019.

[39] G. Spagnuolo, «Input data by HCPB for BOP-RM-SAE_2018,» https://idm.euro-fusion.org/?uid=2NX78M, 2019.

[40] P. Di Maio and al., "Cassette concept design development - 2nd phase thermo-hydraulic assessment," EFDA_D_2NEM88, 2019.

[41] Haertl, T. and al, “Rationale for the selection of the operating temperature of the DEMO vacuum vessel,” *Fusion Engineering and Design,* vol. 146, p. 1096–1099, 2019.

[42] S. Ciattaglia e al., «EU DEMO safety and balance of plant design and operating requirements. Issues and possible solutions,» *Fusion Engineering and Design,* vol. 146, pp. 2184-2188, 2019.

[43] IAEA, “IAEA TecDoc 1569 - Liquid Metal Cooled Reactors:Experience in Design and Experiment,” IAEA, Wien, 2007.

[44] USDOE & GIF, “Technology Roadmap Update for Generation IV Nuclear Energy Systems,” 2014.

[45] M. Roldàn Serrano, Concentrating Solar Thermal Technologies, Springer, 2015.

[46] M. Tasbirul Islam, “A comprehensive review of state-of-the-art concentrating solar power (CSP): technologies: Current status and research trends,” *Renewable and Sustainable Energy Reviews,* vol. 91, pp. 987-1018, 2018.

[47] E. Bubelis and W. Hering, “DEMO 16 sectors. HCPB BB with FW cooled in series with BZ & Plant configuration with IHTS+ESS – Conceptual designs and sizing of PHTS, IHTS, ESS and PCS components,” EFDA_D_2MH7AQ, 2019.

[48] R. Haywood, Analysis of Engineering Cycle, Pergamon Press, 1980.

[49] E. Bubelis and W. Hering, “DEMO 16 sectors. HCPB BB with FW cooled in series with BZ & Plant configuration without IHTS+ESS – Conceptual designs and sizing of PHTS and PCS components,” EFDA_D_2MH3H6, 2019.

[50] KWU Siemens, “Conceptual design of the Cooling System for A DEMO Fusion Reactor with Helium Cooled Solid Breeder Blanket,” KWU Siemens - KfK contract No. 315/03179710/0102, 1992.

[51] A. Natalizio and al., “Helium Cooling system design for SEAFP,” SEAFP, SEAFP/R-M8/I1, 1993.

[52] IAEA, “IAEA TecDoc 1198 - Current status and future development of modular high temperature gas cooled reactor technology,” IAEA - TecDoc 1198, Wien, 2001.

[53] G. Melese and R. Katz, Thermal and Flow Design of Helium-Cooled Reactor, America Nuclear Society, 1984.

[54] H. Petersen, «The properties of Helium: Density, Specific Heats, Viscosity, and Thermal Conductivity at Pressures from 1 to 100 bar and from Room Temperature to about 1800 K,» Danish Atomic Energy Commission - Riso Report No. 224, 1970.

[55] National Institute of Standard and Technology, “NIST Chemistry WebBook, SRD 69,” U.S. Secretary of Commerce on behalf of the United States of America, 2018. [Online]. Available:

https://webbook.nist.gov/cgi/fluid.cgi?ID=C7440597&Action=Page. [Accessed 1 November 2019].

[56] W. Wagner and H.-J. Kretzschmar, International Steam Tables - Properties of Water and Steam Based on the Industrial Formulation IAPWS-IF97, Berlin-Heidelberg: Springer, 2008.

[57] K. Vignarooban and al., “Heat transfer fluids for concentrating solar power systems – A review,” *Applied Energy,* vol. 146, pp. 383-396, 2015.

[58] G. Y. Lai, High-Temperature Corrosion And Materials Applications, ASM International, 2007.

[59] A. G. Fernàndez and al., “Thermal characterization of HITEC molten salt for energy storage in solar linear concentrated technology,” *Journal of Thermal Analysis and Calorimetry,* vol. 122, no. 1, pp. 3-9, 2015.

[60] R. Olivares, “The thermal stability of molten nitrite/nitrates salt for solar thermal energy storage in different atmospheres,” *Solar Energy,* vol. 86, pp. 2576-2583, 2012.

[61] L. F. Cabeza, Advances in Thermal Energy Storage Systems, Elsevier - Woodhead Publishing, 2015.

[62] W. Zhai and al., “Modify Hitec molten salt and its properties tests by orthogonal experiment,” in *2nd International Workshop on Materials Engineering and Computer Sciences,* 2015.

[63] M. Xi Ho and C. Pan, “Optimal concentration of alumina nanoparticles in molten Hitec salt to maximize its specific heat capacity,” *International Journal of Heat and Mass Transfer,* vol. 70, pp. 174-184, 2015.

[64] C. Villada and al., “Design and development of nitrate-nitrite based molten salts for concentrating solar power applications,” *Solar Energy,* vol. 188, pp. 291-299, 2019.

[65] C. A. Sequeira, High Temperature Corrosion, Wiley, 2019.

[66] S. Goods, “Creep and the Corrosion Characteristics of Incoloy Alloy 800 in Molten Nitrate Salts,” *Journal of Materials for Energy Systems,* vol. 3, pp. 43-50, 1981.

[67] G. McConohy and A. Kruizenga, “Molten nitrate salts at 600 and 680°C: thermophysical property changes and corrosion of high-temperature nickel alloys,” *Solar Energy,* vol. 103, pp. 242-252, 2014.

[68] A. Fernández e al., «Corrosion properties of a ternary nitrate/nitrite molten salt in concentrated solar technology,» *Renewable Energy,* vol. 80, pp. 177-183, 2015.

[69] A. Fernández e L. Cabeza, «Molten salt corrosion mechanisms of nitrate based thermal energy storage materials for concentrated solar power plants: A review,» *Solar Energy Materials and Solar Cells,* vol. 94, pp. 160-165, 2019.

[70] K. Summers and D. Chidambaram, “Corrosion Behavior of Structural Materials for Potential Use in Nitrate Salts Based Solar Thermal Power Plants,” *Journal of The Electrochemical Society,* vol. 164, pp. 5357-5363, 2017.

[71] S. Bell, T. Steinberg and G. Will, “Corrosion mechanisms in molten salt thermal energy storage for concentrating solar power,” *Renewable and Sustainable Energy Reviews,* vol. 114, no. 109328, 2019.

[72] R. Bradshaw and R. Carling, “Review of the Chemical and Physical Properties of Molten Alkali Nitrate Salts and Their Effect on Materials Used for Solar Central Receivers,” in *Proceedings of The Electrochemical Society, 959-969,* 1987.

[73] Coastal Chemical Co, “Hitec heat transfer salt,” Report of Coastal Chemical Co. LLC, Houston, TX..

[74] J. Slusser and al., “Corrosion in Molten Nitrate-Nitrite Salts,” *Journal of Metals,* pp. 24-27, 1985.

[75] M. Zhu e al., «Electrochemical study on the corrosion behaviors of 316 SS in HITEC molten salt at different temperatures,» *Solar Energy Materials and Solar Cells* , vol. 186, pp. 200-207, 2018.

[76] W. Xie and al., “Corrosion Resistance of Stainless Steel and Pure Metal in Ternary Molten Nitrate for Thermal Energy Storage,” *Energy Procedia,* vol. 158, pp. 4897-4902, 2019.

[77] D. K. Federsel and al., “High-temperature and Corrosion Behavior of Nitrate Nitrite Molten Salt Mixtures Regarding their Application in Concentrating Solar Power Plants,” *Energy Procedia,* vol. 69, pp. 618-625, 2015.

[78] Q. Peng and al., “High-temperature thermal stability of molten salt materials,” *International Journal Of Energy Research,* vol. 32, pp. 1164-1174, 2008.

[79] E. Bettis, L. Alexander and H. Watts, “Design Studies Of A Molten-Salt Reactor Demonstration Plant,” Oak Ridge National Laboratory, 1972.

[80] B. E.G., “Heat Transfer Salt For High Temperature Steam Generation,” Oak Ridge National Laboratory, ORNL-TM-3777, 1972.

[81] F. Cismondi, “Progress of the conceptual design of the European DEMO Breeding Blanket, Tritium Extraction and Coolant Purification Systems,” in *Proceeding of International Symposyum of Fusion Nuclear Technology 14,* 2019.

[82] A. Santucci and al., “The coolant purification system in DEMO: Interfaces and requirements,” *Fusoin Engineering and Design,* vol. 124, pp. 744-747, 2017.

[83] D. Stolten and V. Scherer, Transition to Renewable Energy Systems, Wiley, 2013.

[84] M. J. Montes Pita, *Coastal Chemical data from UNED,* Private communication, 2017.

[85] H. Latham and P. Clarkson, “Fusion Balance of Plant Assessment,” Rolls-Royce Technical Report, EFDA_D_2LLNBX, 2013.

[86] IAEA, “IAEA TecDoc 1531 - Fast Reactor Database 2006 (update),” IAEA - TecDoc 1531, Wien, 2006.

[87] E. Nonbøl, “Description of the Advanced Gas Cooled Type of Reactor (AGR),” Risø National Laboratory Report, Roskilde, Denmark, 1996.

[88] H. Fricker, “The THTR Steam Generator: Design, Manufacture And Installation,” in *Proceedings Of Technology Of Steam Generators - IAEA Specialists Meeting*, Winterthur, Switzerland, 1988.

[89] W. Schuetzenduebel, “Steam Generators For High-Temperature Gas-Cooled Reactor Plants in the U.S.A.,” Gulf General Atomic Report - GA-10338, San Diego, California, 1971.

[90] R. Shah and D. Sekulić, Fundamentals of Heat Exchanger Design, Wiley, 2003.

[91] E. U. Schlunder, Handbook of Heat Exchager Design, Hemisphere Publishing, 1983.

[92] IAEA, “IAEA Power Reactor Database,” IAEA, 04 November 2019. [Online]. Available: https://pris.iaea.org/PRIS/home.aspx. [Accessed 05 November 2019].

[93] N. Kolev, Multiphase Flow Dynamics 5 - Nuclear Thermal-Hydraulics, Springer, 2015.

[94] J. Riznic, Steam Generators for Nuclear Power Plants, Woodhead Publishing - Elsevier, 2017.

[95] Rosatom, “https://www.rosatom.ru/en/,” [Online]. Available: https://www.rosatom.ru/upload/iblock/0be/0be1220af25741375138ecd1afb18743.pdf. [Accessed 05 11 2019].

[96] H. Fenech, Heat Tranfer and Fluid Flow in Nuclear System, Pergamon Press, 1981.

[97] IAEA, “IAEA TecDoc 1691 - Status of Fast Reactor Research and Technology Development,” IAEA, Wien, 2012.

[98] J. Guidez and G. Prêle, Superphénix, Atlantic Press, 2017.

[99] T. Mitra and al., “Challenges in Manufacture of PFBR Steam Generators,” *Energy Procedia,* vol. 7, pp. 317-322, 2011.

[100] S. L. Mannan and al., “Selection Of Materials For Prototype Fast Breeder Reactor,” *Transactions of the Indian Institute of Metals,* vol. 56, no. 2, pp. 155-178, 2003.

[101] D.-H. Hahn and al., “Conceptual design of the sodium-cooled fast reactor KALIMER-60,” *Nuclear Engineering and Technology,* vol. 39, no. 3, 2007.

[102] OECD Nuclear Energy Agency, «GIF 2014, Technology roadmap update for Gen IV nuclear energy systems,» OECD Nuclear Energy Agency, 01 2014. [Online].

Available: https://www.gen-4.org/gif/upload/docs/application/pdf/2014-03/gif-tru2014.pdf. [Consultato il giorno 06 11 2019].

[103] A. Mathews, “The Early Operation Of The Helical Once-Through Boilers At Heysham 1 And Hartlepool,” in *Proceedings Of A Specialists Meeting on Technology Of Steam Generators For Gas-Cooled Reactors - IAEA,* Winterthur, 1987.

[104] M. El-Nagdy and A. Papa, “Design and performance of the helically coiled boilers of two AGR power stations in the United Kingdom,” in *Proceedings of A Specialists Meeting on Technology Of Steam Generator For Gas-Cooled Reactors - IAEA,* Winterthur, 1987.

[105] J. L. Everett III and E. J. Kohler, “Peach bottom unit no. 1: A high performance helium cooled nuclear power plant,” *Annals of Nuclear Energy,* vol. 5, no. 8-10, pp. 321-335, 1978.

[106] H. A.L. and R. Walker, “Fort St. Vrain Nuclear Generating Station Construction And Testing Experience,” *Nuclear Engineering And Design,* vol. 26, pp. 16-26, 1974.

[107] D. Schwarz and R. Baumer, “THTR OPERATING EXPERIENCE,” *Nuclear Engineering and Design,* vol. 109, pp. 199-205, 1988.

[108] Z. Zhang and al., “The Shandong Shidao Bay 200 MWe High-Temperature Gas-Cooled Reactor Pebble-Bed Module (HTR-PM) Demonstration Power Plant: An Engineering and Technological Innovation,” *Engineering,* vol. 2, pp. 112-118, 2016.

[109] M. Esch, D. Knoche and A. Hurtad, “Numerical Discretization Analysis of a HTR Steam GeneratorModel for the Thermal-hydraulics code TRACE,” *Nuclear Technology & Radiation Protection,* vol. 26, pp. 31-38, 2014.

[110] K. Kugeler e Z. Zhang, Modular High-temperature Gas-cooled Reactor Power Plant, Springer, 2019.

[111] R. Bäumer and al.A, “Construction And Operating Experience with the 300-MW THTR Nuclear Power Plant,” *Nuclear Engineering and Design,* vol. 121, pp. 155-166, 1990.

[112] M. Esch e al., «State of the Art of Helium Heat Exchanger development for Future HTR-Projects,» in *Proceedings of the 4th International Topical Meeting on High Temperature Reactor Technology,* Washington, 2008.

[113] Z. Zhang and al., “Design aspects of the Chinese modular high-temperature gas-cooled reactor HTR-PM,” *Nuclear Engineerignand Design,* vol. 236, pp. 485-490, 2006.

[114] Z. Zhang and al., “Current status and technical description of Chinese 2×250MWth HTR-PM,” *Nuclear Engineering and Design,* vol. 239, pp. 1212-1219, 2009.

[115] J. Olson, X. Li and X. Wu, “Tube and shell side coupled thermal analysis of an HTGR helical tube once through steam generator using porous media method,” *Annals of*

Nuclear Energy, vol. 64, pp. 67-77, 2014.

[116] H.-J. Allelein and K. Verfondern, “Major milestones of HTR development in Germany and still openresearch issues,” *Annals of Nuclear Energy,* vol. 116, pp. 114-127, 2018.

[117] D. Hoffman and L. Mears, “Outlook for MHTGR project development,” *Energy,* vol. 16, no. 1-2, pp. 107-110, 1991.

[118] W. H. N. a. F. M. e. K. K. N. H. a. B. D. Scheuermann, “The High Temperature Gas-cooled Reactor: Safety considerations of the (V)HTR-Modul,” JRC - EUR 28712 EN - Publications Office of the European Union, Luxembourg, 2017.

[119] W. Jansing, H. Breitling, R. Candeli and H. Teubner, “KVK and status of the High Temperature Component development,” IAEA, Jülich, 1986.

[120] W. Rohsenow, J. Hartnett and C. Y., Handbook of Heat Tranfer, McGraw-Hill , 1998.

[121] T. Bergman, A. Lavine, F. Incropera and D. Dewitt, Fundamentals of Heat and Mass Tranfer, John Wiley & Sons, 2011.

[122] R. K. Shah and A. Pignotti, “Influence of a Finite Number of Baffles on Shelland-Tube Heat Exchanger Performance,” *Heat Transfer Engineering,* vol. 18, no. 1, pp. 82-94, 1997.

[123] TEMA, Standards of the Tubular Exchanger Manufacturers Association, Tarrytown: Tubular Exchanger Manufacturers Association, Inc., 2007.

[124] K. Thulukkanam, Heat Exchanger Design Handbook, CRC Press Taylor & Francis Group, 2013.

[125] K. Bell, “Delaware method for shell side design,” in *Heat Exchangers: Thermal-Hydraulic Fundamentals and Design,* Washington, Hemisphere/McGraw-Hill, 1981.

[126] T. Kuppan, Heat Exchanger Design Handbook, CRC Press Taylor & Francis Group, 2013.

[127] S. Kakaç, H. Liu and A. Pramuanjaroenkij, Heat Exchangers -Selection, Rating, and Thermal Design, CRC Press, 2012.

[128] C. McDonald, “Helium turbomachinery operating experience from gas turbine power plants,” *Applied Thermal Engineering,* vol. 44, pp. 108-142, 2012.

[129] M. Cumo and A. Naviglio, Thermal hydraulic design of components for steam generation plants, CRC Press, 1991.

[130] G. Spagnuolo and al., “Breeding Blanket Load Specifications Document,” EFDA_D_2NLL6N, 2019.

[131] M. Jawad, Stress in ASME pressure vessels, boilers and nuclear components, John Wiley & Sons, 2018.

[132] H. A. Schmutz, P. Sabharwall and C. Stoots, “Tritium Formation and Mitigation in High Temperature Reactors - INL/EXT-12-26758,” Idaho National Laboratory, Idaho Falls, 2012.

[133] J. Bell, “Tritium Permeation Through Steam Generator Materials,” in *International conference on radiation effects and tritium technology for fusion reactors*, Gatlinburg, 1975.

[134] M. Fütterer, E. D'Agata and R. X., “Is tritium an issue for high temperature reactors?,” *Nuclear Engineering and Design*, vol. 306, pp. 160-169, 2016.

[135] M. Fütterer, X. Raepsaet and E. Proust, “Tritium permeation through helium-heated steam generators of ceramic breeder blankets for DEMO,” *Fusion Engineering and Design*, vol. 29, p. 225–232, 1995.

[136] B. Gainey, “A review of tritium behavior in HTGR systems,” General Atomic, San Francisco, 1976.

[137] J. Bell and al., “Tritium Permeability Of Structural Materials And Surface Effects On Permeation Rates,” in *Tritium technology in fission, fusion, and isotopic application*, Dayton, 1980.

[138] Foster Wheeler Solar Development Corporation, “Molten Salt Steam Generator - Subsystem Research Experiment Phase 1—Final Report,” Sandia National Laboratories, 1982.

[139] ASME, “ASME BPVC - Section II - Part D - Material Properties,” in *ASME Boiler and Pressure Vessel Code - 2015*, ASME, 2015, p. 777.

[140] V. Gnielinski, “New equations for heat and mass transfer in turbulent pipe and channel flow,” *Int. Chem. Eng.*, vol. 16 , no. 2, p. 359–368, 1976.

[141] M. El-Genk, B. Su and X. Guo, “Heat transfer experiments and correlations for natural and forced circulations of water in rod bundles at low reynolds numbers,” *International Journal of Heat and Mass Transfer*, vol. 36, no. 9, pp. 2359-2374, 1993.

[142] N. Todreas and M. Kazimi, Nuclear Systems - Volume I - Therma Hydraulic Fundamentals, CRC Press, 2012.

[143] J. P. Holman, Heat Transfer, McGraw-Hill, 2009.

[144] ASME, “ASME BPVC - Section III - Division 1 - Subsection NB,” in *ASME Boiler and Pressure Vessel Code - 2015*, ASME, 2015, p. 109.

[145] C. Bachmann, “WP12 DEMO Operational Concept Description,” EFDA_D_2LCY7A, 2012.

[146] ASME, “ASME BPVC - Section VIII - Division 1,” in *ASME Boiler and Pressure Vessel Code - 2015*, ASME, 2015.

[147] Invensys Systems, Inc, HEXTRAN 9.0 Keyword Manual, 2002.

[148] M. Alperen, E. Kayabaşi e H. Kurt, «Detailed comparison of the methods used in the heat transfer coefficient and pressure loss calculation of shell side of shell and tube heat exchangers with the experimental results,» *Energy Sources, Part A: Recovery, Utilization, and Environmental Effects,* 2019.

[149] R. Serth and T. Lestina, Process Heat Transfer - Principles, Applications and Rules of thumb, Academic Press - Elsevier, 2014.

[150] S. Kakac, R. Shah and W. Aung, Handbook of single-phase convective heat transfer, Wiley-Interscience , 1989.

[151] F. White, Fluid Mechanics, McGraw-Hill Higher Education, 2008.

[152] G.-H. Gim and al., “Fluid-structure interaction in a U-tube with surface roughness and pressure drop,” *Nuclear Engineering and Technology,* vol. 46, no. 5, pp. 633-640, 2014.

[153] E. Smith, Advances in Thermal Design of Heat Exchnagers, Wiley, 2005.

[154] P. Gilli, “Heat Transfer and Pressure Drop for Cross Flow through Banks of Multistart Helical Tubes with Uniform Inclinations and Uniform Longitudinal Pitches,” *Nuclear Science And Engineering,* vol. 22, pp. 298-314, 1965.

[155] V. Gnielinki, “Heat Transfer in Helically Coiled Tubes,” in *VDI Heat Atlas,* Springer-Verlag Berlin Heidelberg, 2010, pp. 709-711.

[156] J. Gou and al., “An assessment of heat transfer models of water flow in helically coiled tubes based on selected experimental datasets,” *Annals of Nuclear Energy,* vol. 110, pp. 648-667, 2017.

[157] P. Mishra e S. Gupta, «Momentum transfer in curved pipes. I. Newtonian Fluids,» *Industrial & Engineering Chemistry Process Design and Development,* vol. 18, pp. 130-137, 1979.

[158] A. Owhadi, “Boiling in Self-induced Radial Acceleration Fields (PhD. Thesis),” University of Michigan Ann Arbor., 1966.

[159] A. Owhadi, “Forced convection boiling inside helically coiled tubes,” *International Journal of Heat and Mass Transfer,* vol. 11, pp. 1179-1793, 1968.

[160] J. Chen, “Correlation for boiling heat transfer to saturated fluids in convective flow,” *Industrial & Engineering Chemical Process Design and Development,* vol. 5, no. 3, pp. 322-329, 1966.

[161] M. Kind and Y. Saito, “Saturated Flow Boiling,” in *VDI Heat Atlas,* Springer, 2010, pp. 813-827.

[162] L. Zhao, «Convective boiling heat transfer and two-phase flow characteristics inside a

small horizontal helically coiled tubing once-through steam generator,» *International Journal of Heat and Mass Transfer,* vol. 46, pp. 4779-4788, 2003.

[163] Y. Chung and al., “Boiling heat transfer and dryout in helically coiled tubes under different pressure conditions,” *Annals of Nuclear Energy,* vol. 71, pp. 298-303, 2014.

[164] D. Steiner and J. Taborel, “Flow Boiling Heat Transfer in Vertical Tubes Correlated by an Asymptotic Model,” *Heat Transfer Engineering,* vol. 13, no. 2, pp. 43-69, 1992.

[165] S. Jayanti and G. Hewitt, “Prediction of onset of nucleate boiling, net vapour generation and subcooled CHF in coiled tubes,” *Wärme- und Stoffübertragung,* vol. 26, pp. 301-305, 1991.

[166] J. Collier and J. Thome, Convective Boiling and Condensation, Oxford: Oxford University Press, 1994.

[167] G. Berthoud and S. Jayanti, “Characterization of dryout in helical coils.,” *International Journal of Heat and Mass Transfer,* vol. 33, no. 7, p. 1451–1463, 1990.

[168] K. Hwang and al., “Experimental study of flow boiling heat transfer and dryout characteristics at low mass flux in helically-coiled tubes,” *Nuclear Engineering and Design,* vol. 273, pp. 529-541, 2014.

[169] U. NRC, TRACE V5.840 Theory Manual, Washington: U.S. Nuclear Regulatory Commission, 2014.

[170] D. Groeneveld, “Post-dryout heat transfer: physical mechanisms and a survey of prediction methods,” *Nuclear Engineering and Design,* vol. 32, pp. 283-294, 1975.

[171] D. Groeneveld, “Post-Dryout Heat Transfer at Reactor Operating Conditions,” in *Paper presented at the National Topical Meeting on Water Reactor Safety,* Salt Lake City, 1973.

[172] E. Grimison, “Correlation and Utilization of New Data on Flow Resistance and Heat Transfer for Cross Flow of Gases over Tube Banks,” *Trans. ASME,* vol. 59, no. 7, pp. 583-594, 1937.

[173] W. Kast and H. Nirschl, “Pressure Drop in Flow Through Pipes,” in *VDI Heat Atlas,* Springer-Verlag Berlin Heidelberg, 2010, pp. 1058-1063.

[174] M. Cumo and al., “The influence of curvature in post dry-out heat transfer,” *International Journal of Heat and Mass Transfer,* vol. 15, pp. 2045-2062, 1972.

[175] L. Friedel, “Improved friction pressure drop correlation for horizontal and vertical two phase pipe flow,” in *European Two-phase Flow Group Meeting,* Ispra, 1979.

[176] R. Le Feuvre, “A method of modelling the heat transfer and flow resistance characteristics of multi-start helically-coiled tube heat exchangers,” in *8th International Heat Tranfer Conference,* San Francisco, 1986.

[177] D. Rennels and H. Hudson, Pipe Flow - A practical and Comprehensive Guide, Wiley, 2012.

[178] M. Rouaud, Probability, Statistics and Estimation - Propagation of Uncertainties in Experimental Measurement, 2017.

[179] R. Serrano-López, J. Fradera and S. Cuesta-López, “Molten salts database for energy applications,” *Chemical Engineering and Processing: Process Intensification,* vol. 73, pp. 87-102, 2013.

[180] T. Bott, Fouling of Heat Exchangers, Elsevier, 1994.

[181] H. Fricker, “The internal instrumentation of the THTR Steam Generator,” in *IAEA Specialists' Meeting on Technology of Steam Generators ror Gas-Cooled Reactors*, Winterthur, 1987.

[182] C. Henry and C. Elter, “Thermohydraulic Verification during THTR Steam Generator Commissioning,” in *IAEA Specialists' Meeting on Technology of Steam Generators ror Gas-Cooled Reactors*, Winterthur, 1987.

[183] ASME, «ASME BPVC - Section III - Division 5 - High Temperature Reactors,» in *ASME Boiler and Pressure Vessel Code - 2015,* ASME, 2015, pp. 47-120.

[184] K. Singh and A. Soler, Mechanical Design of Heat Exchangers and Pressure Vessel Components, Springer-Verlag, 1984.

[185] M. Jawad e J. Farr, Structural Analysis and Design of Process Equipment, Wiley, 2019.

[186] J. Farr and M. Jawad, Guidebook for the design of ASME section VIII pressure vessels - 4th Ed., New York: ASME Press, 2010.

[187] M. Jawad, Design of Plate and Shell Structures, New York: ASME Press, 2004.

[188] IAEA, “IAEA TecDoc 1682 - Advances in Nuclear Power Process and Heat Applications,” IAEA, Wien, 2012.

[189] Wagner, “Design of the Helium Cooling System and the Auxiliary Systems,” KWU Siemens - SEAFP Final Report - Task M8, Erlangen, 1994.

[190] W. Jansing, “Testing of High Temperature Components in the Component Testing Facility,” in *IAEA Specialists' Meeting on Heat Exchanging Components of Gas-Cooled Reactors*, Dusseldorf, 1987.

[191] S. E. Menon, Gas Pipeline Hydraulics, Taylor & Francis, 2005.

[192] M. Mohitpeur, H. Golshan and M. A., Pipeline Design & Construction, New York: ASME Press, 2007.

[193] API RP 14E, Recommended Practice for Design and Installation of Offshore Production Platform Piping Systems, American Petroleum Institute, 1991.

[194] Standards Norway, «NORSOK P-001 - Process system design,» Standards Norway, 2006.

[195] F. Becker and al., "NUREG/CG-1696 - Integration of NDE Reliability and Fracture Mechanics," U.S. Nuclear Regulatory Commission, 1980.

[196] X. Li and al., "Safety Analysis for Hot Gas Duct Vessel in HTR-PM," *Nuclear Technology,* vol. 174, no. 1, pp. 29-40, 2011.

[197] A. Tarallo, «PBS50 - BB Primary Heat Transfer System - CAD model,» EFDA_D_2NUTW3, 2019.

[198] A. Tarallo, «DEMO 16 sectors, HCPB BB plant configuration with IHTS+ESS: Pre-conceptual 3D CAD model of: BB/DIV/VV PHTS, DHRS, IHTS, ESS and PCS,» EFDA_D_2MS5R8, 2019.

[199] I. Idelchik, Handbook of Hydraulic Resistance, New Delhi: Jaico Publishing House, 2008.

[200] D. Lioce, *Private Communication,* 2019.

[201] L. White, "A review of the existing Gas-Cooled reactor circulators with application of the lesson learned to the new production reactor circulators," Idaho National Laboratory, Idaho Falls, 1990.

[202] IAEA, "Gas-Cooled Reactor Coolant Circulator And Blower Technology," IAEA, San Diego, 1987.

[203] I. Weisbrodt, "Summary report on technical experiences from high-temperature helium turbomachinery testing in Germany," IAEA.

[204] K. Kugeler and S. R., Hochtemperaturreaktortechnik (German), Jülich: Springer-Verlag, 1989.

[205] C. McDonald and M. Nichols, "Helium Circulator Design Considerations For Modular High Temperature Gas-cooled Reactor Plant," in *32nd International Gas Turbine Conference*, Anaheim, 1986.

[206] O. Balje, Turbomachines: A Guide to Design, Selection, and Theory, Wiley, 1981.

[207] S. Garitta, Ph.D Thesis, University of Palermo, Palermo, 2017.

[208] E. Vallone, "Numerical assessment of the thermal-hydraulic performances of the ITER blanket cooling system," Ph.D Thesis, University of Palermo, Palermo, 2018.

[209] ANSYS, Inc, ANSYS CFX - Solver Theory Guide, 2018.

[210] H. Versteeg and W. Malalasekra, An Introduction to Computational Fluid Dynamics, Pearson Education, 2007.

[211] H. Pletcher, D. Anderson and J. Tannehill, Computational Fluid Mechanics and Heat Transfer, CRC Press, 2013.

[212] F. Menter, “Two-equation Eddy-viscosity Turbulence Model for Engineering,” *American Institute of Aeronautics and Astronautics Journal,* vol. 32, no. 8, pp. 1598-1605, 1994.

[213] G. Mesina, “A History of RELAP Computer Codes,” *Nuclear Science and Engineering,* vol. 182, pp. V-IX, 016.

[214] The RELAP5-3D© Code Development Team, “Relap5-3D© Code Manual - Volume I: Code Structure, System Models and Solution Methods,” Idaho National Laboratory, Idaho Falls, 2014.

[215] Committee on the Safety of Nuclear Installations, “Best Practice Guidelines for the Use of CFD in Nuclear Reactor Safety Application - Revision,” OECD-NEA, 2015.

[216] P. Roache, Fundamentals of Computational Fluid Dynamics, Hermosa Publishers, 2003.

[217] The RELAP5-3D© Code Development Team, “RELAP5-3D© Code Manual Volume II: User’s Guide and Input Requirements,” Idaho National Laboratory, Idaho Falls, 2014.

[218] G. Zhou and al., “Thermal hydraulics activities for the consolidated HCPB breeding blanket of EU DEMO,” in *Proceedings of the 14th International Symposium on Fusion Nuclear Technology,* Budapest, 2019.

[219] S. D'Amico, I. Moscato and al., “Preliminary thermal-hydraulic analysis of the EU-DEMO Helium-Cooled Pebble Bed fusion reactor by using the RELAP5-3D system code,” in *Proceedings of the 14th International Symposium on Fusion Nuclear Technology,* Budapest, 2019.

[220] M. Ilic and al., “HETRA experiment for investigation of heat removal from the first wall of helium-cooled-pebble-bed test blanket module,” *Fusion Engineering and Design,* vol. 86, pp. 2250-2253, 2011.

[221] G. Zhou, “Definition of elementary load cases and load cases combination,” EUROfusion Report EFDA_D_2NUETW, 2019.

[222] M. Liu and al., “Review on concentrating solar power plants and new developments in high temperature therma lenergy storage technologies,” *Renewable and Sustainable Energy Reviews,* vol. 53, pp. 1411-1432, 2016.